High resolution 3D Rayleigh wave velocity model of China and surrounding area

Inauguraldissertation
zur Erlangung des akademischen Doktorgrades

eingereicht am Fachbereich Geowissenschaften,
der Freien Universität Berlin

vorgelegt von

Shantanu Pandey

Januar 11, 2013

Als Dissertation angenommen vom Fachbereich Geowissenschaften
der Freien Universität Berlin.

auf Grund der Gutachten
von Prof. Dr. Rainer Kind
und Prof. Dr. Frederik J. Tilmann

Date of Desputation: den 11 Januar 2013, Berlin

Eidesstattliche Erklärung

Bei der eingereichten Dissertation zu dem Thema *"High resolution 3D Rayleigh wave velocity model of China and surrounding area"* handelt es sich um meine eigenständig erbrachte Leistung.

- Ich habe nur die angegebenen Quellen und Hilfsmittel benutzt und mich keiner unzulässigen Hilfe Dritter bedient. Insbesondere habe ich wörtlich oder sinngemäß aus anderen Werken übernommene Inhalte als solche kenntlich gemacht.

- Die Arbeit oder Teile davon habe ich nicht an einer Hochschule des In- oder Auslands als Bestandteil einer Prüfungs- oder Qualifikationsleistung vorgelegt.

- Ich versichere an Eides statt, dass ich nach bestem Wissen die reine Wahrheit erklärt und nichts verschwiegen habe.

Statement of Authorship

The thesis I have submitted entitled *"High resolution 3D Rayleigh wave velocity model of China and surrounding area"*

- I have only used the sources indicated and have not made unauthorised use of services of a third party. Where the work of others has been quoted or reproduced, the source is always given.

- I have not presented this thesis or parts thereof to a university as part of an examination or degree.

- I affirm that the above is the absolute truth to the best of my knowledge and that I have not concealed anything.

_____

Shantanu Pandey
11 Januar 2013

Abstract

China is located at the triple junction where the Indian plate, the Pacific plate and the Eurasian plate meet. This makes this region very interesting from the geodynamic point of view. The most significant is the continental collision between the Indian and Eurasian plate, which started at (∼50 Mya). It was this event that gave rise to the Himalayas which is the highest mountain range and to the Tibetan plateau which constitutes the tickest crust on Earth. China itself has three major Precambrian cratons: the North China craton (also called Sino-Korean craton), the Yangtze craton (also called South China craton) and the Tarim block. The interactions among these different blocks have formed the present day tectonic features and caused many intraplate earthquakes. These tectonics settings have made China an interesting place for various kind of studies as all of these events have left their imprint on the upper mantle structure. It is generally agreed that the lithosphere is thick in west China while much of the lithospheric root was lost beneath the cratons in east China. It is still an open debate whether the mantle lithosphere beneath the Tibetan plateau has doubled its thickness as did the crust above or whether much of the thickened lithosphere was removed by mantle convection and delamination.

For the present work we carry out our research with two objectives :

(A) Constructing a high resolution three-dimensional velocity model of the upper mantle.

(B) Probing convection and deformation of the mantle through analysis of seismic anisotropy.

In our study we determine the three dimensional Sv wave speed and the azimuthal anisotropy model by analyzing vertical component multimode Rayleigh wave seismograms. We use data of broadband stations within and around China. We construct the three dimensional model using a two step procedure. In the first step we use the automated ver-

sion of the Cara & Lévêque (1987) waveform inversion technique. Secondary observables were used to model modeling each multimode Rayleigh waveform to determine the path-averaged mantle Sv wave speed structure. We have used the 3SMAC model for the crustal part and a smooth version of PREM for the upper mantle velocity structure as an initial model. In the second stage we combine the 1-D velocity models in a tomographic inversion to obtain the three dimensional Sv wave speed structure and the azimuthal anisotropy as a function of depth.

The velocity model achieved, showed that the upper most part of our model (till 200 km) is in good agreement with the tectonics, though below 200 km there seems to be loss of resolution. There is a clear distinction in terms of the lithospheric thickness from east to west China. In the west, including Tibet and Pamir, the thickness of lithosphere nearly reaches 200 km. Whereas in the eastern part of the Yangtze craton, 70-80 km of the lithospheric thickness is observed. The absence of lithosphere in the North China carton suggests that in this region the thickness is less than 70 km, which is beyond the resolving power of our method. Deep lithospheric roots with thickness around 100-150 km can be observed in the Tarim basin, the Sichuan basin and the Ordos block. It is widely accepted that the extent of the Indo-Eurasian collision deformation is being restricted by the Tarim basin in the north and in the east by the Ordos block and the Sichuan basin. The model is also comparable with results of various receiver function and SS precursor studies.

The pattern of azimuthal anisotropy in central and western Tibet shows a clear indication of decoupling between the crust and mantle. The orientation of the anisotropy is changing from east-west at shallow depth to north-south at deeper depth. Though in the eastern part of Tibet along the Kunlun fault and the Sichuan basin the orientation remains the same through all depths. This is a clear indication for coupled crust and mantle.

Zusammenfassung

In China treffen drei wichtige Kontinentalplatten aufeinander: die indische Platte, die pazifische Platte, sowie die eurasische Platte. Dies macht diese Region aus geodynamischer Sicht sehr interessant. Die bedeutenste geologische Struktur ist die noch sehr junge Kontinentalkollision zwischen indischer und eurasischer Platte (∼50 Mya). Dieses Ereignis führte zur Ausbildung des himalayischen Gebirgskette und einer sehr mächtigen Krustenstruktur in der Region Tibet. In China finden sich drei bedeutende präkambrische Kratonstrukturen: der Nord-China-Kraton (Sino-Korean-Kraton), der Süd-China-Kraton (Yangtze-Kraton) und der Tarim-Block. Die Interaktion zwischen den einzelnen Blöcken ist für die heute sichtbaren tektonischen Strukturen, sowie für viele der intrakontinentalen Erdbeben, verantwortlich. Diese tektonischen Vorraussetzungen machen China zu einem sehr interessanten Platz für eine Vielzahl von unterschiedlichen Untersuchungen. All diese Ereignisse haben ihre Spuren in der Struktur des oberen Mantels hinterlassen. Im allgemeinen wird eine mächtige Lithosphäre im Westen Chinas angenommen. In den östlichen Kratonen Chinas geht man von einem Verlust der lithosphärischen Wurzel aus. Nach wie vor ist die Frage offen ob der litospärische Mantel unter Tibet seine Mächtigkeit verdoppelt hat oder große Teile der Lithospäre durch Mantelkonvektion und Delamination entfernt wurden.

Die vorliegende Arbeit verfolgt zwei Ziele:

(A) Erstellung eines hochauflösenden dreidimensionalen Geschwindigkeitsmodels des oberen Mantels.

(B) Erforschung der Mantelkonvektionen und Manteldeformationen durch Analyse der seismischen Anisotropie.

In dieser Arbeit wird ein dreidimensionales Model der Sv-Wellen Geschwindigkeit sowie

der azimuthalen Anisotropie berechnet. Dieses wird durch die Analyse der vertikalen Komponente von mehrmodigen Rayleigh-Wellen-Seismogramen erstellt. Für die Analyse werden Daten von Breitbandstationen in China und angrenzenden Regionen verwendet. Das dreidimensionale Modell wird in zwei Schritten berechnet. Im ersten Schritt wird eine automatisierte Wellenform-Inversionstechnik Cara & Lévêque (1987) verwendet. Sekundäre Messgrößen werden für die Modellierung von mehrmodigen Rayleigh Wellenformen verwendet. Aus diesen wird dann eine über den Pfad gemittelte Sv-Wellengeschwindigkeitstruktur berechnet. Als Ausgangsmodelle wurden das 3SMAC-Modell für die Krustengeschwindigkeiten, sowie eine glatte Version des PREM Models für die Wellengeschwindigkeiten des oberen Mantels verwendet. In einem zweiten Schritt werden die eindimensionalen Geschwindigkeitsmodelle mittels tomographischer Inversion zu einem dreidimensionalen Model der seismischen Geschwindigkeit und der azimuthalen Anisotropie kombiniert.

Der obere Teil unseres Modells (bis 200 km Tiefe) lässt sich gut mit den vorherrschenden tektonischen Strukturen erklären. Ab einer Tiefe von 200 km lässt die Auflösung des Models allerdings stark nach und erschwert weitere Interpretationen. Es kann deutlich zwischen Lithospärenmächtigkeiten im Osten und Westen Chinas unterschieden werden. Im Westen Chinas, einschliesslich Tibet und Pamir, erreicht die Lithospäre Mächtigkeiten bis zu 200 km, wohingegen sie im Yangtze-Kraton im Osten Chinas jediglich Mächtigkeiten von 70-80 km erreicht. Das komplette Fehlen der Lithospäre im Norden Chinas spricht für eine Mächtigkeit von unter 70 km, diese liegt jedoch unter dem Auflösungsvermögen unserer Methode. Lithosphärische Wurzeln mit einer Tiefe von bis zu 100-150 km können im Tarim-Basin, im Sichuan-Basin, sowie im Ordos-Block beobachtet werden. Desweiteren gilt als gesichert, dass sich die Deformation aufgrund der Kollision von indischer und eurasicher Platte auf das Tarim-Basin im Norden und auf das Sichuan-Basin im Osten beschränkt. Das Model ist vergleichbar mir Ergebnissen aus verschiedenen Receiver Func-

tion und SS Precursor Studien.

Die Strukturen der azimuthalen Anisotropie in Zentral- und Westtibet deuten auf eine Entkopplung der Krust vom Mantel hin. Die Orientierung der Anisotropie ändert sich von Nord-Süd in geringen Tiefen hin zu Ost-West in größeren Tiefen. In Teilen Tibets entlang der der Kunlun Störung und im Sichuan-Basin gibt es keinen Wechsel der Anistropierichtung im Bereich von 75-125 km Tiefe. Dies deutet auf eine Kopplung von Kruste und Mantel hin.

Contents

List of Figures

Chapter 1

Introduction

The quest in geophysics has always been to delineate, as far as possible, the minute deep internal geological/geodynamical structure of the Earth. The whole operation of adducing the geology in one dimension (1D), two dimension (2D) or three dimension (3D) from geophysical measurements forms the domain of interpretation, a word which aptly implies indeterminate nature. However, the interpretation with a certain degree of confidence level is labeled as inversion of geophysical data. The objective in applied geophysics is to obtain a minimal set of parameters to completely describe the system and laws relating these to any set of measurements. A coherent set of such laws is a physical theory to the extent that the parameter can only be estimated from measurements one may equivalently consider that the relevant law impose some relationships between the results of some measurements (Tarantola & Valette, 1982).

The seismic waves propagation velocity in the Earth depends on various factors related to the propagation medium viz. lithology, temperature, pressure and composition but also, the wave propagation direction and particle motion for each individual phase should be taken into consideration when anisotropy effects are taken into account. The 3D interpre-

tation of the variations in the travel time of seismic waves from different observed phases can be realized by seismic tomography. It involves compiling the information, by measuring different facet of seismogram and inferring it with the material's physical parameters through the solution of geophysical inverse problem. Some of the important tomographic inversion techniques are: (i) the reflection or refraction travel time tomography which make use of certain phases arrival time measurements, (ii) the finite-frequency travel time tomography which apart from the travel time information also make use of wave diffraction effects and (iii) the waveform inversion which involves the matching of synthetic waveform with the recorded waveform.

Earlier to the emergence of inversion techniques in computational seismology was extremely difficult to quantify both algebraically and numerically the dispersed surface wave package that presents the strongest signal in the seismogram. The first formulation of the surface wave dispersion problem was done by Stoneley (1928) for a Rayleigh wave propagating in two layer model resting over a half-space though a restricted set of some specific parameters (Dziewonski & Romanowicz, 2007). Haskell (1953) adapted the elastic media approach and made it suitable for computing dispersion (of both Rayleigh and Love wave) curves for a layered medium underlain by a half-space. This method involves the multiplication of matrices famously known as Haskell's matrix, which has been applied in the computation of synthetic seismograms using the reflectivity method (Fuchs & Müller, 1971).

Early 1970's marked the evolution of geophysical inverse theory (Backus & Gilbert, 1967, 1968, 1970; Backus, 1970a,b,c) providing the necessary tool to deal with the inevitable 'ill-posed' nature of geophysical inverse problems that ultimately led to the development of seismic tomography. Aki & Lee (1976) dealing with local-scale body-wave tomography and

Dziewonski (1984) used long-period data for imaging the upper mantle through matching the synthetic and observed waveforms. This development ultimately led to the mapping of large scale heterogeneity of the earth in much greater details, however, the non-linear nature of the relationship between the parameters describing the model and the recorded signal is a computational intensive process that has always been a contentious issue in this regard.

In most of the tomographic inversions of surface wave data, the long-period seismograms are first interpreted in terms of dispersion and/or attenuation curves before performing the inversion in terms of laterally and vertically varying material properties. An alternative to this approach is to perform a direct waveform inversion as proposed by Cara & Lévêque (1987) inverting a set of secondary observables built up from the seismogram thus enhancing the signal-to-noise ratio and making the relation between model parameters and inverted observables more linear. The approach of Cara & Lévêque (1987) found its wide spread applications in different parts of the Globe: viz in Antarctica (Sieminski et al., 2003), in Australia (Debayle, 1999; Debayle & Kennett, 2000a), in Afro/Arabia (Debayle et al., 2001), in South America (Heintz et al., 2005), in Iceland (Pilidou et al., 2004) and in East Asia (Priestley et al., 2006).

The tectonic history of China has attracted many geoscientists over many decades for various kinds of investigations. The fundamental mode surface wave studies in China have achieved a resolution of several hundred kilometres showing features that correlates well with the large geological units (Romanowicz, 1982; Griot et al., 1998; Ritzwoller & Levshin, 1998; Curtis et al., 1998; Huang et al., 2003; Friederich, 2003). These studies conclude that the lithosphere in China territories extends to a thickness of more than $\sim$200 km in the western China and to less than $\sim$100 km in eastern China. However, there can be signif-

icant differences at the regional scale. For example, Griot et al. (1998) and Huang et al. (2003) observed a thick lithosphere beneath the Tibetan plateau, while others reported a thin mantle lid (Romanowicz, 1982) or a missing lithosphere (Friederich, 2003) beneath central and northern Tibet. The discrepancy probably arises from the different resolution power of the different data sets as well as from the different methodological approaches. Lebedev & Nolet (2003), Priestley et al. (2006) and Feng & An (2010) have observed that the upper mantle structure of eastern Asia can be better constrained by fitting multi-mode surface waveforms but it is significant to mention that these investigators have used only few stations in China, for which waveform data was available. We believe that the final results obtained in this work contain a higher resolution model representing finer details due to the usage of extensively large dataset within the area under investigation and also, due to the large data set with and increased number of shorter paths resulting in a better constraint of the results obtained. Moreover, recently Obrebski et al. (2012) performed joint inversion of body and surface wave data in this region and the reported results corroborate with the results obtained in this work.

Using different methods of analysis like SS-precursors (Heit et al., 2010) and S receiver functions (Kumar et al., 2006) a thick lithosphere beneath Tibetan plateau is acknowledged fact, rejecting a series of models invoking convective removal of a thickened Asian lithosphere in northern Tibet (Houseman et al., 1981). Furthermore, during this work we compared our results with the S receiver functions results from (Kumar et al., 2006) and noticed a good agreement of the general depth of lithosphere, however, the extent of subducting Indian and Asian lithosphere remains an unresolved issue between these two method as presented by (Figure 4.16).

The research work outlined and carried out in the present thesis will aim specifically in

(i) constructing the high resolution seismic velocity model of upper mantle for the Tibet and surrounding area including China, and (ii) to probe mantle flow involving the azimuthal anisotropy. Part (i), which is generating the velocity model, is performed through Rayleigh-wave tomography whereas for part (ii) the azimuthal anisotropy information has been derived from the final velocity model.

The structure of this thesis follows like this:

First we presented a small introduction of the work in the present chapter (Chapter 1), which is followed by Chapter 2 in which we describe the tectonic setting of China. In this chapter we divide the study area in blocks based in the know geologic setting and tectonic history. This division will help in interpreting the final model obtained where some striking features were obtained.

Chapter 3 begins with brief introduction about basic concepts related with the surface waves. We describe the two stage method used in order to achieve the 3D Sv velocity model for the China and surrounding area and also, we explained the technique used by us for obtaining the 3D azimuthal anisotropy for the study area.

In Chapter 4 we presented the 3D velocity model describing the Sv wave heterogeneity in the upper mantle for the study area. The 3D azimuthal anisotropy model is also presented along with the velocity model. Apart from the discussion of the result we presented a few information which is helpful to understand the technical aspects of the result with relation to the synthetic test for the reliability of the model also presented here. In the last chapter (Chapter 5) we give the main conclusion of the research work presented in this thesis.

Chapter 2

Study Area

2.1 Tectonic History

Mainland China is known as a conglomerate of various continental fragments. They are separated by mountain ranges, folds, faults and the world's heighest plateau (metaphorically known as the roof of the world). These fragments consist of cratons (North and South China cratons) and basins (Tarim, Qaidam, Junggar, Sichuan and Songliao). Numerous tectonic events are responsible for the present shape of the region. During the late Proterozoic (∼550 Mya) North and South China were part of Eastern Gondwana for millions of years. Later (∼450 Mya), the South China craton and the North China craton rifted away from Gondwana and moved across the ancient shrinking Proto-Tethys Ocean. A new ocean was forming at its southern end, the Paleo-Tethys Ocean. For most of the Paleozoic (250-500 Mya), the North China Craton was an independent continent surrounded by oceans located in the extreme north of the Earth. During the Triassic (200-250 Mya) it collided with Siberia and Kazakhstania, completely closing the Proto-Tethys to comprise the last stage in the formation of Pangaea. Meanwhile South China became an independent continent. Cimmeria, a microcontinent that consisted of today's Tibet, Iran, Turkey,

and parts of Southeast Asia rifted away from Gondwana (just as North and South China did earlier), and was heading towards Laurasia. The Paleo-Tethys Ocean started to shrink, while the new Tethys Ocean expanded. In the Middle Triassic (200-250 Mya), the eastern portion of Cimmeria collided with South China, and together they drew northwards, towards Laurasia. In the Early Jurassic (150-200 Mya) epoch, South China collided with North China, forming China as we know it today. North China and South China have been together since their collision in the Jurassic (Li, 1998; Yang, 1998; Yin & Harrison, 2000). During the Early Cretaceous (60-150 Mya) major break-up of Pangaea began, when the minor supercontinent of Gondwana separated into multiple continents (Africa, South America, India, Antarctica, and Australia). In the late Cretaceous ($\sim$90 Mya), with the splitting of Gondwana, India (or the Indian Plate) charged across the equator and began moving north, at rate of 15 cm yr^{-1} and began closing the Tethys Ocean. It is believed to have begun colliding with Asia between 55 and 50 Mya in the Eocene (30-60 Mya) epoch of the Cenozoic. It was after the collision of the Indian plate with Asia that the rate of convergence reduced from 10 cm yr^{-1} to about 5cm yr^{-1}.

A key element in understanding plate tectonics is the knowledge of the lithosphere-asthenosphere boundary (LAB). The LAB is the boundary at which the Earth's rigid outer shell that forms the plates (lithosphere) floats over the highly viscous, mechanically weak asthenosphere, in geological time scale. It is important to have a clear understanding of the above mentioned time scales and motions of the blocks while interpreting any seismological results. The scenario described above regarding the motion of different blocks leads us to divide the study area into three major tectonic blocks: the North China Craton (NCC), the South China Craton (SCC) and the Tibetan Plateau. Then there are a few small blocks which also contribute to the present tectonic situation, like the Qaidam basin, the Sichuan basin, the Ordos block and the Tarim basin.

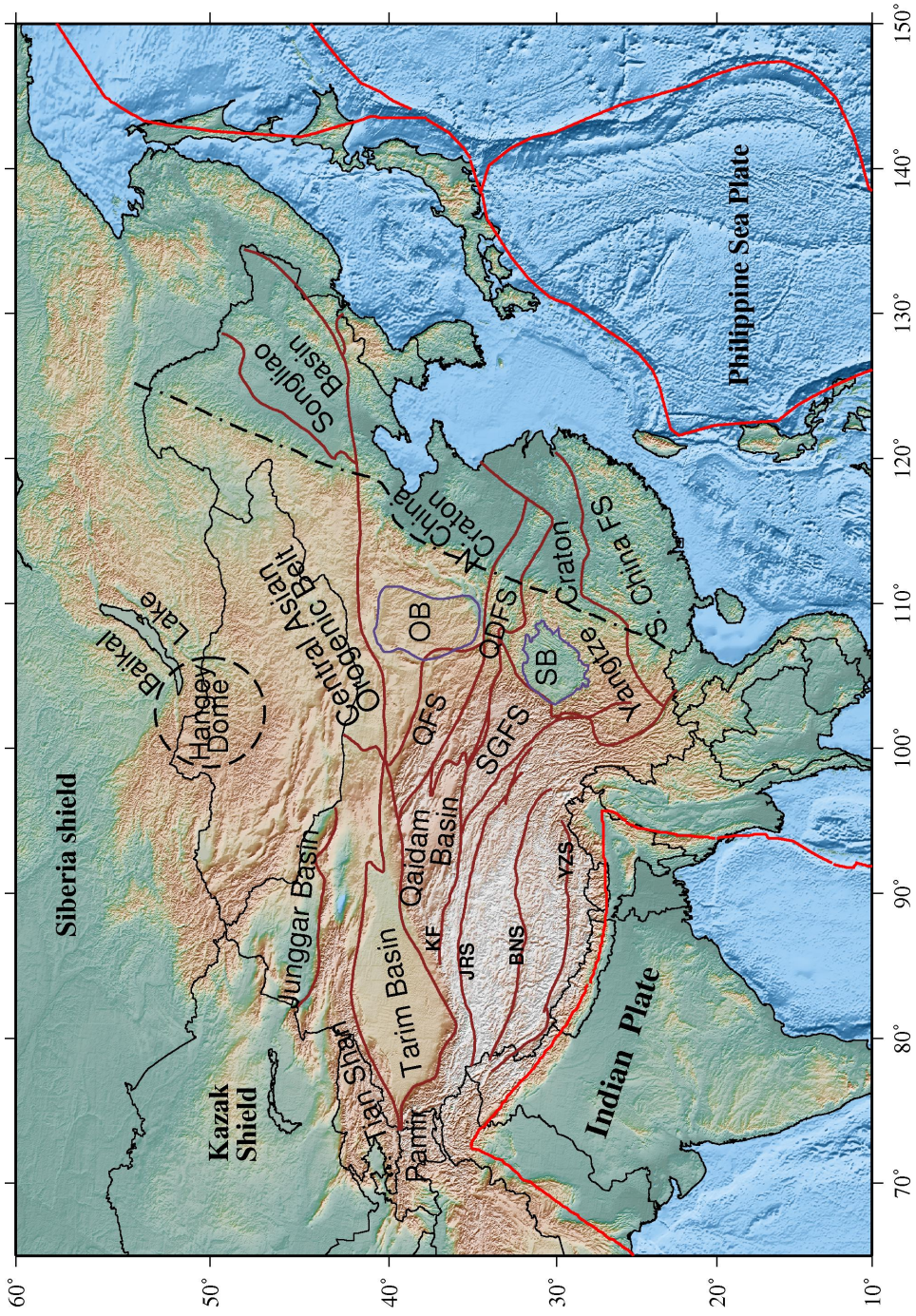

Figure 2.1: Topography map of China and the surrounding area with major tectonic units boundary lines. Tectonic boundary lines: Tarim basin, Junggar basin, Qinling FS (Fold System), Qilian FS, Songliao basin, North China Craton, Yangtze Craton, South China FS and SGFS, Songpan-Ganzi Fold System (SGFS) are form Zhang et al. (2011b). Sichuan basin (SB) and Ordos block boundary lines are from Obrebski et al. (2012). Suture lines: Kunlun fault (KF), Jinsha-River suture (JRS), Bangong-Nujiang suture (BNS) and Yarlung-Zangbu suture (YZS) are from Styron et al. (2010). The Plate boundary are defined by red line. Black colour dashed-dot line denotes the North-South Gravity Lineament Xu (2007). The black dash circle shows the approximate area around Hangey dome

2.2 Tectonic Setting

China is geologically highly heterogeneous, consisting of Precambrian platforms surrounded by accreted continental fragments and fold belts of various ages. The heterogeneity is most striking with the sharp contrast between the newly formed Tibetan Plateau in the west with an average elevation of 5000 m related to the India-Eurasia collision ∼60 Mya ago and the Archean core of the Sino-Korean and Yangtze cratons in the east (Figure 2.1). This heterogeneity in geology also makes the tectonics of China and surrounding areas very complex. Present day China is part of the Eurasian plate, except for the Himalayas and the Coastal Range of Taiwan, which are margins of the Indian and Philippine Sea plates, respectively. It consists of nuclei of Precambrian cratons (North and South China) and a mosaic of later accreted micro-continents and fold belts (part of the Tibetan Plateau).

In broad sense of tectonic block the whole mainland China can be divided in four groups. The first one is Tarim basin which appears as a strong and old block with littel to no seismicity at all (Figure 2.3). Then the second one is Tibet that is the result of accretion of various micro-continents, full of fold belts and fault lines. The third one, North China Block (NCB) consists of Songliao basin in the north and the NCC (also known as Sino-Korean craton) in the south. Last and fourth one is the South China Block (SCB) which is combination of Yangtze craton and the precambrian Cathaysia Block (South China fold system as in figure 2.1). Both the NCB and the SCB were parts of the supercontinent Rodinia in the early Neoproterozoic (at 1.0 Gya). The breakup of Rodinia separated the NCB and the SCB from the other former Rodinian continent. As mentioned before, the collision between NCB and SCB occurred during the late Triassic to middle Jurassic along the Qinling-Dabie Orogenic belt which is the distinguishing boundary between them (Liang et al., 2004; Ma et al., 1984; Ni & Barazangi, 1984; Sodoudi et al., 2006).

Two major processes controlled the Cenozoic tectonics of East Asia, firstly the collision of the India and Eurasia plates that started at about 40–70 Mya; and secondly the subduction of the Pacific (and later the Philippine Sea) plate that started during the late Mesozoic. The India-Eurasia collision is the biggest event in Cenozoic tectonic history of Asia. The Himalayan-Tibetan orogen was built upon a complex tectonic assemblage of micro-continents and island arcs accreted onto the southern margin of Eurasia since the early Paleozoic. The India-Eurasia collision caused the formation of the Himalayas, thickening of the Tibetan crust, and the uplift of the Tibetan Plateau. At least 1400 km of north-south shortening has been absorbed by the orogen since the onset of the collision (Yin & Harrison, 2000; Molnar & Tapponnier, 1975; Tapponnier & Molnar, 1977; Replumaz et al., 2004; Chen et al., 2010; Zhang et al., 2011b; Li et al., 2006).

2.2.1 North China craton (NCC)

The NCC is one of the oldest continental nuclei in the world. It is composed of Archean and Proterozoic rocks in the eastern China continent (Li, 1998). Its basement is divided into three blocks: the eastern and the western Blocks and the intervening Trans-North China Orogen. A craton is usually characterized by high velocity with a thick keel (lithospheric root ∼200 km) like one sees in the Siberian craton, the Kaapvaal craton (South Africa) and in many more. The eastern block of NCC is unusual for a craton as it is severely affected by lithospheric thinning. It experienced significant tectonic rejuvenation with dramatic regional variations in the late Mesozoic and Cenozoic, evidenced by the widespread lithospheric extension, voluminous magmatism and large-scale basin formation (Zheng et al., 2006). During this period, the thick cratonic lithosphere lost a significant proportion of its deep mantle keel from 200 km to less than 80 km (Figure 2.2). The seismic

structural images together with geological, petrological, geochemical and mineral physics data suggest that the fundamental destruction of the eastern NCC lithosphere may have been triggered mainly by the deep subduction of the Pacific plate, especially during the Late Mesozoic. This loss of lithosphere is also reported in many previous studies (Menzies et al., 1993; Menzies & Xu, 1998; Xu, 2001; Xu & Zhao, 2009). This makes the NCC a natural laboratory to study the modification process of the old Archean craton.

Apart from the lithospheric thinning another intriguing structural feature of the NCC is the NNE-SSW trending North-South Gravity Lineament (NSGL) separating the mountain range in the Trans-North China orogenic belt and the basin in the eastern part (shown as a black dash-dot line in figure 2.1). The two geological units on the opposite sides of the NSGL differ significantly, not only in surface topography but also in deep tectonics, as manifested by striking contrasts in altitude, gravity as well as in lithological stratum (Zhu et al., 2011). This lineament runs over 3500 km from northeast China to south China and is $\sim$100 km wide. The Bouguer anomaly decreases rapidly from -100 mGal in the west to -40 mGal in the east (Li & Yang, 2011). In the east of the NSGL of NCC is dominated by lowland with an altitude of less than 200 m. The average crust thickness beneath this region is thin (<35 km) with a minimum of $\sim$28 km beneath the Bohai Sea in the east (Li et al., 2006). The regional Bouguer gravity anomaly is weakly negative and high heat transfer indicates thin lithosphere (<80 km). In contrast the western NCC, which comprises the Ordos block is characterized by high elevated land (>500 m, up to 3500 m), thick crust (>40 km) and negative Bouguer anomalies indicating thick lithosphere (>100 km) (Ma et al., 1984; Chen, 2010; Xu, 2007; Zheng et al., 2006; Obrebski et al., 2012).

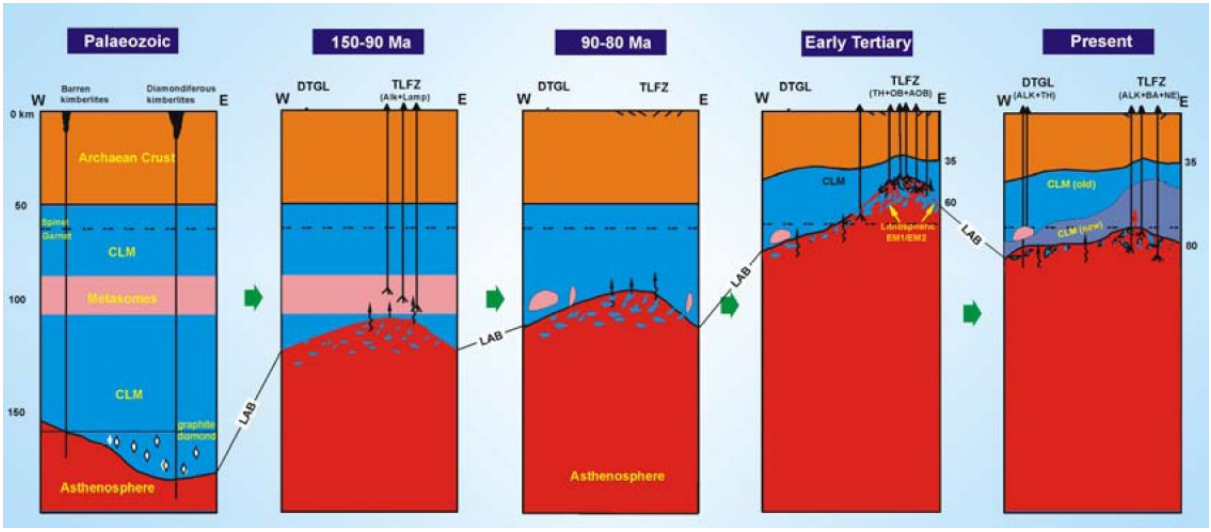

Figure 2.2: Historical view-point depicting the lithospheric thinning during late Mesozoic to Cenozoic [*after* Xu (2001)]. The transition depicted here through this sketch shows the thick and cold (blue colour) lithosphere nearly 180-200 km in the Palaeozoic era compare to thin and hot lower lithosphere nearly 60-80 km in the present situation.

2.2.2 South China Block (SCB)

Amalgamation of the Proterozoic Yangtze Craton and the South China Fold Belt (figure 2.1) to form the South China Block first occurred during 1.0–0.85 Gya. The closure of the eastern Paleo-Tethys Ocean during the Late Triassic-Early Jurassic led to the collision of the North China Craton and the South China Block along the Qiling-Dabie fold belt. The unified South China Block has been central to recent studies on the Precambrian crustal evolution and position of South China in Proterozoic supercontinents (Charvet et al., 2010; Zhou et al., 2012). The two major Precambrian blocks – the Yangtze Block to the northwest and the Cathaysia Block to the southeast defined by the boundary of Jiangshan-Shaoxing fault zone.

In general the SCB is same as the NCC. The NSGL divides the whole block topographically as well as tectonically. Also the way, the western part of NCC has prominently stable

Ordos block which remains unperturbed with surrounding deformation, the western part of SCB consist of Sichuan block. One of the striking resemblances in both the Ordos block and the Sichuan basin is little to no seismicity (Figure 2.3). Except the Sichuan is low-elevated area (basin) than Ordos block. The Sichuan Basin is part of the Yangtze craton that has been in a stable sedimentary environment since the late Paleozoic except that parts of the craton experienced folding during the Eocene and Oligocene (Yin, 2010). The western and southern boundaries of the Sichuan Basin formed as the eastern/southeastern margin of the Tibetan Plateau divided by the LongmenShan thrust fault (Li et al., 2009; Zhang et al., 2010a, 2011a; Chen et al., 2010; Feng & An, 2010).

2.2.3 Tibet

It has long been established that the reason for the creation of Tibet is the collision of the Indian plate with the Eurasian plate during the last ∼50 Ma. The crust appears to have been formed by the process of accretion which can be divided into four sections, from north to south: the Songpan-Ganzi terrane, then the Qiangtang Block, the Lhasa Block and the Himalayan block. Though these blocks are not indicated in the figure 2.1, but these terrains or block are divided by different sutures from the south (as shown in figure): the Yarlung-Zangbo Suture (YZS), the Bangong-Nujiang Suture (BNS) and the Jinsha-River Suture. The Kunlun fault (KF) up in the north is considered to be the northern most extent of the Tibetan Plateau, which is the boundary between the high altitude Songpan-Ganzi terrane and the Qaidam Basin (Figure 2.1). The Tibetan Plateau has on an average elevation of ∼4-5 km above sea level with very thick crust ∼70 km (Zhang et al., 2011b). An important feature of this collision is the absence of deep seismicity (with few exception in the south, figure 2.3) indicates that the Indian plate does not descend deep beneath Tibet. Still it is debatable whether the lithosphere beneath the Tibetan plateau

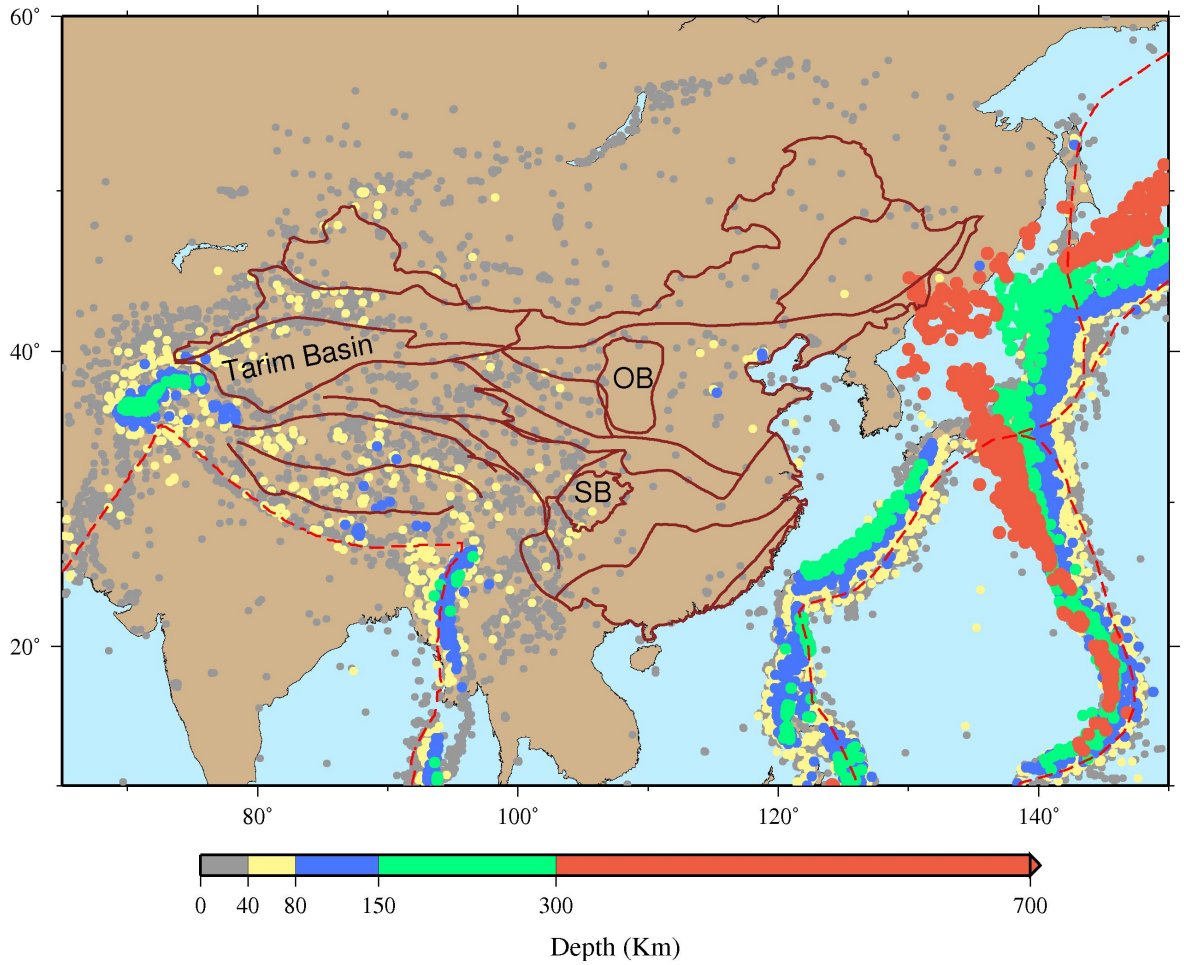

Figure 2.3: The map showing the seismicity in the region are plotted in dots. Different colours of the dot indicates the depth of the earthquake as shown in the scale below the map. The location and depth values used here for this plot are from EHB catalog (Engdahl & Hilst, 1998)

has doubled its thickness as did the crust above, or much of the thickened lithosphere was removed by mantle convection and delamination.

2.3 Data

For more than 2 decades most of the seismological studies in the region have focused on the Tibetan Plateau and its surrounding area (Nábelek et al., 2009; Mechie et al., 2011; Li et al., 2008; Haines et al., 2003). The deployment of permanent stations and temporary

experiments have multiplied in China over the last decade. Stations in China are never short of recorded events given its closeness to seismically active areas like the Pacific plate subduction under Japan, the Philippine sea plate and the Alpide belt, which extends from Java to Sumatra through the Himalayas till the Mediterranean. The waveform data from more than 400 stations with registration ranging from 1999 to 2007 has been requested from different agencies. We requested waveform data of 47 broadband stations from the Chinese Digital Seismic Network (CDSN) which have never been used for this kind of study. In addition to this, waveform data was requested from the IRIS and GEOFON data center, for more than 300 temporary station within China and nearly 100 stations around China. The station distribution with their respective network code is shown in figure 2.4. The complete list of stations including lattitude, longitude and there network code is availabel at the end of this thesis (Appendix A).

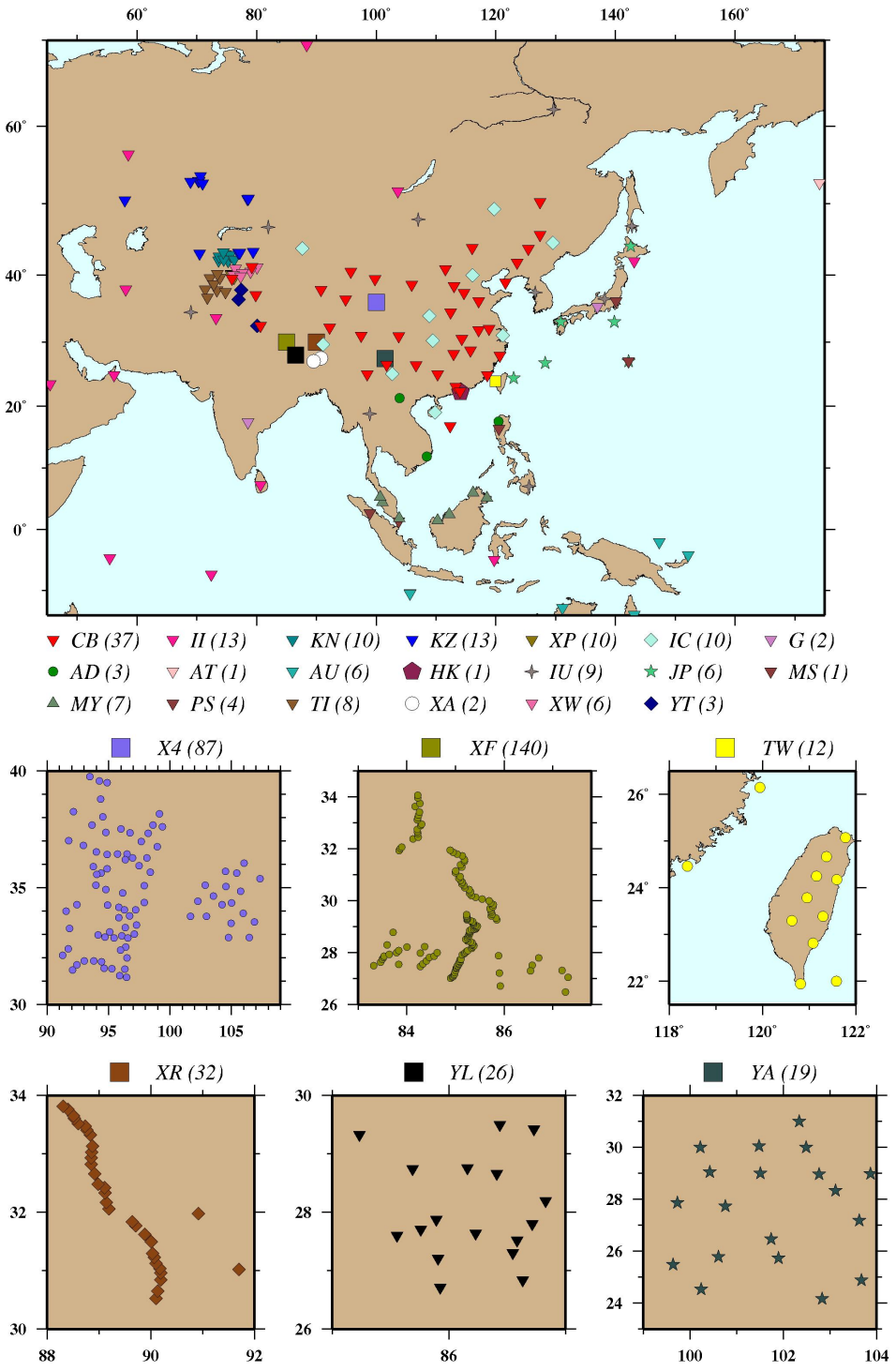

Figure 2.4: The map showing the location of the stations used for the study. Each network is assigned with separate symbol and colour which are plotted on the map. The bottom part of the figure is the detail station map of the temporary network containing stations in big numbers but in small area (squares in the main map). In the middel is the informaion regarding each symbols assigned to different network with the number of station falls under that network next to the name within brackets. Detail list is is given in Appendix A.

Chapter 3

Methodology

3.1 Introduction

The bulk of knowledge of the Earth's internal structure is derived from studies of the propagation of elastic waves generated by earthquakes. Two distinct groups of these considered seismic waves are body waves and surface waves. Body waves can travel deep in the Earth and energy transfer takes place in compressional (P) and shear (S) waves. Surface waves (Rayleigh wave and Love wave) are confined to the outer parts of the solid Earth. For laterally homogeneous models, Rayleigh waves are radially polarized (P/SV) and exist at any free surface, whereas Love waves are transversely polarized and require some velocity increase with depth (or a spherical geometry).

Seismograms are the seismic records of the propagation of elastic waves generated due to the Earth's ground motion that are used by seismologist as observation. In many records (excluding deep events), the obvious visible fact is that the surface waves are generally the strongest arrivals in comparison to body waves at teleseismic distances (See Figure 3.1). The surface waves contain a great deal of information about crust and upper mantle

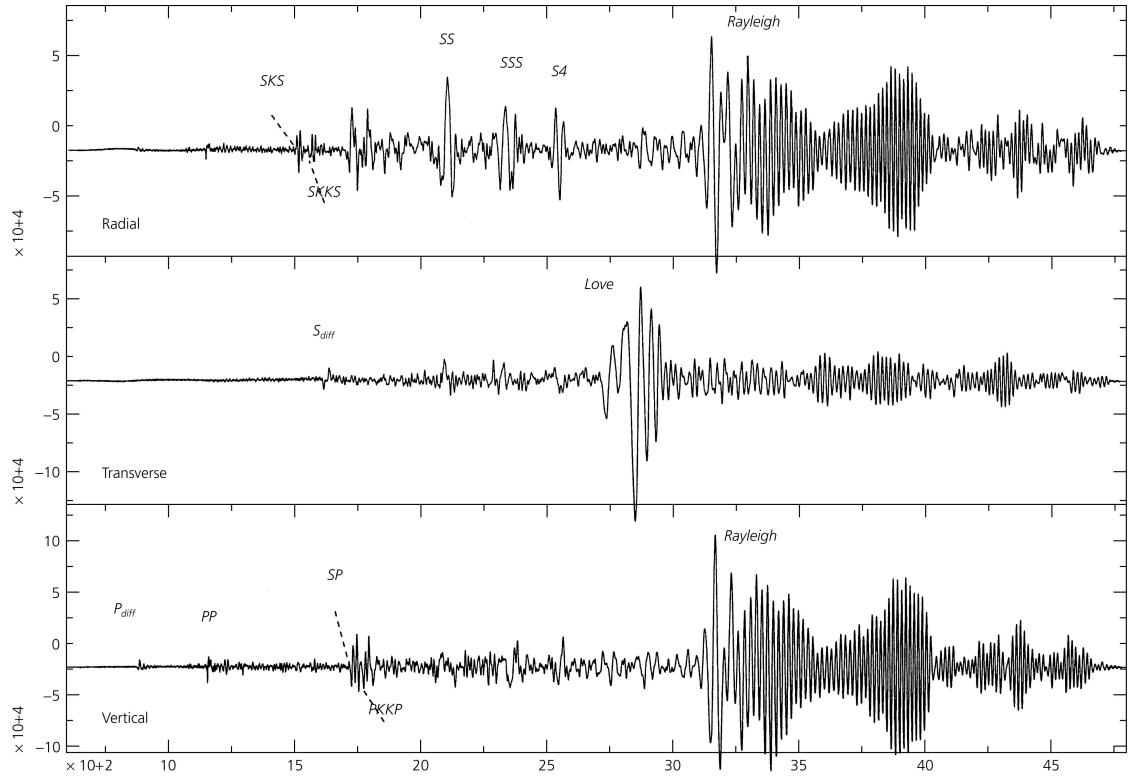

Figure 3.1: The figure shows the recording of an event of magnitude $M_w = 7.7$ from Stein & Wysession (2005). The example shows two types of surface wave recording on the seismogram: Rayleigh and Love waves. The Rayleigh wave can be recorded on vertical and radial component, while Love wave can be recorded on transverse component only.

structure as well as about the seismic source. In comparison to body waves where each phase arrives at a station at certain time, providing the information about velocity. The seismic velocity of surface waves must be measured at different frequencies from a single seismogram. Therefore, the surface wave observation is regarded as a powerful tool providing direct constraints to the velocity versus depth profile between the source and receiver (Shearer, 2009).

A characteristic, mostly exploited in the surface wave observation, is dispersion. By definition, the phenomenon that surface waves travel with different velocities at different frequencies is known as *Dispersion*. It is quantified by determining group velocity and

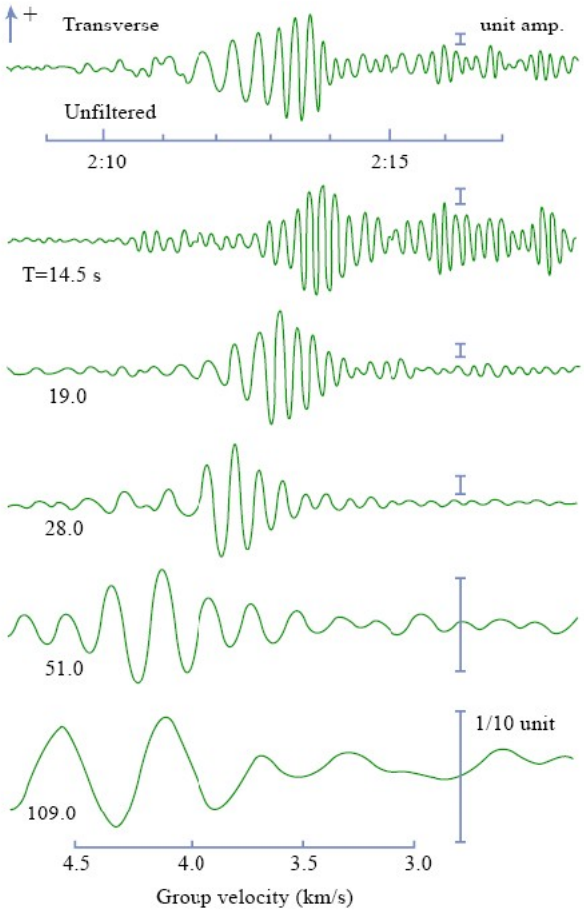

Figure 3.2: Example of dispersion of wave packet from Lay & Wallace (1995). Trace at the top is the unfiltered one. Later part of the recording are the narrow-band filtered trace with the central period shown at the left side of each trace. Note that (from bottom to top) the lower frequency reaches first then the higher frequency.

phase velocity as a function of wave period. Group velocity is the velocity at which energy of a particular frequency propagates, whereas phase velocity is the velocity at which a specified phase (a peak or a trough) within the waveform travels. The dispersion changes the shape of a surface wave as it travel through the medium (See Figure 3.2). Lower frequencies usually arriv earlier than the higher frequencies. The usefulness of surface waves in determining subsurface elastic properties arises from the way in which they disperse. This feature of dispersion is not visible in body waves as in that case all frequencies travel with similar velocity. Different models result in different dispersion curves.

Equation 3.1 defines the dispersion curves for Love wave propagating within a layer over half-space medium :

$$\tan\left[h\omega\sqrt{\tfrac{1}{\beta_1^2}-p^2}\right]=\frac{\mu_2\sqrt{p^2-\frac{1}{\beta_2^2}}}{\mu_1\sqrt{\frac{1}{\beta_1^2}-p^2}} \tag{3.1}$$

where velocity for top layer is β_1 and velocity β_2 in a layer over half-space. $C_x = 1/p$ is the phase velocity, where p is the slowness and μ_1 and μ_2 are material constant for these respective layers. Figure 3.3 shows a plot of the tangent (left side of the equation) versus right hand side of the equation 3.1 over an interval of velocity (β_1 to β_2 on x-axis denoted as C_x in the figure). For a given value of frequency, (ω), a finite number of solution exist. These solutions are known as *modes* where the leftmost (in the figure 3.3) being fundamental (n=0) to the higher modes, or overtones (n=1,2,3 and so on).

Figure 3.3 illustrates equation 3.1 for a certain period (5 s) using a model with 40 km thick continental crust. The top layer with velocity (β_1) of 3.9 km s^{-1} and density (ρ_1) of 2.8 g cm^{-3} underlain by a half-space with the velocity (β_2) of 4.6 km s^{-1} and density (ρ_2) of 3.3 g cm^{-3} is given by Stein & Wysession (2005). Using these set of values three set of solutions is possible (or mode n = 0,1,2) as also shown in figure 3.3. With the increase in the period the number of solutions (in terms of modes) decreases is also visible in figure 3.7.

From the interference of waves travelling with certain velocities due to their dispersive nature, we obtain a general form of the equations for group (u) or phase (c) velocity. Once the location and origin time of the source are known, calculation of group velocity can

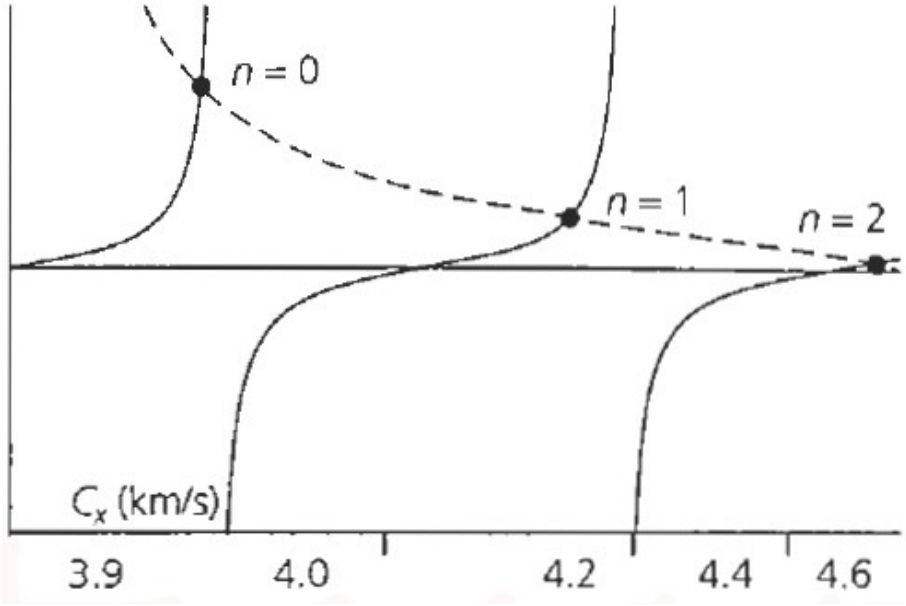

Figure 3.3: Graphical representation for the solution of dispersion curve calculation using eq. 3.1 [from Stein & Wysession (2005)]. The example is for Love wave in a layer over a half-space. Solid and dash lines represents the left and right side of the equation, respectively. The values used here are explained in the text.

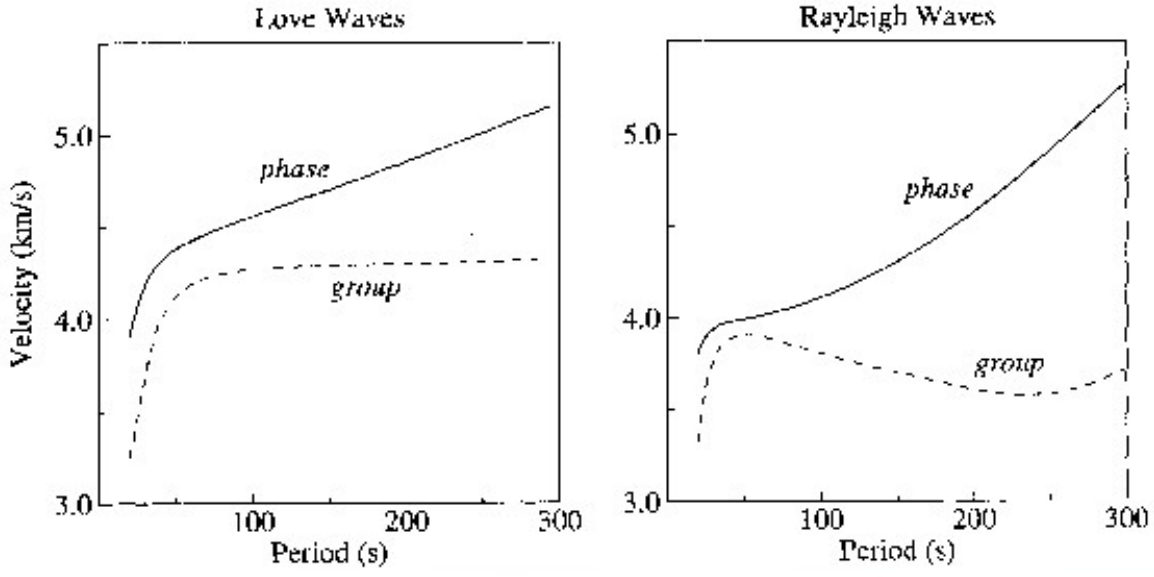

Figure 3.4: Plots for the fundamental Love and Rayleigh wave dispersion curves computed from the isotropic PREM model. Dash lines in the plot for group velocity and solid lines for the phase velocity [from (Shearer, 2009)].

be easily carried out. Group velocity may be estimated from a surface wave record at a single station by determining the travel time to the station for the envelope of energy at a particular frequency. This can be achieved by applying narrow band-pass filters to the record to isolate the wave packet for a target frequency (Figure 3.2). For two stations, group velocity can be determined by measuring the difference in the arrival time of the filtered wave packet. Calculation of phase velocity is done by computing a frequency-time representation based on the Fourier spectrum of the record to determine the phase of each frequency component. The relationship of the group and phase velocities is written as:

$$\textit{Phase velocity :} \qquad c = \frac{\omega}{k} \tag{3.2}$$

$$\textit{Group velocity :} \qquad u = \frac{d\omega}{dk} \tag{3.3}$$

where ω is angular frequency and k is the wave number. The fact that the surface wave velocity varies depending on the depth range sampled by each period makes surface wave dispersion useful for studying earth structure by solving relevant seismological inverse problem using the dispersion curve (Figure 3.4).

Many interesting questions concerning the properties of a physical system can be answered only indirectly by analysing their physical manifestations. Success in quantifying the parameters of such a system or function of these parameters, which themselves are not directly measurable, depends on the limits of meaningful inferences that can be determined from the observable data. Computing values of the observable parameters from the

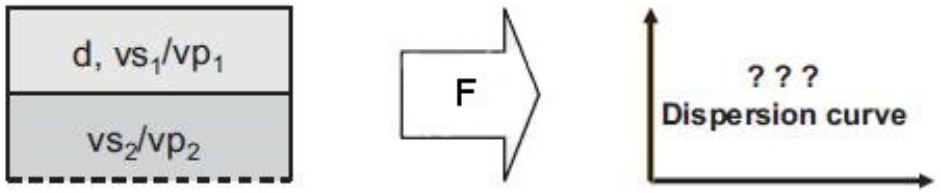

(a) Forward Modeling

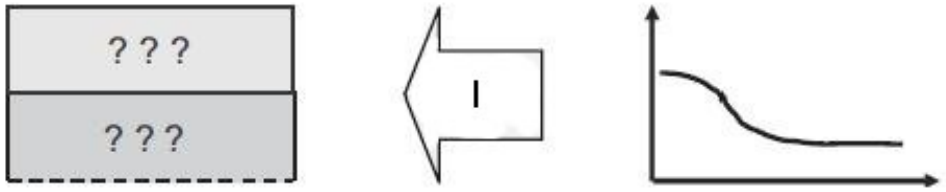

(b) Inverse Modeling

Figure 3.5: Cartoon depicting the basic principle of Forward and Inverse problem in geophysics. (a) The forward modeling is the calculation of theoretical dispersion curve from the known physical parametrs parameters of the material. (b) The inverse problem is the opposite of the forward problem where the physical parameters are derived from the observation in this case is the dispersion curve.

known arbitrary values of the model parameters constitutes the solution of the forward problem whereas inferring the values of the model parameters from the observed values of the observable parameters defines the solution of the inverse problem. The tenability of the derived information rests on the basis of a physical theory connecting model parameters and the observed data and on an adequate description of the system by a minimal set of parameters to be determined from the observed data. These constitute the basic statement of an inverse problem.

Inverse problem theory in the wide sense has been developed by people working with geophysical data. The reason is that geophysicists try to understand the Earth's interior but are doomed to use only data collected at the Earth's surface. Geophysical problems are always underdetermined in some sense, but as geophysical data contain a lot of information, it is worthwhile to try to develop methods for extracting it. Since long, such

methods have been only empirical. Backus (1970a,b,c) made the first systematic exploration of the mathematical structures of the inverse problem. Backus & Gilbert (1967, 1968, 1970) introduced interesting concepts, for instance "model resolution" and "averaging kernel". Their work was at the origin of a very fruitful development of quantitative methods of data interpretation in geophysics (Tarantola, 2005). Tomographic inversion of massive surface wave data sets for obtaining the subsurface elastic parameters is the latest development. However, the accuracy of the dispersion curve is crucial in obtaining reliable subsurface elastic parameters.

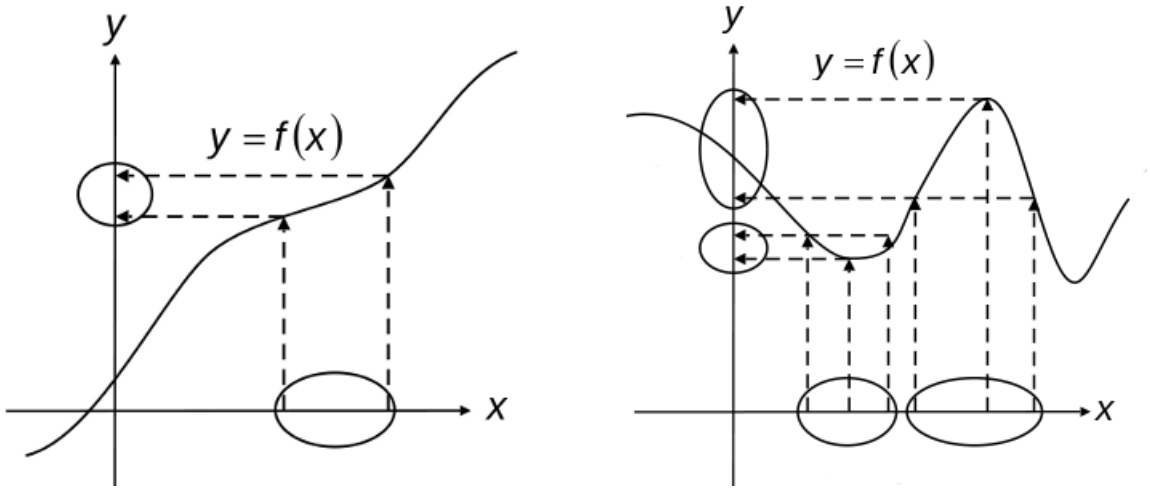

(a) Weakly non-linear problem **(b)** Strongly non-linear problem

Figure 3.6: Example for (a) weakly non-linear function can be approximated as Linear problem, unique solution and (b) Strongly Non-linear problem, non-unique solution

One can infer elastic properties, density, shear wave velocity and layer thickness by analyzing dispersion curve which can be characterized as an inverse problem (Figure 3.5). Scientific models are generally adequately described by more than one parameter. With these models, it is also possible to calculate various theoretical characteristics. For instance, a characteristic of the model may be a curve which is numerically represented by a vector of n_{obs} components. Hence the forward problem is a function that transforms a

parameter space of dimension, n_{param} (number of involved parameters) into the observable space of dimension n_{obs}. If the function is linear, linear algebra is used to solve the inverse problem. However, in most situations, the relationship is nonlinear and as such, even the forward problem cannot be solved analytically. For example in Figure 3.6, there could be many sets of physical parameters giving the identical dispersion curve. In most cases, an inversion technique is essential to calculate the set of parameters that corresponds to the observables. The number of solutions of the inverse problem is generally a complex issue. For instance, if the forward function is simply, $y = x^2$ between two one-dimensional spaces, the inverse problem has two solutions, which is an example of non-uniqueness (Figure 3.6).

3.2 Surface waveform tomography

Ideally, the aim in seismology has always been to explain every wiggle on the record but the whole broadband seismic signal is a bit complex for any kind of direct inference. Therefore it requires data processing involving filtering, picking of the onset times of selected phases, determination of dispersion curve and number of other information for extracting certain characteristic data for suitable tectonic interpretation. Ever since the first global tomographic model of the upper mantle (Woodhouse & Dziewonski, 1984; Dziewonski, 1984), seismic tomographic methods have gone through a lot of improvements.

In most tomographic inversions of surface wave data the commonly used approaches are:

1) Interpretation of long-period seismograms in terms of dispersion and/or attenuation curve. But the relation between surface wave dispersion and the seismic velocity structure of the Earth is non-linear. The structure inferred from the waveform inversion is unsatisfactory mainly due to the fact that the relation between data and

structure is approximate and also that the relation is not invertible in the strict sense.

2) Direct waveform inversion, also known as waveform fitting by iteratively estimating the model.

The direct waveform inversion is a principal property of the geophysical inversion problem, simply because of the non-linear relation between the model parameters and the ground motion records. There are numerous techniques used to reduce this non-linearity as much as possible. The most popular technique used is the iterative method where the synthetic seismograms are calculated by changing the model in order to fit the observed seismogram. For example, Nolet et al. (1986) formulated the conjugate gradient method for non-linear optimization of surface waves and Nolet (1990) describe the partitioned waveform inversion.

Surface wave tomography is now commonly performed to map either upper mantle heterogeneities or anisotropy or both. Most of these studies rely on the inversion of phase or group velocity data related to the fundamental mode of Rayleigh and Love waves. Other surface wave investigations have dealt with the distribution of seismic attenuation (Q) versus depth (Canas & Mitchell, 1978; Nataf et al., 1986; Li & Romanowicz, 1996; Montagner, 2007; Friederich, 2003). Inversions of all these fundamental mode data in terms of depth varying functions have limited resolving power. The use of higher modes together with the fundamental mode is used to enhance the vertical resolution. For a given surface wave mode, the penetration depth increases with increase in period and also for a given period, it increases with increase in mode rank (Figure 3.7). As a result the fundamental mode constrains the shallow structure and higher modes constrain the deeper structure in addition to adding complimentary information on shallow structure. Collecting accurate higher mode is another problem. For the periods of interest when studying the upper man-

tle (40-160s), the group velocities of the different higher modes are so close to each other that classic methods of analysis cannot be used to isolate them. To solve this problem, different techniques based upon the separation of modes in the wave-number domain have been proposed (Nolet, 1975; Lévêque et al., 1991).

In the present work, we use the Cara & Lévêque (1987) method which offers an alternative to the waveform inversion. The technique which they proposed is an intermediate approach where the signal-to-noise ratio is enhanced prior to inversion for a particular mode-branch by cross-correlation technique proposed by Dziewonski et al. (1972). Thus in this method, the pure mode synthetics are cross-correlated with the recorded signal prior to any further analysis. Instead of extracting directly the phase or group velocities from complex time-frequency images, other secondary observables are defined in a way that their

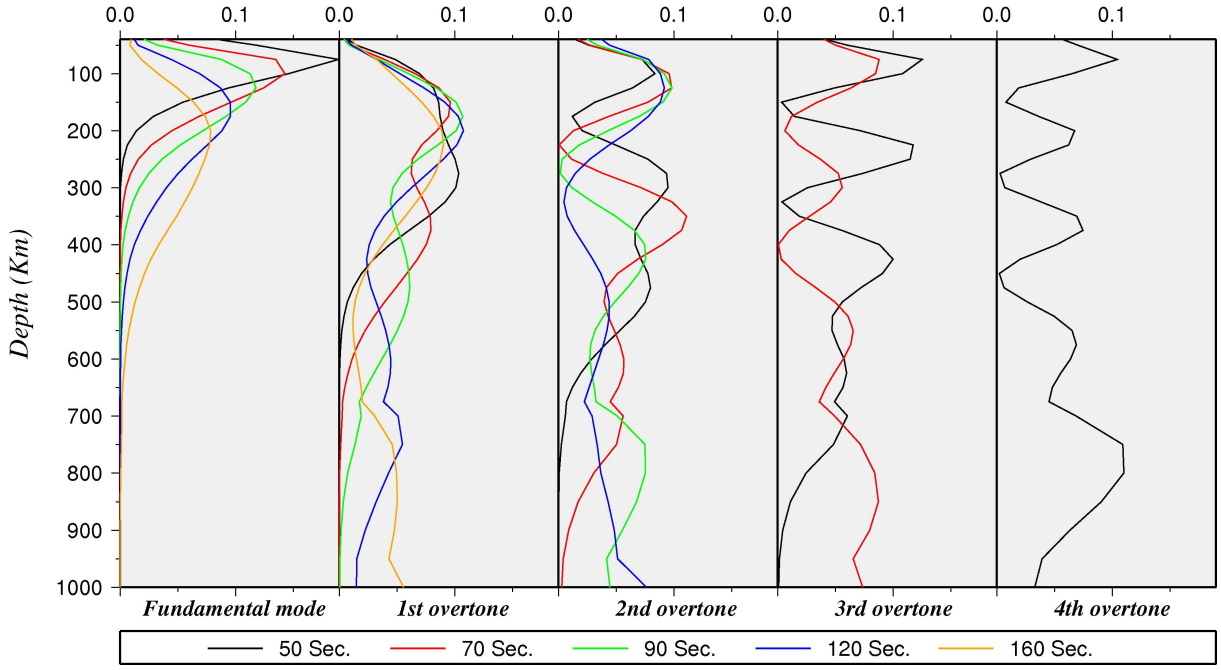

Figure 3.7: Theoretical sensitivity kernel for the fundamental and first four higher modes of Rayleigh waves at periods of 50 s (black), 70 s (red), 90 s (green), 120 s (blue) and 160 s (orange). The curves represent the relative partial derivatives of the phase velocity according to the shear-wave velocity $[(V_{sv}/C)\ (\partial C/\partial V_{sv})]$.

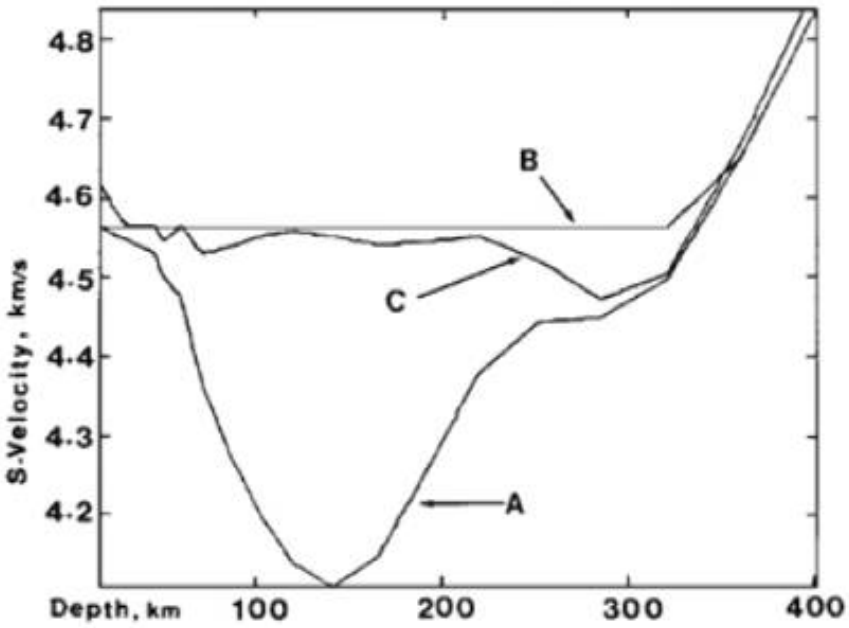

Figure 3.8: Figure as shown Cara & Lévêque (1987) to prove the independence of the inversion method on initial and/or reference model. They demonstrated that after 8 iteration, reaches the final model C which is close to the real model B from the starting model A.

dependence to the model parameters is as linear as possible. Their approach is designed to minimize the dependence on the starting model. As illustrated through figure 3.8 by Cara & Lévêque (1987) wherein they have applied the inversion technique using synthetic seismogram generated out of two modes, using the actual model "B". For the test of the inversion scheme they took a rough initial model "A" but still managed to estimate the model "C" which is quite close to the actual one. Due to the efficiency of the algorithm, the successful inversion of a seismogram and obtaining the final model can be achieved in few number of iteration.

The techniques used in the present work for constructing 3D Sv velocity model are spread in two distinct steps previously employed in a number of regional scale surface wave tomographic studies (Debayle, 1999; Debayle & Kennett, 2000b; Pilidou et al., 2004; Heintz et al., 2005; Priestley et al., 2006). The first step, which comprises the automated

waveform inversion of Cara & Lévêque (1987), is employed to find a path-averaged 1D radially stratified upper-mantle model compatible with the waveform of each individual seismogram as defined in Debayle (1999). In the second step, the continuous regionalization scheme of Montagner (1986) and Debayle & Sambridge (2004) is applied to the path-averaged models to retrieve local structure. The outcome of this inversion scheme has generated a 3D model of Sv wave-speed variation and azimuthal anisotropy beneath the China and surrounding area.

3.3 STEP 1 : Waveform Inversion

The waveform of the surface wave portion of a seismogram is well known to depend in a highly non-linear way on the elastic parameters. Modelling surface wave waveforms can be performed in a number of different ways. Performing the inversion of data directly is possible (Nolet et al., 1986), however it is computationally inefficient due to highly non-linear relationship between a perturbation of the synthetic waveform and the elastic parameters describing the velocity model. It is a common practice in such inversion process to use some quantities that can be derived from the seismograms, such as phase velocity dispersion (Montagner, 1986), or path integral over seismic velocity as non-linear optimization (Nolet, 1990). This indirect scheme proved much more efficient as their quasi-linear dependence on the elastic parameters.

3.3.1 Filtered cross-correlogram : Secondary observables

The surface wave part of the seismograms to be modelled is assumed to be represented by a finite sum of pure-mode (each individual mode) synthetics computed for a laterally

homogeneous medium. This is one of the basic assumptions used here, that the observed seismogram can be represented by multimode surface waves (See Figure 3.9). The multimode surface wave signal can be represented by assuming the finite sum of N pure-mode synthetics $s_p(t)$ given by

$$s_p(t) = g(x) \int I(\omega) \quad S(\omega) \quad e^{-\alpha_p(\omega)x} \quad e^{i[\omega t - k_p(\omega)x]} d\omega \tag{3.4}$$

where x is the epicentral distance, $g(x)$ the geometric expansion, ω is the circular frequency, $I(\omega)$ is the instrumental response, p is the mode rank, $S(\omega)$ is the complex source excitation, $\alpha_p(\omega)$ is the apparent attenuation factor and $k_p(\omega)$ is the wavenumber function. The function $k_p(\omega)$ and the stress displacement function, which are required for estimating the source excitation function $S(\omega)$, were computed using Takeuchi & Saito (1972) algorithm.

Cara & Lévêque (1987) coined the concept of secondary observables, which are built from the seismogram using cross-correlation techniques prior to performing inversion process. As given by Lerner-Lam & Jordan (1983), the contribution of a given mode in the output signal is reinforced by cross-correlation techniques, but the non-linearity is reduced by using secondary observables based on the amplitude of the envelope of these cross-correlogram functions. The secondary observables are derived from cross-correlogram functions, $g_p(\omega_q, t)$, which are built from seismogram, $s(t)$, by cross-correlation with a set of pure-mode synthetic seismogram, $\hat{s_p}(t)$ (mode p) :

$$g_p(\omega_q, t) = h(\omega_q, t) * s(t) * \check{s_p}(-t) \tag{3.5}$$

where $*$ denotes convolution, $h(\omega_q, t)$ is the impulse response of the band-pass filter centered on the circular frequency ω_q (period range for this study 50-160 s) and the $\check{s_p}$ is the complex conjugate of $\hat{s_p}$. The value of mode p ranges from 0 (fundamental) to 4 (fourth higher mode). The application of the two operators '$\hat{s_p}(-t)$' and '$h(\omega_q, t)$' to the complex signal $s(t)$ allows us to reinforce the level of a given mode p and to perform a rough separation of the information related to different depths by band-pass filtering. First, the

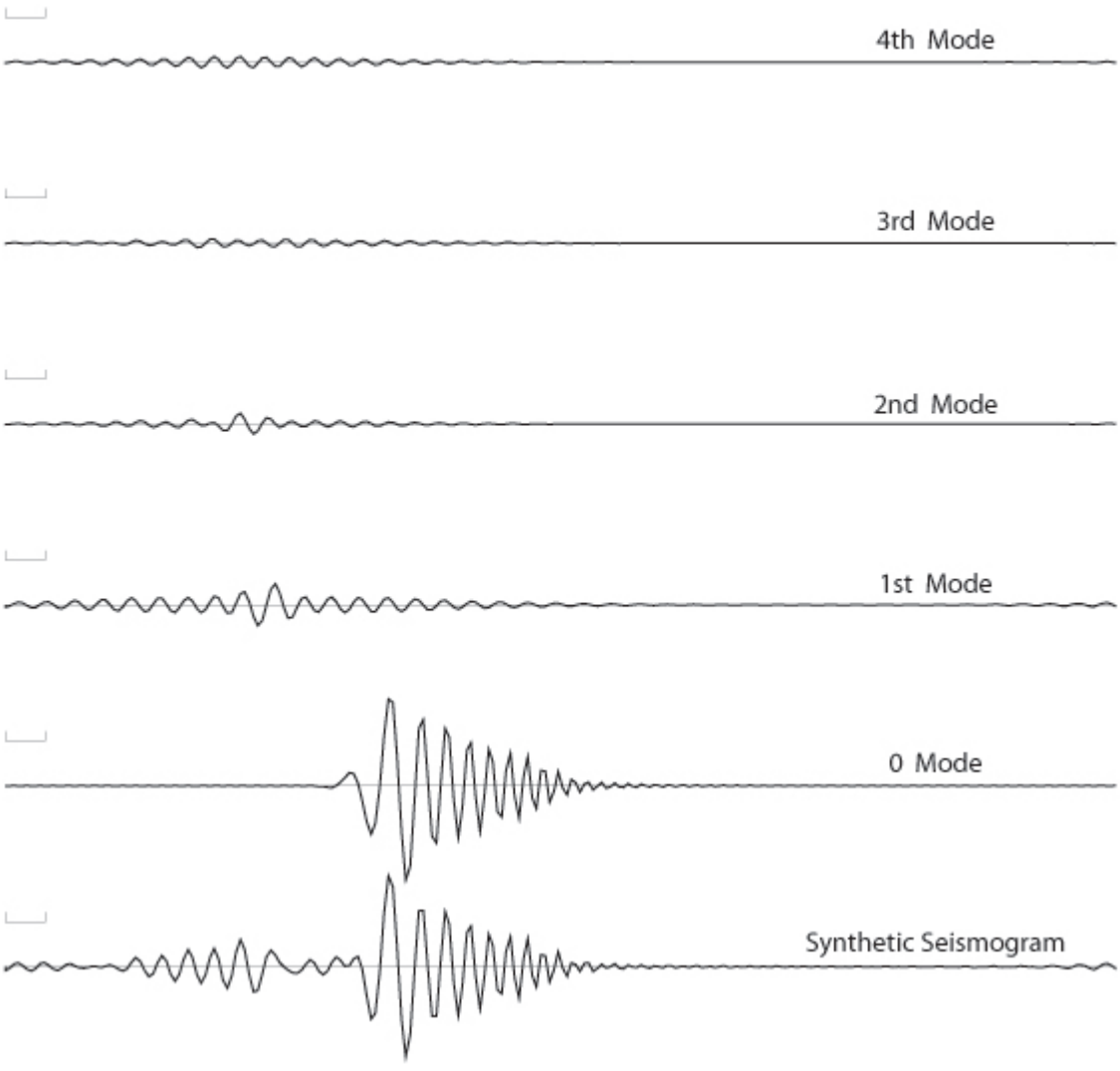

Figure 3.9: Example showing the synthetic seismogram (bottom trace) as the summation of the fundamental to 4th higher mode traces.

cross-correlation improves the signal-to-noise ratio, reinforcing the component similar to the pure-mode synthetics in the data and leaving the noise dispersed, and second, the frequency filtering produces a segmentation of the information related to different wavelengths and thus to different depth ranges.

Each cross-correlogram function, $g_p(\omega_q, t)$, can be represented by two types of secondary observables: sampling three values taken at different time lag on the envelope of $g_p(\omega_q, t)$ and one parameter representing the phase $\varphi\left[g_p(\omega_p, t)\right]$ at the time of maximum amplitude (preferable as closer to $\mathrm{t} = 0$ s). The information contained by one filtered cross-correlogram function is thus represented by four parameters. The maximum number of secondary observables used for representing one seismic signal is thus $4 \times p \times q$, where p being the number of modes and q the number of filters. This small number of parameters has proven to be enough to develop a workable inversion algorithm converging to the observed waveform in a small number of iterations (Lévêque et al., 1991).

3.3.2 Data : Automated selection

The waveforms are allowed to automatically fit. It is obligatory to discuss the various aspect of the analysis such as noise and error detection and data rejection procedure along with automatic selection of the set of secondary observables. The procedure is very well described in Debayle (1999), which makes it possible to use an enormous volume of data. The first requisite to begin with is the computation of synthetic seismogram for a given earthquake-station path. As defined earlier with equation 3.4 the code of Takeuchi & Saito (1972) is used for the computation of the synthetic seismogram. Source parameter information is taken from the Global CMT catalogue and to calculate the stress-displacement functions required to compute source excitation functions. The 3D *a priori* model 3SMAC

(Nataf & Ricard, 1996) for the crust is combined with a smoothed PREM model (Dziewonski & Anderson, 1981) for the upper mantle as the initial and reference model. Since we do not invert for the crust, each path is being corrected with averaged 3SMAC model. If the calculated synthetic seismogram for the inverted initial model in its first run does not predict the amplitude of the real seismogram within a factor of 5, it will be rejected attributing to the poor knowledge of source parameter.

Figure 3.10 shows the scenario of the waveform fitting after the calculation of the synthetic seismogram for the starting model. The event occurred on June 4, 2008 located at the depth of 204 km in the Japan region (41.57° N, 139.15° E). This event was recorded at the station A22 (36.43° N, 96.49° E) close to the Qaidam basin, of the network $X4$. From the lower panel of the figure the x-axis is represented by the velocity, with 7 km s^{-1} bar mark on left side of the axis and 3.5 km s^{-1} on the right side.The dominant fundamental mode is observed between 3.5 km s^{-1} and 4 km s^{-1} on the actual signal denoted by data (lower part of the figure 3.10). The less energetic overtone has higher group velocity. The initial synthetic trace replicates the actual data trace. The only difference is in the miss-match of the phases, where the actual data is bit delayed. On the upper panel of the figure is shown the envelopes of the cross-correlogram function filtered at 50 s, 90 s and 160 s. The observed seismogram is cross-correlated with the reference pure-mode synthetic seismogram (not necessarily for each mode for higher period) denoted as 'data'. The full synthetic seismogram is also cross-correlated with the same pure-mode synthetic seismogram, denoted as 'synt'. In the case of fundamental mode the largest maxima can be easily found close to the centre (reference point or time t_0=0). This is because of the small difference in the arrival time of fundamental mode for actual and synthetic seismogram. For modes 1 to 4 the cross-correlogram is still dominated by the amplitude of the most energetic fundamental mode envelope.

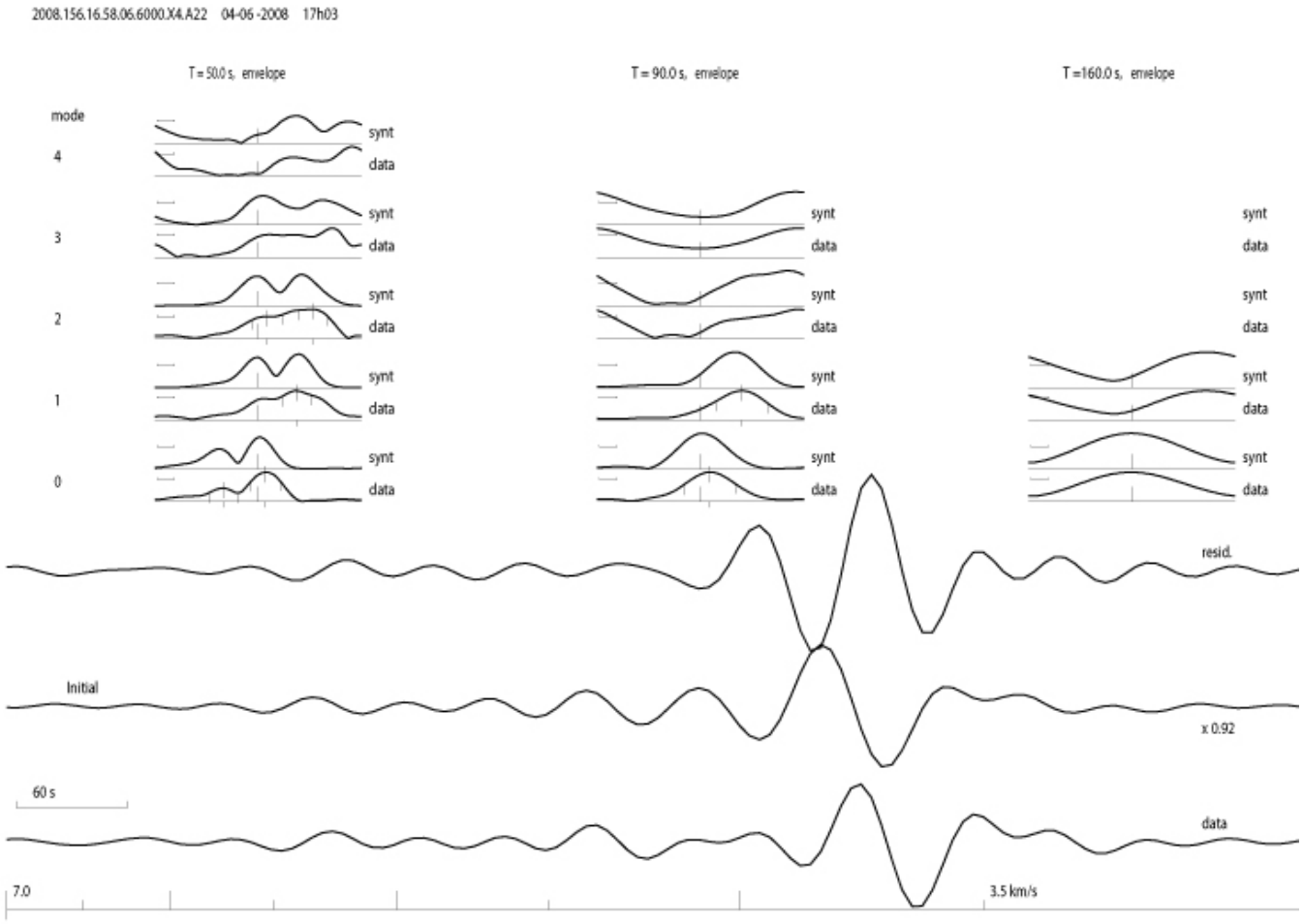

Figure 3.10: Situation before inversion for the event on 2008 June 4, recorded at station A22. The lower part of the figure shows the observed seismogram (labelled 'data'), the synthetic seismogram computed for the initial model ('initial') and their difference ('residual'). The upper part of the figure shows the envelopes of the filtered cross-correlogram functions $g_p(w_q, t)$ for modes p ranging from mode 0 to 4 and for filters centred on 50 s (left column), 90 s (central column) and 160 s (right column) periods. The central bar on the x-axis shows the reference time t_0=0. The bars on the cross-correlated traces are the point sampled for the inversion.

The above mentioned problems can be encountered during the automated sampling of observed cross-correlogram function which was discussed in the previous section (Section 3.3.1). The cross-correlogram function can have complex shapes with several maxima, especially when several energetic modes interfere. This situation is true in the case of intermediate depth or moderatle shallow depth eartquake (70 to 150 km). For example, in the case of the fundamental mode which normally possess high energy (Figure 3.10), we cannot pick the maximum value as it would lead to the contamination of the $g_p(\omega_q, t)$. An alternative to this would be to select the closest maximum with respect to the reference time ($t = 0$), where the maximal energy of the considered mode is expected if the cross-correlated signals are not delayed. This approach demands a good reference model which predicts well the arrival times on the actual seismogram.

There could be a situation where several maxima exists near $t = 0$. In such cases each lobe is represented by three values, as presented in Figure 3.10. For each mode two sets of lobes of the cross-correlograms filtered at 50 s have been sampled by three values. Then for the selection of the secondary observables following criteria is being adopted:

(a) All the significant maxima of the envelope are extracted. A maxima is considered to be significant when the ratio between the amplitude of the maximum and the average of the minima of the envelope is greater than a threshold value (3 in this case).

(b) If several maxima are extracted, the two best are selected, using the ratio $A_{max}/\left|t_{max} - t_0\right|$ as a criterion, where A_{max} is the amplitude of maximum, t_{max} the time of that maximum amplitude and t_0 the reference time.

(c) The instantaneous phase of the cross-correlogram is taken at the maximum with the highest $A_{max}/\left|t_{max} - t_0\right|$ ratio.

This compromise is extremely effective as it favours the lobe closest to the reference time t_0, where the mode under consideration is expected. When the choice between two lobes is ambiguous, both are selected, as the aim here is to be able to invert for each point of the envelope of the cross-correlogram. This can increase the computation time because of the addition of redundant information but at the same time it will ensure the coverage of all the information of the waveform helping to reduce the residual energy between the observed and synthetic seismogram.

3.3.3 Inversion

The automatic selection of the secondary observables has already been discussed. Another important aspect stated initially is the noise-level detection, choice of mode and period for the analysis. The first step is to define a bandwidth over which the seismogram can be analyzed to evaluate the signal-to-noise ratio (SNR) within five different periods: 50, 70, 90, 120 and 160 s. The bandpass filtering of $g_p(\omega_q, t)$ within the central frequency ω_q range of periods of 50-160 s is stricter than previous studies (Debayle, 1999; Debayle & Kennett, 2003). At each period, SNR is deemed adequate if the ratio between the maximum amplitude of the signal (part of the record arriving with a group velocity larger than 3.3 km s^{-1}) and the maximum amplitude of the envelope of noise (part of the record arriving with a group velocity smaller than 3.3 km s^{-1}) is greater than 3. The central frequency of the bandpass filter is chosen according to the following sequence of priority: (i) 50, 90 and 160 s; (ii) 50, 70 and 120 s; (iii) 50 and 90 s; (iv) 50 and 70 s. A minimum period range of 50-70 s is thus imposed in the analysis of the waveform data. At 60 s period, the use of a filtered cross correlogram is sufficient to constrain the Sv velocity to a depth greater than 150 km, even when only the fundamental mode is taken into account in the inversion (Lévêque et al., 1991).

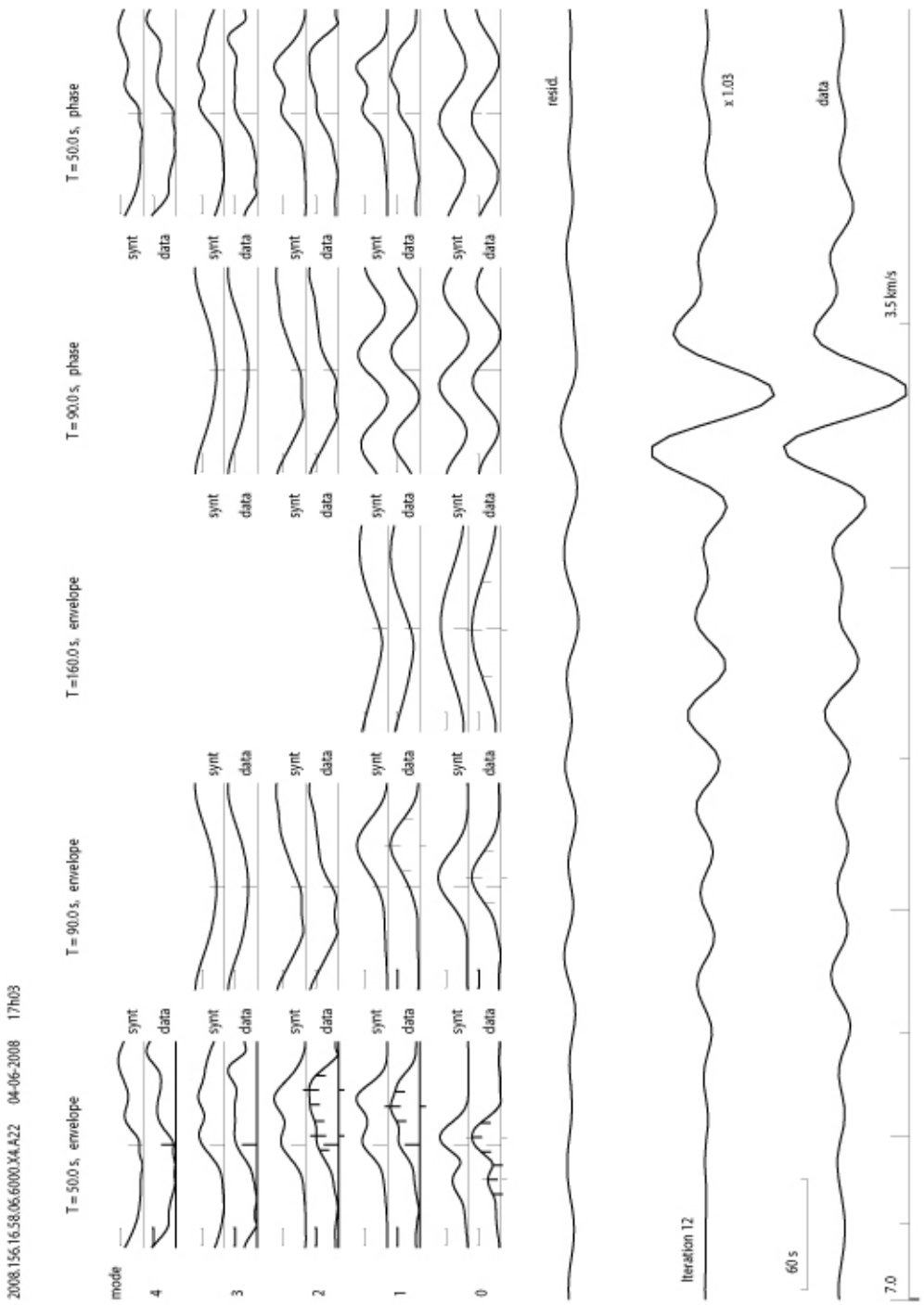

Figure 3.11: Situation after inversion for the same event as figure 3.10. The instantenious phase information is being added later. Shown as the two columns on the right side of the upper panel. The x-axis scale is different for each mode and periods.

Waveform fitting inversion technique is performed in four stages. In first stage the real filtered envelope at long period (more than 50s) are matched. In second stage the envelope of short period (50s) are included. Only after matching the envelope for the short period the process moves to third and fourth stages which are related to matching the instantaneous phases. While matching the instantaneous phases, similar routine is followed; in third stage adding the instantaneous phases of the filtered cross-correlogram at 70s or 90s depending upon the central frequency chosen while matching the envelope for long period. In fourth stage the phases for the short period is added. This approach is close to Heijst & Woodhouse (1997), however in the present study the inversion process is not separated mode by mode and also allows avoiding 2π phase shift. All the modes for a given frequency, which contributes more than 1% of the total energy of synthetic seismogram is considered. Due to the weak non-linearity of the secondary observables, for the envelope of $g_p(\omega_p, t)$ and the phase $\varphi[g_p(\omega_p, t)]$, this non-linear algorithm converges in in a small number of iterations.

Surface waves are sensitive to seven elastic parameters, the velocities of vertical and horizontal propagation for $P\,(\alpha_v, \alpha_h)$ and $S\,(\beta_v, \beta_h)$ waves and a parameter η related to propagation at intermediate angles, as well as the quality factor Q_β and the density ρ. In the present research work, we inverted long period Rayleigh wave in terms of Sv wave speed while keeping the V_P/V_S ratio. The attenuation (parameterized by $\log(Q_\beta)$) and the scalar seismic moment $\log(M_0)$ of the source is also being inverted to ensure adequate scaling of the signal. As mentioned earlier the source information is taken from the CMT catalogue and the values regarding this are same for each individual earthquake. The inversion is not performed for crustal structure, allowing to ignore non-linearity problem near crustal discontinuity when inverting the seismogram, eliminating the short-period part of the signal which is most difficult to model due to its great sensitivity to lateral heterogeneities. The strategy is to use an *a priori* model with an average crustal structure

(3SMAC) adapted for the path and to invert only for upper mantle parameters. Figure 3.11 shows the example after the successful application of the automated inversion scheme.

3.4 STEP 2 : Tomographic Inversion from 1D to 3D

The outcome of the waveform inversion process is a one dimensional (1D) velocity model information with depth for each path between a station and an epicentre. The 1D model for each path represents an average of the velocity structure encountered along the path. A three-dimensional (3D) velocity model is built from the inverting all 1D model using a linear inversion procedure. In the second stage, we combine the 1D velocity models in a tomographic inversion using a continuous regionalization algorithm developed by Montagner (1986) to obtain both the isotropic component of 3D Sv-wave speed heterogeneity and the azimuthal anisotropy as a function of depth. The basic assumption for this procedure is that at a given depth z, each 1D model $\beta_v(z)$ represents the path-averaged structure along the earthquake-receiver (great circle) trajectory (C) :

$$\frac{1}{\beta_v(z)} = \frac{1}{L}\int_C \frac{1}{\beta_v(z,\theta,\phi)} dl \tag{3.6}$$

where L is the path-length and

$$\beta_v(z,\theta,\phi) = \beta_v^{isotr}(z,\theta,\phi) \times [1 + A_1\cos(2\theta) + A_2\sin(2\theta)] \tag{3.7}$$

is the total 2D velocity distribution to be determined. This distribution includes an isotropic term of $\beta_v^{isotr}(z, \theta, \phi)$ and azimuthal anisotropy terms, the magnitude and direction of which are controlled by coefficients A_1,A_2 and the propagation direction azimuth, θ, respectively (Lévêque et al., 1998), described in detail, in the next section (Section 3.5.1).

The simplest way to retrieve seismic heterogeneities from these path averaged velocity model would be to divide the earth into different tectonic provinces. This exercise will decrease the size of the inverse problem by making it pure-path inversion and the parameters at each depth correspond to only few tectonic regions (Dziewonski, 1971). But such a priori information regarding tectonic boundary may not be valid for all the depths (especially deeper depths). A much better approach would be to divide the earth in large number of small regular blocks which makes the inversion underdetermined and in order to stabilize the solution *a priori* information on the model must be introduced.

A classical least square solution for discrete linear inversion problem proposed by Tarantola & Valette (1982):

$$\hat{\mathbf{m}} = \mathbf{m}_0 + C_{m0}G^t(GC_{m0}G^t + C_{d0})^{-1}(\mathbf{d} - G\mathbf{m}_0) \tag{3.8}$$

where $\hat{\mathbf{m}}$ is the inverted model, $\mathbf{m}_0$ is the a priori model, t denotes the transpose, a priori covariance matrix on the model represented by C_{m0} and a priori covariance matrix on the data represented by C_{d0}. G is the matrix of partial derivatives $\delta s/L_i$ where δs is the seg-

ment of path i (refer to euation 3.6).

In practice, we discretize the model and use 1° by 1° cells (Montagner & Tanimoto, 1990). Then we correlate neighboring points (r, r') separated by distance $\Delta_{r,r'}$ using a Gaussian filter introduced in the inversion via an *a priori* covariance matrix on the model C_{m0}. The idea is to decrease the size of the cells used to parameterize the tomographic model so that they become infinitesimally small and increasing the unknown towards infinity making the problem strongly underdetermined (less data than model parameter). In order to stabilize the solution an *a priori* constraint in the form of model $\mathbf{m_0}$ and covariance function $C_{m0}(r, r')$. Montagner (1986) defines $C_{m0}(r, r')$ in the form of

$$C_{m0}(r, r') = \sigma(r)\sigma(r') \quad exp\left(\frac{-\Delta^2_{r,r'}}{2L^2_{corr}}\right) \tag{3.9}$$

The role of C_{m0} is to control the amplitude of velocity perturbation using an *a priori* standard deviation ($\sigma(r)$, $\sigma(r')$) and to ensure that we obtain a smooth model using horizontal correlation length (L_{corr}). An *a priori* covariance matrix on the data (path average models) C_{d0} is also introduced to take into account data error. C_{d0} and C_{m0} allows to regularize the inverse problem so that a stable inverse solution is obtained (Montagner & Tanimoto, 1991; Debayle & Sambridge, 2004).

The method described here is very flexible. For example, the use of a Gaussian covariance function on the model also deals in a natural way with the effect of uneven data sampling. Indeed, the Tarantola & Valette (1982) least squares approach can be seen as

a way of finding the model that gives the best fit to the data while keeping as "close" as possible to the *a priori* information. The smoothness of the inverted model in poorly sampled regions is therefore mostly constrained by the width of the Gaussian covariance function, while in regions with higher ray density the need for a satisfactory data fit results in a rougher model. For this study, we have used $L_{corr} = 250$ km and $\sigma = 0.05$ km s^{-1}. The value of L_{corr} was chosen keeping in mind the average wavelength of the data (Sieminski et al., 2004).

3.5 Seismic Anisotropy

Anisotropy is the medium property being directionally dependent unlike isotropy, which implies identical medium properties in all directions. In seismology the seismic anisotropy describe the directional dependence of seismic wave speed within the Earth. The knowledge of seismic anisotropy is crucial to understand the mantle dynamics and continental evolution. Several studies have been conducted indicating the presence of anisotropy in the Earth; mineral physicists and geologist aiming for the microscopic scale, and seismologist for the macroscopic scale. The presence of anisotropy has long been established at most depth ranges, though amplitudes may vary owing to several factors and conditions like type of minerals, magnitude and history of stress and strain, temperature and pressure, environmental geometry, melt and water content (Savage, 1999). Seismic anisotropy within the crust can be largely related to the sediment stratification and the preferred orientation of cracks, orienting themselves in the plane perpendicular to the direction of the stress. In the mantle lithosphere, it is usually explained by deformation-induced preferred crystallographic orientation of anisotropic minerals. The main constituent mineral is olivine which is strongly anisotropic; the velocity difference between fast and slow axis is larger

than 20%. Other minerals such as orthopyroxene or clinopyroxene are anisotropic as well (more than 10%) (Montagner, 1998). Other constituents such as garnet display a cubic crystallographic structure which contributes very little. Anisotropy in asthenosphere is supposed to be influenced by present day mantle deformation, whereas in lithosphere it is more likely influenced by frozen-in deformation linked with convective motion in asthenosphere (Anderson, 1989).

Several surface wave studies (Montagner & Tanimoto, 1991; Trampert & Woodhouse, 2003; Lévêque et al., 1998) have established some understanding of the relation between seismic anisotropy and the plate motion. There are two types of anisotropy which can describe the 3D anisotropy in the earth. The *radial* anisotropy (or polarization anisotropy or transverse isotropy) describes the discrepancy between the horizontally polarized Love and vertically polarized Rayleigh-wave velocities (Anderson, 1965; Babuška & Cara, 1991; Nolet, 2008). The *azimuthal* anisotropy depends on velocity utilizing the azimuthal variation of wave propagation. The azimuthal anisotropy was first observed by Hess (1964) from P_n wave and by Forsyth (1975) using Rayleigh waves.

The olivine crystals are highly anisotropic mineral and found in the upper mantle. The phenomenon usually proposed to explain seismic anisotropy is the preferential orientation of the olivine crystal. The oriented olivine model is widely accepted as it allows one to explain P_n velocity variation with azimuth, SKS-wave splitting and both azimuthal and radial anisotropy of the surface waves (Lévêque et al., 1998). From the observational point there are certain elementary differences between radial and azimuthal anisotropy. Radial anisotropy can not be observed directly but is inferred from the inversion of Love and Rayleigh wave velocity data. The azimuthal anisotropy on the other hand can be directly observed for body wave as well as surface (either Rayleigh or Love) wave velocity

(Montagner & Nataf, 1986; Debayle & Sambridge, 2004). In this thesis we aim to retrieve anisotropy as a function of depth from the observed azimuthal variations of Rayleigh wave velocity by following the approach put forward by Smith & Dahlen (1973).

3.5.1 Method: Azimuthal anisotropy

Retrieving the azimuthal anisotropy for surface wave is quite straightforward assuming that ray theory is valid. Smith & Dahlen (1973) have derived for slightly anisotropic medium, the azimuthal dependence of the phase and group velocity of Rayleigh and Love wave in the form of :

$$C(T) = C_0(T) + A_1(T)cos(2\theta) + A_2(T)sin(2\theta) + A_3(T)cos(4\theta) + A_4(T)sin(4\theta) \quad (3.10)$$

where T is period and θ is the azimuth along the path. $C_0(T)$ is the isotropic term representing the local value of the phase and group velocities and $A_1(T)$, $A_2(T)$, $A_3(T)$ and $A_4(T)$ are the anisotropic coefficients. Even a simplest parameterization of equation 3.10 adds four new parameters (A_i) to the isotropic velocity (C_0) at every location in the model. Since this implies the increase in the number of unknown parameters in an already ill-posed inverse problem, it is worthwhile to consider ignoring some of the A_i term altogether (Nolet, 2008; Babuška & Cara, 1991). In a global inversion for azimuthal anisotropy, Trampert & Woodhouse (2003) suggested that Love waves are insensitive to 2θ terms (A_1 and A_2). Montagner & Tanimoto (1991) showed weak dependence of Rayleigh waves on

A_3 and A_4 terms (4θ terms).

The local values of $C_0(T)$, $A_1(T)$, $A_2(T)$, $A_3(T)$ and $A_4(T)$ can be inverted for an isotropic term associated with the local shear velocities and for anisotropic terms corresponding to linear combinations of the elastic coefficients as shown by Montagner & Nataf (1986). The inversion at depth is straightforward because the partial derivatives needed are those of a transversely isotropic medium with a vertical axis of symmetry. In the case of Rayleigh waves the largest partial derivatives for the anisotropic terms are associated with the $\cos(2\theta)$ and $\sin(2\theta)$ terms and the azimuthal variation for a long-period Sv wave propagating horizontally with velocity β_v at a given depth z can be approximated with the following expression involving only the 2θ variation (Lévêque et al., 1998):

$$\delta\hat{\beta}_v(z) = \delta\beta_v(z) + A_1 \ \ cos(2\theta) + A_2 \ \ sin(2\theta) \tag{3.11}$$

where $\delta\hat{\beta}_v$ is the perturbation of the shear-wave velocity obtained beneath a given path with the waveform inversion, $\delta\beta_v$ is the perturbation of the elastic coefficient β_v and θ is the azimuth. Parameters $\delta\beta_v$, A_1 and A_2 are retrieved from $\delta\hat{\beta}_v$ using the continuous regionalization algorithm of Montagner (1986) as described in the previous section 3.4. Similar to *a priori* information for the 3D Sv velocity tomographic inversion, here also while retrieving the azimuthal information same parameter (different value) being used. These information are Gaussian and is characterized by two parameters: a horizontal correlation length (L_{corr} = 250 km) and *a priori* standard deviation (σ_a = 0.005 km s^{-1}). The value of standard deviation for the anisotropy (σ_a = 0.005 km s^{-1}) is much smaller

than what we used for the standard deviation for the velocity ($\sigma_{\beta_v} = 0.05$ km s^{-1}), but it is required to obtain reasonable amplitudes using the expected values of elastic coefficients for the upper mantle as estimated by (Estey & Douglas, 1986).

Chapter 4

Results and Discussion

As pointed out in the previous chapter (See section 3.3 : Waveform Inversion) we resorted to an 'extremely strict process' for waveform inversion that involved a total of 50,338 1D path averaged models for constructing the 3D Rayleigh wave velocity model of the area under investigation. The term 'extremely strict process' is used here because of the fact that for the purpose of waveform inversion we used a total of 234,566 waveform data as input out of which a whopping 184,228 waveform data got rejected due to strict criterion imposed on information content. This procedure allowed only $\sim$21% of the total waveform data for being used to model the full waveform. Figure 4.1 shows the path coverage density used for constructing the sought after model. In the process, for almost entire China region we have achieved a minimum of over 500 paths per $2^\circ \times 2^\circ$ cell and for the entire Asia a minimum of 200 paths are crossing each grid.

Along with the 3D anisotropic model we also present the azimuthal anisotropy. To understand quantitatively the azimuthal distribution of path coverage required for the anisotropy we took help of Voronoi diagram (See figure 4.2). For constructing the required Voronoi diagram we first chose a uniform set of nodes with $2^\circ \times 2^\circ$ grid as a starting

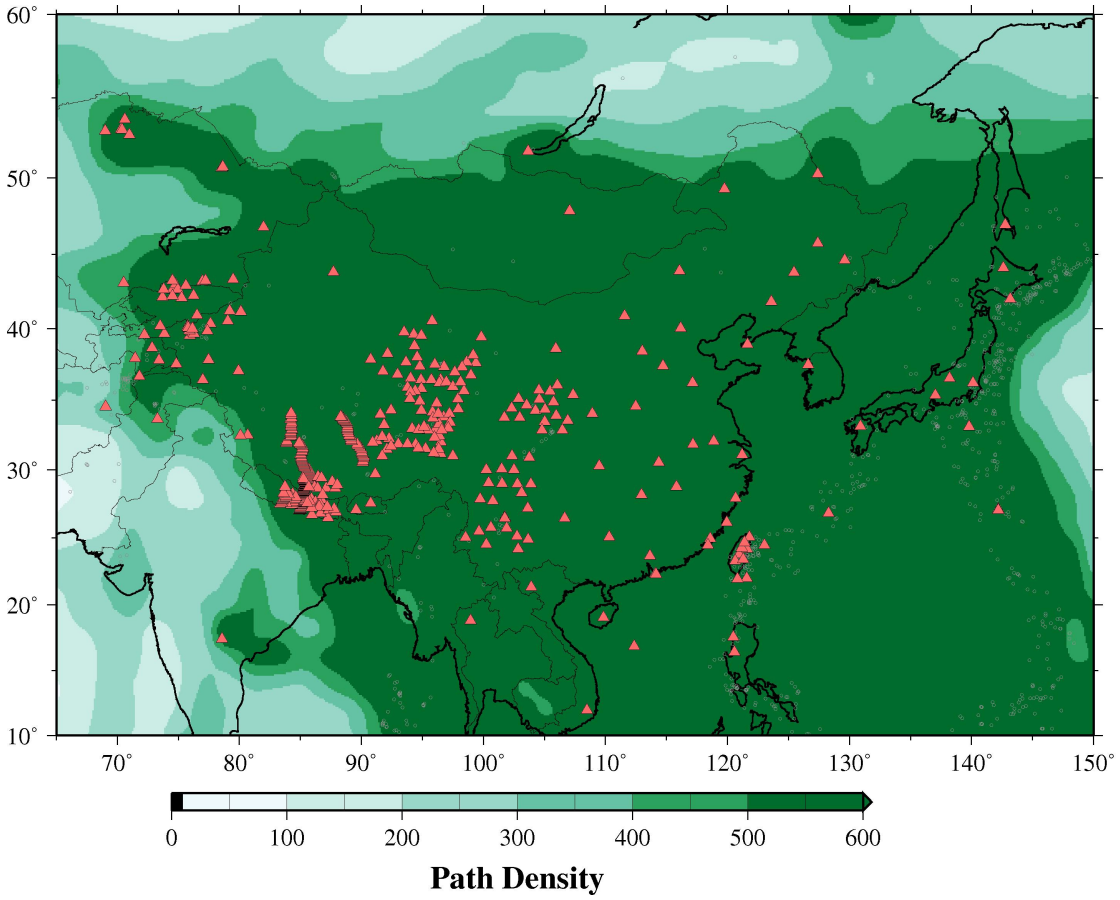

Figure 4.1: Path coverage density map. Using 50338 paths we achieved more than 500 paths crossing each $2^\circ \times 2^\circ$ cell for entire mainland China.

point (Debayle & Sambridge, 2004). From this initial point we generated the "optimized" Voronoi diagram by simply deleting the nodes based on the azimuth of path distribution. The Rayleigh wave $\cos(2\theta)$ $\sin(2\theta)$ variation (See equation 3.11) are periodic in π, therefore the criteria is to subdivide 180° azimuth range into 5 azimuth bins of 36° for each individual cell. In order to keep the node intact each bin should be sampled by at least one path, failing which results in deleting that node. This way the final optimized $2^\circ \times 2^\circ$ grid remain intact. This intact grid is visible in all over the Asia. Figure 4.2 provide the confidence of having sufficient azimuthal distribution of paths to be able to geometrically resolve the azimuthal anisotropy.

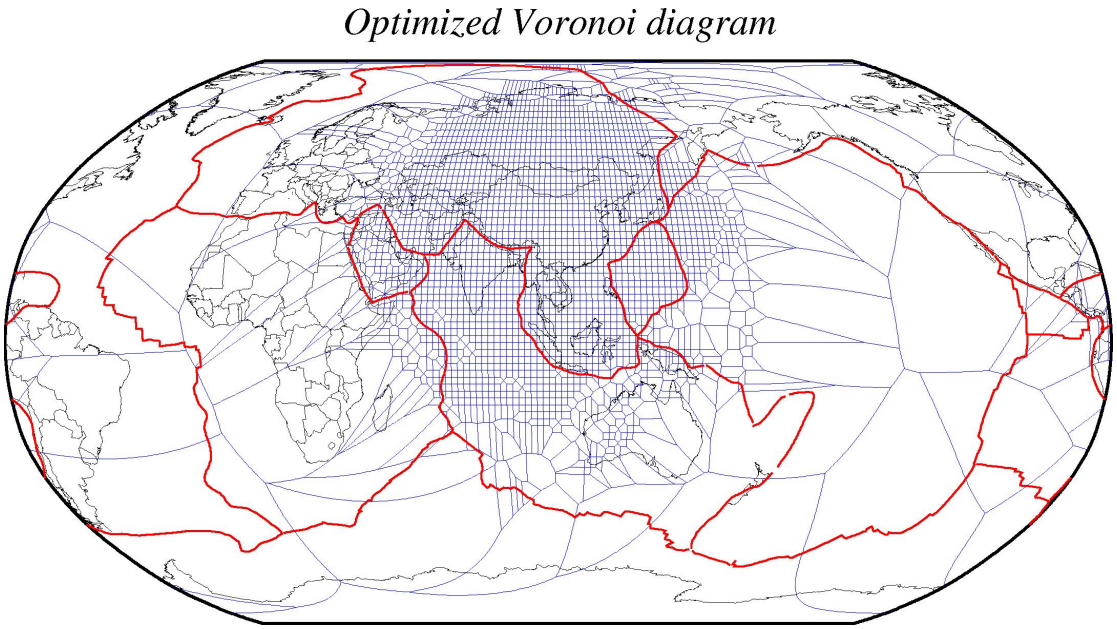

Figure 4.2: Optimized Voronoi diagram showing the coverage of $2^\circ \times 2^\circ$ area for which the $\cos(2\theta)$, $\sin(2\theta)$ azimuthal variation of the Sv wave can be resolved.

Figure 4.3 shows the distribution of the path length. In order to avoid finite source effects all the path lengths considered for waveform inversion were greater than 1000 km. Half of the rays have path length shorter than 6000 km. Ray paths longer than 6000 km are also included in this study to increase ray coverage. Ritzwoller et al. (2002) examined the effect of off-great circle propagation and found that shorter paths ($\sim$5000km), follow adequately the great-circle assumption. This effect is tested on our result by repeating the entire analysis by using only shorter paths ($\leq$6000 km) and using all paths. It is found that the bias due to longer paths is not recognizable. Result of this test is made available in the Appendix C.

4.1 Horizontal Depth Section

Figure 4.4 represents horizontal sections of the 3D inversion results at various depth levels. At depth slices of 75 km and 100 km the variation in velocity perturbation observed is of

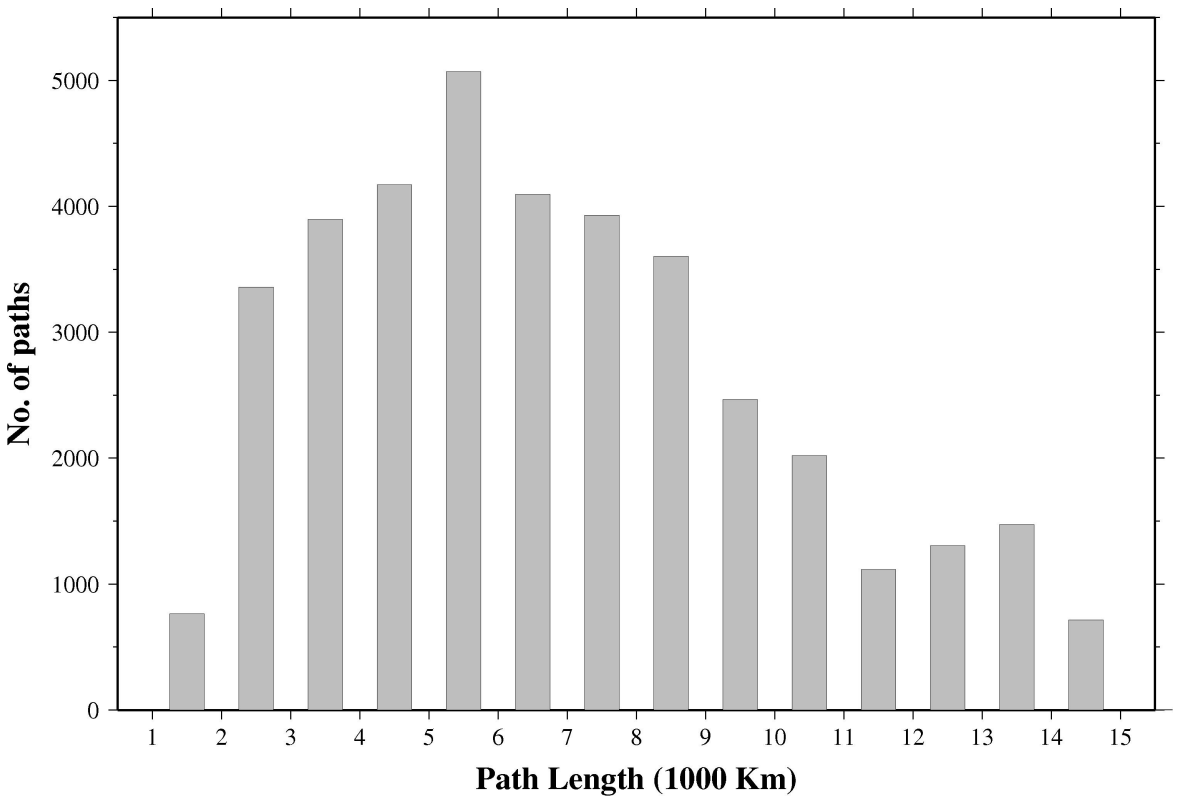

Figure 4.3: The distribution of the path length of the data. On an average nearly half of the data are $\leq$6000km

the order of approximately $\pm 10\%$ in comparison to the reference value. These reference values can be seen at the bottom of each depth slice and the values are changing for each one of them. These two depth slices are marred with wide-spread low velocities in Tibet, Pamir, Central Asian Orogenic Belt (CAOB) and in the oceanic areas. In the northwest Pacific subduction zones the low velocity anomalies coincide with plate boundaries indicating the mantle wedge. Observed low velocities in Tibet and Pamir region could be the artefact because of the thick crust taken in the initial model. Still the extent of these low velocity anomalies are very well constrained by the high velocity anomalies of the Indian plate in the south, by Tarim Basin in the north and by Sichuan Basin and Ordos Block in the east. The high velocity anomalies in India, Tarim, Sichuan, Ordos as well as Songliao Basin are indications of the mantle lithosphere. The two cratons namely: the North China

Craton and the Yangtze Craton are separated by Dabie-Qinling orogenic belt. The western part of the North China Craton, the Ordos block, is characterized by high velocity mantle lid, where the low velocities in the eastern part indicate a shallow depth of asthenosphere as observed in 100 km depth slice. In the Pacific subduction zone, high velocity oceanic plate versus low velocity overriding mantle wedge is clearly observed.

S wave anomalies at 150 km and 200 km depths reflect the variation in the lithospheric thickness. High velocity anomalies indicate lithosphere and low velocity anomalies indicate asthenosphere. In general western China including Tibet, Tien Shan-Pamir, Sichuan Basin, and Ordos Block is characterized by thick lithosphere. As stated above, the lithosphere beneath eastern China is thin. The north of India at exactly central part of the plate boundary has high velocities. The Songliao Basin in the northeast China has also high velocities. The extent of lithosphere beneath Tibet and Pamir reaches up to 200-225 km (for complete model depth slice see appendix B). To the east, high velocity oceanic subducting plate is clearly observable. One of the striking features observed at 150 km depth slice is the restrain of high velocity to the west side of the North-South Gravity Lineament (NSGL).

The amplitude of S wave anomalies reduced significantly (approximately $\pm 5\%$) at depths below 250 km. Instead of high velocities beneath Tibet and Tien Shan, low velocity asthenosphere dominates the region. High velocity in eastern China results from the subducted Pacific oceanic lithosphere. Taiwan and southern Japan are characterized by high velocity anomaly due to triple junctions or the turning point of convergent oceanic plates.

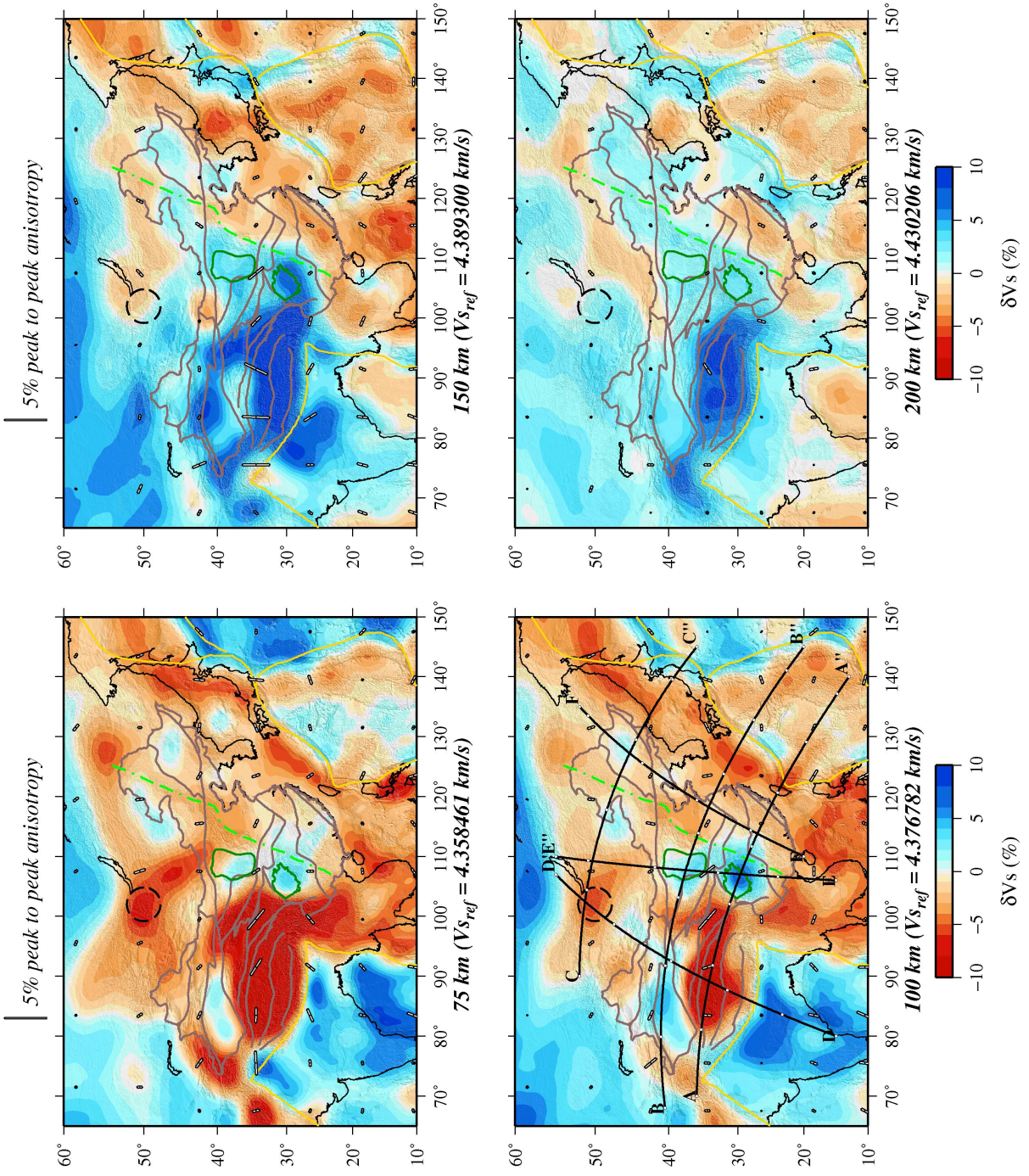

Figure 4.4: The Sv-wave heterogeneity for the depths 75, 100, 150 and 200 km. The reference value for the negative (red) and positive (blue) perturbation are given under each depth slice mentioning the depths. The boundary lines and there explanations are same as plotted on the figure 2.1.

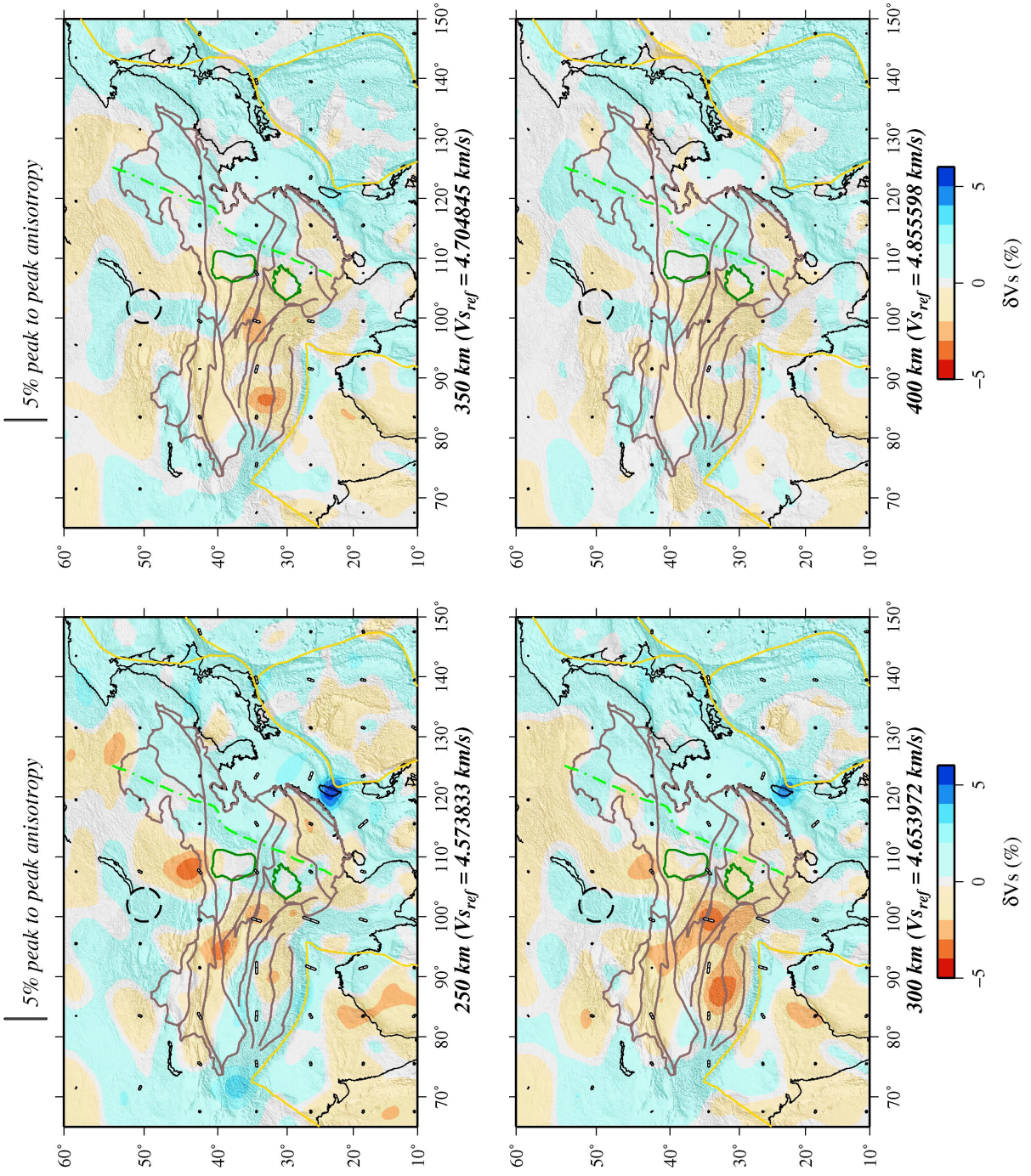

Figure 4.4: *Continued* for the depths 250, 300, 350 and 400 km.

4.2 Vertical Profile Section

A total of six vertical profile sections are presented dissecting all the major tectonic units after careful examination of the depth sections for the anomalies. Section AA", BB" and CC" are approximately oriented in east-west direction, while sections DD", EE" and FF" aligned in north-south direction (Figure 4.5 4.6). Locations of the sections are demarcated on the 100 km horizontal map given in figures 4.4. For each section we have plotted S velocity perturbation as well as the absolute velocities. The anomalies in the velocity perturbation depend on the reference model, and features such as low velocity zones (i.e. negative velocity gradients with depth) are more readily identified on absolute velocity profiles. Topography and major tectonic features along each section are plotted at the top of each section. Also we have plotted the seismicity which are the relocated earthquakes from the EHB catalogue (Engdahl & Hilst, 1998) shown as black dots.

In discussing the anomaly pattern in these profiles it is pertinent to mention, as discussed earlier, that the low velocity artefact may be related with underestimated crustal thickness. Profile AA" originates from southernmost Pamir, passing through central Tibet, Sichuan Basin, South China fold belt and terminates at Philippine Sea. Seismic high velocity anomalies can be clearly observed related to these major tectonic units. A strong low velocity zone exists beneath Tibet down to a depth of 100 km. A pronounced high velocity anomaly is observed beneath entire Tibet down to a depth of 200 km and is interpreted as the mantle lithosphere. The extent of low and high velocities in Tibet is sharply bounded by the mantle lithosphere of the Sichuan Basin in the east. All these anomalies can be clearly observed both in relative and absolute velocity images. In this profile the abrupt transition of high velocity in the continental region to the oceanic area of Philippine Sea where low velocity indicates a thin lithosphere. The high velocity beneath Taiwan at depth

range of 100-300 km may represent the turning point of the oceanic subductions.

Profile BB" moves a little to the north from the profile AA" and passes through two cratonic regions of Tarim Basin and North China Craton with Tien Shan and Philippine Sea at extreme ends. High velocity mantle lithosphere can be clearly seen beneath Tarim Basin in the velocity perturbations as well as in the absolute velocity. The high velocity zone can be extended in the velocity perturbation image in the west beneath Tien Shan and in the east beneath the Qilian FS. In the North China craton (NCC) it can be divided easily in two parts (shown in profile BB" between 3000-5000 km of x-axis), a high velocity mantle lithosphere that exists beneath Ordos Block constituting the western part of the NCC and a thin mantle lithosphere, as marked by the low mantle velocity in the eastern part of NCC. Farther east the subducted oceanic slab of the Philippine Sea and the Pacific plates are observed by the high velocity anomalies, marked by the slab seismicity.

The profile CC" crosses the Hangay Dome, the Songliao Basin, Japan and ends in Pacific Sea plate. The low velocity beneath Hangay Dome can be clearly observed extending upto a depth of 100 km at the southern tip of Baikal Lake. The high velocity zone close to the low velocity beneath Hangay Dome can be interpreted as edge of Siberian shield. Beneath Songliao Basin in the northeast China the high velocity perturbation can be observed to at least a depth of 250 km. The Pacific subducted slab is clearly visible as high velocity region in the mantle beneath Japan and NE China all along the seismicity.

One of the three north-south oriented profile is DD", which originates from south of India, covers the central part of Tibet, the Qaidam basin and reaches Hangay Dome in Siberia. The India-Eurasia collision zone can be best demonstrated by this profile. The most significant feature of our mantle cross-section is the northerly dipping high velocity

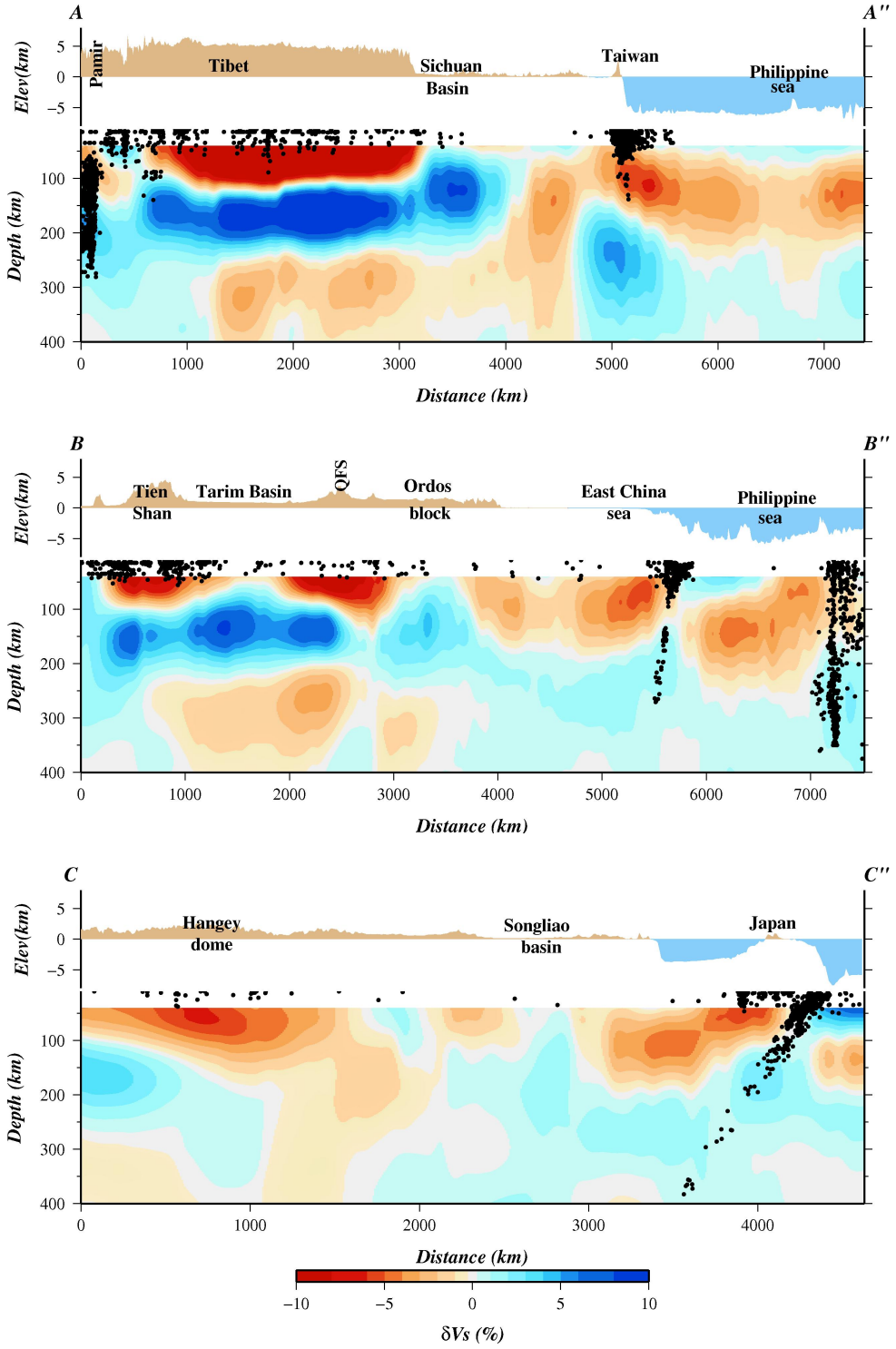

Figure 4.5: The vertical profile (AA",BB",CC") section of perturbation velocity for the lines shown in 100 km depth slice of figure 4.4.The earthquakes (black dots) are projected over 200 km strip (100 km each side of profile lines).

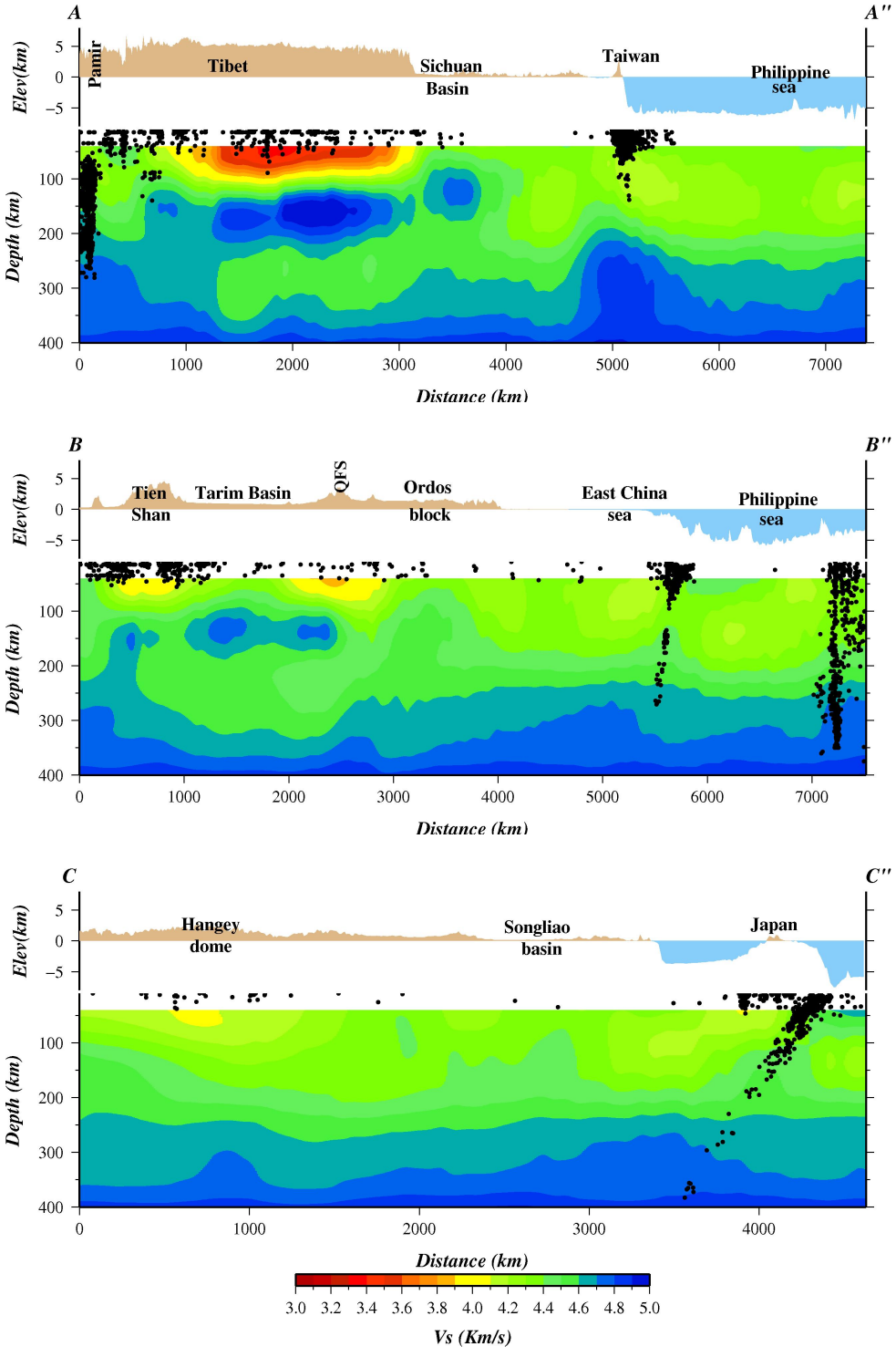

Figure 4.5: *Continued* showing absolute velocity

zone at the depth of upper mantle, representing the Indian mantle lithosphere underthrusting approximately the entire Tibet. Two separate segments of the high velocity lithosphere is clearly observed, first one just at the plate boundary and second one at the staring of the Qaidam basin. The Eurasian plate can be seen north of Qaidam Basin and is shallower ($\sim$50 km jump) than the Indian plate.

Profile EE" is specifically drawn for Sichuan Basin (SB) and Ordos Block (OB) with South China on one side and Mongolia on the other. The SB and OB are the western part of Yangtze craton and the NCC respectively. As stated earlier, these two lithospheric blocks act as resistant blocks to the lithospheric flows created by the Indian-Asian collision. Also the lithospheric thicknesses of these blocks are prominent in comparison to the thin Eastern part. The SB is a more pronounced high velocity body, both in perturbation and in absolute velocities, extending to a depth of $\sim$175 km. The OB reaches a depth of $\sim$150 km and is less pronounced in the section of absolute velocity.

For the profile FF" we moved a little to the east from the profile EE". The profile line is located in east China passing through the eastern parts of the North China craton, the eastern flank of the Yangtze Cratons (YC) and ends at South China Fold System (SCFS). The section is dominated by low velocity perturbation with few exceptions. The biggest one is under Songliao basin which is reaching up to 300 km. The region beneath SCFS and YC up to 70-80 km is interpreted as the mantle lithosphere (see the section 4.5 for detail explanation).

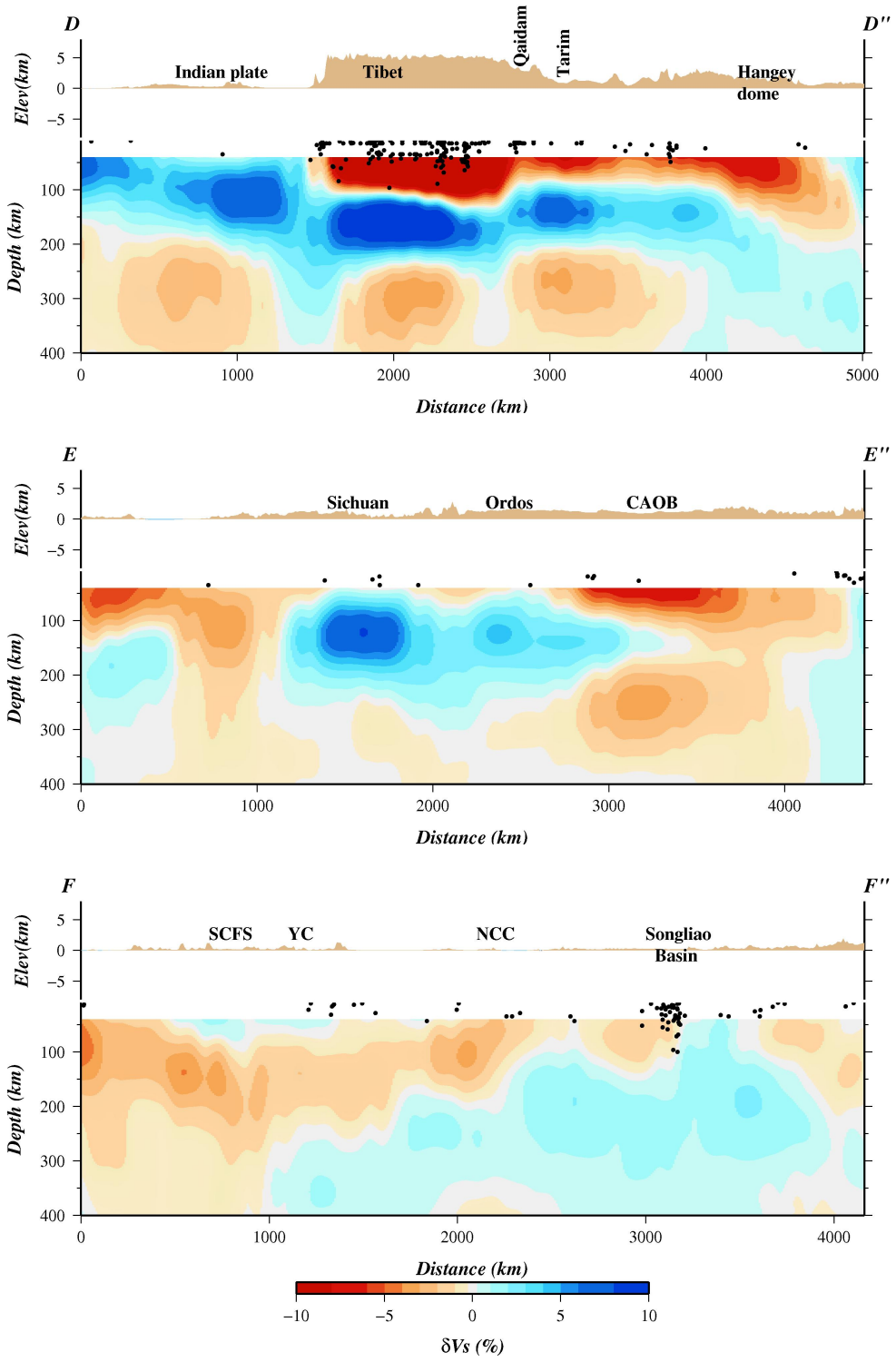

Figure 4.6: The vertical profile (DD",EE",FF") section of perturbation velocity for the lines shown in 100 km depth slice of figure 4.4. The earthquakes (black dots) are projected over 200 km strip (100 km each side of profile lines).

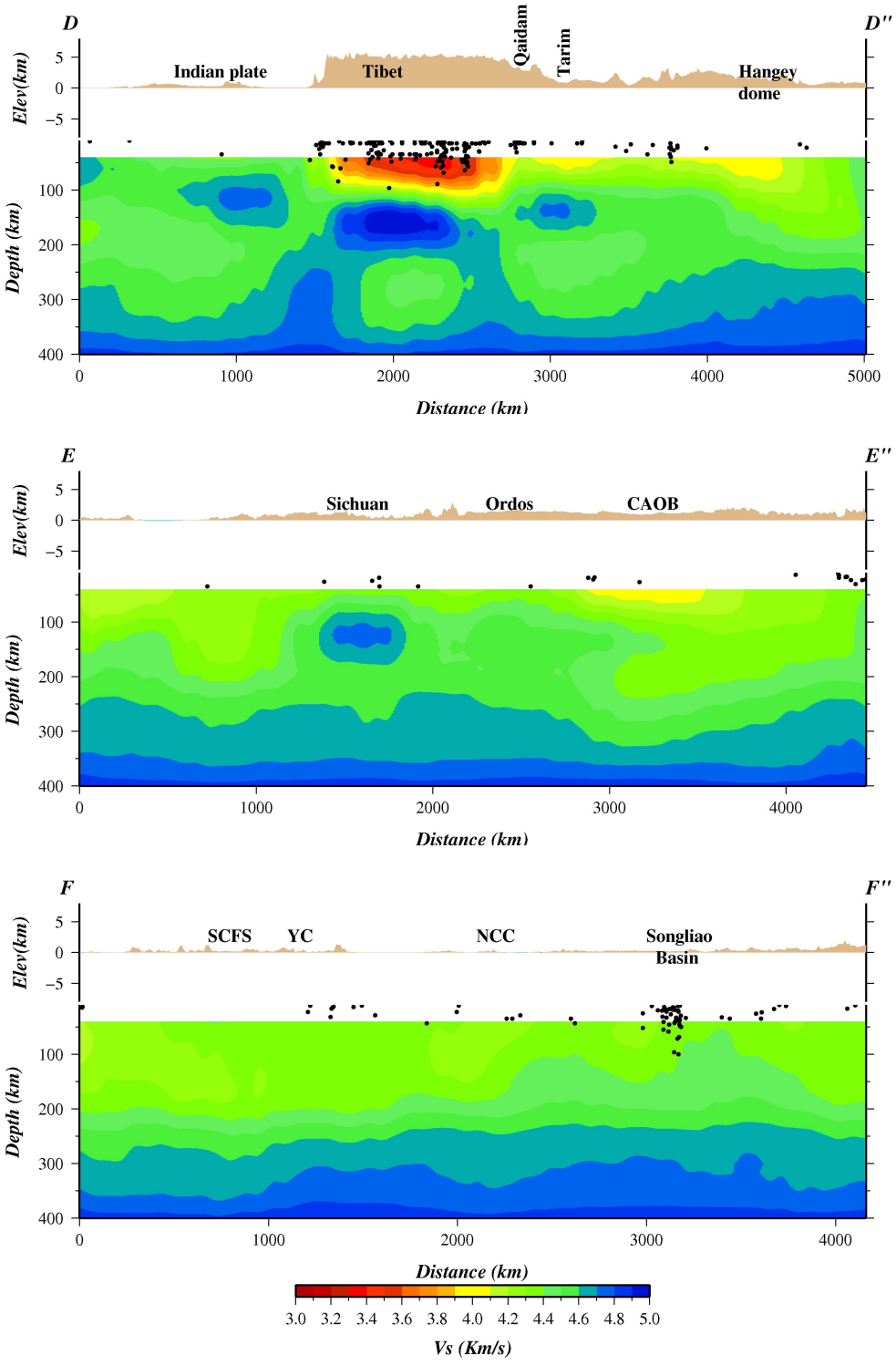

Figure 4.6: *Continued* showing absolute velocity

4.3 Azimuthal Anisotropy Section

In this section we present the result of azimuthal anisotropy (Figure 4.7) derived from the obtained velocity model. In the figure 4.7 we have removed the velocity information so that the amplitude and the direction of the anisotropy fabric can be easily recognized. The result at all depths shows large amplitude (up to ∼5-7%) in some specific regions like Tibet, the Eastern Himalaya Syntax and the turning point of plate boundary beneath Taiwan.

The pattern of anisotropy direction in Tibet at 75 km depth is aligned sub-parallel to the plate boundary or the Himalaya. This alignment is more or less oriented in E-W direction. At greater depths ($\geq$ 125 km), the alignment pattern changes in western Tibet where it found to be oriented along N-S direction. The eastern part of Tibet remains unperturbed till 175 km depth. Anisotropy for the 75 km depth, which is the sub-crustal lithosphere, acknowledges the fact that thick crust within Tibet can be either a result of current deformations, or it can be inherited from the geological past. The exception to this is in the Qaidam basin, the western part of Ordos block and Sichuan basin where the fabric follows the curved tectonics and oriented in NW-SE direction. For the lithospheric part in continent the anisotropy can either be interpreted as mainly frozen or as a primary effect of recent plate motion. Assuming an olivine-dominated mineralogy, the pattern of fast directions can thus be plausibly interpreted in terms of the azimuth of shear strain responsible for crystal orientation. The result obtained in the present research work is also in agreement with the northward movement of the Indian plate clearly suggests that the plate motion is plausible reason for this phenomenon.

Anisotropy in the asthenosphere (at depth more than 200 km) is visibly strong in two areas, at the eastern flank of the Indian plate bending (at Burma) and at the turning point

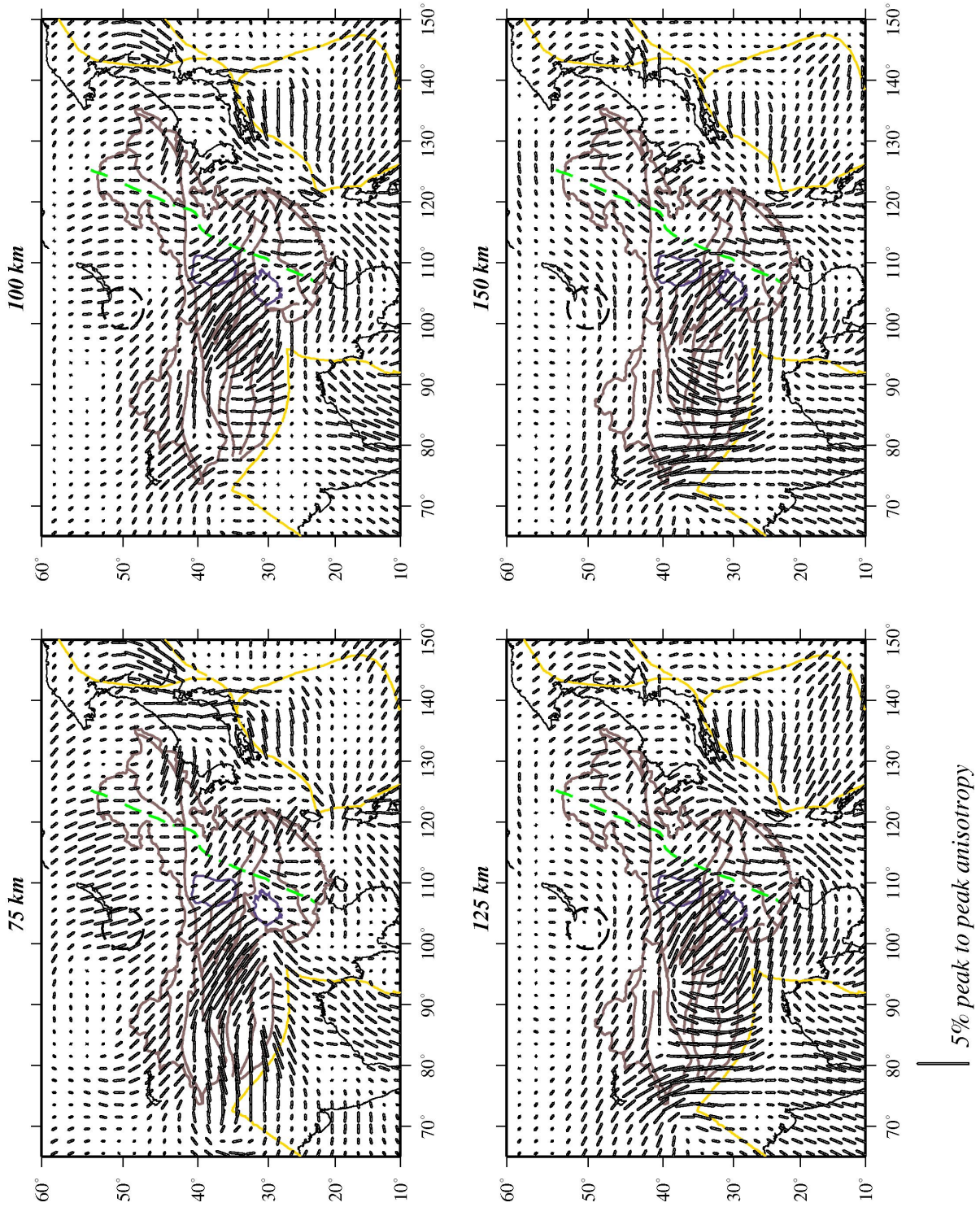

Figure 4.7: Distribution of azimuthal anisotropy for 75, 100, 125 and 150 km shown my black lines. To scale the strength of the line a bar scale of 5% is provided at the bottom of the figure.

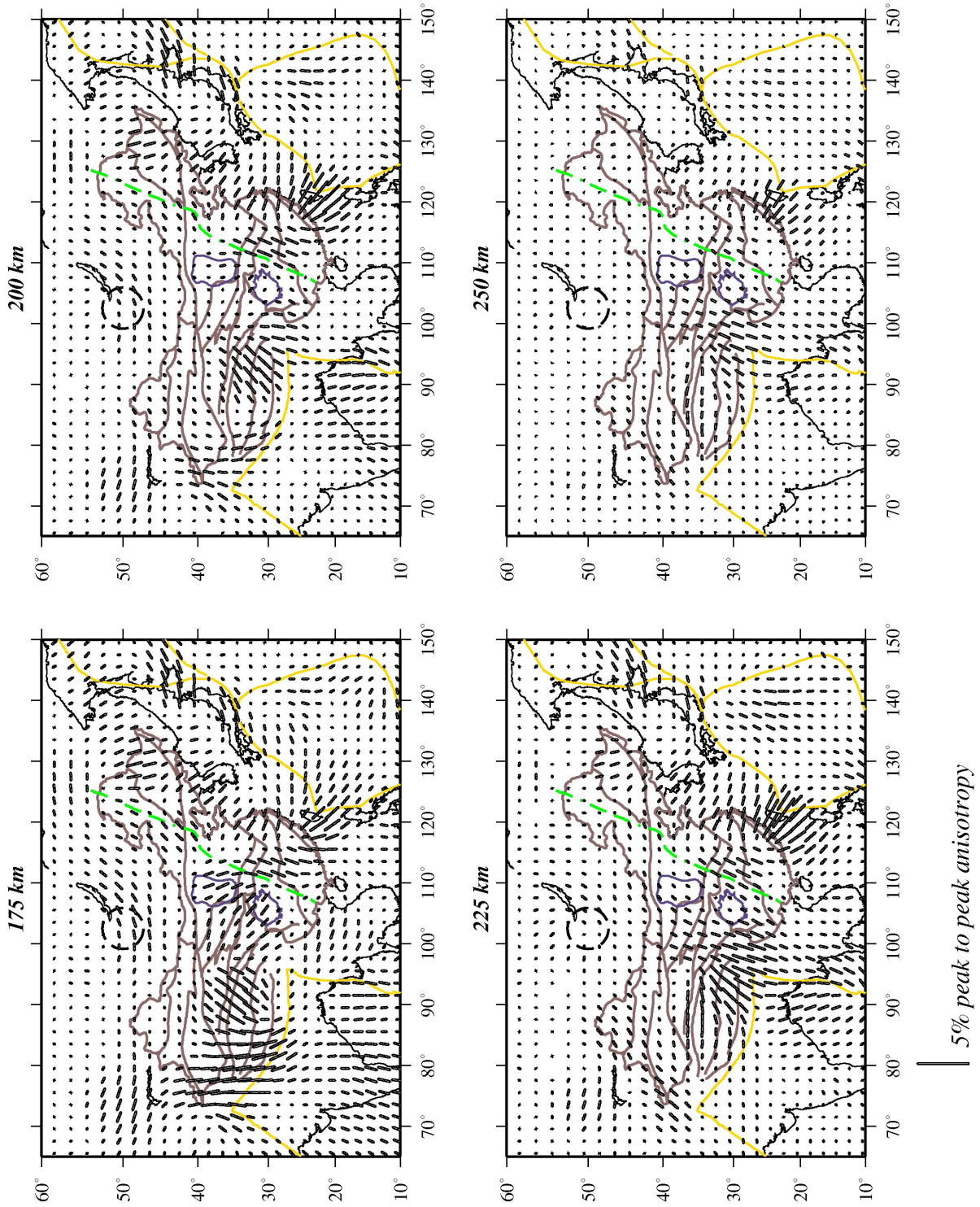

Figure 4.7: *Continued* showing for 175, 200, 225 and 250 km depth.

of the Philippine Sea plate beneath Taiwan.

4.4 Resolution Test

As mention in Chapter 3, using two stage methodology many factors can influence the reliability of the model. In the stage one of calculating 1D path-averaged model the artefact caused by non-inverted crustal structure along the path, wrong estimation of focal mechanism at source, mode coupling or off-great circle path effect could influence the result. For off-great circle path effect we have already discussed at the start of this chapter (for detail see Appendix C). Cara & Lévêque (1987) demonstrated the weak or non-dependence over the reference model. However even with the error in crustal structure the effect on the final result is quite small or none at all (Debayle & Kennett, 2000a). A good path density (Figure 4.1) and azimuthal coverage (Figure 4.2) like we have used in the present research work is a basic requirement for avoiding the influence of these artefacts, as demonstrated with the mentioned figures.

4.4.1 Checkerboard Test

The image accuracy is not quite easy to quantify, however, the well known checkerboard tests are capable of providing at least a quantitative measurements of the ability of a particular data set in resolving the associated existing features. We conducted a number of checkerboard tests to examine the ability of the selected data set to recover the S-wave velocity anomalies of different sizes. Figure 4.9 depicts the result of this test with seismic anomalies extending over 500 $\times$ 500 km grid size horizontally and 100 km vertically. Alternating high and low velocity anomalies with magnitudes of $\pm 6\%$ are spread over the entire volume, separated by zero percent anomaly. The size corresponds to the associ-

ated anomalies in the final models, which we ought to interpret. We calculated synthetic Rayleigh wave seismograms for the same ray paths, source parameters, and frequency contents analogous to that of the observed data and resorted to the same inversion procedure.

The result of the test conducted confirms that the anomalous features can be recovered in the entire volume. At shallow depth ($<$ 200 km) the known input model can be almost completely recovered. At depths range of 200-400 km approximately half of the magnitude of the anomalous features can be recovered. The synthetic test shown in figure 4.9 provides an intuitive example of the ability of the adopted procedure to recover a particular model from the ray coverage and a priori choices of the models. However, as observed by Lévêque et al. (1993) such a test does not give guarantee that other synthetic models having larger size structure will be better retrieved in all circumstances. Keeping this observation in to consideration, we performed other synthetic test with seismic anomalies with 750 $\times$ 750 km and 1000 $\times$ 1000 km grid sizes horizontally with 50 km and 100 km vertically respectively. Due to dense coverage, all these known input models are always retrieved. It is therefore can safely be assumed that seismic anomalies larger than 500 km are reasonably well resolved by our data in the uppermost 400 km.

4.4.2 Flat Model Test

The second stage of the adapted methodology aims to retrieve lateral variations in shear wave velocity by combining each path between seismic events and recording stations at all depth. The controlling factor for mapping the sharp lateral transition in the scheme of regionalization is the correlation length (L_{corr}). The correlation length can smoothen out the model perturbation when sufficient paths are available, however it can also create the smearing effect at places which are not sampled by the surface waves (Lévêque et al., 1998).

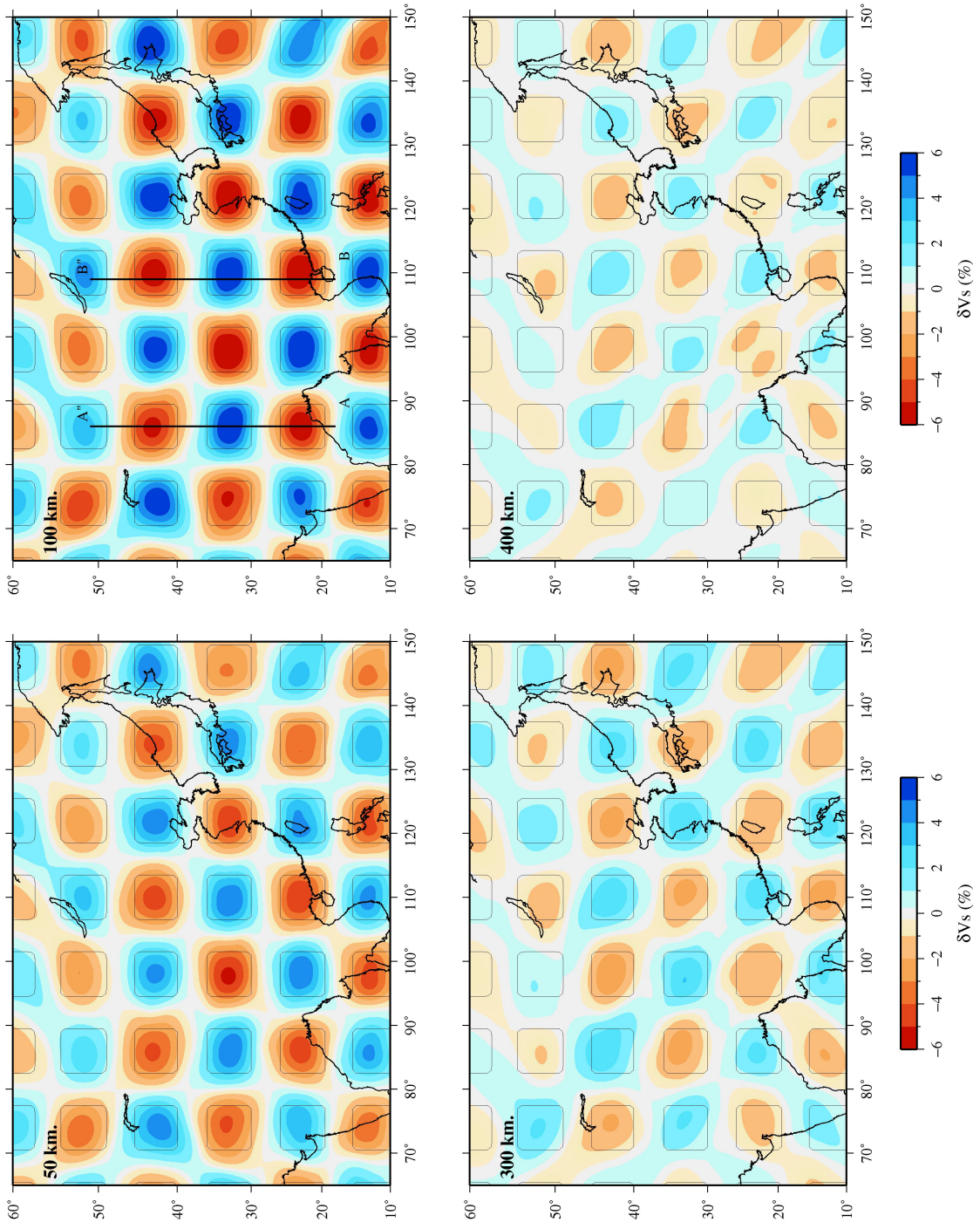

Figure 4.8: Checkerboard resolution test for 500 km × 500 km × 100 km block shown as black square line. The anomaly used here for the creating checkerboard model is ±6% separated by zero percent anomalies. The result is shown for the four depths of 50, 100, 300 and 400 km mentioned within each depth slice.

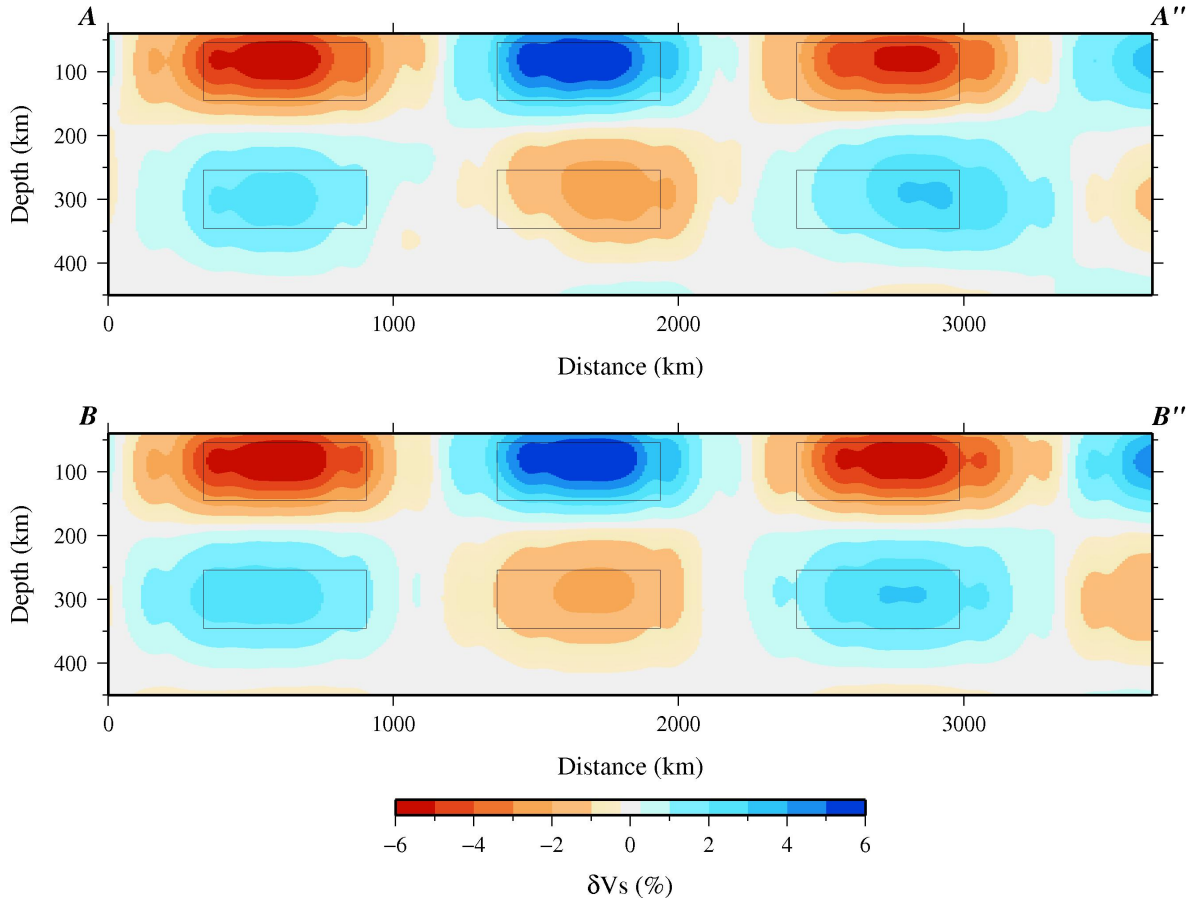

Figure 4.9: Profile of AA" and BB" for Checkerboard test. The lines are shown in 100 km result of figure 4.8.

This aspect is checked with a simple analytical test by adding 5% and 15% anomalies to the *a priori* model representing laterally homogeneous structured synthetic model. This synthetic model is then being used to generate the synthetic dataset of 1-D path averaged model. Then these synthetically generated 1-D path averaged models were subjected to the regionalization scheme, like we did for the original dataset. From the output thus obtained (See Figure 4.10) it is evident that the considered correlation length value allows us to retrieve the flat model uniformly for the area of interest. The smearing around the edges can be interpreted as the effect of the width of the Gaussian of the correlation length.

4.4.3 Anisotropy Test

Anisotropy is described by a vector quantity that requires two attributes, namely: amplitude and direction. For estimating the resolving power we designed three different kinds of tests. In the first synthetic test we used the isotropic 3SMAC velocity model for the entire 1D path-averaged model. We generated synthetic data and process them in the same way as for the observed data base of 1D path-averaged model. Figure 4.11 contains the initial and final results for the test conducted. The inverted model shows a smoothed image of 3SMAC velocity model and also displays the azimuthal anisotropy. The major discrepancy in the anisotropy result is visible in 50 km depth slice. The reason for this could be assigned to the trade-off between azimuthal anisotropy and the short-wavelength heterogeneity. Moreover in other depth slices the amplitude is almost negligible.

The second synthetic test is related with the resolving power of the direction of anisotropy. For this purpose a flat 1D model is considered introducing a 45° anisotropy with changing its direction every 10° as shown in the figure 4.12 (with heading INPUT). The actual 1D path averaged velocity values are replaced by the one generated for the synthetic model

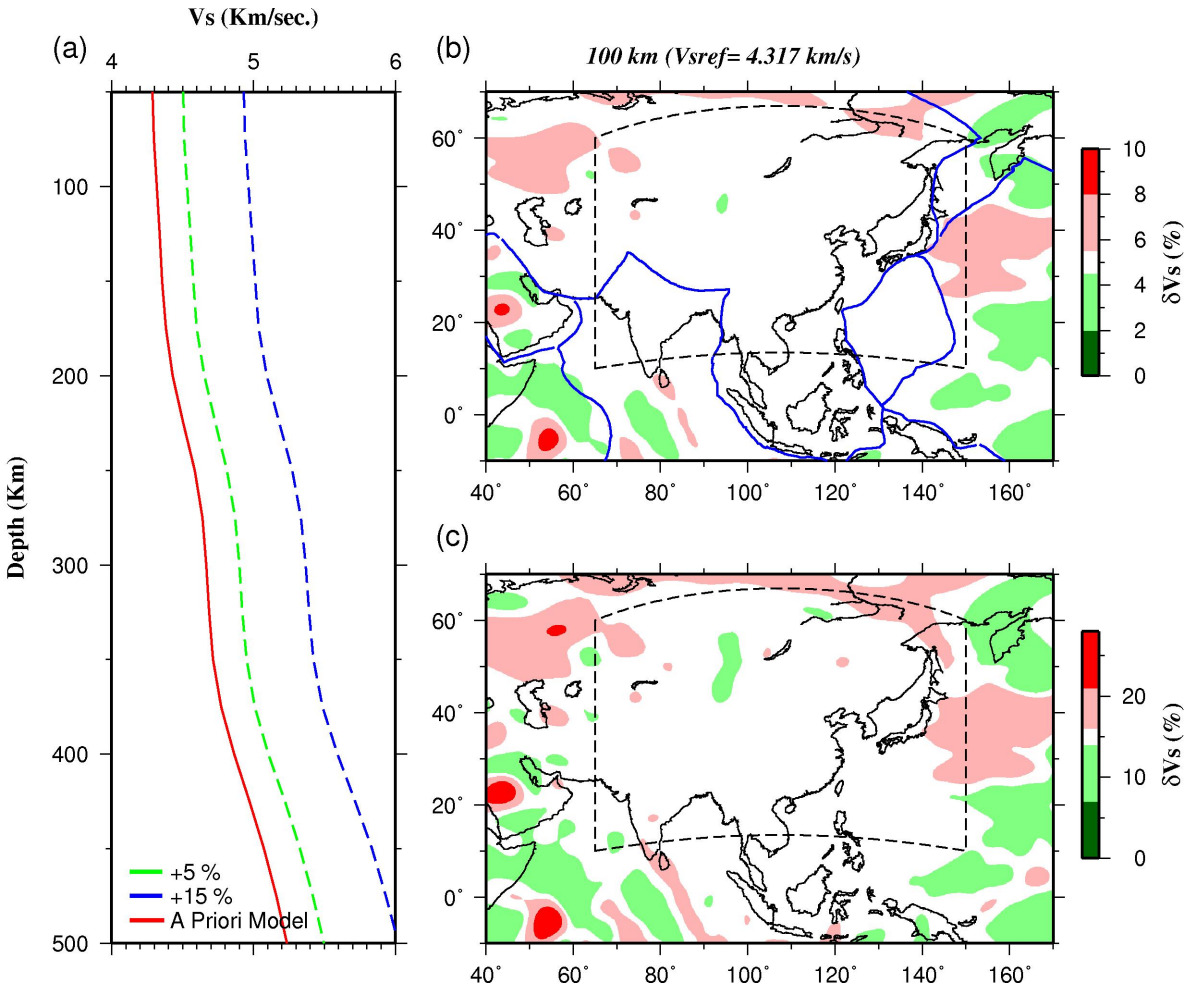

Figure 4.10: Flat model resolution tests for the (a) two flat models of 5% (green) and 15% (blue) form the average final model (red). On the top of right side is the result of the 5% flat model test and below is the result for the 15% flat model test.

and same 3D inversion scheme is used. The results thus obtained are presented in figure 4.12 showing the recovery of the input direction over most of the study area. Though the strength of the amplitude is not fully recovered but wherever we recovered the strength the direction of anisotropy is same as that of the input. The third test is similar to the previous one with little modification. In this test we have used the checker formation of the anisotropy with 45° orientation and changing its direction every 10° by 10°. The result (Figure 4.13) of this test is very poor as the recovery of the amplitude is very low (∼1%). Thus we can conclude that it is difficult to recover a pattern of anisotropy with such a

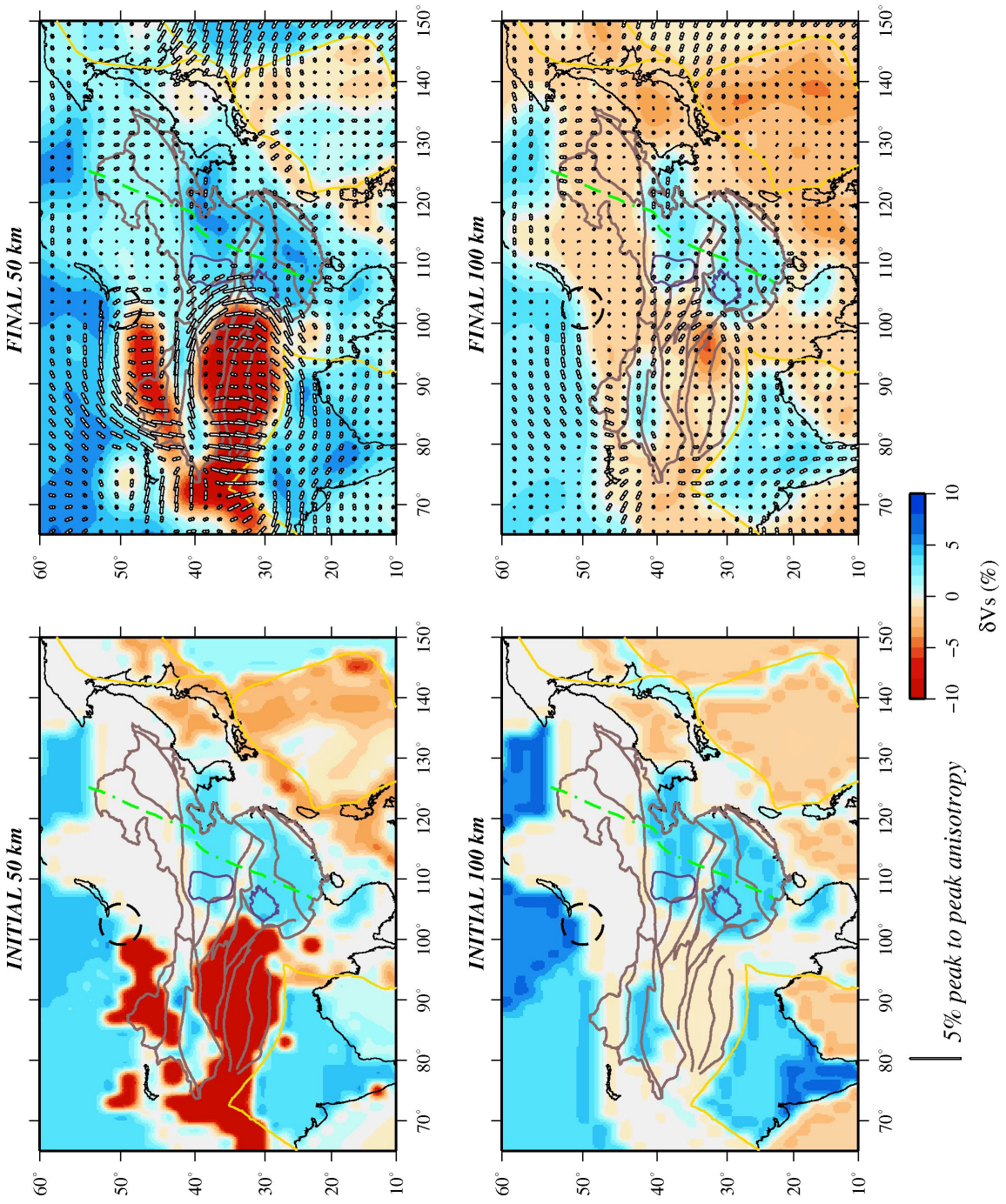

Figure 4.11: Figure showing the initial and final anisotropy synthetic test using an isotropic 3SMAC (zero anisotropy) as an input velocity model for depth 50 and 100 km.

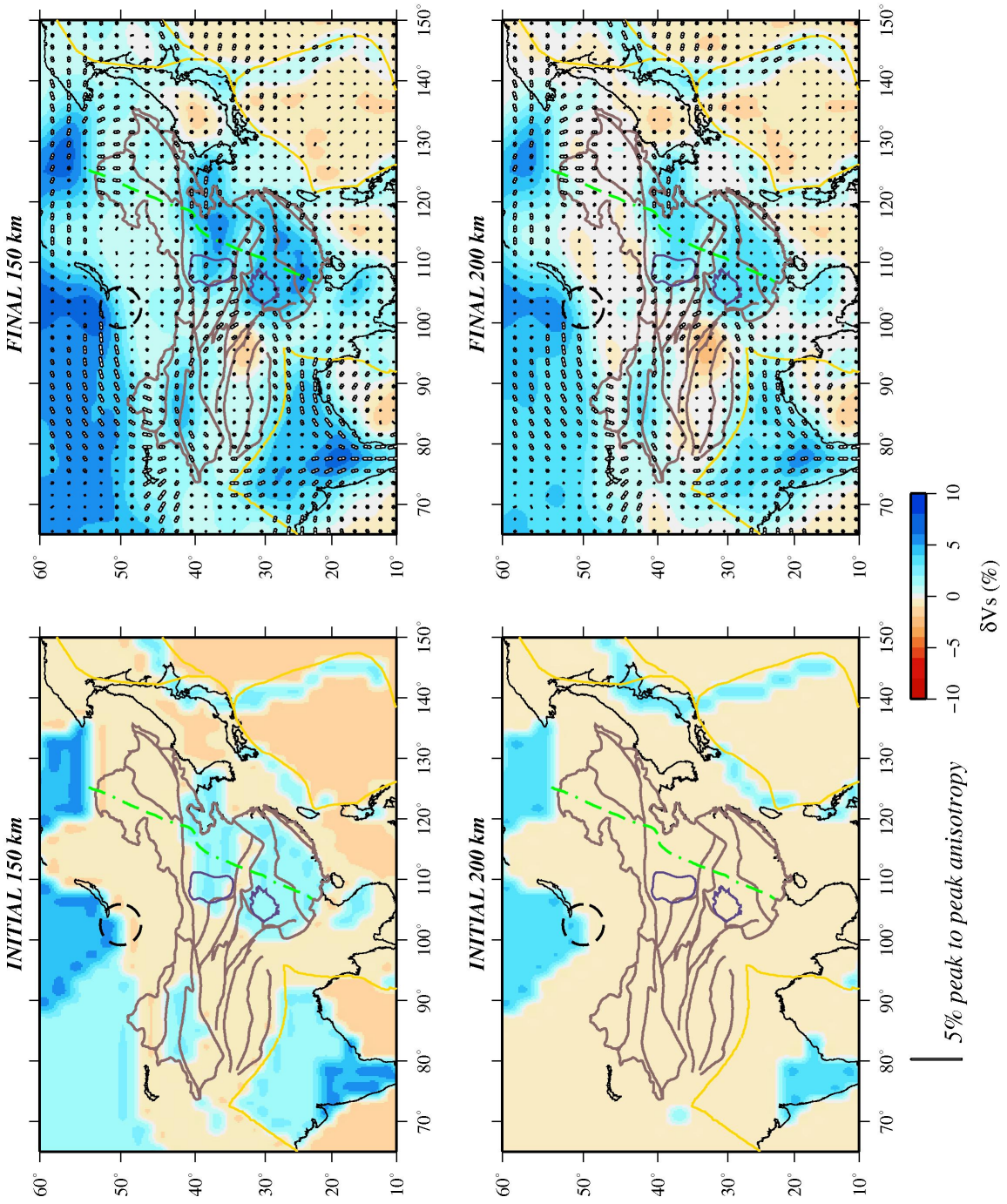

Figure 4.11: *Continued* for depth 150 and 200 km.

rapid change in direction.

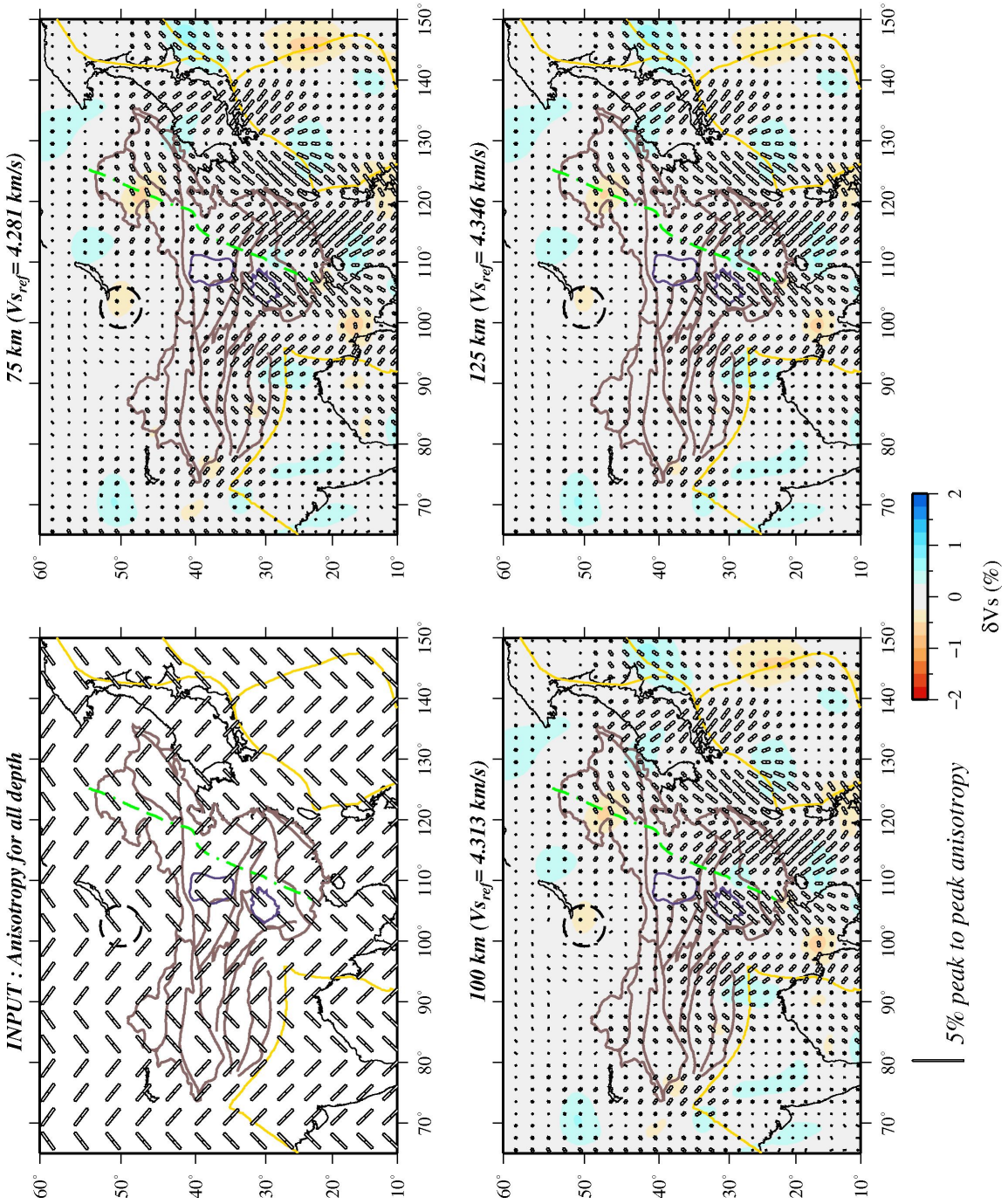

Figure 4.12: Synthetic anisotropy result: the anisotropy of 45° orientation changing after every 10° in longitude for a flat model at every depth shown as INPUT.

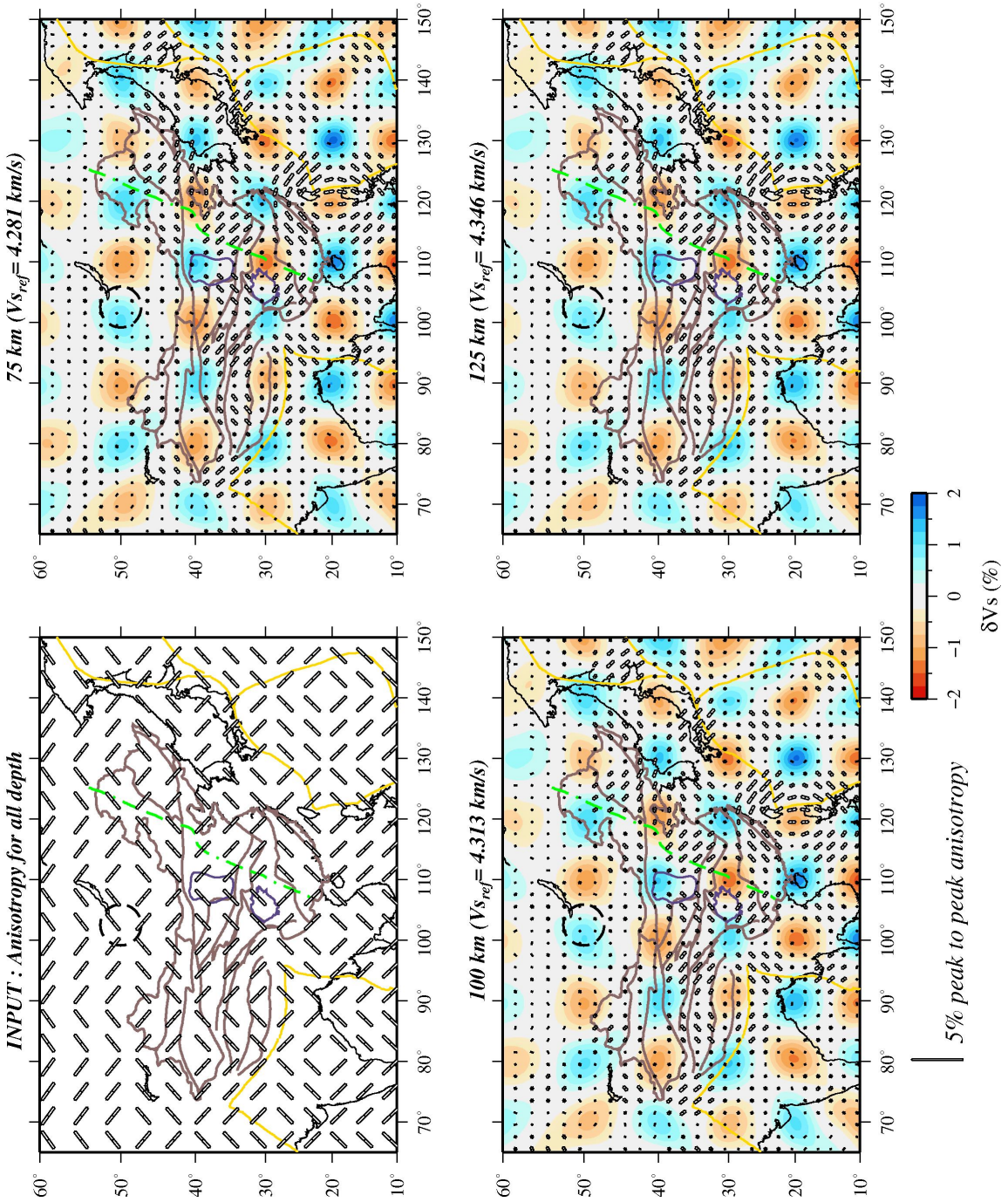

Figure 4.13: Synthetic anisotropy result: the anisotropy of 45° orientation changing after every 10° in longitude and latitude for a flat model at every depth shown as INPUT.

4.5 Discussion

Once satisfied with various tests regarding resolving powers of the data set and the tomographic inversion methodology used, the entire observed data set is utilized in generating 3D velocity model of the area under consideration. This velocity model can be interpreted geologically under known frame work. The mantle lithosphere of China comprises two major cratons, the North China Craton and the Yangtze Craton, separated by fold thrust belts. However the thickness of the lithosphere does not follow the geographic locations of these tectonic units. Generally the lithosphere is thin in east China and thick in the west (see Figure 4.4). From numerous other studies (Huang et al., 2003; Lebedev & Nolet, 2003; Priestley et al., 2006; Priestley & McKenzie, 2006; Feng & An, 2010; Fang et al., 2010; Obrebski et al., 2012) it is almost established that there exists a thin lithosphere in the eastern part of China in comparison to the western part. The border of this demarcation can be taken as along the North-South Gravity Lineament (Xu, 2007; Obrebski et al., 2012). In the Eastern part of the North China Craton the lithosphere is too thin to be observed or resolved. But in the Yangtze Craton and in the South China Fold System we recognize some high velocity anomaly sufficient enough to indicate the presence of lithosphere (Figure in appendix B for depths of 50 and 75 km). For the qualification of this statement we performed an inversion test excluding any path that crosses through the Tibet. This test gives the confidence that the image outside Tibet is not biased by the crustal heterogeneity and represents true mantle velocity perturbations. Result of this test is presented in appendix D with the profile lines of EE" and FF" same as in figure 4.6c. It is commonly agreed (Menzies & Xu, 1998) that the lithosphere is thinned in Mesozoic and the depleted cratonic lithospheric root is removed in East China. In receiver functions studies the lithosphere thickness beneath NCC was estimated around 60 km (Sodoudi et al., 2006; Chen et al., 2008; Chen, 2009) and beneath YC around 70-80 km. The heat flow studies

also support these results (Ma et al., 1984).

To the west of the NSGL the picture of lithosphere is entirely different. This part of the cratons has thick lithospheric root preserved beneath Ordos Block and Sichuan Basin (See figure 4.1, 4.6b). The thickness of lithosphere in OB reaches as deep as ∼150 km whereas in SB it is ∼175 km. Profile AA" shows a significant difference in the extent of the lithospheric thickness between the Tibet (∼200 km) and the Sichian basin. Though Zhang et al. (2010b) in there migrated P-receiver function image drawn the line for LAB for the eastern Tibet (60-80 km) to western tip of Sichuan basin(∼100 km). The total extent of there profile length is nearly 500 km which is beyond the scope of the resolving power of our method. Another very prominent high velocity body in our result is Tarim basin also reaching to the same depth level as of SB (∼175 km). These cratonic bodies seems to block the Indian-Asian collision by forming the north (Tarim basin) and east borders (Ordos block and Sichuan basin) and probably acted as rigid bodies resisting the plate motion and lithospheric flow during the collision and post-collision processes (Clark & Royden, 2000; Royden et al., 2008). The northward moving Indian plate has a thickness of 100-175 km with its thickest part in the north central India adjacent to Tibet. The lithosphere beneath much of the Pamir-Tibetan plateaus has been double its thickness during the Indo-Asian collision with a maximum thickness over 200 km beneath the Tibetan plateau. The doubled thickness of the lithosphere is a result of the Indo-Asian collision. A northward penetration of the Indian plate beneath most part of the Tibetan plateau is evident in our result (Figures 4.4,4.6 and 4.16).

Regarding tomographic results pertaining to the northern most part of the study area we observe a prominent low velocity anomaly located beneath the Hangay Dome at the tip of the Baikal Lake. This has been identified as the feature related to volcanic field as

observed by many others (Priestley et al., 2006; Friederich, 2003). The extent of this low velocity anomaly does not reach more than 125 km. The low velocity zone is also observed in south of Tarim and Qaidam basins, which can at best be seen at 125 km horizontal section (Figure 4.4). This low velocity zone, also observed by Feng & An (2010), is constrained in a much smaller area and is extending to a greater depth separating the Tibetan plateau from the Tarim basin.

The tectonic diversity of China discussed in relation to the velocity model is also evident in the azimuthal anisotropy also. Even within Tibet the Global Position System (GPS) measurements documented a gradual change of surface motion from northward in southern Tibet to a clockwise rotation motion around the Eastern Himalayan Syntaxes with respect to stable Eurasia (Zhang et al., 2004). From the result of azimuthal anisotropy obtained in the present work at shallow depth, the orientation of the fast polarized axis correlates well with the surface geological feature. The depth-dependent change in alignment of the anisotropy in the India-Eurasia collision zone has also been reported previously (Vinnik et al., 2007; Singh et al., 2007; Huang et al., 2004). For most of the eastern part of Tibet the alignment of anisotropy is oriented east-west for the shallow part (see Figure 4.7 for 75 km). The north-south orientation of the deeper part of anisotropy ($>$ 100 km) can be correlated with the present day plate deformation. The interesting feature of the result is in northeast and east of Tibet where the direction doesn't change (up to 200 km) (Zhang et al., 2011a; León Soto et al., 2012). Even the results of SKS splitting (Flesch et al., 2005) for this particular region is in aggrement with our results. The depth-variation anisotropy are plotted together in the figure 4.14 with anisotropy result at two depths, 75 km (red) and 125 km (blue). The close observations of these results clearly suggest a strong decoupling between the crust and lithospheric mantle in the western Tibet. Similar phenomenon is observed in North America by Yuan & Romanowicz (2010) and Yuan et al. (2011). For

the eastern Tibet this observation is not visible.

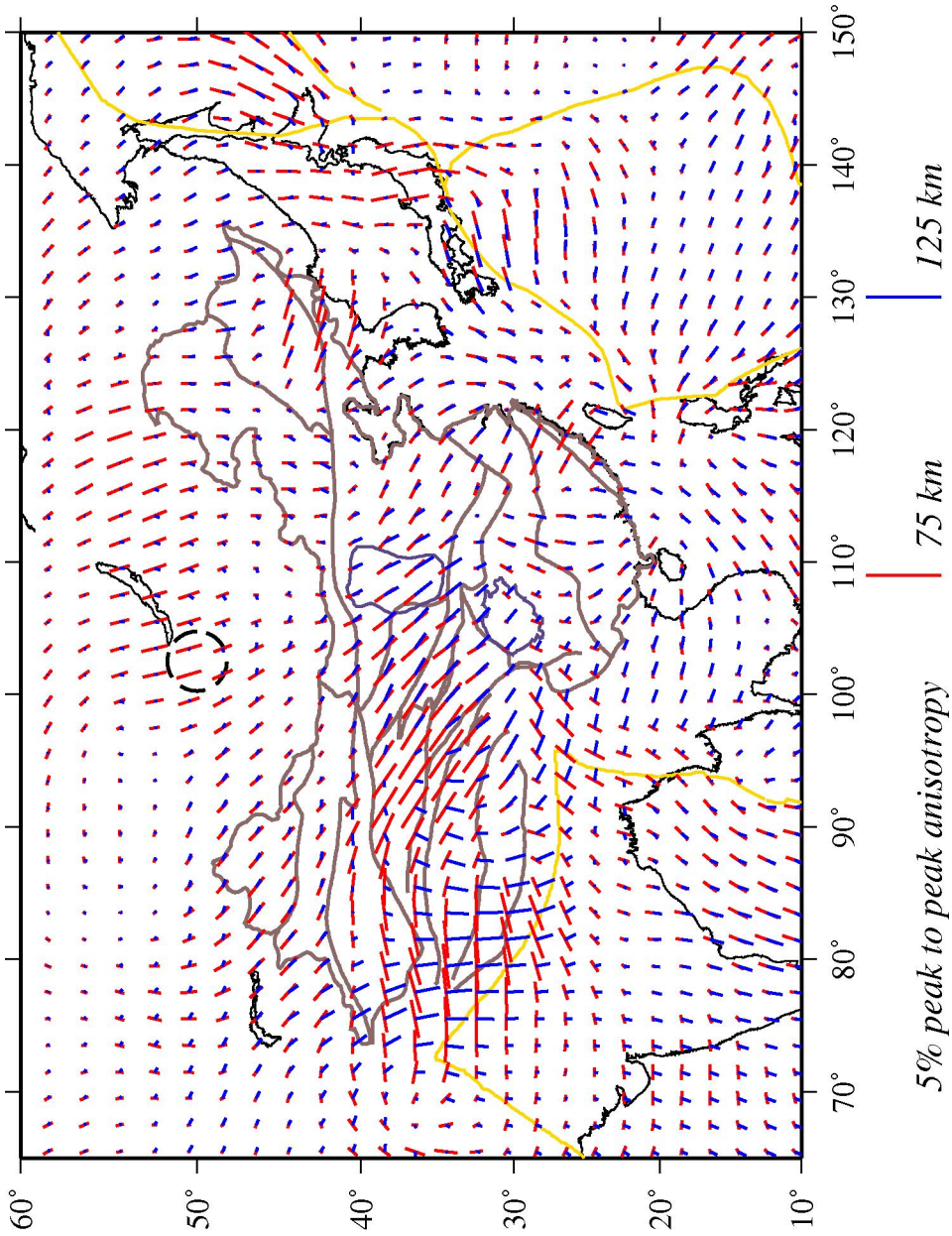

Figure 4.14: Result of azimuthal anisotropy distribution for the 75 km (red) and the 125 km (blue) result drawn over each other. The bar scale of 5% is given below in two different colour.

4.6 Comparison with SS precursors and Receiver Functions results

Propagation of body waves is influenced by the seismic velocity variation in the upper mantle. Analysis of reflected SS and converted Ps waves at the mantle discontinuities may provide information on average seismic velocity in the upper mantle. While surface waves constrain the average seismic velocity along the path, propagation of body waves contains more local information. The 410 km and 660 km mantle discontinuities marking the top and bottom of the mantle transition zones are generally thought to mark the mineralogical phase changes within the mantle. Experimental studies have shown that both reactions are sensitive to temperature and have Clapeyron slopes of opposite signs. In the absence of other effects, a lateral increase in temperature at the level of the transition zone should be reflected in a deepening of the 410 km discontinuity and a shallowing of the 660 km discontinuity (and vice versa). However, the arrival times of the mantle discontinuity phases can be significantly influenced by the average seismic wave velocities in the upper mantle, which is in turn controlled by tectonic factors such as thickness of the crust and lithosphere, velocity changes in the lithosphere and asthenosphere. As a result the two discontinuities will be apparently shifted in the same direction in the time series.

4.6.1 Comparison of upper mantle velocity variations derived by surface wave inversion with SS precursors

The underside reflected SS wave (means bouncing back inside the earth) can be observed in the seismograms as precursors to the SS wave. The differential time of the SS precursor at the mantle discontinuities ($S410S$ and $S660S$) and the mother phase SS is a function

of the depth of the reflector as well as the average velocity in the upper mantle. Heit et al. (2010) created a long profile of SS precursors and found parallel time variation in the $S410S$ and $S660S$ phases along the profile (see Figure 4.15 for profile location), which is consistent with shear wave velocity variation in the upper mantle. In Figure 4.15 mid-panel we plotted deviation of the $S410S$ time in percent of a reference value (160 s) shown in red colour line and compared it with perturbation of the average velocities (Sv) over 400 km depth range shown in black colour line, along the same profile. For calculation of the average velocity in the upper 400 km we have integrated the 3SMAC model for the crust into the inverted 3D model. The profile extends from Tibet across North China Craton to the Pacific subduction zone. The absolute velocity along the profile (Figure 4.15, lower panel) exhibits low velocities in the shallow mantle beneath Tibet and high velocities of the mantle lithosphere below. The $S410S$ time perturbation curve has the same shape with the curve of average shear wave velocity variations in the upper mantle, derived by the surface wave tomography. Both curves show negative values beneath Tibet and increases to the East and become positive beneath the Pacific regions. The difference of the two curves can be explained by different lateral resolutions of the two methods and the time change caused by the real variation of the reflection (the 410 km) depth.

4.6.2 Comparison of upper mantle velocity variations derived by surface wave inversion with receiver functions

In a similar manner Figure 4.16 presents a comparison (average Vs over 400 km) between the average velocity perturbation derived by the surface wave inversion and that derived by receiver functions along three profiles in Tibet. Kind et al. (2002) and Zhao et al. (2010) observed a delay in the 410 and 660-km discontinuity phases in northeast Tibet

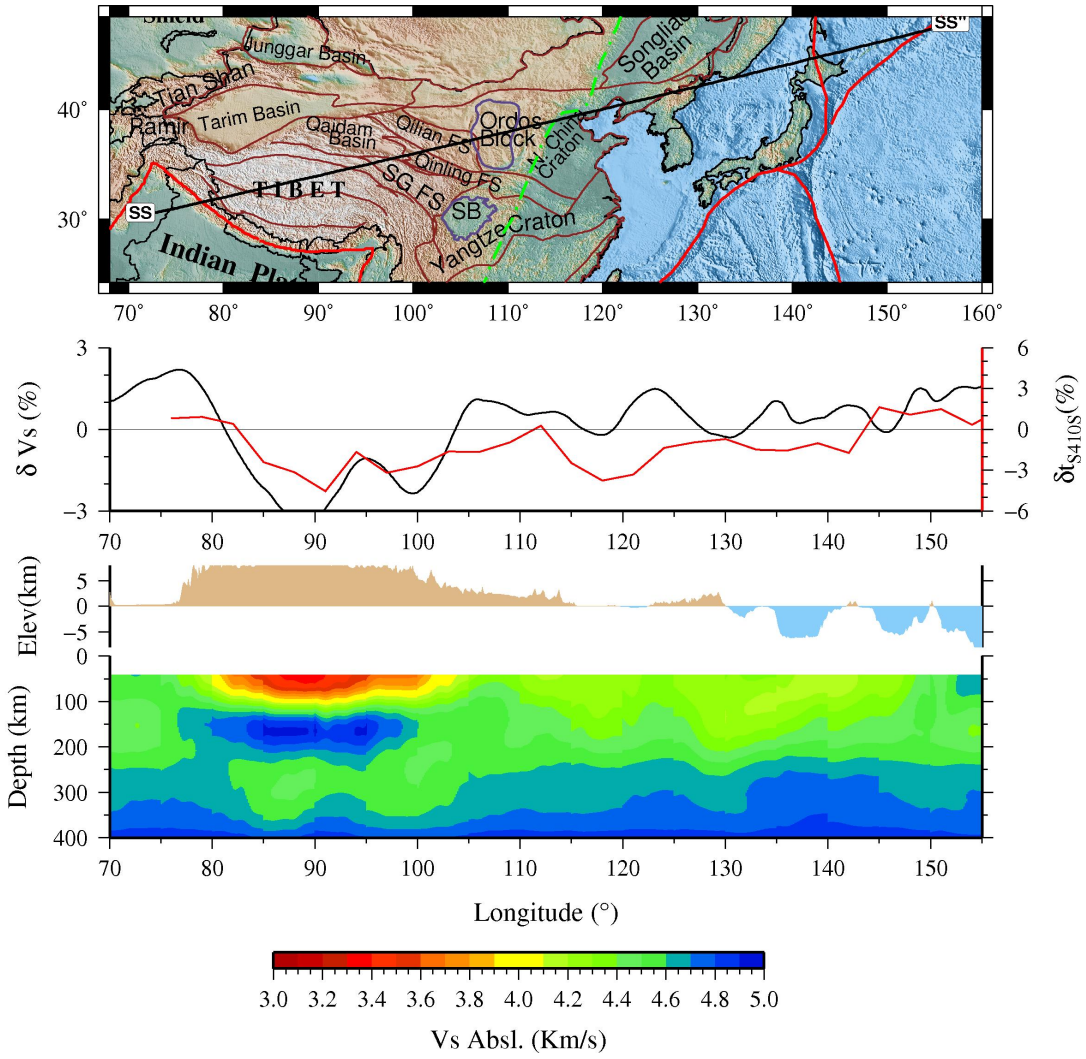

Figure 4.15: The cross-section profile of the tomographic model comapring with the *SS* precursor (Heit et al., 2010) for the upper mantle. On the top is the map showing the profile line in use. In the middel part is the comparison (in %) plot of average upper mantle velocity model of our result (black line) and the plot of $S410s$ time (red line). Bottom part is the profile of absolute velocity model.

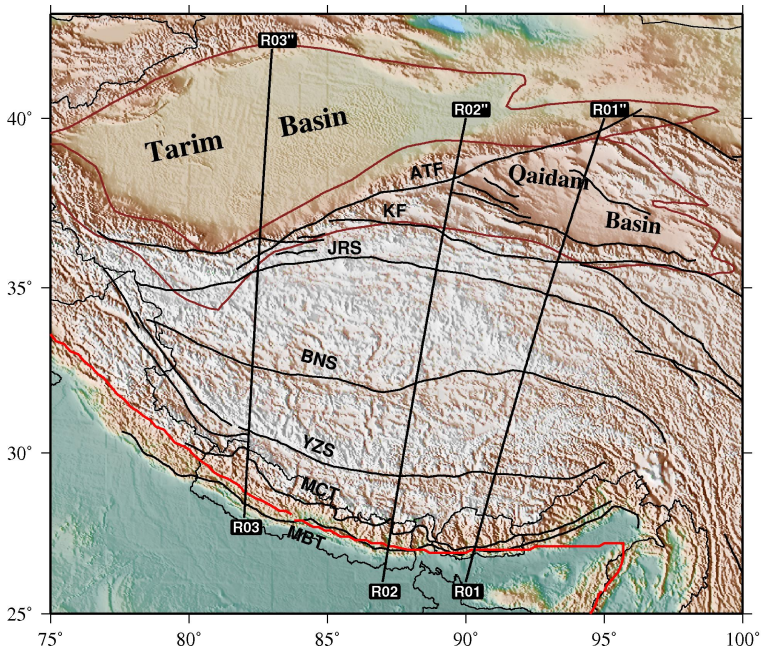

Figure 4.16: Map showing the receiver function profile lines as used in Zhao et al. (2010)

and interpreted it as the effect of velocity reduction in the upper mantle. The top panel of each profile is similar to the previous profile of SS precursor. However, in the present case the red line indicates the perturbation of the $P410s$ instead of $S410S$ and the black line is same as described before. Along the east (R01-R01") and central (R02-R02") sections, the perturbations of $P410s$ and average velocities (Vs) appear to maintain constant separation across the profiles, while both phases appear to be depressed in the north. On the west section (R03-R03") the delay is the minimum, which is in agreement with the lateral variation of the strongly deformed Tibetan lithospheric block. We marked the positions of the Moho and LAB observed by Zhao et al. (2010) on the absolute velocity profiles derived by the surface wave inversion. The high velocity mantle lithosphere is in agreement with the results of the receiver function LAB shown by the white colour lines in the profile (Figure 4.16). The mismatch at few locations can be explained due to different resolving powers of the two methods.

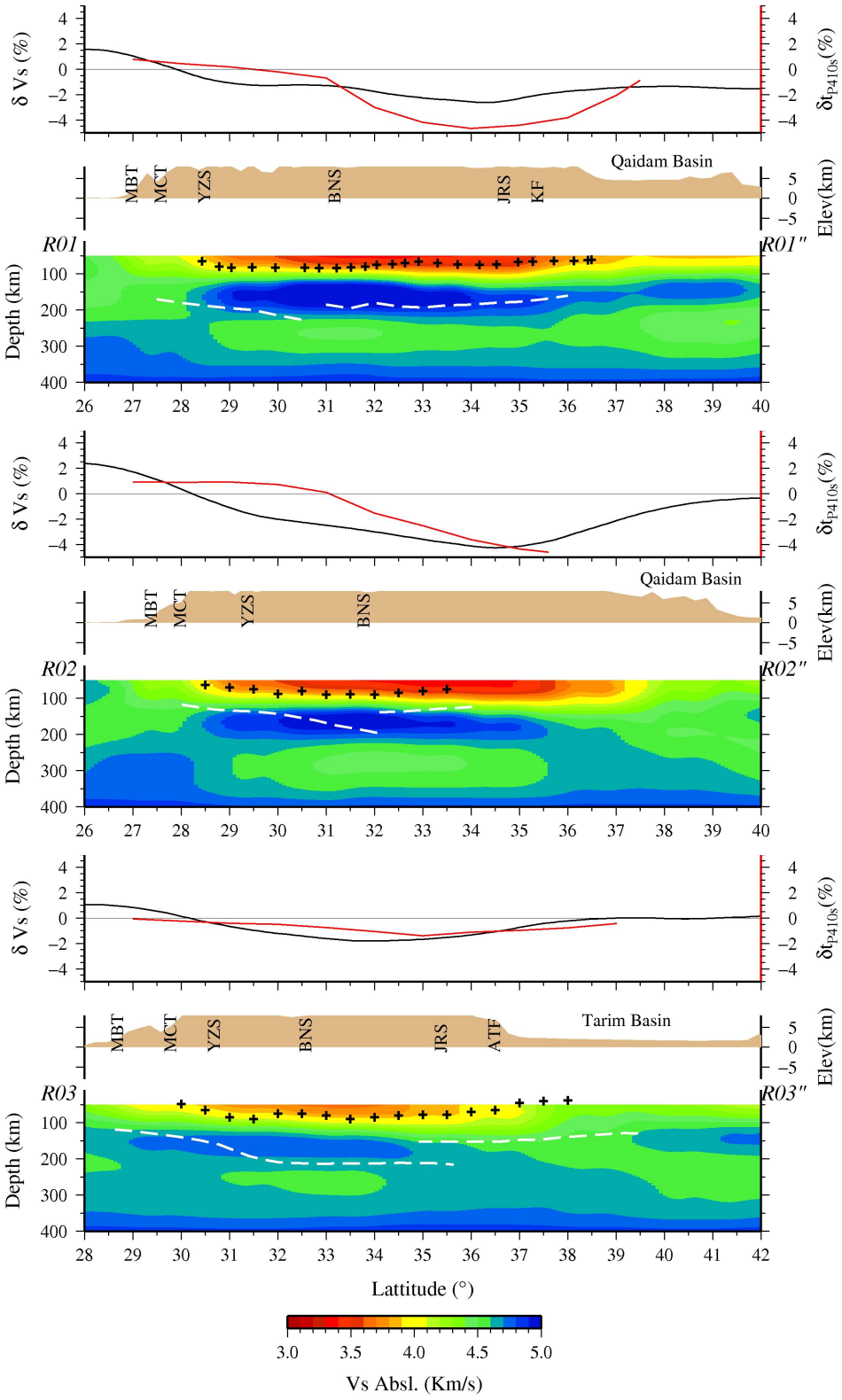

Figure 4.16: The upper part of each profile is the comparison of the average upper mantle model (in %) with three receiver function profile picking time of the conversion of $P410s$ (in %). On the absolute velocity profile marked with the Moho (black cross) and LAB (white dash line) as observed by Zhao et al. (2010)

Chapter 5

Conclusion

The objective of the present work was the generation of high resolution three dimensional Rayleigh wave velocity models of China and surrounding region so that the present day geodynamics of the region is understood more clearly and reliably. For this purpose the alternative to the conventional tomographic inversion of surface wave data, wherein the long period seismograms are first interpreted in terms of dispersion and/or attenuation curves before performing inversion in terms of laterally and depth-varying properties, developed by Cara & Lévêque (1987) is used taking a total of 234566 wave form data that is subjected to the rigorous test during which a total of 184228 waveform got rejected leaving only 50338 waveform data for tomographic inversion.

In the process we derived 3-D upper mantle absolute shear wave velocities by modeling fundamental and higher mode surface wave waveforms. In this endeavour we have extended the multi-mode surface wave tomography of Eastern Asia of Priestley et al. (2006) by adding more permanent stations data within China and constrained the study area to China and its close vicinity. The reduced inter-station distances enabled us to reduce the lateral smoothing using a smaller Gaussian correlation length during the regionalization

approach increasing lateral resolution in the process. A 3-D Sv velocity model over China and adjoining area is created with a good resolution from the top of upper mantle to a depth of 400 km. Velocity anomalies are better and more sharply defined in the model. The velocity perturbation decreases from 10% at shallow depths to 2% at depths range of 300-400 km. Regions with low velocity anomalies in the uppermost mantle correlate well with regions of thick crust derived by different seismic and gravity data analysis (Li et al., 2006; Zhang et al., 2011b). The over-thickened Tibetan crust is sharply bounded by the Indian Plate in the South, by Sichuan Basin and Ordos Block in the East and by Tarim Basin in the North. The difference of thick and thin lithosphere in the North China Block and South China Block is demarcated by the North-South Gravity Lineament. At 100-200 km depth the model correlates well with the lateral variation of the thickness of the mantle lithosphere. The lithosphere is generally thinner in East China and thick in West China. The thickest lithosphere is beneath the Pamir-Tibetan plateaus reaching a thickness of 200 km. Also observed as relatively thick lithosphere ($>$ 100km) are the Indian Plate, Sichuan Basin, Ordos Block and Tarim Basin. The lithosphere in the eastern part of the North China Craton and Yangtze Craton is too shallow to be well resolved.

The azimuthal anisotropy patterns is observed to behave distinctly in the different blocks of China with their respective tectonic history. The orientation can be interpreted in terms of ongoing tectonic deformation or movement. We have tried to show in our result a possible coupling (north-east and east of Tibet) and decoupling (central to western Tibet) between the crust and the lithosphere.

Bibliography

Aki, K. & Lee, W. H. K., 1976, Determination of three-dimensional velocity anomalies under a seismic array using first P arrival times from local earthquakes: 1. A homogeneous initial model, *Journal of Geophysical Research*, **81**(23), 4381–4399.

Anderson, D., 1989, *Theory of the Earth*, Blackwell Scientific Publications, Boston.

Anderson, D. L., 1965, Recent evidence concerning the structure and composition of the Earth's mantle, *Physics and Chemistry of The Earth*, **6**, 1–131.

Babuška, V. & Cara, M., 1991, *Seismic Anisotropy in the Earth*, Kluwer Academic Publishers.

Backus, G., 1970, Inference from inadequate and inaccurate data, III, *Proceedings of the National Academy of Sciences*, **67**(1), 282–289.

Backus, G. E., 1970, Inference from inadequate and inaccurate data, II, *Proceedings of the National Academy of Sciences*, **65**(2), 281–287.

Backus, G. E., 1970, Inference from inadequate and inaccurate data, I, *Proceedings of the National Academy of Sciences*, **65**(I), 1–7.

Backus, G. E. & Gilbert, J. F., 1967, Numerical Applications of a Formalism for Geophysical Inverse Problems, *Geophysical Journal International*, **13**(1-3), 247–276.

Backus, G. E. & Gilbert, J. F., 1968, The Resolving Power of Gross Earth Data, *Geophysical Journal International*, **16**(2), 169–205.

Backus, G. E. & Gilbert, J. F., 1970, Uniqueness in the Inversion of Inaccurate Gross Earth Data, *Philosophical Transactions of the Royal Society A: Mathematical, Physical and Engineering Sciences*, **266**(1173), 123–192.

Canas, J. A. & Mitchell, B. J., 1978, Lateral variation of surface-wave anelastic attenuation across the Pacific, *Bulletin of the Seismological Society of*, **68**(6), 1637–1650.

Cara, M. & Lévêque, J. J., 1987, Waveform inversion using secondary observables, *Geophysical Research Letters*, **14**(10), 1046–1049.

Charvet, J., Shu, L., Faure, M., Choulet, F., Wang, B., Lu, H., & Breton, N. L., 2010, Structural development of the Lower Paleozoic belt of South China: Genesis of an intracontinental orogen, *Journal of Asian Earth Sciences*, **39**(4), 309–330.

Chen, L., 2009, Lithospheric structure variations between the eastern and central North China Craton from S- and P-receiver function migration, *Physics of the Earth and Planetary Interiors*, **173**(3-4), 216–227.

Chen, L., 2010, Concordant structural variations from the surface to the base of the upper mantle in the North China Craton and its tectonic implications, *Lithos*, **120**(1-2), 96–115.

Chen, L., Tao, W., Zhao, L., & Zheng, T., 2008, Distinct lateral variation of lithospheric thickness in the Northeastern North China Craton, *Earth and Planetary Science Letters*, **267**(1-2), 56–68.

Chen, Y., Niu, F., Liu, R., Huang, Z., Tkalčić, H., Sun, L., & Chan, W., 2010, Crustal structure beneath China from receiver function analysis, *Journal of Geophysical Research*, **115**(B3), 1–22.

Clark, M. K. & Royden, L. H., 2000, Topographic ooze: Building the eastern margin of Tibet by lower crustal flow, *Geology*, **28**(8), 703–706.

Curtis, A., Trampert, J., Snieder, R., & Dost, B., 1998, Eurasian fundamental mode surface wave phase velocities and their relationship with tectonic structures, *Journal of Geophysical Research*, **103**(B11), 26919–26947.

Debayle, E., 1999, SV-wave azimuthal anisotropy in the Australian upper mantle: preliminary results from automated Rayleigh waveform inversion, *Geophysical Journal International*, **137**(3), 747–754.

Debayle, E. & Kennett, B. L. N., 2000, The Australian continental upper mantle: Structure and deformation inferred from surface waves, *Journal of Geophysical Research*, **105**(B11), 25423–25450.

Debayle, E. & Kennett, B. L. N., 2000, Anisotropy in the Australasian upper mantle from Love and Rayleigh waveform inversion, *Earth and Planetary Science Letters*, **184**(1), 339–351.

Debayle, E. & Kennett, B. L. N., 2003, Surface-wave studies of the Australian region, *Geological Society of America Special Papers*, **372**, 25–40.

Debayle, E. & Sambridge, M., 2004, Inversion of massive surface wave data sets: Model construction and resolution assessment, *Journal of Geophysical Research*, **109**(B2).

Debayle, E., Lévêque, J. J., & Cara, M., 2001, Seismic evidence for a deeply rooted low-velocity anomaly in the upper mantle beneath the northeastern Afro/Arabian continent, *Earth and Planetary Science Letters*, **193**(3-4), 423–436.

Dziewonski, A. & Anderson, D. L., 1981, Preliminary reference Earth model, *Physics of The Earth and Planetary Interiors*, **25**(4), 297–356.

Dziewonski, A. & Romanowicz, B., 2007, 1.01 - overview, in *Treatise on Geophysics*, edited by G. Schubert, pp. 1–29, Elsevier, Amsterdam.

Dziewonski, A., Mills, J., & Bloch, S., 1972, Residual dispersion measurement - A new method of surface-wave analysis, *Bulletin of the Seismological*, **62**(I), 129–139.

Dziewonski, A. M., 1971, Upper mantle models from 'pure-path'dispersion data, *Journal of Geophysical Research*, **76**(11), 2587–2601.

Dziewonski, A. M., 1984, Mapping the Lower Mantle: Determination of Lateral Heterogeneity in P Velocity up to Degree and Order 6, *Journal of Geophysical Research*, **89**(B7), 5929–5952.

Engdahl, E. R. & Hilst, R. V. D., 1998, Global teleseismic earthquake relocation with improved travel times and procedures for depth determination, *Bulletin of the*, **88**(3), 722–743.

Estey, L. H. & Douglas, B. J., 1986, Upper Mantle Anisotropy: A Preliminary Model, *Journal of Geophysical Research*, **91**(B11), 11393–11406.

Fang, L., Wu, J., Ding, Z., & Panza, G. F., 2010, High resolution Rayleigh wave group velocity tomography in North China from ambient seismic noise, *Geophysical Journal International*, pp. 1171–1182.

Feng, M. & An, M., 2010, Lithospheric structure of the Chinese mainland determined from joint inversion of regional and teleseismic Rayleigh-wave group velocities, *Journal of Geophysical Research*, **115**(B6), 1–16.

Flesch, L. M., Holt, W. E., Silver, P. G., Stephenson, M., Wang, C. Y., & Chan, W. W., 2005, Constraining the extent of crust–mantle coupling in central Asia using GPS, geologic, and shear wave splitting data, *Earth and Planetary Science Letters*, **238**(1-2), 248–268.

Forsyth, D. W., 1975, The Early Structural Evolution and Anisotropy of the Oceanic Upper Mantle, *Geophysical Journal International*, **43**(1), 103–162.

Friederich, W., 2003, The S -velocity structure of the East Asian mantle from inversion of shear and surface waveforms, *Geophysical Journal International*, **153**(1), 88–102.

Fuchs, K. & Müller, G., 1971, Computation of Synthetic Seismograms with the Reflectivity Method and Comparison with Observations, *Geophysical Journal of the Royal Astronomical Society*, **23**(4), 417–433.

Griot, D. A., Montagner, J. P., & Tapponnier, P., 1998, Phase velocity structure from Rayleigh and Love waves in Tibet and its neighboring regions, *Journal of Geophysical Research*, **103**(B9), 21215–21232.

Haines, S. S., Klemperer, S. L., Brown, L., Guo, J., Mechie, J., Z., W., Ross, A., & Meissner, R., 2003, INDEPTH III seismic data: From surface observations to deep crustal processes in Tibet, *Tectonics*, **22**(1), 1–18.

Haskell, N. A., 1953, The dispersion of surface waves on multilayered media, *Bulletin of the Seismological Society of America*, **43**(1), 17–34.

Heijst, H. J. & Woodhouse, J. H., 1997, Measuring surface-wave overtone phase velocities using a mode-branch stripping technique, *Geophysical Journal International*, **131**(2), 209–230.

Heintz, M., Debayle, E., & Vauchez, A., 2005, Upper mantle structure of the South American continent and neighboring oceans from surface wave tomography, *Tectonophysics*, **406**(1-2), 115–139.

Heit, B., Yuan, X., Bianchi, M., Kind, R., & Gossler, J., 2010, Study of the lithospheric and upper-mantle discontinuities beneath eastern Asia by SS precursors, *Geophysical Journal International*, **183**(1), 252–266.

Hess, H. H., 1964, Seismic Anisotropy of the Uppermost Mantle under Oceans, *Nature*, **203**(4945), 629–631.

Houseman, G. A., McKenzie, D. P., & Molnar, P., 1981, Convective instability of a thickened boundary layer and it's relevance for the thermal evolution of continental convergent belts, *Journal of Geophysical Research*, **86**(B7), 6115–6132.

Huang, Z., Su, W., Peng, Y., Zheng, Y., & Li, H., 2003, Rayleigh wave tomography of China and adjacent regions, *Journal of Geophysical Research*, **108**(B2).

Huang, Z., Peng, Y., Luo, Y., Zheng, Y., & Su, W., 2004, Azimuthal anisotropy of Rayleigh waves in East Asia, *Geophysical Research Letters*, **31**(15), 1–4.

Kind, R., Yuan, X., Saul, J., Nelson, D., Sobolev, S. V., Mechie, J., Zhao, W., Kosarev, G., Ni, J., Achauer, U., & Jiang, M., 2002, Seismic images of crust and upper mantle beneath Tibet: evidence for Eurasian plate subduction., *Science (New York, N.Y.)*, **298**(5596), 1219–21.

Kumar, P., Yuan, X., Kind, R., & Ni, J., 2006, Imaging the colliding Indian and Asian lithospheric plates beneath Tibet, *Journal of Geophysical Research*, **111**(B6), 1–11.

Lay, T. & Wallace, T., 1995, *Modern global seismology*, Academic Pr.

Lebedev, S. & Nolet, G., 2003, Upper mantle beneath Southeast Asia from S velocity tomography, *Journal of Geophysical Research*, **108**(B1).

León Soto, G., Sandvol, E., Ni, J. F., Flesch, L., Hearn, T. M., Tilmann, F., Chen, J., & Brown, L. D., 2012, Significant and vertically coherent seismic anisotropy beneath eastern Tibet, *Journal of Geophysical Research*, **117**(B5).

Lerner-Lam, A. L. & Jordan, T. H., 1983, Earth structure from fundamental and higher-

mode waveform analysis, *Geophysical Journal of the Royal Astronomical Society*, **75**(3), 759–797.

Lévêque, J., Debayle, E., & Maupin, V., 1998, Anisotropy in the Indian Ocean upper mantle from Rayleigh- and Love-waveform inversion, *Geophysical Journal International*, **133**(3), 529–540.

Lévêque, J. J., Cara, M., & Rouland, D., 1991, Waveform inversion of surface wave data: test of a new tool for systematic investigation of upper mantle structures, *Geophysical Journal International*, **104**(3), 565–581.

Lévêque, J. J., Rivera, L., & Wittlinger, G., 1993, On the use of the checker-board test to assess the resolution of tomographic inversions, *Geophysical Journal International*, **115**(1), 313–318.

Li, C., van der Hilst, R. D., Meltzer, A. S., & Engdahl, E. R., 2008, Subduction of the Indian lithosphere beneath the Tibetan Plateau and Burma, *Earth and Planetary Science Letters*, **274**(1-2), 157–168.

Li, H., Su, W., Wang, C. Y., & Huang, Z., 2009, Ambient noise Rayleigh wave tomography in western Sichuan and eastern Tibet, *Earth and Planetary Science Letters*, **282**(1-4), 201–211.

Li, S., Mooney, W. D., & Fan, J., 2006, Crustal structure of mainland China from deep seismic sounding data, *Tectonophysics*, **420**(1-2), 239–252.

Li, X.-D. & Romanowicz, B., 1996, Global mantle shear velocity model developed using nonlinear asymptotic coupling theory, *Journal of Geophysical Research*, **101**(B10), 22245–22272.

Li, Y. & Yang, Y., 2011, Gravity data inversion for the lithospheric density structure

beneath North China Craton from EGM 2008 model, *Physics of the Earth and Planetary Interiors*, **189**(1-2), 9–26.

Li, Z. X., 1998, Tectonic history of the major East Asian lithospheric blocks since the mid-Proterozoic: A synthesis, in *Mantle Dynamics and Plate Interactions in East Asia*, edited by M. F. J. Flower, S. L. Chung, C. H. Lo, & T. Y. Lee, vol. 27 of **Geodynamics Series**, pp. 221–243, American Geophysical Union, Washington, D. C.

Liang, C., Song, X., & Huang, J., 2004, Tomographic inversion of Pn travel times in China, *Journal of Geophysical Research*, **109**(B11), 1–19.

Ma, X., Liu, G., & Su, J., 1984, The structure and dynamics of the continental lithosphere in north-northeast China, *Annales geophysicae*, **2**(6), 611–620.

Mechie, J., Kind, R., & Saul, J., 2011, The seismological structure of the Tibetan Plateau crust and mantle down to 700 km depth, *Geological Society, London, Special Publications*, **353**(1), 109–125.

Menzies, M. A. & Xu, Y. G., 1998, Geodynamics of the North China Craton, in *Mantle Dynamics and Plate Interactions in East Asia*, edited by M. F. J. Flower, S. L. Chung, C. H. Lo, & T. Y. Lee, vol. 27 of **Geodynamics Series**, pp. 155–165, American Geophysical Union, Washington, D. C.

Menzies, M. A., Fan, W., & Zhang, M., 1993, Palaeozoic and Cenozoic lithoprobes and the loss of >120 km of Archaean lithosphere, Sino-Korean craton, China, *Geological Society, London, Special Publications*, **76**(1), 71–81.

Molnar, P. & Tapponnier, P., 1975, Cenozoic tectonics of Asia: effects of a continental collision, *Science*, **189**, 419–426.

Montagner, J. P., 1986, Regional three-dimensional structures using long-period surface waves, *Annales geophysicae. Series B. Terrestrial and planetary physics*, **4**(3), 283–294.

Montagner, J. P., 1998, Where Can Seismic Anisotropy Be Detected in the Earth's Mantle? In Boundary Layers..., *Pure and Applied Geophysics*, **151**(4), 223.

Montagner, J. P., 2007, 1.16 - deep earth structure - upper mantle structure: Global isotropic and anisotropic elastic tomography, in *Treatise on Geophysics*, edited by G. Schubert, pp. 559–589, Elsevier, Amsterdam.

Montagner, J. P. & Nataf, H. C., 1986, A Simple Method for Inverting the Azimuthal Anisotropy of Surface Waves, *Journal of Geophysical Research*, **91**(B1), 511–520.

Montagner, J. P. & Tanimoto, T., 1990, Global Anisotropy in the Upper Mantle Inferred From the Regionalization of Phase Velocities, *Journal of Geophysical Research*, **95**(B4), 4797–4819.

Montagner, J. P. & Tanimoto, T., 1991, Global Upper Mantle Tomography of Seismic Velocities and Anisotropies, *Journal of Geophysical Research*, **96**(B12), 20337–20351.

Nábelek, J., Hetényi, G., Vergne, J., Sapkota, S., Kafle, B., Jiang, M., Su, H., Chen, J., & Huang, B.-S., 2009, Underplating in the Himalaya-Tibet collision zone revealed by the Hi-CLIMB experiment., *Science (New York, N.Y.)*, **325**(5946), 1371–4.

Nataf, H. C. & Ricard, Y., 1996, 3SMAC: an a priori tomographic model of the upper mantle based on geophysical modeling, *Physics of the Earth and Planetary Interiors*, **95**(1-2), 101–122.

Nataf, H.-C., Nakanishi, I., & Anderson, D. L., 1986, Measurements of Mantle Wave Velocities and Inversion for Lateral Heterogeneities and Anisotropy 3. Inversion, *Journal of Geophysical Research*, **91**(B7), 7261–7307.

Ni, J. & Barazangi, M., 1984, Seismotectonics of the Himalayan collision zone: Geometry of the underthrusting Indian plate beneath the Himalaya, *Journal of Geophysical Research*, **89**(B2), 1147–1163.

Nolet, G., 1975, Higher Rayleigh modes in western Europe, *Geophysical Research Letters*, **2**(2), 60.

Nolet, G., 1990, Partitioned Waveform Inversion and Two-Dimensional Structure Under the Network of Autonomously Recording Seismographs, *Journal of Geophysical Research*, **95**(B6), 8499–8512.

Nolet, G., 2008, *A Breviary of Seismic Tomography: Imaging the Interior of the Earth and Sun*, Cambridge University Press, Cambridge.

Nolet, G., van Trier, J., & Huisman, R., 1986, A formalism for nonlinear inversion of seismic surface waves, *Geophysical Research Letters*, **13**(1), 26–29.

Obrebski, M., Allen, R. M., Zhang, F., Pan, J., Wu, Q., & Hung, S. H., 2012, Shear wave tomography of China using joint inversion of body and surface wave constraints, *Journal of Geophysical Research*, **117**(B1), 1–15.

Pilidou, S., Priestley, K., Gudmundsson, O., & Debayle, E., 2004, Upper mantle S -wave speed heterogeneity and anisotropy beneath the North Atlantic from regional surface wave tomography: the Iceland and Azores plumes, *Geophysical Journal International*, **159**(3), 1057–1076.

Priestley, K. & McKenzie, D., 2006, The thermal structure of the lithosphere from shear wave velocities, *Earth and Planetary Science Letters*, **244**(1-2), 285–301.

Priestley, K., Debayle, E., McKenzie, D., & Pilidou, S., 2006, Upper mantle structure of eastern Asia from multimode surface waveform tomography, *Journal of Geophysical Research*, **111**(B10), 1–20.

Replumaz, A., Kárason, H., van der Hilst, R. D., Besse, J., & Tapponnier, P., 2004, 4-D evolution of SE Asia's mantle from geological reconstructions and seismic tomography, *Earth and Planetary Science Letters*, **221**(1-4), 103–115.

Ritzwoller, M. H. & Levshin, A. L., 1998, Eurasian surface wave tomography: Group velocities, *Journal of Geophysical Research*, **103**(B3), 4839–4878.

Ritzwoller, M. H., Shapiro, N. M., Mikhail, P. B., & Levshin, A. L., 2002, Global surface wave diffraction tomography, *Journal of Geophysical Research*, **107**(B12), 1–13.

Romanowicz, B., 1982, Constraints on the structure of the Tibet Plateau from pure path phase velocities of Love and Rayleigh waves, *Journal of Geophysical Research*, **87**(B8), 6865–6883.

Royden, L. H., Burchfiel, B. C., & van der Hilst, R. D., 2008, The geological evolution of the Tibetan Plateau., *Science*, **321**(5892), 1054–8.

Savage, M. K., 1999, Seismic anisotropy and mantle deformation: What have we learned from shear wave splitting?, *Reviews of Geophysics*, **37**(1), 65.

Shearer, P., 2009, *Introduction to seismology*, Cambridge Univ Pr, 2nd edn.

Sieminski, A., Debayle, E., & Lévêque, J. J., 2003, Seismic evidence for deep low-velocity anomalies in the transition zone beneath West Antarctica, *Earth and Planetary Science Letters*, **216**(4), 645–661.

Sieminski, A., Lévêque, J. J., & Debayle, E., 2004, Can finite-frequency effects be accounted for in ray theory surface wave tomography ?, *Geophysical Research Letters*, **31**, 1–4.

Singh, A., Kumar, M. R., & Raju, P. S., 2007, Mantle deformation in Sikkim and adjoining Himalaya: Evidences for a complex flow pattern, *Physics of the Earth and Planetary Interiors*, **164**(3-4), 232–241.

Smith, M. L. & Dahlen, F. A., 1973, The Azimuthal Dependence of Love and Rayleigh Wave Propagation in a Slightly Anisotropic Medium, *Journal of Geophysical Research*, **78**(17), 3321–3333.

Sodoudi, F., Yuan, X., Liu, Q., Kind, R., & Chen, J., 2006, Lithospheric thickness beneath the Dabie Shan, central eastern China from S receiver functions, *Geophysical Journal International*, **166**(3), 1363–1367.

Stein, S. & Wysession, M., 2005, *An introduction to seismology, earthquakes, and earth structure*, Wiley-Blackwell.

Styron, R., Taylor, M., & Okoronkwo, K., 2010, Database of Active Structures From the Indo-Asian Collision, *Eos, Transactions American Geophysical Union*, **91**(20), 181.

Takeuchi, H. & Saito, M., 1972, Seismic surface waves, in *Seismology: Surface Waves and Earth Oscillations*, edited by B. A. Bolt, vol. 11 of **Methods In Computational Physics**, pp. 217–295, Academic Press, San Diego, Calif.

Tapponnier, P. & Molnar, P., 1977, Active faulting and tectonics in China, *Journal of Geophysical Research*, **82**(20), 2905–2930.

Tarantola, A., 2005, *Inverse Problem Theory and Methods for Model Parameter Estimation*, Society for Industrial and Applied Mathematics.

Tarantola, A. & Valette, B., 1982, Generalized nonlinear inverse problems solved using the least squares criterion, *Reviews of Geophysics*, **20**(2), 219–232.

Trampert, J. & Woodhouse, J. H., 2003, Global anisotropic phase velocity maps for fundamental mode surface waves between 40 and 150 s, *Geophysical Journal International*, **154**(1), 154–165.

Vinnik, L., Singh, A., Kiselev, S., & Kumar, M. R., 2007, Upper mantle beneath foothills of the western Himalaya: subducted lithospheric slab or a keel of the Indian shield?, *Geophysical Journal International*, **171**(3), 1162–1171.

Woodhouse, J. H. & Dziewonski, A. M., 1984, Mapping the Upper Mantle: Three-

Dimensional Modeling of Earth Structure by Inversion of Seismic Waveforms, *Journal of Geophysical Research*, **89**(B7), 5953–5986.

Xu, P. & Zhao, D., 2009, Upper-mantle velocity structure beneath the North China Craton: implications for lithospheric thinning, *Geophysical Journal International*, **177**(3), 1279–1283.

Xu, Y. G., 2001, Thermo-tectonic destruction of the archaean lithospheric keel beneath the sino-korean craton in china: evidence, timing and mechanism, *Physics and Chemistry of the Earth, Part A: Solid Earth and Geodesy*, **26**(9-10), 747–757.

Xu, Y. G., 2007, Diachronous lithospheric thinning of the North China Craton and formation of the Daxin'anling–Taihangshan gravity lineament, *Lithos*, **96**(1-2), 281–298.

Yang, K., 1998, A plate reconstruction of the Eastern Tethyan orogen in southwestern China, in *Mantle Dynamics and Plate Interactions in East Asia*, edited by M. F. J. Flower, S. L. Chung, C. H. Lo, & T. Y. Lee, vol. 27 of **Geodynamics Series**, pp. 269–287, American Geophysical Union, Washington, D. C.

Yin, A., 2010, Cenozoic tectonic evolution of Asia: A preliminary synthesis, *Tectonophysics*, **488**(1-4), 293–325.

Yin, A. & Harrison, T. M., 2000, Geologic Evolution of the Himalayan-Tibetan Orogen, *Annual Review of Earth and Planetary Sciences*, **28**(1), 211–280.

Yuan, H. & Romanowicz, B., 2010, Lithospheric layering in the North American craton., *Nature*, **466**(7310), 1063–8.

Yuan, H., Romanowicz, B., Fischer, K. M., & Abt, D., 2011, 3-D shear wave radially and azimuthally anisotropic velocity model of the North American upper mantle, *Geophysical Journal International*, **184**(3), 1237–1260.

Zhang, J., Gao, R., Zeng, L., Li, Q., Guan, Y., He, R., Wang, H., & Lu, Z., 2010, Relationship between characteristics of gravity and magnetic anomalies and the earthquakes in the Longmenshan range and adjacent areas, *Tectonophysics*, **491**(1-4), 218–229.

Zhang, P. Z., Shen, Z., Wang, M., Gan, W., Bürgmann, R., Molnar, P., Wang, Q., Niu, Z., Sun, J., Wu, J., Hanrong, S., & Xinzhao, Y., 2004, Continuous deformation of the Tibetan Plateau from global positioning system data, *Geology*, **32**(9), 809.

Zhang, Q., Sandvol, E., Ni, J., Yang, Y., & Chen, Y. J., 2011, Rayleigh wave tomography of the northeastern margin of the Tibetan Plateau, *Earth and Planetary Science Letters*, **304**(1-2), 103–112.

Zhang, Z., Yuan, X., Chen, Y., Tian, X., Kind, R., Li, X., & Teng, J., 2010, Seismic signature of the collision between the east Tibetan escape flow and the Sichuan Basin, *Earth and Planetary Science Letters*, **292**(3-4), 254–264.

Zhang, Z., Yang, L., Teng, J., & Badal, J., 2011, An overview of the earth crust under China, *Earth-Science Reviews*, **104**(1-3), 143–166.

Zhao, J., Yuan, X., Liu, H., Kumar, P., Pei, S., Kind, R., Zhang, Z., Teng, J., Ding, L., Gao, X., Xu, Q., & Wang, W., 2010, The boundary between the Indian and Asian tectonic plates below Tibet., *Proceedings of the National Academy of Sciences of the United States of America*, **107**(25), 11229–33.

Zheng, T., Chen, L., Zhao, L., Xu, W., & Zhu, R., 2006, Crust–mantle structure difference across the gravity gradient zone in North China Craton: Seismic image of the thinned continental crust, *Physics of the Earth and Planetary Interiors*, **159**(1-2), 43–58.

Zhou, L., Xie, J., Shen, W., Zheng, Y., Yang, Y., Shi, H., & Ritzwoller, M. H., 2012, The structure of the crust and uppermost mantle beneath South China from ambient noise and earthquake tomography, *Geophysical Journal International*, **189**(3), 1565–1583.

Zhu, R. X., Chen, L., Wu, F. Y., & Liu, J. L., 2011, Timing, scale and mechanism of the destruction of the North China Craton, *Science China Earth Sciences*, **54**(6), 789–797.

ACKNOWLEDGMENT

Having an opportunity to acknowledge the help I have had, in completing the research work towards the doctoral degree, is really the thing I have been waiting for. And here the names first come to my mind are that of my learned supervisors Prof. Dr. Rainer Kind and Dr. Xiaohui Yuan, who have guided me in real sense. I wish to express my deep sense of gratitude and appreciation to them for their stimulating supervision with invaluable suggestions, keen interest, constructive criticisms and constant encouragement during the course of the present study. I learned a lot from them not only in the academic area but in other spheres of life also. I wholeheartedly acknowledge their full cooperation that I received from the very beginning of this work up to the completion in the form of this thesis.

I wish to express my warm and sincere thanks to Prof. Dr. Frederik Tilmann, Head of the Section Seismology (2.4) at the German Research Centre for Geosciences (GFZ) Potsdam, for extending his valuable advice and every sort of help as and when sought for. His extensive discussions around my work and perspective comment has improved chapters of this work.

I would like to express my gratitude to the committee members of my thesis for taking their precious time to consider my work.

I am especially thankful to Dr. Eric Debayle, University of Lyon, France to take out time for the stimulating discussion. Eric was generous enough in providing his codes for the data analysis and also his help and advice from time to time as when needed. My sincere thanks also goes to Dr. Keith Priestley, Cambridge University, U.K. whose critical and timely shared valuable insights in the relevance of the study proved critical in complition

of this work.

I would like to make a special note of thank to all my colleagues at GFZ for their co-operation, help and the warmth they have extended to me. Many thanks to Dr. Benjamin Heit, Dr. Forough Sodoudi and Dr. Xueqing Li for there encouragement and support especially when it was required most during my PhD work. Special thanks to Mrs. Liane Lauterjung for making GFZ a more pleasant place to work at.

When hurdles appeared insurmountable and target unachievable, the encouragement and camaraderie of friends helped keep things in perspective. I wold like to take this opportunity to thank Dr. Marcelo Bianchi and Amerika Manzanares. I am also grateful to Armelle who has been a close friend, who helped lighten the burden and would like to specially thank for keep reminding me with famous phrase of 'I can do it' whenever I was in doubt. I also express my abounding feelings of gratitude to all those who helped me in this course but have not been listed here.

In the end I would like to express my heartfelt gratitude to my family. My father, Prof. Sri Niwas who has been my biggest support and strength all these years. My mother, Mrs. Shashi Pandey who always believed in me, most of the time more than me. My sister, Mrs. Shalini Chaubey who is my friend, philosopher and guide in my life. I would like to dedicate my this work to my late brother Mr. Amit Pandey, who I lost very recently. I can never thank him enough for what he did for me and taught me so many things what I know today.

Appendix A

List of Station

List of station locations and elivation are given below. In the last three column of the table is the information about the number of waveform selected and rejected. Third column from right (in yellow) is the total number of input waveform for the inversion then in the next column (in red) is the number of waveform rejected and in the last column (in green) is the selected waveform form which the model is generated.

No.	***Net.***	***Sta.***	***Lat.***	***Lon.***	***Elev.***	***Input WF***	***Rejected***	***Selected***
1	AD	DLV	11.95	108.48	50	239	152	87
2	AD	SLV	21.33	103.91	50	250	189	61
3	AD	SZP	17.55	120.46	50	232	166	66
4	AT	SMY	52.73	174.1	58	92	61	31
5	AU	COEN	-13.96	143.18	240	435	347	88
6	AU	MANU	-2.04	147.37	141.5	245	180	65
7	AU	MTN	-12.84	131.13	137.4	884	621	263
8	AU	RABL	-4.19	152.16	277	258	182	76
9	AU	XMI	-10.45	105.69	252	375	229	146

Continued on next page .....

No.	*Net.*	*Sta.*	*Lat.*	*Lon.*	*Elev.*	*Input WF*	*Rejected*	*Selected*
10	AU	XMIS	-10.48	105.65	243.5	1035	636	399
11	CB	AXX	40.51	95.8	1178	858	727	131
12	CB	BNX	45.74	127.41	198	879	724	155
13	CB	CAD	31	97.5	3200	727	627	100
14	CB	CD2	30.91	103.76	628	947	915	32
15	CB	CN2	43.8	125.45	223	867	713	154
16	CB	CNS	28.18	112.93	81	899	792	107
17	CB	DL2	38.91	121.63	62	604	485	119
18	CB	GOM	36.43	94.87	2802	843	807	36
19	CB	GTA	39.41	99.81	1341	1293	1216	77
20	CB	GUL	25.08	110.29	150	910	798	112
21	CB	GYA	26.46	106.66	1162	556	548	8
22	CB	GZH	23.09	113.34	11	962	960	2
23	CB	HEF	31.84	117.17	65	665	618	47
24	CB	HEH	50.25	127.41	168	1235	1188	47
25	CB	HHC	40.85	111.56	1169	1214	1123	91
26	CB	HNS	37.42	114.71	20	963	821	142
27	CB	HTA	37.07	79.92	1358	910	880	30
28	CB	HTG	37.86	90.76	3210	293	275	18
29	CB	KSH	39.52	75.92	1314	568	476	92
30	CB	LYN	34.55	112.47	170	1191	984	207
31	CB	NAQ	32.25	92.25	4500	350	319	31
32	CB	NJ2	32.05	118.85	45	878	768	110

Continued on next page .....

No.	*Net.*	*Sta.*	*Lat.*	*Lon.*	*Elev.*	*Input WF*	*Rejected*	*Selected*
33	CB	NNC	28.78	115.8	78	855	775	80
34	CB	PZH	26.5	101.74	1160	757	652	105
35	CB	QZH	24.94	118.59	21	877	770	107
36	CB	SNY	41.83	123.58	54	1171	1115	56
37	CB	SQH	32.5	80.68	4300	482	421	61
38	CB	SZN	22.32	114.08	30	754	684	70
39	CB	TIA	36.21	117.12	300	1207	1163	44
40	CB	TIY	38.43	113.02	850	1022	935	87
41	CB	TNC	25.03	98.52	1650	875	763	112
42	CB	WHN	30.54	114.35	26	877	842	35
43	CB	WUS	41.2	79.21	1440	327	291	36
44	CB	WZH	27.93	120.66	20	928	889	39
45	CB	XLT	43.89	116.07	1020	831	664	167
46	CB	XSA	16.85	112.35	0	161	152	9
47	CB	YCH	38.6	105.93	1700	770	667	103
48	G	HYB	17.42	78.55	510	1917	1373	544
49	G	INU	35.35	137.03	132	1243	872	371
50	HK	HKPS	22.28	114.14	196.3	142	102	40
51	IC	BJT	40.02	116.17	137	2596	1866	730
52	IC	ENH	30.28	109.49	500	2811	2026	785
53	IC	HIA	49.27	119.74	620	2595	1909	686
54	IC	KMI	25.12	102.74	1940	2791	1952	839
55	IC	LSA	29.7	91.13	3645	2549	2000	549

Continued on next page .....

No.	*Net.*	*Sta.*	*Lat.*	*Lon.*	*Elev.*	*Input WF*	*Rejected*	*Selected*
56	IC	MDJ	44.62	129.59	220	2829	1930	899
57	IC	QIZ	19.03	109.84	240	2341	1715	626
58	IC	SSE	31.09	121.19	40	2355	1659	696
59	IC	WMQ	43.81	87.7	844	2511	1867	644
60	IC	XAN	34.03	108.92	630	2071	1633	438
61	II	AAK	42.64	74.49	1645	941	757	184
62	II	ABKT	37.93	58.12	678	1345	1134	211
63	II	ARU	56.43	58.56	250	2426	1864	562
64	II	DGAR	-7.41	72.45	1	969	660	309
65	II	ERM	42.02	143.16	40	945	741	204
66	II	KAPI	-5.01	119.75	300	1157	803	354
67	II	MSEY	-4.67	55.48	475	1895	1280	615
68	II	NIL	33.65	73.27	629	237	204	33
69	II	NRIL	69.5	88.44	92	339	278	61
70	II	PALK	7.27	80.7	460	2292	1703	589
71	II	RAYN	23.52	45.5	631	1531	1195	336
72	II	TLY	51.68	103.64	579	2452	1708	744
73	II	UOSS	24.95	56.2	284.4	668	520	148
74	IU	CHTO	18.81	98.94	320	3289	2368	921
75	IU	DAV	7.07	125.58	149	1937	1611	326
76	IU	INCN	37.48	126.62	79	4315	3008	1307
77	IU	KBL	34.54	69.04	1913	931	759	172
78	IU	MAJO	36.55	138.2	405	3853	2739	1114

Continued on next page .....

No.	*Net.*	*Sta.*	*Lat.*	*Lon.*	*Elev.*	*Input WF*	*Rejected*	*Selected*
79	IU	MAKZ	46.81	81.98	590	2839	2230	609
80	IU	ULN	47.87	107.05	1610	2518	1846	672
81	IU	YAK	62.03	129.68	96	2638	1894	744
82	IU	YSS	46.96	142.76	148	2553	1797	756
83	JP	ASAJ	44.12	142.59	220	839	644	195
84	JP	CBIJ	27.1	142.18	150	590	368	222
85	JP	JHJ2	33.12	139.81	70	539	377	162
86	JP	JNU	33.13	130.88	540	533	367	166
87	JP	JOW	26.84	128.27	220	720	531	189
88	JP	YOJ	24.47	123.01	32	652	487	165
89	KN	AAK	42.63	74.49	1680	1733	1345	388
90	KN	AML	42.13	73.69	3400	1956	1532	424
91	KN	CHM	43	74.75	655	1663	1301	362
92	KN	EKS2	42.66	73.78	1360	2236	1737	499
93	KN	KBK	42.66	74.95	1760	1985	1566	419
94	KN	KZA	42.08	75.25	3520	1383	1088	295
95	KN	TKM2	42.92	75.6	2020	2161	1683	478
96	KN	UCH	42.23	74.51	3850	1514	1212	302
97	KN	ULHL	42.25	76.24	2040	1694	1325	369
98	KN	USP	43.27	74.5	740	2049	1563	486
99	KZ	AKTK	50.43	58.02	360	440	412	28
100	KZ	AKTO	50.43	58.02	379	935	735	200
101	KZ	BRVK	53.06	70.28	315	571	525	46

Continued on next page .....

No.	*Net.*	*Sta.*	*Lat.*	*Lon.*	*Elev.*	*Input WF*	*Rejected*	*Selected*
102	KZ	BVAR	53.02	70.39	361	962	744	218
103	KZ	CHKZ	53.68	70.62	120	1474	1314	160
104	KZ	KKAR	43.11	70.51	524.9	1744	1728	16
105	KZ	KNDC	43.22	76.97	900	448	356	92
106	KZ	KUR21	50.62	78.53	200	221	170	51
107	KZ	KURK	50.71	78.62	240	1430	1234	196
108	KZ	PDG	43.33	79.48	1280	852	794	58
109	KZ	TLG	43.25	77.22	1210	778	718	60
110	KZ	VOS	52.72	70.98	300	2022	1738	284
111	KZ	ZRNK	52.95	69	380	1708	1499	209
112	MS	BTDF	1.36	103.77	64	600	379	221
113	MY	IPM	4.48	101.03	247	882	607	275
114	MY	KKM	6.04	116.21	830	1052	771	281
115	MY	KOM	1.79	103.85	49	872	603	269
116	MY	KSM	1.47	110.31	66	1063	768	295
117	MY	KUM	5.29	100.65	74	782	606	176
118	MY	LDM	5.18	118.5	177	772	591	181
119	MY	SBM	2.45	112.21	237	820	534	286
120	PS	BAG	16.41	120.58	1507	558	411	147
121	PS	OGS	27.06	142.2	20	374	268	106
122	PS	PSI	2.69	98.92	987	1696	1249	447
123	PS	TSK	36.21	140.11	350	874	662	212
124	TI	ALI8	37.79	73.4	3941	196	160	36

Continued on next page .....

No.	*Net.*	*Sta.*	*Lat.*	*Lon.*	*Elev.*	*Input WF*	*Rejected*	*Selected*
125	TI	BAR8	37.94	71.45	2101	574	480	94
126	TI	DKO8	39.55	72.22	2533	200	152	48
127	TI	ISH8	36.68	71.79	2686	333	266	67
128	TI	KOK8	38.66	72.85	3729	286	240	46
129	TI	NUR8	39.64	73.86	2956	217	198	19
130	TI	P03	40.17	73.49	1760	375	288	87
131	TI	SHA8	37.54	74.82	3850	478	376	102
132	TW	KMNB	24.46	118.39	43	2174	1938	236
133	TW	LYUB	22	121.58	40	310	265	45
134	TW	MATB	26.15	119.95	75.1	887	765	122
135	TW	NACB	24.17	121.59	130	2514	1800	714
136	TW	SSLB	23.79	120.95	450	2410	1761	649
137	TW	TDCB	24.25	121.16	1295	1203	919	284
138	TW	TPUB	23.3	120.63	370	2304	1724	580
139	TW	TWGB	22.82	121.08	195	2372	1788	584
140	TW	TWKB	21.94	120.81	90	1141	877	264
141	TW	WFSB	25.07	121.78	750	1370	992	378
142	TW	YHNB	24.67	121.37	775	1602	1206	396
143	TW	YULB	23.39	121.3	294.7	2273	1738	535
144	X4	A01	36.43	94.87	2800	443	341	102
145	X4	A04	36.54	94.02	2793	220	174	46
146	X4	A05	37.02	91.74	4070	431	329	102
147	X4	A07	36.81	92.95	3091	22	18	4

Continued on next page .....

No.	*Net.*	*Sta.*	*Lat.*	*Lon.*	*Elev.*	*Input WF*	*Rejected*	*Selected*
148	X4	A22	36.44	96.49	2810	9	5	4
149	X4	A23	36.45	95.74	2772	76	58	18
150	X4	B02	32.97	94.14	4780	234	174	60
151	X4	C01	35.81	94.89	4000	269	220	49
152	X4	C02	35.64	94.4	4431	539	458	81
153	X4	C03	35.9	93.76	4500	38	26	12
154	X4	C04	35.57	94.04	4750	284	223	61
155	X4	C08	34.28	92.43	4600	233	187	46
156	X4	C10	33.26	91.84	4920	462	349	113
157	X4	C13	34	91.55	4800	219	181	38
158	X4	C14	32.1	91.26	4700	102	78	24
159	X4	C15	31.48	92.08	4500	6	4	2
160	X4	D01	34.16	95.83	4350	363	265	98
161	X4	D04	35.09	97.91	4264	211	159	52
162	X4	D06	33.79	96.73	4160	261	205	56
163	X4	D07	34.78	96.17	4650	262	186	76
164	X4	D08	34.92	94.78	4413	286	206	80
165	X4	D09	35.12	93.96	4471	439	316	123
166	X4	D10	34.37	97.92	4500	524	384	140
167	X4	D11	34.06	97.21	4550	101	80	21
168	X4	D12	33.41	97.28	4340	474	354	120
169	X4	D13	33.01	97.11	3700	447	336	111
170	X4	D14	32.95	96.08	4220	522	395	127

Continued on next page .....

No.	*Net.*	*Sta.*	*Lat.*	*Lon.*	*Elev.*	*Input WF*	*Rejected*	*Selected*
171	X4	D15	32.85	95.44	4000	548	411	137
172	X4	D16	33.29	96.36	4330	216	179	37
173	X4	D17	33.72	95.84	4300	537	400	137
174	X4	D18	32.89	94.7	4500	542	393	149
175	X4	D19	34.27	94.92	4700	340	252	88
176	X4	D21	31.87	93.03	4500	247	196	51
177	X4	D22	31.84	94.44	4200	7	6	1
178	X4	D23	31.54	95.26	3900	433	338	95
179	X4	D24	31.16	96.47	4000	523	397	126
180	X4	D25	31.99	96.51	4000	425	318	107
181	X4	D26	32.46	96.39	3900	338	248	90
182	X4	F01	34.05	96.3	4300	377	271	106
183	X4	F03	32.85	96.58	4400	18	8	10
184	X4	F04	32.33	95.97	4000	488	361	127
185	X4	F06	33.1	95.11	4530	108	73	35
186	X4	F12	31.51	96.32	4100	52	39	13
187	X4	F13	31.24	95.91	3600	327	246	81
188	X4	F14	31.56	94.65	3850	539	413	126
189	X4	F15	31.87	93.78	4050	472	361	111
190	X4	F16	31.69	92.42	4600	296	226	70
191	X4	F17	32.39	91.71	4700	244	192	52
192	X4	GS01	34.27	104.24	1500	226	171	55
193	X4	GS02	33.78	102.97	2000	61	49	12

Continued on next page .....

No.	*Net.*	*Sta.*	*Lat.*	*Lon.*	*Elev.*	*Input WF*	*Rejected*	*Selected*
194	X4	GS03	34.43	102.29	2000	148	122	26
195	X4	GS04	35.05	104.57	2000	236	181	55
196	X4	GS05	34.65	103.54	2000	247	196	51
197	X4	GS06	35.11	102.89	1500	34	22	12
198	X4	GS07	34.35	105.04	1500	248	191	57
199	X4	GS08	33.48	105	1500	214	168	46
200	X4	GS09	32.87	106.46	1654	38	28	10
201	X4	GS10	33.54	106.91	1690	210	163	47
202	X4	GS11	33.91	105.97	1250	225	177	48
203	X4	GS12	34.85	105.75	1480	242	194	48
204	X4	GS13	35.64	105.45	1200	220	169	51
205	X4	GS14	35.7	104.53	1200	170	131	39
206	X4	GS15	35.38	107.34	1200	77	67	10
207	X4	GS16	36.05	106.06	1750	150	111	39
208	X4	GS17	33.77	101.7	2600	15	12	3
209	X4	GS18	32.87	104.78	1200	238	184	54
210	X4	H01	36.21	96.39	3120	208	156	52
211	X4	H02	36.27	96.96	2781	152	120	32
212	X4	H04	35.94	97.49	3192	157	117	40
213	X4	H05	35.66	98.41	3705	208	160	48
214	X4	H06	36.28	98.12	3221	171	123	48
215	X4	H08	36.77	98.96	3111	74	51	23
216	X4	H09	37.61	99.39	3629	46	37	9

Continued on next page .....

No.	*Net.*	*Sta.*	*Lat.*	*Lon.*	*Elev.*	*Input WF*	*Rejected*	*Selected*
217	X4	H10	37.68	98.63	3634	88	73	15
218	X4	H11	38.16	99.17	4085	3	2	1
219	X4	H12	37.34	98.23	3502	142	103	39
220	X4	H13	36.97	97.65	3707	144	111	33
221	X4	H14	37.35	96.75	2879	8	6	2
222	X4	H15	37.52	96	3433	131	99	32
223	X4	H16	37.37	94.78	2832	149	104	45
224	X4	H17	38.03	94.55	2860	134	104	30
225	X4	H18	37.68	93.66	2735	152	111	41
226	X4	H19	38.26	92.14	2704	67	52	15
227	X4	H20	38.8	94.35	2881	130	96	34
228	X4	H21	39.58	94.27	1795	141	99	42
229	X4	H22	39.76	93.49	1553	137	111	26
230	X4	H23	39.51	94.9	2177	165	128	37
231	XA	BUMT	27.55	90.77	2772	114	93	21
232	XA	CHUK	27.08	89.55	2263	115	83	32
233	XF	H0020	27.02	84.91	24	83	59	24
234	XF	H0040	27.07	84.94	33	228	180	48
235	XF	H0050	27.09	84.95	38	187	152	35
236	XF	H0070	27.13	84.97	51	270	205	65
237	XF	H0080	27.17	84.98	75	206	167	39
238	XF	H0100	27.23	84.99	162	238	179	59
239	XF	H0130	27.32	85.01	523	136	118	18

Continued on next page .....

No.	*Net.*	*Sta.*	*Lat.*	*Lon.*	*Elev.*	*Input WF*	*Rejected*	*Selected*
240	XF	H0160	27.4	85.02	461	174	159	15
241	XF	H0170	27.42	85.03	396	228	190	38
242	XF	H0190	27.47	85.04	505	258	217	41
243	XF	H0200	27.5	85.05	563	159	151	8
244	XF	H0220	27.56	85.07	1883	205	182	23
245	XF	H0230	27.58	85.07	2316	317	271	46
246	XF	H0250	27.63	85.1	1737	245	208	37
247	XF	H0260	27.67	85.09	1854	375	290	85
248	XF	H0280	27.73	85.1	1289	169	133	36
249	XF	H0290	27.76	85.11	1162	212	178	34
250	XF	H0350	27.91	85.14	525	94	85	9
251	XF	H0370	27.97	85.19	595	201	175	26
252	XF	H0380	28	85.21	1448	276	240	36
253	XF	H0400	28.06	85.23	1932	258	222	36
254	XF	H0410	28.08	85.26	1989	226	210	16
255	XF	H0440	28.17	85.34	1442	167	123	44
256	XF	H0460	28.22	85.36	1693	279	236	43
257	XF	H0480	28.27	85.38	1789	303	251	52
258	XF	H0490	28.31	85.35	2121	223	168	55
259	XF	H0500	28.34	85.35	2275	196	146	50
260	XF	H0510	28.39	85.35	2741	253	192	61
261	XF	H0520	28.41	85.31	2897	194	143	51
262	XF	H0530	28.45	85.24	3071	194	140	54

Continued on next page .....

No.	*Net.*	*Sta.*	*Lat.*	*Lon.*	*Elev.*	*Input WF*	*Rejected*	*Selected*
263	XF	H0540	28.49	85.22	3247	94	81	13
264	XF	H0550	28.52	85.22	3390	201	153	48
265	XF	H0560	28.56	85.25	3663	169	126	43
266	XF	H0580	28.63	85.27	3696	276	209	67
267	XF	H0590	28.67	85.28	3865	29	27	2
268	XF	H0600	28.71	85.28	3933	166	131	35
269	XF	H0610	28.75	85.3	4042	270	205	65
270	XF	H0620	28.79	85.3	4036	222	167	55
271	XF	H0630	28.82	85.29	4077	250	189	61
272	XF	H0641	28.86	85.29	4142	445	347	98
273	XF	H0650	28.9	85.33	4288	58	50	8
274	XF	H0655	28.9	85.38	5151	70	64	6
275	XF	H0660	28.92	85.42	4872	196	165	31
276	XF	H0670	28.94	85.44	4770	221	173	48
277	XF	H0680	28.98	85.44	4696	115	94	21
278	XF	H0690	29.02	85.46	4735	43	36	7
279	XF	H0700	29.06	85.42	4742	174	136	38
280	XF	H0710	29.09	85.38	4760	239	179	60
281	XF	H0720	29.14	85.36	4712	201	181	20
282	XF	H0730	29.17	85.36	4753	205	161	44
283	XF	H0740	29.2	85.36	4666	131	109	22
284	XF	H0750	29.23	85.31	4697	77	57	20
285	XF	H0760	29.27	85.24	4683	53	47	6

Continued on next page .....

No.	*Net.*	*Sta.*	*Lat.*	*Lon.*	*Elev.*	*Input WF*	*Rejected*	*Selected*
286	XF	H0770	29.31	85.24	4519	169	137	32
287	XF	H0780	29.34	85.24	4678	264	206	58
288	XF	H0790	29.38	85.23	4723	185	162	23
289	XF	H0800	29.41	85.23	4785	230	183	47
290	XF	H0810	29.47	85.23	4791	291	234	57
291	XF	H1000	29.27	85.86	4560	100	81	19
292	XF	H1010	29.34	85.84	4753	216	172	44
293	XF	H1020	29.41	85.74	5039	207	187	20
294	XF	H1030	29.48	85.75	5012	266	209	57
295	XF	H1040	29.56	85.74	5115	277	213	64
296	XF	H1050	29.64	85.72	5219	116	90	26
297	XF	H1060	29.71	85.71	5232	187	130	57
298	XF	H1070	29.78	85.76	5261	66	45	21
299	XF	H1071	29.77	85.77	5347	93	76	17
300	XF	H1080	29.85	85.78	5403	164	134	30
301	XF	H1090	29.92	85.73	5260	293	244	49
302	XF	H1100	29.99	85.7	5315	256	202	54
303	XF	H1110	30.07	85.55	5435	150	131	19
304	XF	H1120	30.14	85.41	5479	230	203	27
305	XF	H1130	30.21	85.33	5378	233	187	46
306	XF	H1140	30.28	85.3	5185	131	115	16
307	XF	H1150	30.36	85.31	5120	305	263	42
308	XF	H1160	30.43	85.29	5217	228	194	34

Continued on next page .....

No.	*Net.*	*Sta.*	*Lat.*	*Lon.*	*Elev.*	*Input WF*	*Rejected*	*Selected*
309	XF	H1170	30.5	85.2	4846	107	96	11
310	XF	H1180	30.58	85.18	4974	100	91	9
311	XF	H1190	30.65	85.14	4831	232	197	35
312	XF	H1200	30.72	85.14	4822	172	145	27
313	XF	H1210	30.78	85.11	4874	214	183	31
314	XF	H1220	30.86	85.07	4776	215	187	28
315	XF	H1230	30.93	85.1	4778	215	179	36
316	XF	H1250	31.08	85	4850	291	229	62
317	XF	H1260	31.15	85.01	4942	294	233	61
318	XF	H1280	31.3	85.13	4732	256	211	45
319	XF	H1290	31.38	85.1	4822	172	136	36
320	XF	H1310	31.52	85.18	5218	298	237	61
321	XF	H1320	31.58	85.19	5225	234	210	24
322	XF	H1340	31.73	85.14	5064	193	166	27
323	XF	H1350	31.8	85.03	4973	236	186	50
324	XF	H1360	31.86	84.95	4988	205	184	21
325	XF	H1370	31.95	84.89	4736	206	170	36
326	XF	H1420	31.93	83.84	4955	72	61	11
327	XF	H1421	32.01	83.87	4792	142	123	19
328	XF	H1422	32.06	83.9	4620	183	164	19
329	XF	H1430	32.38	84.13	4485	197	183	14
330	XF	H1440	32.45	84.24	4554	198	177	21
331	XF	H1460	32.6	84.22	4665	208	197	11

Continued on next page .....

No.	*Net.*	*Sta.*	*Lat.*	*Lon.*	*Elev.*	*Input WF*	*Rejected*	*Selected*
332	XF	H1470	32.67	84.22	4687	277	230	47
333	XF	H1480	32.75	84.22	4655	125	103	22
334	XF	H1500	32.89	84.29	5075	241	202	39
335	XF	H1510	32.95	84.3	4964	191	159	32
336	XF	H1530	33.12	84.22	4660	260	210	50
337	XF	H1540	33.19	84.23	4824	259	221	38
338	XF	H1560	33.31	84.25	4584	208	196	12
339	XF	H1570	33.42	84.26	4700	268	223	45
340	XF	H1590	33.63	84.17	4830	294	239	55
341	XF	H1600	33.75	84.27	4678	227	186	41
342	XF	H1620	33.97	84.22	5100	309	259	50
343	XF	H1630	34.07	84.23	5342	176	154	22
344	XF	NBENS	28.24	84.37	735	91	75	16
345	XF	NBIRA	26.48	87.27	12	9	8	1
346	XF	NBUNG	27.88	85.89	1191	51	38	13
347	XF	NDOML	27.98	84.28	352	72	57	15
348	XF	NG010	27.46	84.28	114	86	65	21
349	XF	NG020	27.57	84.33	110	81	61	20
350	XF	NG030	27.68	84.4	136	90	64	26
351	XF	NG040	27.82	84.46	197	82	60	22
352	XF	NG050	27.86	84.56	325	23	18	5
353	XF	NG060	28	84.62	1097	46	34	12
354	XF	NGUMB	27.56	83.84	530	68	55	13

Continued on next page .....

No.	*Net.*	*Sta.*	*Lat.*	*Lon.*	*Elev.*	*Input WF*	*Rejected*	*Selected*
355	XF	NHILE	27.05	87.32	2088	90	74	16
356	XF	NJANA	26.71	85.92	11	22	19	3
357	XF	NNAMC	27.8	86.71	3523	30	28	2
358	XF	NP010	27.49	83.32	40	83	67	16
359	XF	NP020	27.63	83.46	68	87	69	18
360	XF	NP030	27.75	83.5	283	48	35	13
361	XF	NP035	27.81	83.52	774	61	48	13
362	XF	NP040	27.87	83.54	1364	89	65	24
363	XF	NP050	27.94	83.64	752	90	72	18
364	XF	NP060	28	83.79	707	91	71	20
365	XF	NP071	28.08	83.84	821	66	50	16
366	XF	NP080	28.21	84	811	83	61	22
367	XF	NP090	28.29	83.59	1038	73	64	9
368	XF	NP100	28.78	83.72	2735	57	45	12
369	XF	NPHAP	27.52	86.58	2488	37	36	1
370	XF	NRUMJ	27.3	86.55	1319	32	29	3
371	XF	NSIND	27.21	85.91	465	34	28	6
372	XF	NTUML	27.32	87.2	360	6	4	2
373	XP	AHQI	40.07	75.8	2397	317	273	44
374	XP	AQKE	39.76	76.09	1402	388	312	76
375	XP	ATSH	39.72	76.16	1290	215	196	19
376	XP	KKTM	39.87	76.04	1583	286	246	40
377	XP	KMSK	39.63	76.26	1246	231	187	44

Continued on next page .....

No.	*Net.*	*Sta.*	*Lat.*	*Lon.*	*Elev.*	*Input WF*	*Rejected*	*Selected*
378	XP	KRUK	39.87	75.9	1843	324	264	60
379	XP	ORTO	40.16	75.78	2678	376	310	66
380	XP	TEGL	40	75.86	2130	350	293	57
381	XP	TLKC	40.11	75.78	2500	366	299	67
382	XP	TRKX	40.04	75.78	2307	361	293	68
383	XR	DONG	31.98	90.91	4610	157	131	26
384	XR	SANG2	31.02	91.7	4715	20	14	6
385	XR	ST00	30.53	90.1	4810	16	13	3
386	XR	ST01	30.65	90.13	4792	178	138	40
387	XR	ST03	30.85	90.19	4796	9	7	2
388	XR	ST04	30.96	90.19	4736	189	145	44
389	XR	ST05	31.04	90.17	4836	184	147	37
390	XR	ST06	31.12	90.1	5084	169	134	35
391	XR	ST07	31.23	90.07	5079	29	26	3
392	XR	ST08	31.3	90.03	4899	172	137	35
393	XR	ST10	31.49	90.01	4670	126	94	32
394	XR	ST12	31.63	89.88	4661	179	139	40
395	XR	ST14	31.77	89.71	4607	88	76	12
396	XR	ST15	31.83	89.64	4577	163	134	29
397	XR	ST19	32.06	89.19	4596	174	137	37
398	XR	ST20	32.17	89.14	4584	135	107	28
399	XR	ST22	32.33	89.12	4707	165	124	41
400	XR	ST23	32.42	89.11	4727	164	120	44

Continued on next page .....

No.	*Net.*	*Sta.*	*Lat.*	*Lon.*	*Elev.*	*Input WF*	*Rejected*	*Selected*
401	XR	ST24	32.48	88.98	4905	71	64	7
402	XR	ST26	32.66	88.92	4849	12	11	1
403	XR	ST28	32.82	88.85	4843	170	122	48
404	XR	ST29	32.93	88.85	4829	183	144	39
405	XR	ST30	33.03	88.85	4955	150	114	36
406	XR	ST31	33.14	88.88	4847	154	117	37
407	XR	ST33	33.33	88.83	5032	166	132	34
408	XR	ST34	33.41	88.76	4989	41	31	10
409	XR	ST35	33.48	88.74	4941	177	131	46
410	XR	ST36	33.52	88.6	5070	162	121	41
411	XR	ST37	33.61	88.52	5161	170	127	43
412	XR	ST38	33.65	88.5	5069	17	13	4
413	XR	ST39	33.76	88.4	5077	178	141	37
414	XR	ST40	33.81	88.31	4964	47	30	17
415	XW	AKSU	41.14	80.11	1109	189	135	54
416	XW	CHAT	40.92	76.52	3031	195	154	41
417	XW	KOPG	40.5	79.04	1114	119	104	15
418	XW	PIQG	40.32	77.63	1736	120	105	15
419	XW	TGMT	40	76.14	1823	138	110	28
420	XW	XIKR	39.82	77.37	1134	149	118	31
421	YA	MC01	31	102.35	2244	236	171	65
422	YA	MC03	30	102.49	1099	230	156	74
423	YA	MC04	30.06	101.48	3466	249	177	72

Continued on next page .....

No.	*Net.*	*Sta.*	*Lat.*	*Lon.*	*Elev.*	*Input WF*	*Rejected*	*Selected*
424	YA	MC05	29.99	100.22	3939	249	177	72
425	YA	MC07	29.05	100.42	3656	234	174	60
426	YA	MC08	29	101.51	2917	258	203	55
427	YA	MC09	28.96	102.76	1095	186	139	47
428	YA	MC10	28.98	103.87	448	174	140	34
429	YA	MC11	28.33	103.12	2036	248	186	62
430	YA	MC13	27.74	100.76	2730	203	170	33
431	YA	MC14	27.86	99.74	3330	214	175	39
432	YA	MC16	27.18	103.63	1952	200	148	52
433	YA	MC17	26.47	101.74	1153	207	151	56
434	YA	MC19	25.73	101.9	1173	144	131	13
435	YA	MC20	25.78	100.61	1562	221	175	46
436	YA	MC21	25.49	99.64	2476	151	113	38
437	YA	MC22	24.53	100.24	1064	115	105	10
438	YA	MC24	24.17	102.83	1896	232	169	63
439	YA	MC25	24.89	103.67	2050	235	174	61
440	YL	BIRA	26.48	87.27	12	158	128	30
441	YL	BUNG	27.88	85.89	1191	126	102	24
442	YL	DINX	28.66	87.12	4374	158	148	10
443	YL	GAIG	26.84	86.63	166	65	60	5
444	YL	HILE	27.05	87.32	2088	203	175	28
445	YL	ILAM	26.91	87.92	1181	171	138	33
446	YL	JANA	26.71	85.92	77	61	48	13

Continued on next page .....

No.	*Net.*	*Sta.*	*Lat.*	*Lon.*	*Elev.*	*Input WF*	*Rejected*	*Selected*
447	YL	JIRI	27.63	86.23	1866	65	59	6
448	YL	LAZE	29.14	87.59	4011	47	38	9
449	YL	MAZA	28.67	87.86	4367	50	42	8
450	YL	MNBU	28.76	86.16	4500	76	62	14
451	YL	NAIL	28.66	86.41	4378	36	25	11
452	YL	NAMC	27.8	86.71	3523	13	12	1
453	YL	PHAP	27.52	86.58	2488	117	111	6
454	YL	PHID	27.15	87.76	1176	240	183	57
455	YL	RBSH	28.2	86.83	5100	126	100	26
456	YL	RC14	29.5	86.44	4756	44	31	13
457	YL	RUMJ	27.3	86.55	1319	124	112	12
458	YL	SAGA	29.33	85.23	4524	177	138	39
459	YL	SAJA	28.91	88.02	4351	43	34	9
460	YL	SIND	27.21	85.91	465	126	96	30
461	YL	SSAN	29.42	86.73	4585	203	157	46
462	YL	SUKT	27.71	85.76	745	80	68	12
463	YL	THAK	27.6	85.56	1551	51	37	14
464	YL	TUML	27.32	87.2	360	136	117	19
465	YL	XIXI	28.74	85.69	4660	83	61	22
466	YT	104	37.85	77.46	1342	61	51	10
467	YT	116	36.44	77.01	3753	8	2	6
468	YT	141	32.49	80.09	4251	67	55	12

Appendix B

Complete Model

Here we present the complete result in form of depth section from 50 km to 475 km.

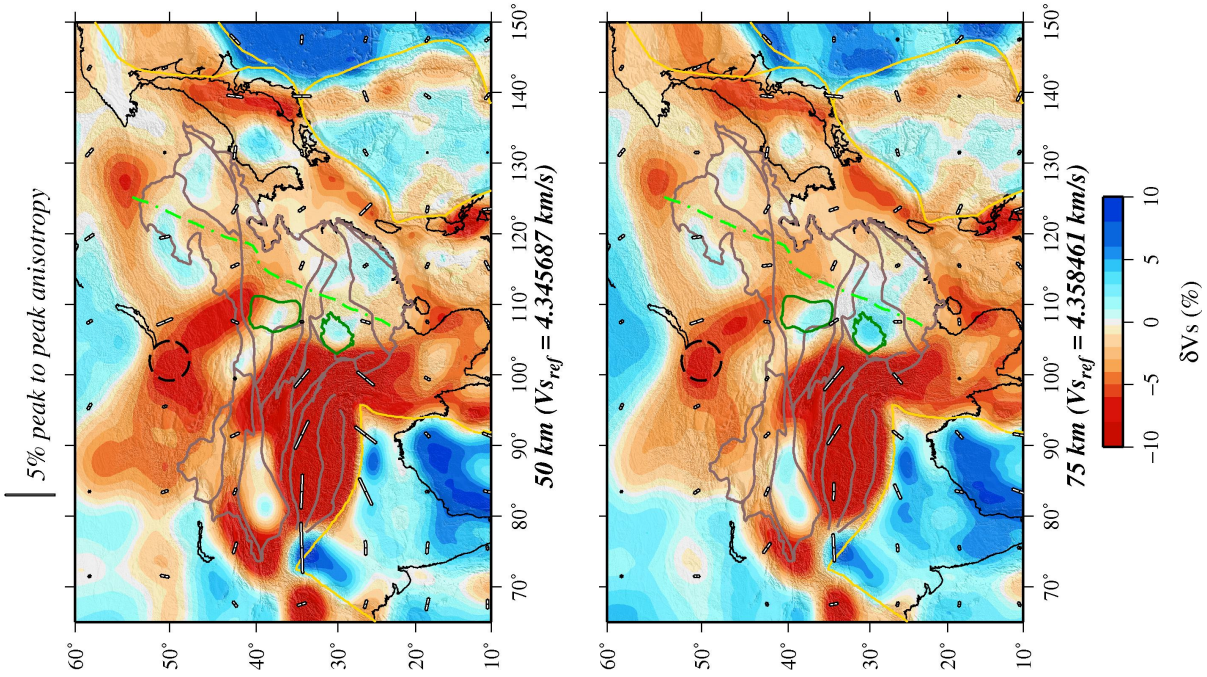

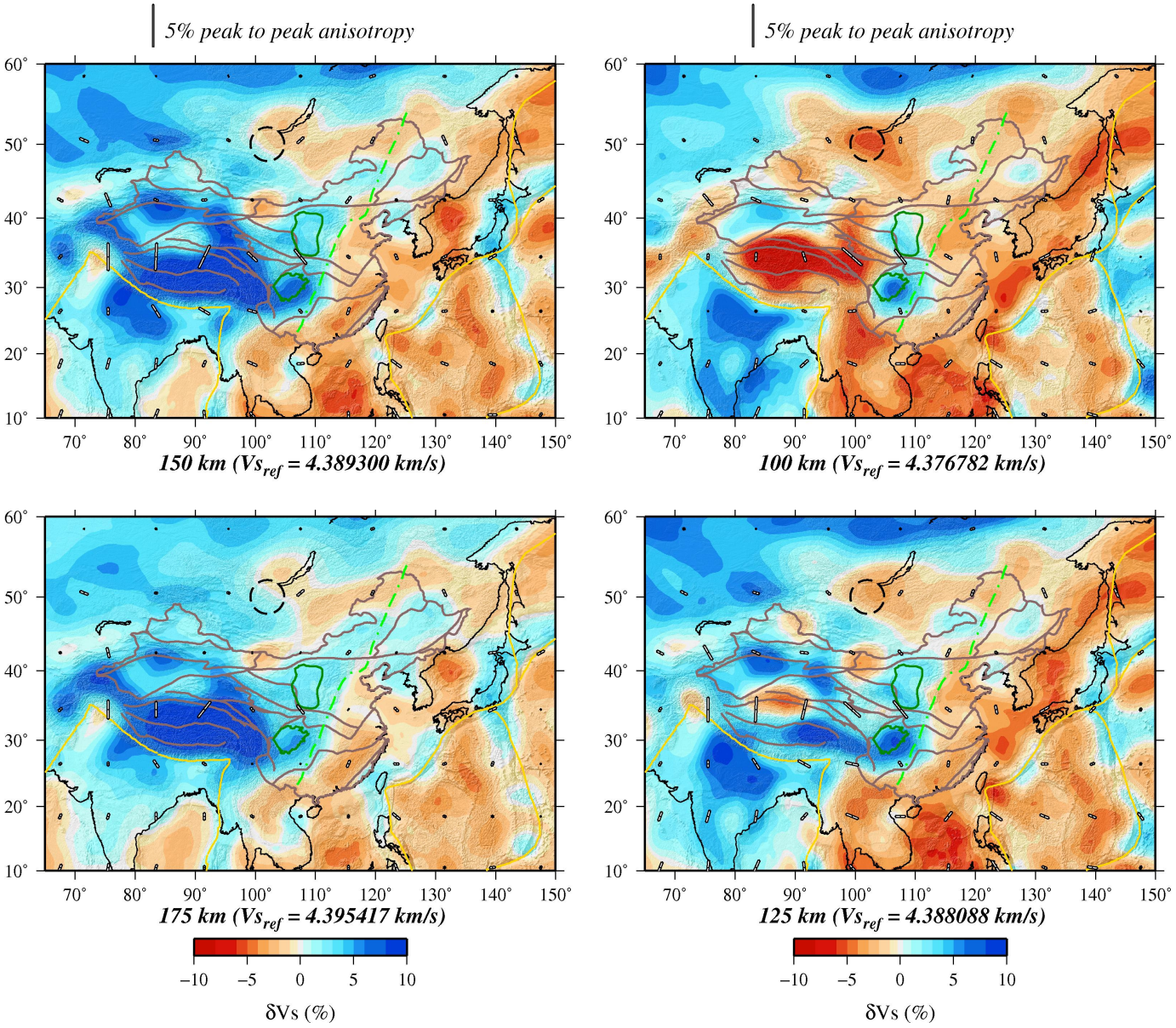
5% peak to peak anisotropy
5% peak to peak anisotropy
150 km (Vs$_{ref}$ = 4.389300 km/s)
100 km (Vs$_{ref}$ = 4.376782 km/s)
175 km (Vs$_{ref}$ = 4.395417 km/s)
125 km (Vs$_{ref}$ = 4.388088 km/s)
−10 −5 0 5 10
δVs (%)
−10 −5 0 5 10
δVs (%)

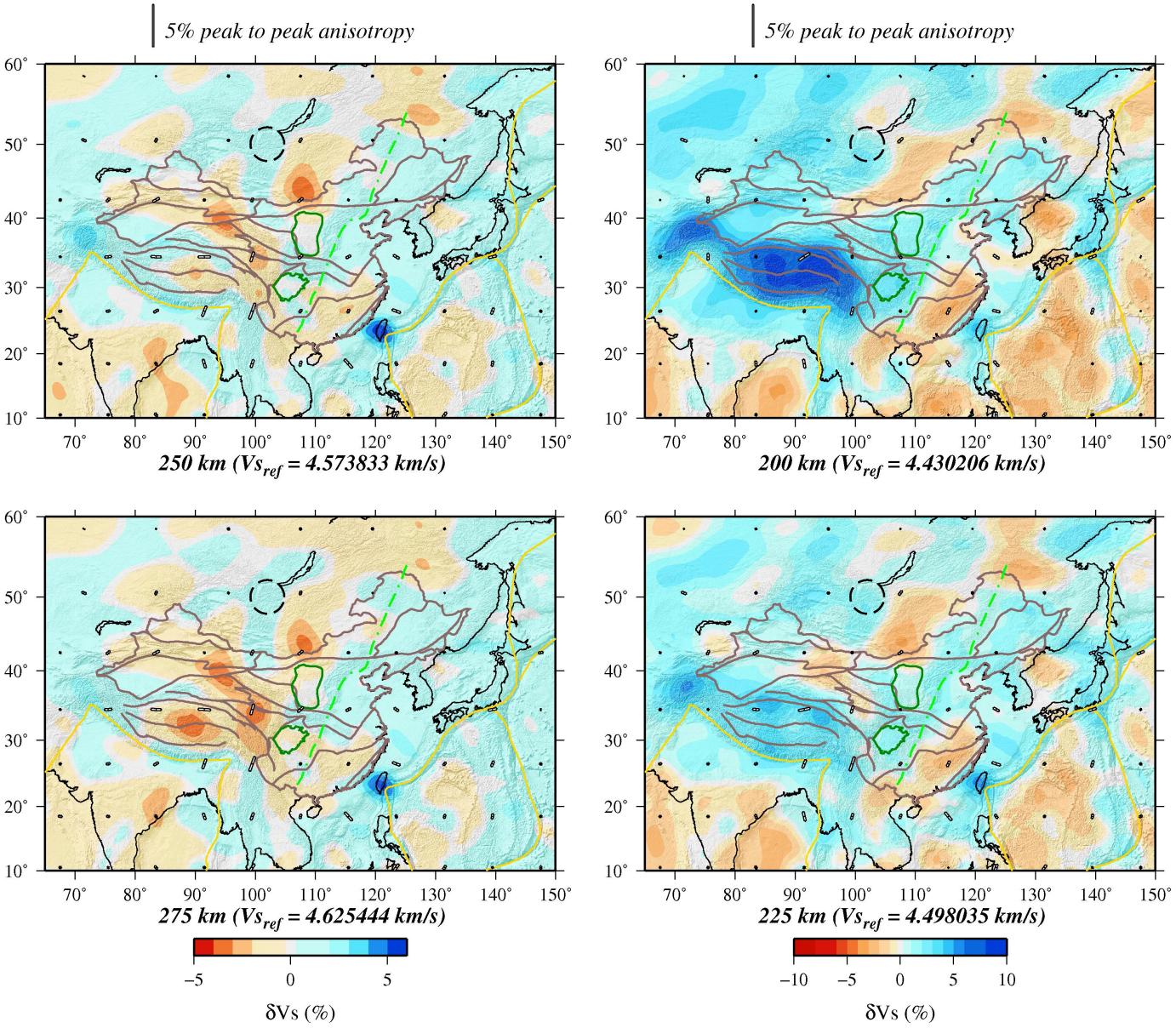
5% peak to peak anisotropy
5% peak to peak anisotropy
250 km (Vs$_{ref}$ = 4.573833 km/s)
200 km (Vs$_{ref}$ = 4.430206 km/s)
275 km (Vs$_{ref}$ = 4.625444 km/s)
225 km (Vs$_{ref}$ = 4.498035 km/s)
−5 0 5
−10 −5 0 5 10
δVs (%)
δVs (%)

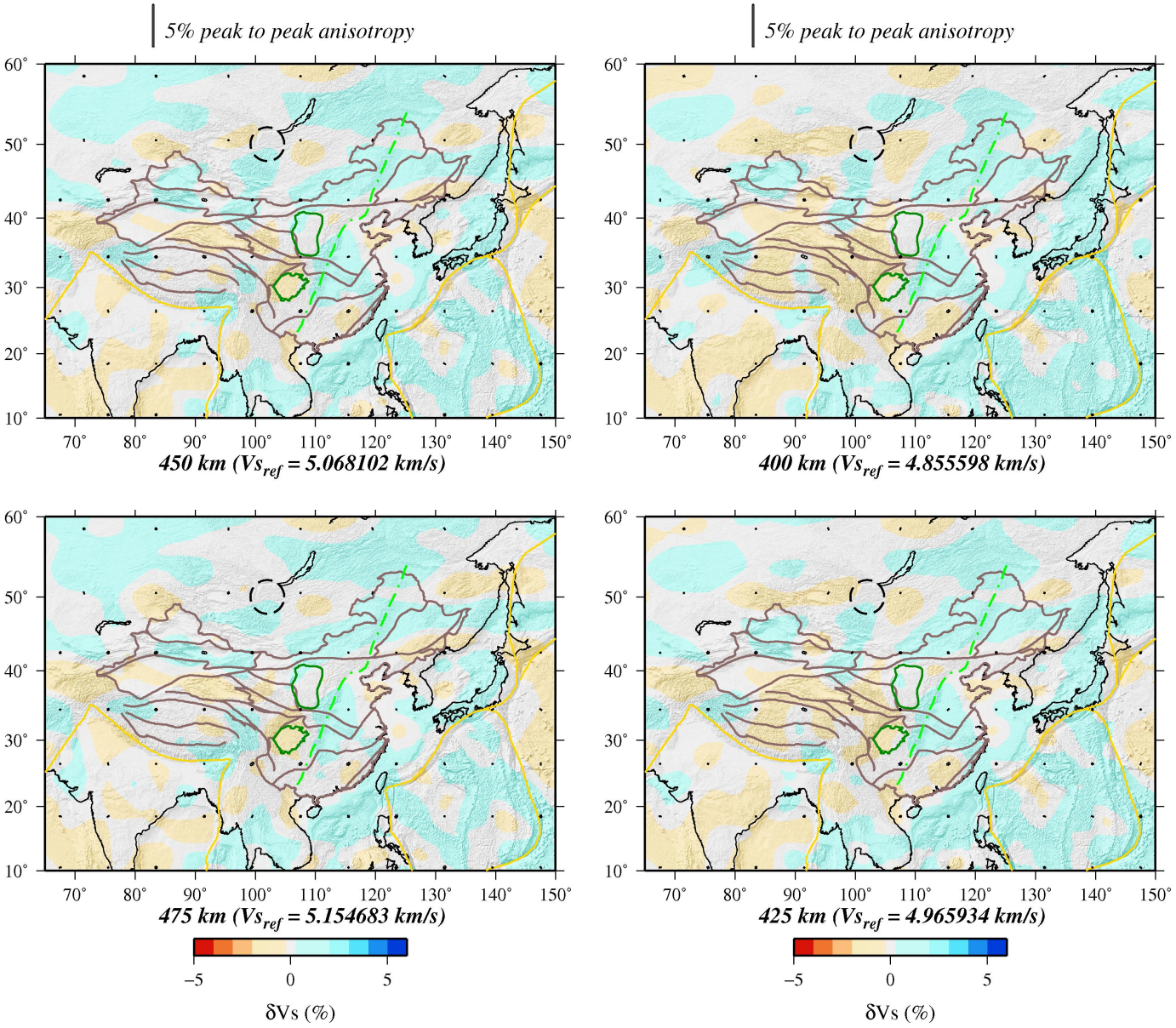
5% peak to peak anisotropy
5% peak to peak anisotropy
60°
50°
40°
30°
20°
10°
70°
80°
90°
100°
110°
120°
130°
140°
150°
450 km (Vs$_{ref}$ = 5.068102 km/s)
400 km (Vs$_{ref}$ = 4.855598 km/s)
475 km (Vs$_{ref}$ = 5.154683 km/s)
425 km (Vs$_{ref}$ = 4.965934 km/s)
−5
0
5
δVs (%)
δVs (%)

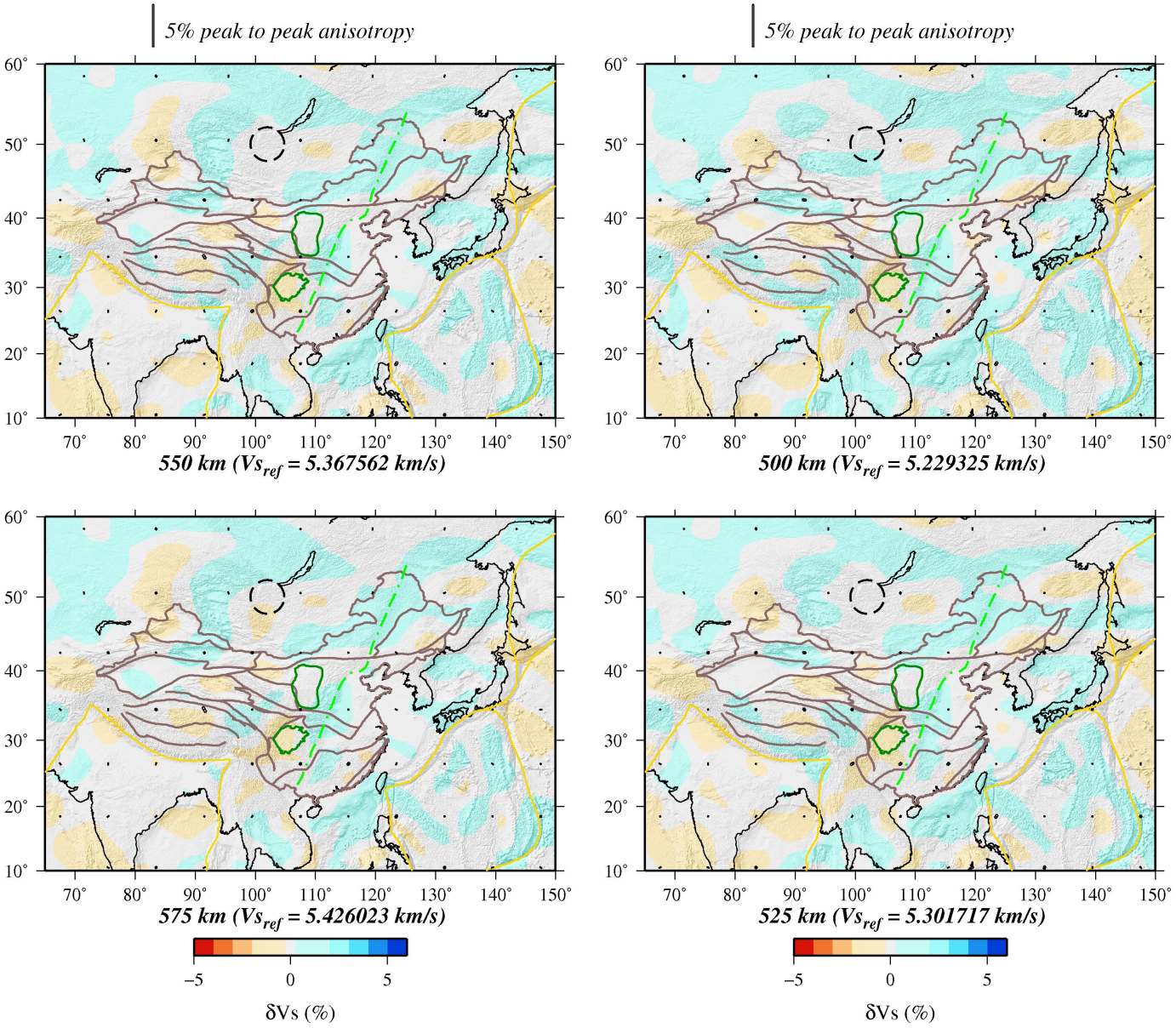
5% peak to peak anisotropy
5% peak to peak anisotropy
60°
50°
40°
30°
20°
10°
70°
80°
90°
100°
110°
120°
130°
140°
150°
550 km (Vs$_{ref}$ = 5.367562 km/s)
500 km (Vs$_{ref}$ = 5.229325 km/s)
575 km (Vs$_{ref}$ = 5.426023 km/s)
525 km (Vs$_{ref}$ = 5.301717 km/s)
−5
0
5
δVs (%)
δVs (%)

Appendix C

Test 1: 60 degree epicentral distance

Here we present the experimental result considering only those paths whose lengths are shorter than 6000 km. Half of the rays (exactly 27,083 out of 50,338) have path length falls under the category of shorter than 6000 km. Though we used the paths longer than 6000 km in the study (Figure 4.3) to increase ray coverage. So this experiment aim to test the susceptible to off great-circle deviations and multi-pathing. We present the result for the same and found that the bias due to longer paths is not recognizable. The effect of off-great circle propagation tends, if there is any, to slightly blur the image, and is negligible.

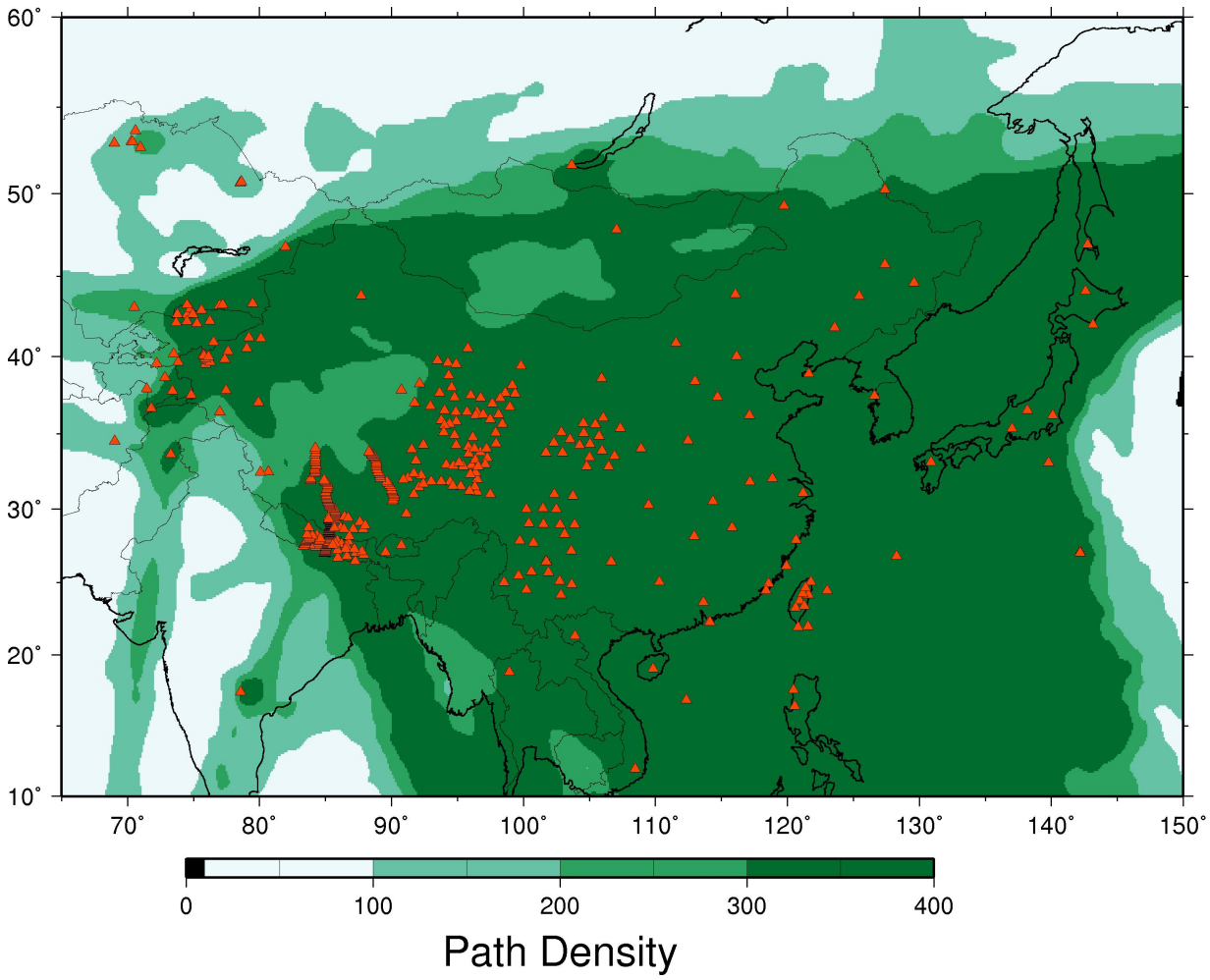
60˚
50˚
40˚
30˚
20˚
10˚
70˚
80˚
90˚
100˚
110˚
120˚
130˚
140˚
150˚
0
100
200
300
400
Path Density

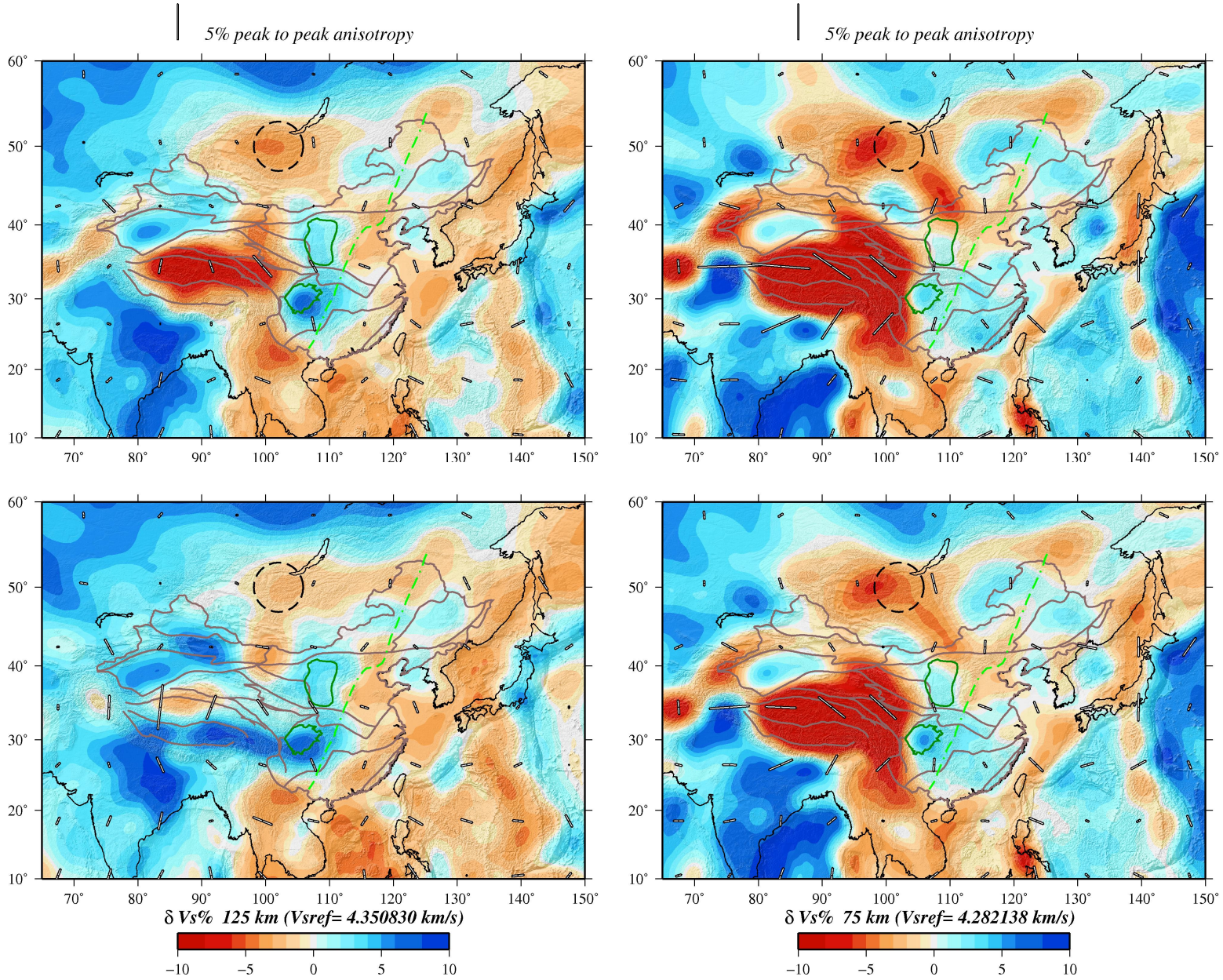
5% peak to peak anisotropy
5% peak to peak anisotropy
60°
50°
40°
30°
20°
10°
70°
80°
90°
100°
110°
120°
130°
140°
150°
δ Vs% 125 km (Vsref= 4.350830 km/s)
δ Vs% 75 km (Vsref= 4.282138 km/s)
−10
−5
0
5
10

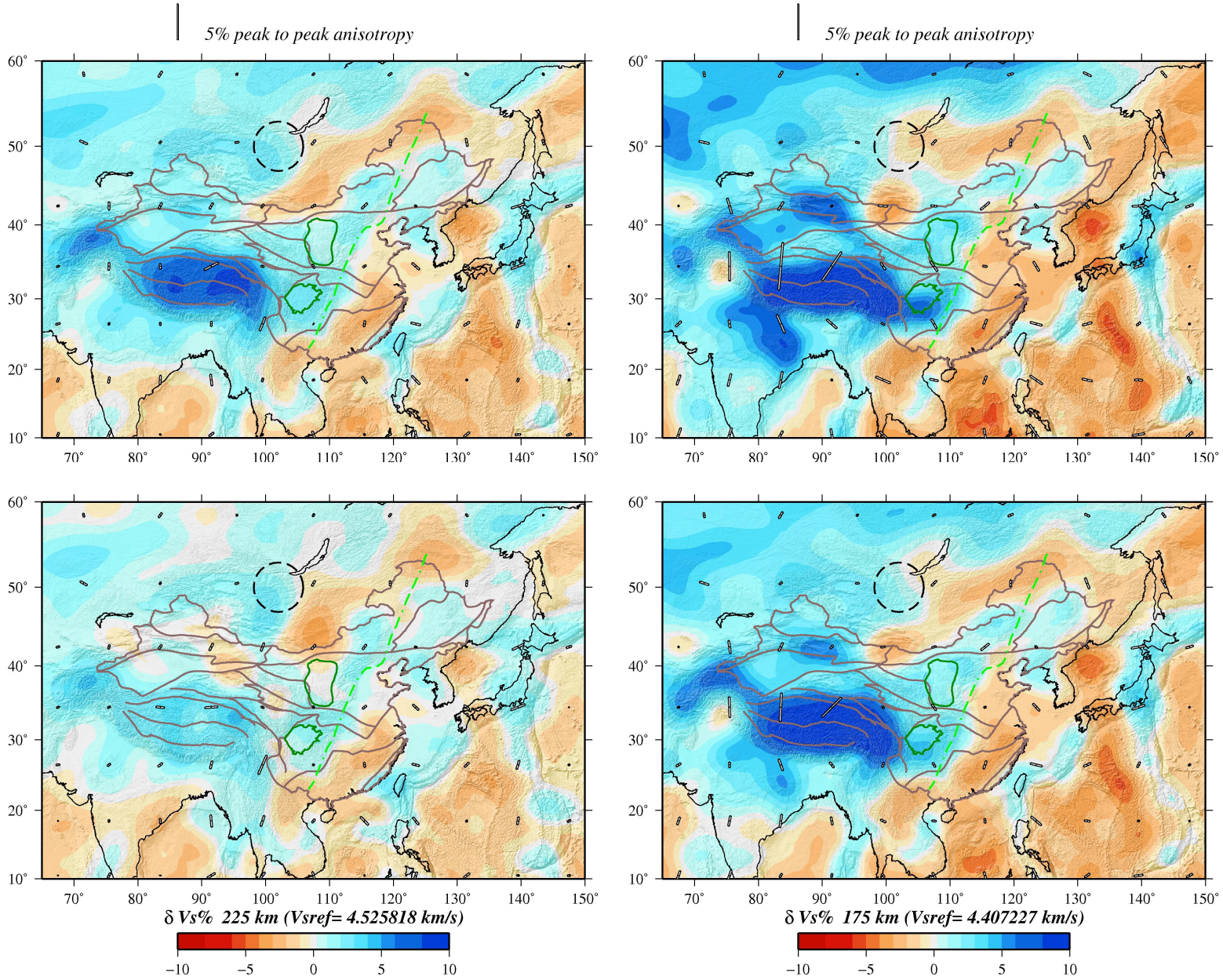
5% peak to peak anisotropy
5% peak to peak anisotropy
60°
50°
40°
30°
20°
10°
70°
80°
90°
100°
110°
120°
130°
140°
150°
δ Vs% 225 km (Vsref= 4.525818 km/s)
δ Vs% 175 km (Vsref= 4.407227 km/s)
−10
−5
0
5
10

Appendix D

Test 2: Exclude Path from Tibet

This experiment was desigen to address the issue of artifact in shallow mantle due to the underestimation of the 3SMAC crust. So we for the regionalization inversion we consider only those path which are not passing through the Tibet where the crustal thickness is huge (60-70 km). This experiment shows that in actual model the values outside the Tibet (especially the North China craton and South China craton) are not biased by the the crustal heterogenity.

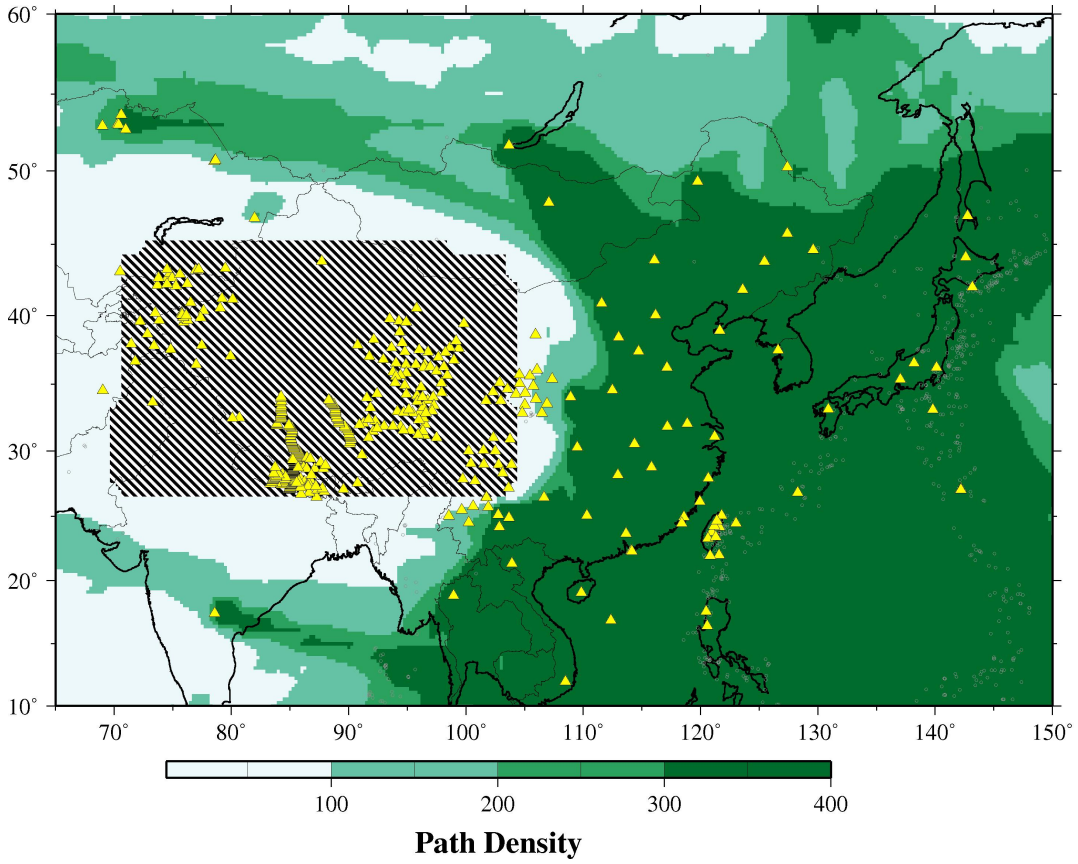
60°
50°
40°
30°
20°
10°
70°
80°
90°
100°
110°
120°
130°
140°
150°
100
200
300
400
Path Density

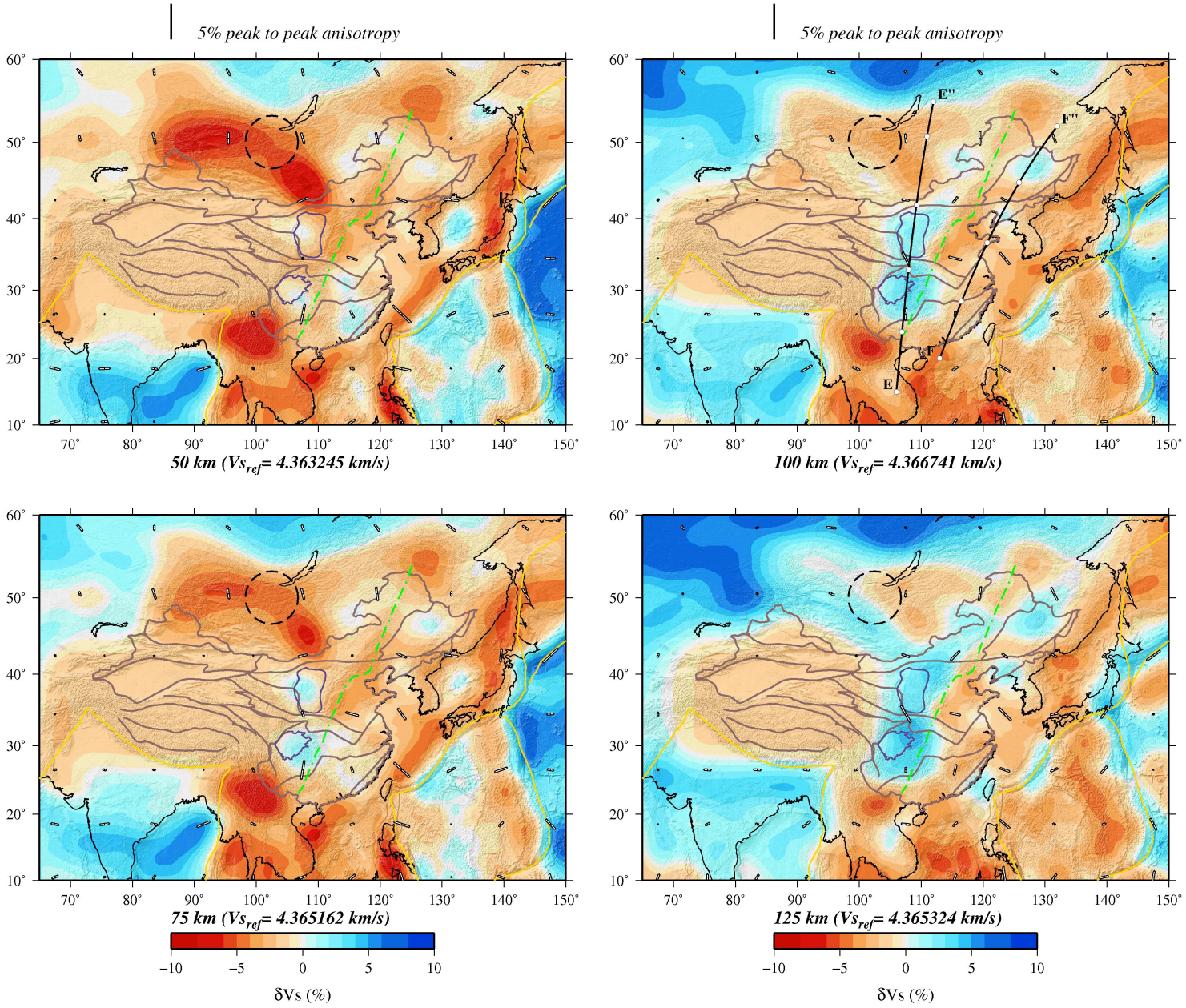
5% peak to peak anisotropy
5% peak to peak anisotropy
E''
F''
F
E
50 km (Vsref= 4.363245 km/s)
100 km (Vsref= 4.366741 km/s)
75 km (Vsref= 4.365162 km/s)
125 km (Vsref= 4.365324 km/s)
−10 −5 0 5 10
δVs (%)
−10 −5 0 5 10
δVs (%)

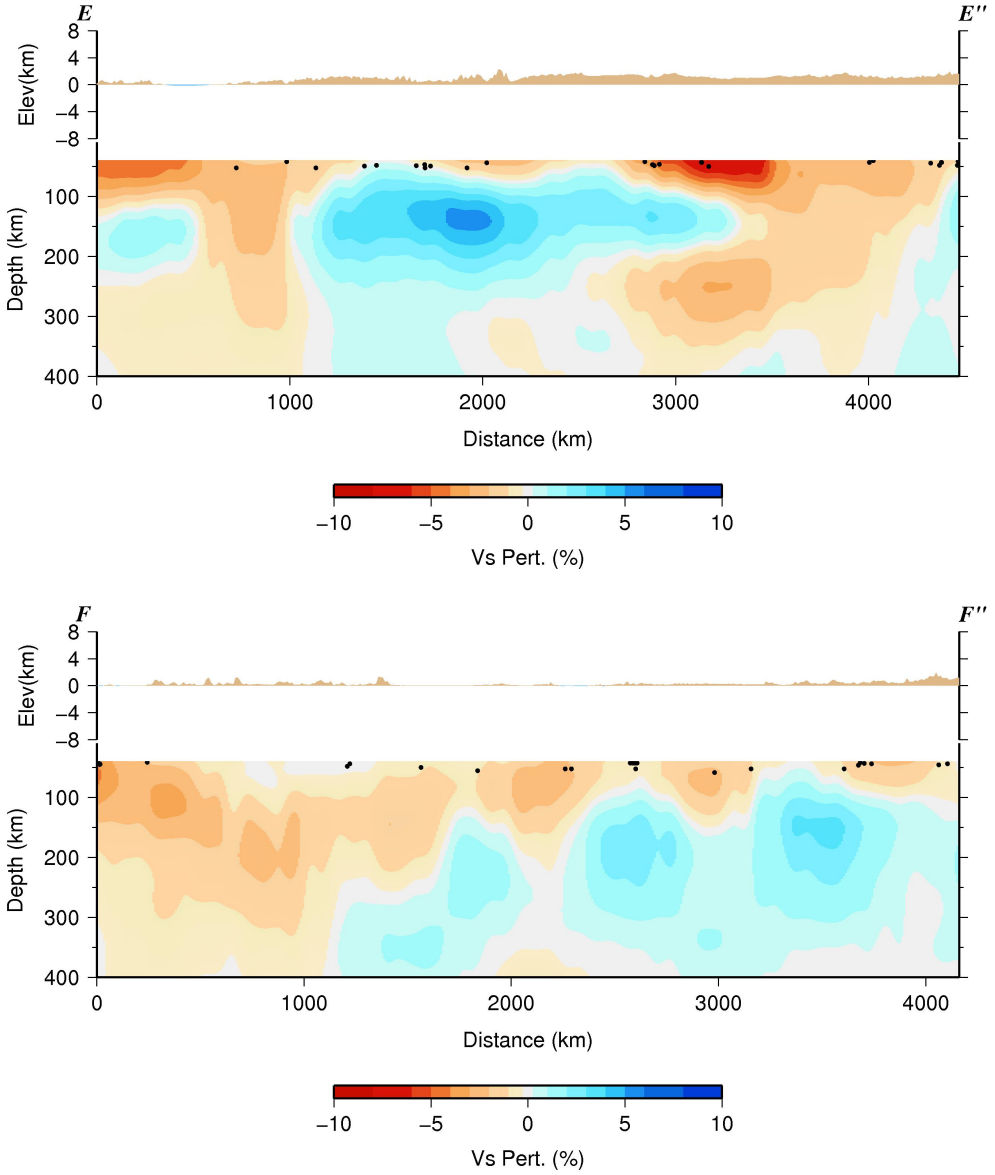
E
E''
Elev(km)
8
4
0
−4
−8
Depth (km)
100
200
300
400
0
1000
2000
3000
4000
Distance (km)
−10
−5
0
5
10
Vs Pert. (%)
F
F''
Elev(km)
8
4
0
−4
−8
Depth (km)
100
200
300
400
0
1000
2000
3000
4000
Distance (km)
−10
−5
0
5
10
Vs Pert. (%)

Appendix E

Manuscript

This is the copy of manuscript submitted to *Earth and Planetary Sciences Letters* (EPSL) that contains part of the result presented in this thesis. The title of the manuscript is "High resolution 3D Rayleigh wave velocity model of China and surrounding areas".

High Resolution 3D Rayleigh wave velocity model of China and surrounding area

Shantanu Pandey,[1] Xiaohui Yuan,[1] Eric Debayle,[2] Keith Priestley,[3] Rainer Kind,[1,4] Frederik Tilmann,[1,4] Xueqing Li,[1]

[1] *Deutsches GeoForschungsZentrum GFZ, Telegrafenberg, 14473 Potsdam, Germany*

[2] *Laboratoire de Sciences de la Terre, Centre National de la Recherche Scientifique, Université Lyon 1 et Ecole Normale Supérieure de Lyon, France*

[3] *Bullard Laboratories, University of Cambridge, Cambridge, UK*

[4] *Freie Universität Berlin, Germany*

Abstract

The lithosphere of China is made by accretion of three major Precambian cratons: the North China craton (Sino-Korean craton), the Yangtze craton (South China craton) and the Tarim basin. The ongoing convergence between India and Eurasia has dramatically modified the lithosphere, approximately doubling crustal thickness below the Tibetan plateau. Subduction of the Pacific and Philippine sea plates has played a major roll in destroying the lithospheric root beneath East China. Here we present a three-dimensional model of shear wave velocity for the upper mantle of China and the surrounding region by analyzing 50338 vertical component multimode Rayleigh wave seismograms. We analyse 47 permanent and more than 300 temporary broadband stations inside China and also 97 permanent stations outside China to achieve uniformly high path density coverage everywhere within China. The procedure for generating 3-D shear wave velocity model involves combination of all 1-D path average models obtained by modeling each waveform of Rayleigh wave seismogram up to the 4th higher mode in a tomographic inversion scheme. The dense station network and the use of multi-modes analysis help to achieve a lateral resolution of a few hundred kilometers with resolving power down to 400 km depth. We interpret the high velocity mantle lid as seismic evidence of the lithosphere. The lithosphere is to the first order thin in east China and thick in the west with a maximum thickness of more than 200 km in much of the Tibet-Pamir plateau. High-velocity Indian mantle lithosphere gradually increases its thickness from ∼100 km in south India to

more than 150 km in north India and underthrusting the Tibetan plateau to south of Qaidam basin. Deep lithospheric roots with lithospheric thickness exceeding 100-150 km are also observed in Tarim basin, Sichuan basin and Ordos block. The lithosphere in the eastern part of the North China craton and the Yangtze craton is close to or thinner than 70 km, therefore, not well resolved here. Adjacent to these areas, the lithosphere in the South China fold system has a thickness of 70-80 km, whereas no sublithospheric low velocity zone was observed beneath Songliao basin. A large-scale subhorizontal high velocity body is observed at depths of 150-400 km beneath the entire east China cratonic areas. We interpret this observation as evidence for mantle lithosphere delamination that may explain the decratonization of the North China and the Yangtze cratons. The upper mantle velocity model is compatible with various receiver function and SS precursor results in the aspect of shear wave travel times in the upper mantle.

Keywords: Rayleigh wave, surface wave, tomography, fundamental mode, higher mode, China.

---

1. Introduction

China is an assembly of ancient continental fragments separated by fold belts, which were accreted from late Proterozoic to Cenozoic (Huang et al., 1980). Its present tectonics has been profoundly shaped by the Indo-Asian continental collision in the southwest and the subduction of the NW Pacific plate and the Philippine Sea plates in the east with resistance by the Siberian shield in the north (Fig. 1). China has three major Precambrian cratons: the North China craton (NCC, also called Sino-Korean craton), the Yangtze craton (YC, also called South China craton) and the Tarim block. The interactions among different blocks have formed the tectonic features today and caused many intraplate earthquakes(Ma, 1987; Ma et al., 1984; Yin and Harrison, 2000; Liu et al., 2007). The convergence of Indian and Eurasian plates, started 50 million years ago, has created the world's largest plateau and is pushing the crust and mantle lithosphere out of its way to the east (Royden et al., 2008). he NW Pacific and Philippine Sea plate subduction zone produced substantial heterogeneity in the mantle beneath east China, as well as widespread uplift, volcanism and extension. North China and Mongolia comprise the major part of the Central Asian Orogenic Belt, which was accreted due to the resistance of the Siberian shield (Windley

et al., 2007). All of these events have left their imprint on the upper mantle structure. Unraveling the tectonic history and understanding the tectonic processes require a better knowledge of the China lithosphere.

High-viscosity lithospheric plates moving over a lower-viscosity asthenosphere is a basic element of plate tectonics. The terms lithosphere and asthenosphere were originally defined with reference to rheology, with the lithosphere essentially behaving as elastic solid, and the asthenosphere deforming as a viscous fluid (Barrell, 1914). Later on, additional terms like thermal, chemical or seismic lithosphere have been introduced (Anderson, 1995), with the seismic lithosphere being defined as the high velocity lid overlying a low velocity asthenosphere. The term lithospheric thickness has also been associated with a point of inflection in the velocity-depth relationship (McKenzie et al., 2005; Eaton et al., 2009). For the present work it is the later property which is of most importance.

Regional body wave tomography is sensitive to lateral variations but has poor vertical resolution in the shallow mantle, due to smearing along near-vertical propagation paths. Surface wave tomography has a good vertical resolution because of sensitivity of surface wave dispersion to depth. However, sampling continental upper mantle requires long period surface wave with large horizontal path length (Sieminski et al., 2004; Li et al., 2008; Priestley and Tilmann, 2009). Body wave tomography has resolution where there are crossing ray paths. The resolution normally begins at a depth roughly equal to the average inter-station distance, valid for regional body wave tomography. The depth resolution of the fundamental mode surface wave is normally limited to the shallower 200 km, but can extend to a depth of more than 400 km by including higher modes (Debayle, 1999; Lebedev and Nolet, 2003; Priestley et al., 2006; Feng and An, 2010).

China is a very suitable place for surface wave study, as there are not only a lot of earthquakes in plate boundary zones around China, but also many intraplate earthquakes within China. Fundamental mode surface wave studies of China have reached a resolution of several hundred kilometers showing features correlated with the large geological units (Romanowicz, 1982; Griot et al., 1998; Ritzwoller and Levshin, 1998; Curtis et al., 1998; Huang et al., 2003; Friederich, 2003; Feng and An, 2010). These studies generally agree that the lithosphere reaches a thickness of more than 200 km in western China and thins to less than 100 km in eastern China. However, there can be important difference at the more regional scale. For example, Griot et al. (1998) and Huang et al. (2003) observed a thick lithosphere beneath the Ti-

betan plateau, while others reported a thin mantle lid (Romanowicz, 1982) or a missing lithosphere (Friederich, 2003) beneath the central and northern Tibet. beneath central and northern Tibet. The discrepancy probably arises from the different resolution power of the different data sets as well as from the different methodological approaches. The resolution can be improved by including surface wave overtones and by increasing the station density. Lebedev and Nolet (2003), Priestley et al. (2006) and Feng and An (2010) have shown that the upper mantle structure of eastern Asia can be better constrained by fitting multi-mode surface waveforms, although they have only used few stations in China, for which waveform data was available. Here we follow the approach used in Priestley et al. (2006). The waveform inversion algorithm was developed by Cara and Lévêque (1987) and aims to model the interference pattern between different modes present in seismogram, rather than attempting to isolate the individual modes (Lévêque et al., 1991). In order to increase the number of stations available we used all publicly available temporary experiment data along with 47 evenly spaced permanent broadband stations in China. The increased number of stations makes the inter-station spacing less than 300 km in east China (Fig. 2). Adding these data has greatly increased the number of short earthquake-station paths available, thus improving the resolution of the surface wave inversion, and reducing the bias caused by the effects of off-great circle propagation. The use of Rayleigh waves analyzed at periods longer than 50s for path lengths greater than a few thousands of kilometers provides a lateral resolution of several hundred kilometers extending to a depth of 400 km.

In the present work we have performed both isotropic and anisotropic inversions. The isotropic components in both case are very similar. We discuss here the isotropic component of the anisotropic inversion because it is less subject to biases. There are few percent of azimuthal anisotropy in the uppermost 200 km. Interpreting this pattern requires further work and will be done in an other paper.

2. Data and Methods

Our data comprise the Rayleigh waves in vertical component seismograms. We utilize the fundamental mode and overtones to a degree of 4. Fig. 3 shows the sensitivity kernels of the Rayleigh-waves of different modes and at different periods. While the fundamental-mode Rayleigh waves can be observed at a broad frequency band, the higher modes are often limited

to higher frequencies. It can be seen that the sensitivity of the fundamental mode is limited to the upper mantle, whereas the higher modes provide additional sensitivity below the mantle transition zone. Note that Fig. 3 is based on a theoretical calculation using a PREM model modified to remove the low velocity layer (Priestley et al., 2006). The depth sensitivity of the observed data can be reduced by diverse factors such as missing frequency content, lack of higher mode excitation, mode conversion due to sharp lateral velocity contrasts and regularization.

The waveform data from more than 400 stations (Fig. 2) with the period span ranging from 1999 to 2007 has been requested from different agencies. We requested waveform data of 47 broadband stations from the Chinese Earthquake Network Centre, many of which have not previously been used for this kind of study. In addition, data from more than 300 temporary stations in China and nearly 100 stations around China were requested from the IRIS and GEOFON data centers. The selected distribution of stations helped in achieving a good path density coverage and azimuthal distribution (Fig. 2).

The techniques used for constructing 3D Sv model proceeds in two distinct stages. It was previously employed in a number of regional scale surface wave tomography studies (Debayle, 1999; Debayle and Kennett, 2000; Pilidou et al., 2004; Heintz et al., 2005; Priestley et al., 2006).

2.1. Waveform inversion

In the first stage we model each waveform by a 1D shear wave velocity model representing the average seismic structure from the source to the receiver. We use the automated version (Debayle, 1999) of the Cara and Lévêque (1987) waveform inversion technique. The observed vertical component data are cross-correlated with pure-mode synthetics computed for a reference model for the fundamental and four higher Rayleigh modes. This produces "observed" and "synthetic" cross-correlograms which are filtered at different frequencies using Gaussian filters. A set of secondary observables is then selected on each envelope of the actual cross-correlograms. The waveform inversion matches these secondary observables with the synthetic envelopes. Once the secondary observables are fitted, the phase of each filtered cross-correlograms is added in the waveform inversion. The use of secondary observables helps to reduce nonlinearity on the model parameters and thus minimizes the dependence on the starting model. This analysis requires two basic assumptions that the observed seismogram can be represented in terms

of multimode surface waves that propagate independently and that they do so along great circle path. The necessary condition for the validity of the first assumption is that the medium should be varying smoothly (Woodhouse, 1974) and for the second that the lateral velocity variations should be not too large..

The waveform fitting procedure is automatic for each seismogram. The period range used here is 50-160 s for the fundamental and up to four higher Rayleigh modes, depending on their signal-to-noise ratio (SNR). At each period, the SNR is deemed adequate if the ratio between the maximum amplitude of the envelope between the signal and noise is greater than 3. Because of the large variation in crustal thickness of the study region, including the extremely thick crust in Tibet as well as oceanic crust at the margins of the study region, we imposed a more restricted bandwidth than Debayle (1999):we analyzed our data in the period range 50-160s, instead of 40-160s in Debayle (1999). The signal is evaluated in five bandwidths centered at 50, 70, 90, 120, and 160s period. The use of longer period allows for reducing the effect of strong lateral variations in the shallow part. Also the deviation from great circle path is fairly negligible for the period range in use (more than 50s) even for the fundamental mode (Debayle and Kennett, 2000; Debayle et al., 2001). The inversion is performed for the upper mantle structure assuming that the crustal structure is known and can be kept fixed in the inversion. We implement a crustal correction by calculating the path average of the crustal layers in the 3SMAC model Nataf and Ricard (1996) for each waveform. We used the smoothed PREM model for the mantle and compute synthetic seismograms using the code from Takeuchi and Saito (1972). Source parameters are taken from the Global CMT catalog. The inversion is considered successful if the final synthetics matches well (Debayle, 1999) the observed seismogram and if the inversion converges towards a unique and stable velocity model. The output of this inversion scheme is a 1-D average model along the great circle path. In this study we obtained 50338 1D path averaged models. For this data set we achieved more that 100 paths crossing per $2^\circ \times 2^\circ$ or the entire study area, and more than 500 paths almost everywhere in China (Fig. 2).

One half of the rays have path length shorter than 6000 km (Fig. 4). We also included the paths longer than 6000 km in the study to increase ray coverage, although longer paths involve larger Fresnel zone and are more susceptible to off great-circle deviations and multi-pathing. We tested this effect by repeating the entire analysis by either using only shorter paths (<

6000 km) or using all paths and found that the bias due to longer paths is not recognizable (see Supplementary Figs. 1 and 2). The effect of off-great circle propagation tends, if there is any, to slightly blur the image, and is negligible.

Because of the imposition of the *a priori* crustal model, anomalies above the Moho are not constrained by the surface wave data but simply reflect the *a priori* model. Anomalies immediately below the Moho are in principle resolved, but will suffer from significant artifacts if there are discrepancies between the actual and assumed crustal structures. Low frequency surface waves also tend to cause low velocities in the crust to bleed into the uppermost mantle.

2.2. Tomographic inversion

In the second stage we combine the 1-D velocity models in a tomographic inversion using a continuous regionalization algorithm developed by Montagner (1986) based on the Bayesian inference approach of Tarantola and Valette (1982) approach can be seen as a way of finding the model that gives the best fit to the data while keeping it as "close" as possible to the a priori information. The smoothness of the inverted model in poorly sampled regions is therefore mostly constrained by the width of the Gaussian covariance function, while in regions with higher ray density the need for a satisfactory data fit allows a rougher model. The Gaussian covariance function between two points r and r' is:

$$C_{m0}(r, r') = \sigma(r)\sigma(r') \quad exp\left(\frac{-\Delta^2_{r,r'}}{2L^2_{corr}}\right) \tag{1}$$

where $\Delta_{r,r'}$ is the distance r and r', σ_j is the standard deviation in point j and L_{corr} is the correlation length (Montagner, 1986). L_{corr} controls the horizontal smoothness of the model and σ_j controls the amplitude of the model perturbation at a geographical point j. The Earth model is discretized in $1^\circ \times 1^\circ$ cells which is much smaller than the surface wave wavelength or Fresnel zone at our period of interest. Although the inversion problem is strongly underdetermined (the number of independent information contained in the data is less than the number of model parameter), the inversion problem is stabilized by the use of appropriate regularization; we chose $L_{corr} = 250$ km and $\sigma = 0.05$ km/s after several trials.

In the next sections we will discuss the reliability of the model by different tests (Figs. 5, 6 and S3-S5). The resulted 3D model is presented in horizontal

sections at different depths from 100 to 300 km (Fig. 7) and along 6 profiles crossing different tectonic regions (Fig. 8).

3. Resolution tests and reliability of the model

In stage one of calculating 1D path-averaged model, artifacts can arise from errors in the assumed crustal model and source parameters. Our experience and previous synthetic tests suggest that the effects of crustal corrections with different crustal models e.g., the 3SMAC or the CRUST2.0 ($http://igppweb.ucsd.edu/\ gabi/rem.html$), are indistinguishable at depths larger than 100 km and are minor at shallower depths (Debayle and Kennett, 2000; Pilidou et al., 2004; Priestley et al., 2008). In addition, a good (redundant) path density and azimuthal coverage like what we have for this work is a basic requirement for reducing the influence of errors in source parameters. Cara and Lévêque (1987) already demonstrated the weakness of the dependence on the reference model, so that we can safely start the inversion from a unique upper mantle model (a smooth version of PREM) with a crustal part adapted to each path.

For the second stage we checked the dependence of the results on the reference model with a simple analytical test (flat model resolution test). We added a uniform perturbation of 5% and 15% of the a priori model, respectively, and performed 3D tomographic inversion based on these two references models (Fig. 5). From the output it is evident that our a priori choices (L_{corr} = 250 km; σ = 0.05 km/s) allow us to retrieve the flat model uniformly for the area of interest. In Fig. 5, we selected a very narrow width for white color (approx. 1%) around the targeted value of the model. The smearing around the edges of the map can be interpreted as the effect of the width of the Gaussian correlation length.

The image accuracy is not so easy to quantify, but the checkerboard tests can provide a quantitative measure of our ability to resolve a particular input model. We conducted a number of checkerboard tests to examine the ability of the selected data set to recover velocity anomalies of different size. Fig. 6 shows the test with seismic anomalies extending over 500×500 km in the middle of the map horizontally and 100 km vertically. Alternating high and low velocity anomalies with magnitudes of ±6% are spread over the entire volume, separated by ∼500 km wide zero percent anomalies. The size corresponds to the anomalies in the final models, which we interpret. We calculated synthetic Rayleigh wave seismograms for the same ray paths,

source parameters, frequency contents as in the observed data and carried out the same inversion procedure. The result of the test shows that the anomalies can be recovered in the entire volume. At shallow depth (< 200 km) the input model can be almost completely recovered. At depths of 200-400 km nearly half of the magnitude of the anomalies can be recovered. The synthetic test shown in Fig. 6 gives an intuitive example on our ability to recover a particular model from our ray coverage and a priori choices. However, as shown by Lévêque et al. (1993) such a test does not demonstrate that other synthetic models with larger size structure will be better retrieved in all circumstances. For this reason, we performed other synthetic test with seismic anomalies with size of the checker of 750×750 km and 1000×1000 km horizontally and with 50 and 100 km vertically. With our dense coverage, all these input models are always retrieved. We therefore assume that seismic anomalies larger than 500 km in horizontal and 50-100 km in vertical direction are reasonably well resolved by our data in the uppermost 400 km.

The study area is very heterogeneous with dramatic variation in the crustal thickness (Li et al., 2006; Zhang et al., 2011). Beneath the orogenic belts of Tibet, Tien Shan and Pamir the maximum crustal thickness reaches more than 80 km, measured by different seismic means (Kind et al., 2002; Li et al., 2006; Zhang et al., 2011). At shallow depth (less than 100 km) the 3D inversion may be affected by errors in our a priori knowledge of the crust. The strongest biases are expected in regions with the thickest crust. To test the effect of the thick crust we removed the paths that cross regions where the crustal thickness is over 60 km (mainly Tibet-Pamir-Tien Shan orogenic belts) and repeat the tomographic inversion. The test is presented in the supplement (Figs. S3-S5). Fig. S3 shows the path density after removing nearly all paths that pass through the Tibet, Pamir and Tien Shan regions, where the crust is thicker than 60 km. We display maps between 50 and 150 km depth in Fig. S4 and two vertical sections EE" and FF" in Fig. S5 which can be compared with Fig. 7 and 8. The eastern part of the maps at 100 and 150 km depths are very similar to the final model (Fig. 7) inverted using the entire dataset, indicating that Sv velocity perturbations are robust in this part of the model, not significantly biased by paths crossing regions with thick crust. The large scale pattern of sections EE" and FF" (Fig.8) is also preserved after the inversion with the reduced data set. At shallower depths (50 and 75 km) high velocity mantle lithosphere are visible beneath Ordos block, Sichuan basin, Songliao basin as well as the South China sold system.

4. Observations

4.1. Horizontal Sections

Fig. 7 shows 6 horizontal sections of the isotropic Sv velocity perturbations of the 3D inversion at depths from 100 to 300 km.

The slice at 100 km depth shows high velocities in India, Tarim basin, Sichuan basin, Ordos block and Songliao basin and wide-spread low velocities elsewhere including Tibet, Central Asian Orogenic Belt (CAOB) and in the oceanic areas. In the northwest Pacific subduction zones the low velocity anomalies following plate boundaries should represent the mantle wedges. In the depth range of 100-200 km we can recognize the downgoing slab by high velocities. At larger depths the resolution is insufficient to clearly image the slab. The west China and CABO are characterized by low velocity anomalies at shallow depths. The low velocity anomaly in Tibet is sharply bounded by the Indian plate to the south, by Tarim basin to the north and by Sichuan basin and Ordos block to the east, which show up as high velocity anomalies typical of continental lithospheric mantle. Our experiment with a reduced dataset (Figs S3-S5) suggests that the image outside Tibet is not significantly biased by the crustal heterogeneity. Beneath Tibet, crustal effect could be more important. However, Debayle and Kennett (2000) show that reasonable errors in crustal thickness have little effect on the mantle structure below 100–125 km depth. In addition, Pilidou et al. (2004) and Priestley et al. (2008) tested a subset of their data using the CRUST2.0 model in place of the 3SMAC crustal model and found little difference in the upper mantle structure beneath Eastern Asia.

S wave anomalies at 125-200 km depth reflect the variation in lithospheric thickness. High velocity anomalies indicate mantle lithosphere. Low velocity anomalies indicate asthenosphere. In general west China including Tibet, Tien Shan-Pamir, Sichuan basin, and Ordos block is characterized by thick lithosphere while the lithosphere beneath east China is thin. The high velocity anomaly in the mantle lithosphere beneath much of Tibet and Pamir regions extends to a depth of 200 km. At 125 km a low velocity zone at the place south of Tarim and Qaidam basins dominates northwest Tibet. At the same place reduced velocities can be followed to a depth of 175 km. The north central India has high velocities. The Songliao basin in NE China has also high velocities. To the east, high velocity oceanic subducting plate is still visible.

The amplitude of S wave anomalies reduces significantly at depths below 200 km. However, the resolution tests also indicate that the magnitude of recovered anomalies of dimensions of a few 100 km is reduced by about 50%, such that the real change in the magnitude of anomalies is hard to quantify. Instead of high velocities beneath Tibet and Tien Shan, low velocity asthenosphere dominates the orogenic regions. High velocities in east China are probably related to subducted Pacific oceanic lithosphere. Taiwan and southern Japan are characterized by high velocity anomalies.

4.2. Vertical Sections

We created 6 vertical sections crossing through major tectonic units (Fig. 8). Section AA", BB" and CC" are approximately in east-west direction, while sections DD", EE" and FF" are in north-south direction. Locations of the sections are indicated on the 100 km horizontal map in Fig. 7. For each section we plotted S velocity perturbation as well as the absolute velocity. Smaller anomalies can be more easily seen in the perturbation image. However, the anomalies depend on the reference model, and features such as low velocity zones (i.e. negative velocity gradients with depth) are more readily identified on absolute velocity profiles. Topography and major tectonic features along each section are plotted on top of each section. Seismicity of a swath width of 200 km along each section is projected on the section.

Section AA" extends from southernmost Pamir and central Tibet through the Sichuan basin and South China fold belt to the Philippine Sea. Seismic anomalies can be clearly seen related to these major tectonic units. A pronounced high velocity anomaly is observed beneath entire Tibet down to a depth of 200 km and is interpreted as the mantle lithosphere. The low-velocity anomaly beneath Tibet is to the east sharply bounded by the mantle lithosphere of the Sichuan basin, seen as high velocity body down to a depth of 200-250 km. All these anomalies can be clearly observed in relative and absolute velocity images. From the continental region east of Sichuan basin to the oceanic area of Philippine Sea the upper mantle is characterized by low velocity, indicating a thin lithosphere. The high velocity beneath Taiwan extends to a depth of 300 km.

Section BB" passes through two cratonic regions of Tarim basin and NCC and extends to the Tien Shan to the west and to the Philippine Sea to the east. The Tien Shan and the Qilian (QFS) orogenic belt are known to have thick crust whereas the Tarim basin has a normal continental crustal thickness (Li et al., 2006; Zhang et al., 2011). High velocity mantle lithosphere

can be clearly seen beneath Tarim basin in the velocity perturbations as well as in the absolute velocity. In the velocity perturbation image, the high velocity body appears to extend to the west beneath Tien Shan and to the east beneath the QFS. High velocity mantle lithosphere exists beneath the Ordos block, which constitutes the western part of the NCC. The east NCC has a thin mantle lithosphere, as seen by the low mantle velocity. Farther east the subducted oceanic slab of the Philippine Sea and the Pacific plates are visible by the high velocity anomalies, indicated by the slab seismicity.

In section CC" the low velocity beneath the CAOB centered at Hangay Dome can be seen as a low velocity anomaly reaching a depth of 100 km at the southern tip of Baikal lake. Songliao basin in the northeast China appears to have a deep lithospheric root as seen in the velocity perturbation, but has no distinct sub-lithospheric low velocity zone. The Pacific subducted slab is clearly visible as high velocity body in the mantle beneath Japan and NE China.

The India-Eurasia collision zone can be best examined on section DD", which cuts through the Indian plate, central Tibet and reaches Hangay Dome in Siberia. The most significant feature of our mantle cross-section is the northerly dipping high velocity body, suggesting the Indian mantle lithosphere underthrusts much of Tibet until Qaidam basin. Beneath Qaidam basin the high velocity mantle layer suddenly jumps to a shallower depth by about 50 km, which we interpret as the start of the Eurasian mantle lithosphere. At either edges of the thick mantle lithosphere beneath the plateau subvertical high velocity bodies are clearly visible penetrating into deep mantle.

Section EE" links Sichuan basin and Ordos block, which form the western parts of the two cratons: the NCC and YC. The lithosphere of both cratons is significantly thicker (>150 km) in the west, while it is much thinner (<70-80 km) in the east. In the section the Sichuan basin and Ordos block can be identified as two separate lithospheric blocks. The Sichuan basin is a more pronounced high velocity body, both in perturbation and in absolute velocities, extending to a depth of ∼175 km. The Ordos block extends to a depth of ∼150 km and is less pronounced in the section of absolute velocity.

Section FF" is located in east China passing through the South China fold system (SCFS), the eastern parts of the YC and the NCC and Songliao basin. The mantle lithosphere beneath the NCC is too thin to be resolved. At shallow depth (70-80 km) beneath SCFS and YC high velocities are visible, which we interpret as the mantle lithosphere. Beneath Songliao basin

high velocities reach a depth of 300 km and spread to the north and south directions in the depth range of 150-400 km beneath the YC and NCC.

5. Discussion

5.1. Segmentation of lithospheric blocks over China

China consists of Precambian cratons separated by Phanerozoic fold belts. However the thickness of the lithosphere does not follow the geographic locations of these tectonic units. It is known from numerous studies (Huang et al., 2003; Lebedev and Nolet, 2003; Priestley et al., 2006; Feng and An, 2010; Feng et al., 2010; Obrebski et al., 2012) that the lithosphere is thin in east China and thick in the west, roughly divided by the North-South Gravity Lineament (NSGL). The NSGL is a major gravity gradient, 100 km wide, which marks the border of the west and east China with distinct topographic, tectonic and seismic properties and, therefore, is recognized for a long time to be important in the evolution of eastern Asian (Xu, 2007). Across the NSGL the Bouguer gravity anomaly increases rapidly from -100 mGal in the west to -40 mGal in the east. Our result (Figs. 7-10) confirms earlier observations but with more detailed information. The depth slice at 100 km in Fig. 7 clearly highlights the deep lithospheric roots of the cratonic blocks, indicated by high velocities. These include Tarim basin, west NCC (Ordos block) and west YC (Sichuan basin). The lithospheric roots extend to ∼150 km depth beneath Ordos block and to ∼175 km depth beneath Tarim basin and Sichuan basin. These cratonic blocks form the north and east borders of the Indian-Asian collision zone and have acted as rigid blocks resisting the plate motion and lithospheric flow during the collisional and post collisional processes (Clark and Royden, 2000; Royden et al., 2008). The northward moving Indian plate has a thickness of 100-175 km with its thickest part in the north central India adjacent to Tibet. The lithosphere beneath much of the Pamir-Tibetan plateaus has doubled its thickness during the Indo-Asian collision with a maximum thickness over 200 km beneath the Tibetan plateau.

In the eastern portion of the NCC and YC, the lithosphere is too thin to be well observed by large-scale surface wave studies (Priestley et al., 2006; Lebedev and Nolet, 2003; Huang et al., 2009; Obrebski et al., 2012). We are able to recognize the high velocity mantle lithosphere of the east YC, but are still missing that of the NCC. Our test shown in the supplement (Figs. S3-S5) demonstrates the robustness of the model for resolving the shallow

mantle lithosphere in east China. The mantle lithosphere of the eastern part of the YC can be seen at 50 and 75 km depths. The mantle lithosphere of the NCC is too thin to be seen on the vertical sections. The thickness of the lithosphere of the two cratons is therefore different. We estimate that the lithosphere of the east YC is 70-80 km, while the lithosphere of the east NCC is thinner than ∼70 km and is, therefore, beyond our resolution power. This conclusion is more obvious on the vertical section FF" (Figs. 8 and S5). The base of the lithosphere beneath the east NCC was estimated by receiver functions as shallow as ∼60 km (Sodoudi et al., 2006; Chen et al., 2008; Chen, 2009), whereas it is ∼10 km deeper in the east YC. It is commonly agreed (Menzies and Xu, 1998; Griffin et al., 1998; Kusky et al., 2007) that the lithosphere has been thinned in Mesozoic and the depleted cratonic lithospheric root has been removed in east China. Probable extension experienced since Mesozoic, together with Cenozoic volcanism occurred in this area (Menzies and Xu, 1998), caused by delamination or thermal erosion of the thick lithospheric root (Kusky et al., 2007), may be responsible for the lithospheric thinning. This interpretation is also supported by high heat flow and extensive seismicity in this area (Ma et al., 1984; Wesnousky et al., 1984).

5.2. Sub-lithospheric structure

Although we aimed to image the continental lithosphere beneath China, we do observed anomalies in the sub-lithospheric mantle. The use of multimode surface waves helped to expand the resolution to depth greater than 200 km.

In the northwest Pacific subduction zones the subducted oceanic lithosphere can be followed to a depth of 200-300 km (Figs. 7 and 8). The widespread low velocity anomalies following plate boundaries is likely to represent the mantle wedges. In the depth range of 100-200 km we can recognize the downgoing slab by high velocities. At larger depths (greater than 300 km) the resolution is insufficient to clearly image the slab. A pronounced high velocity body is clearly visible beneath Taiwan at a depth range of 150-300 km. High velocity anomaly has also been observed by body wave tomography (Huang et al., 2010) and was interpreted as evidence for subducted Eurasian slab beneath Taiwan. Ai et al. (2007) observed a thickening in the mantle transition zone beneath Taiwan, which is compatible with the high velocity Eurasian slab subducted into the mantle transition zone.

No high velocity mantle lithosphere is recognized along the CAOB that extends from Altai Mountains to the east to the Pacific Ocean. Widespread low velocity anomalies exist below the crust to a depth of 300 km (Fig. 7 and Fig. 8 sections C-E). Kustowski et al. (2008) also observed a low velocity upper mantle below the CAOB. The most prominent low velocity anomaly is located beneath the Hangay Dome and is visible down to a depth of 150 km, as also observed by (Priestley et al., 2006).

In Songliao basin, northeast of China, there is no significant low velocity zone in the sub-lithospheric mantle. Instead, high velocities can be seen from the base of the crust continuously to a depth of 300 km and connects in the depth range of 150-400 km to a large-scale subhorizontal high velocity body that spreads from below Songliao basin ∼500 km to the north and more than 2000 km to the south underlying the entire YC and NCC (Fig. 7 and Fig. 8, sections CC" and FF"). Obrebski et al. (2012) observed a fast anomaly at 200 km depth beneath the NCC and interpreted it as a possible delaminated lithospheric root of the NCC. Our result confirms their observation but we found that the high velocity anomalies is distributed in a much larger area, 100-200 km in thickness and ∼3000 km in length. In Fig. S5 the high velocity zone appears to be divided into three separated blocks underneath the YC, NCC and Songliao basin respectively. The high velocity zone is parallel to the Pacific subduction zone and underlies the entire eastern China craton, bordered to the west by the NSGL. It is still unclear when and how the NSGL formed, and whether it is related to the lithospheric deformation. However, based on our observation the entire NSGL coincides with the sub-lithospheric high velocity zone from north to south for ∼3000 km and marks its western border. We interpret that the high velocity body may represent the remnant lithospheric root being initially the lower part of the cratonic mantle lithosphere and having been delaminated since Mesozoic. As the loss of the lithospheric root occurred beneath both the NCC and YC and only in the eastern portion of the two cratons, the decratonization is unlikely caused by the Triasic collision of the NCC and YC cratons, nor is it by the Cenozoic India-Asia collision in the far west. The decratonization of the east China cratons is very likely related to the Mesozoic Pacific subductions beneath east China, that triggered the large-scale lithsopheric delamination.

5.3. Comparison of average upper mantle velocity variations derived by surface wave inversion and by study of SS precursors.

Propagation of body waves is influenced by the seismic velocity variation in the upper mantle. Analysis of seismic waves reflected (SS precursors) or converted (Ps or Sp conversions) at the mantle discontinuities may give information on average seismic velocity in the upper mantle. While surface waves constrain the average seismic velocity along the path, propagation of body waves contains more local information. The 410- and 660-km mantle discontinuities marking the top and bottom of the mantle transition zone are generally thought to mark mineralogical phase changes within the mantle. Experimental studies have shown that both reactions are sensitive to temperature and have Clapeyron slopes of opposite signs (reviewed by Helffrich (2000)). In the absence of other effects, such as changes in water content or in main mantle constituents or metastability caused by fast and cold subduction or by hot upwelling plume, a lateral increase in temperature at the level of the transition zone should be reflected in a deepening of the 410 km discontinuity and a shallowing of the 660 km discontinuity (and vice versa). However, the arrival times of the mantle discontinuity phases can also be significantly influenced by the average velocities in the upper mantle, which are in turn controlled by the thickness of the crust and lithosphere as well as velocity heterogeneity in the lithosphere and asthenosphere. As a result the two discontinuities will apparently be shifted in the same direction in the time series (Kind et al., 2002; Zhao et al., 2010).

The underside reflected SS wave can be observed in the seismograms as a precursor to the SS wave (Shearer, 1991). The differential time of the SS precursor at the mantle discontinuities (S410S and S660S) and the primary phase SS is a function of the depth of the reflector as well as the average velocity in the upper mantle. Heit et al. (2010) created a long profile of SS precursors and found parallel time variation in the S410S and S660S phases along the profile (see Fig. 9a for profile location), which is consistent with shear velocity variation in the upper mantle and constant discontinuity depths. In Fig. 9b we plotted deviation of the S410S time in percent of a reference value (160 s, which is close to the global average of S410S-SS differential time) and compare it with perturbations of the average Vs over 400 km depth range along the same profile. For calculation of the average velocity in the upper 400 km we integrated the 3SMAC model in a depth range of 0-50 km for the crust into the inverted 3D model (>50 km depth). The profile extends from Tibet across the North China craton to the Pacific subduction zone. The absolute

and perturbation velocity along the profile (Fig. 9c and 9d) exhibits low velocities in the shallow mantle beneath Tibet and high velocities in the mantle lithosphere below. The S410S time perturbation curve has the same general shape as the curve of average shear wave velocity variations in the upper mantle, derived by the surface wave tomography but at wavelengths of less than 1000 km the anomalies are no longer correlated. Both curves show negative values beneath Tibet, reflecting the large crustal thickness there, which overwhelms the fast velocities in the mantle. The perturbations increase to the east and become positive beneath the Pacific regions. The comparison confirms that our model is representative for the upper mantle in the study area. The difference of the two curves can be explained by different lateral resolutions of the two methods and possibly the unusual X-shaped Fresnel zone for SS precursors and the time change in the S410S phase caused by the real variation of the discontinuity depth.

5.4. The India-Asia collision zones

In Fig. 10 we compare in a similar manner the average velocity perturbation derived by the surface wave inversion with those derived by receiver functions along three profiles in Tibet. Kind and Yuan (2010) and Zhao et al. (2010) observed a simultaneous time delay in the 410 and 660-km discontinuity phases in northeast Tibet and interpreted it as the effect of velocity reduction in the upper mantle there. The low mantle velocity could indicate high temperature and, together with increased mantle anisotropy (Zhao et al., 2010; Kind and Yuan, 2010) and attenuation of the high frequency Sn propagation (Barazangi and Ni, 1982) in the area, is interpreted as an existence of a distinct Tibetan lithospheric block in this collision zone sandwiched by the Indian and Asian collision plates. The perturbation of the P410s phase along all three lines (red lines in Fig. 10) represent this anomalous mantle behavior by displaying a negative anomaly in the northern Tibeten plateau. The Sv velocity perturbation averaged over a depth range of 400 km (black lines in Fig. 10) presents a similar negative anomaly beneath the plateau, albeit the resolution and sensitivity are different. Along the east (R01) and central (R02) sections, the anomaly in both the perturbations of the P410s phase and that of the Vs is much stronger than along the west section (R03), which is in agreement of the lateral variation of the strongly deformed Tibetan lithospheric block.

Along all the sections we marked the positions of the Moho and LAB observed by Zhao et al. (2010) on the absolute velocity profiles derived by

the surface wave inversion (Fig. 10). Below the crust the high velocity mantle lithosphere often finds agreement with the line drawings of the receiver function LAB. This is the case for the Indian LAB, represented by the white dashed lines in the southern part of the sections. The Asian LAB, indicated by the dashed lines in the central and northern part of the sections, is only matching the high velocity body on east line (R01), but completely overseen by surface waves on central (R02) and west lines (R03). The hundreds of kilometers of lateral resolution might prevent surface waves from observing the fine structure seen by receiver functions. It is also possible that receiver functions do not see the base of the lithosphere, but a mid-lithospheric structure, as reported for the north America cratons (Abt et al., 2010; Kumar et al., 2012).

High velocity Indian plate has also been observed by body wave tomography (e.g., Li et al. (2008)), however, only continuously to beneath the southern most of the Tibetan plateau (see also Kind and Yuan (2010)). Most surface wave studies observed high mantle velocities over much of the plateau (e.g., Huang et al. (2003); Lebedev and Nolet (2003); Priestley et al. (2006, 2008)). This discrepancy was explained by different resolutions of the body wave and surface wave studies (Li et al., 2008; Priestley and Tilmann, 2009). Friederich (2003) is one of the few surface wave works, which observed low velocity zone in the upper 200 km beneath north Tibet. He interpreted it as evidence for convective removal of the mantle lithosphere proposed by Houseman et al. (1981). Our model shows a localized low velocity zone south of Tarim and Qaidam basins (see map at 125 km depth in Fig. 7). The low velocity zone, also observed by Feng and An (2010) and Feng et al. (2010), is constrained in our model in a much smaller area and is extending to a greater depth. We don't observe a large-scale low velocity mantle zone in north Tibet that can represent the upwelling of asthenosphere. The localized mantle low velocity zone marks the northern border of the overthickened Tibetan lithosphere, separating the Tibetan plateau from the Tarim basin and Tien Shan.

At the southern and northern edges of the Tibetan plateau there appear to be rapid changes in the depth of the high velocity mantle lithosphere (Fig. 8, section DD"). The Indian mantle lithosphere than underthrusts beneath the Tibetan plateau has a depth jump at the southern edge of the plateau and disconnects at the northern edge of the plateau to the Asian lithosphere. Starting from these two places two vertically striking high velocity streams exist in depth range of 200-400 km. This is more obvious in the absolute

velocity section. The high velocity stream at the southern edge of Tibet may represent a fraction of Indian mantle lithosphere that is subducting into deep mantle, as observed by body wave tomography citepLi2008. The high velocity body beneath Qaidam basin may indicate the position of the front of the underthrusting Indian lithosphere and represent either the bending and subsequently subduction of the Indian plate or the subduction of the Asian mantle lithosphere (Kind et al., 2002).

6. Conclusion

We derived 3-D upper mantle absolute shear wave velocities by modeling fundamental and higher mode waveforms of surface waves. We extended the multi-mode surface tomography of Eastern Asia of Priestley et al. (2006) by adding more permanent stations within China and constrained the study area to China and its close vicinity. The reduced inter-station distances enabled us to reduce the lateral smoothing by using a smaller Gaussian correlation length during the regionalization approach, thus increasing lateral resolution. We created a 3D S velocity model over China with a good resolution from the top of the upper mantle to a depth of ∼400 km. Compared to earlier studies, velocity anomalies are better and more sharply defined in the model. Similar to Priestley et al. (2006) the velocity perturbation decreases from ∼10% at shallow depths to ∼2% at depths of 300-400 km. Although synthetic recovery tests indicate that magnitude of anomalies below 200 km is not fully recovered, the reduction in percentage anomaly is too large to be explained by the reduced resolution alone. At 100-200 km depth the model is sensitive to the lateral variation of the thickness of the mantle lithosphere. The lithosphere is generally thinner in East China and thick in West China. The lithosphere reach a thickness of 200 km beneath the Pamir-Tibetan plateaus. Also observed as relatively thick lithosphere (>100km) are the Indian plate, Sichuan basin, Ordos block and Tarim basin. The lithosphere in the eastern part of the Yangtze craton is as thin as 70-80 km, whereas the lithosphere of the North China craton is too thin to be resolved. Beneath these two cratons we found evidence for large-scale mantle delamination that could explain the loss of the lithospheric root.

Acknowledgements: The work is funded by the Deutsche Forschungsgemeinschaft. Waveform data are provided by the Chinese Earthquake Network Centre, the IRIS and GEOFON data centres. We appreciate Marcelo Bianchi and James Mechie for the help of computation.

References

Abt, D. L., Fischer, K. M., French, S. W., Ford, H. A., Yuan, H., Romanowicz, B., Sep. 2010. North American lithospheric discontinuity structure imaged by Ps and Sp receiver functions. Journal of Geophysical Research 115 (B9), 1–24.

Ai, Y., Chen, Q. F., Zeng, F., Hong, X., Ye, W., Aug. 2007. The crust and upper mantle structure beneath southeastern China. Earth and Planetary Science Letters 260 (3-4), 549–563.

Anderson, D. L., 1995. Lithosphere, asthenosphere, and perisphere. Reviews of Geophysics 33 (1), 125.

Barazangi, M., Ni, J., 1982. Velocities and propagation characteristics of Pn and Sn beneath the Himalayan arc and Tibetan Plateau: Possible evidence for underthrusting of the Indian continental lithosphere beneath Tibet. Geology 10 (4), 179–185.

Barrell, J., 1914. The strength of the Earth's crust. The Journal of Geology 22 (7), 655–683.

Cara, M., Lévêque, J., 1987. Waveform inversion using secondary observables. Geophysical Research Letters 14 (10), 1046–1049.

Chen, L., Apr 2009. Lithospheric structure variations between the eastern and central North China Craton from S- and P-receiver function migration. Physics of the Earth and Planetary Interiors 173 (3-4), 216–227.

Chen, L., Tao, W., Zhao, L., Zheng, T., Mar 2008. Distinct lateral variation of lithospheric thickness in the Northeastern North China Craton. Earth and Planetary Science Letters 267 (1-2), 56–68.

Clark, M. K., Royden, L. H., Aug 2000. Topographic ooze: Building the eastern margin of Tibet by lower crustal flow. Geology 28 (8), 703–706.

Curtis, A., Trampert, J., Snieder, R., Dost, B., 1998. Eurasian fundamental mode surface wave phase velocities and their relationship with tectonic structures. Journal of Geophysical Research 103 (B11), 26919–26947.

Debayle, E., Jun 1999. SV-wave azimuthal anisotropy in the Australian upper mantle: preliminary results from automated Rayleigh waveform inversion. Geophysical Journal International 137 (3), 747–754.

Debayle, E., Kennett, B. L. N., 2000. The Australian continental upper mantle: Structure and deformation inferred from surface waves. Journal of Geophysical Research 105 (B11), 25423–25450.

Debayle, E., Lévêque, J. J., Cara, M., Dec 2001. Seismic evidence for a deeply rooted low-velocity anomaly in the upper mantle beneath the northeastern Afro/Arabian continent. Earth and Planetary Science Letters 193 (3-4), 423–436.

Eaton, D. W., Darbyshire, F., Evans, R. L., Grütter, H., Jones, A. G., Yuan, X., Apr 2009. The elusive lithosphere–asthenosphere boundary (LAB) beneath cratons. Lithos 109 (1-2), 1–22.

Engdahl, E. R., Hilst, R. V. D., 1998. Global teleseismic earthquake relocation with improved travel times and procedures for depth determination. Bulletin of the 88 (3), 722–743.

Feng, M., An, M., Jun 2010. Lithospheric structure of the Chinese mainland determined from joint inversion of regional and teleseismic Rayleigh-wave group velocities. Journal of Geophysical Research 115 (B6), 1–16.

Feng, M., Lee, S. v. d., An, M., Zhao, Y., Nov 2010. Lithospheric thickness, thinning, subduction, and interaction with the asthenosphere beneath China from the joint inversion of seismic S-wave train fits and Rayleigh-wave dispersion curves. Lithos 120 (1-2), 116–130.

Friederich, W., Apr 2003. The S -velocity structure of the East Asian mantle from inversion of shear and surface waveforms. Geophysical Journal International 153 (1), 88–102.

Griffin, W. L., Andi, Z., O'Reilly, S. Y., Ryan, C. G., 1998. Phanerozoic evolution of the lithosphere beneath the Sino-Korean craton. In: Flower, M. F. J., Chung, S. L., Lo, C. H., Lee, T. Y. (Eds.), Mantle Dynamics and Plate Interactions in East Asia. Vol. 27 of Geodynamics Series. American Geophysical Union, Washington, D. C., pp. 107–126.

Griot, D. A., Montagner, J. P., Tapponnier, P., 1998. Phase velocity structure from Rayleigh and Love waves in Tibet and its neighboring regions. Journal of Geophysical Research 103 (B9), 21215–21232.

Heintz, M., Debayle, E., Vauchez, A., Aug 2005. Upper mantle structure of the South American continent and neighboring oceans from surface wave tomography. Tectonophysics 406 (1-2), 115–139.

Heit, B., Yuan, X., Bianchi, M., Kind, R., Gossler, J., Oct 2010. Study of the lithospheric and upper-mantle discontinuities beneath eastern Asia by SS precursors. Geophysical Journal International 183 (1), 252–266.

Helffrich, G., 2000. Topography of the transition zone seismic discontinuities. Reviews of Geophysics 38 (1), 141.

Houseman, G. A., McKenzie, D. P., Molnar, P., 1981. Convective instability of a thickened boundary layer and its relevance for the thermal evolution of continental convergent belts. Journal of Geophysical Research 86 (B7), 6115–6132.

Huang, T. K., Jen, C., Jiang, C., Chang, Z., Chin, D., 1980. The Geotectonic Evolution of China. Academic Publishing House, Beijing, China, 124.

Huang, Z., Li, H., Zheng, Y., Peng, Y., Oct 2009. The lithosphere of North China Craton from surface wave tomography. Earth and Planetary Science Letters 288 (1-2), 164–173.

Huang, Z., Su, W., Peng, Y., Zheng, Y., Li, H., 2003. Rayleigh wave tomography of China and adjacent regions. Journal of Geophysical Research 108 (B2).

Huang, Z., Wang, L., Zhao, D., Xu, M., Mi, N., Yu, D., Li, H., Li, C., Oct. 2010. Upper mantle structure and dynamics beneath Southeast China. Physics of the Earth and Planetary Interiors 182 (3-4), 161–169.

Kind, R., Yuan, X., Sep. 2010. Seismic images of the biggest crash on Earth. Science (New York, N.Y.) 329 (5998), 1479–80.

Kind, R., Yuan, X., Saul, J., Nelson, D., Sobolev, S. V., Mechie, J., Zhao, W., Kosarev, G., Ni, J., Achauer, U., Jiang, M., Nov 2002. Seismic images of crust and upper mantle beneath Tibet: evidence for Eurasian plate subduction. Science (New York, N.Y.) 298 (5596), 1219–21.

Kumar, P., Kind, R., Yuan, X., Mechie, J., May 2012. US Array Receiver Function Images of the Lithosphere-Asthenosphere Boundary. Seismological Research Letters 83 (3), 486–491.

Kusky, T. M., Windley, B. F., Zhai, M. G., Jan. 2007. Tectonic evolution of the North China Block: from orogen to craton to orogen. Geological Society, London, Special Publications 280 (1), 1–34.

Kustowski, B., Ekström, G., Dziewoński, A. M., Sep 2008. The shear-wave velocity structure in the upper mantle beneath Eurasia. Geophysical Journal International 174 (3), 978–992.

Lebedev, S., Nolet, G., 2003. Upper mantle beneath Southeast Asia from S velocity tomography. Journal of Geophysical Research 108 (B1).

Lévêque, J. J., Cara, M., Rouland, D., Apr 1991. Waveform inversion of surface wave data: test of a new tool for systematic investigation of upper mantle structures. Geophysical Journal International 104 (3), 565–581.

Lévêque, J. J., Rivera, L., Wittlinger, G., Oct 1993. On the use of the checkerboard test to assess the resolution of tomographic inversions. Geophysical Journal International 115 (1), 313–318.

Li, C., Hilst, V. D. D., R., Meltzer, A. S., Engdahl, E. R., Sep 2008. Subduction of the Indian lithosphere beneath the Tibetan Plateau and Burma. Earth and Planetary Science Letters 274 (1-2), 157–168.

Li, S., Mooney, W., Fan, J., Jun 2006. Crustal structure of mainland China from deep seismic sounding data. Tectonophysics 420 (1-2), 239–252.

Liu, M., Yang, Y., Shen, Z., Wang, S., 2007. Active tectonics and intracontinental earthquakes in China: The kinematics and geodynamics. Special Papers - Geological Society of America 2425 (19), 299–318.

Ma, X., May 1987. Summary of the Lithospheric Dynamics in China. Acta Geologica Sinica-English 61 (2), 15–29.

Ma, X., Liu, G., Su, J., 1984. The structure and dynamics of the continental lithosphere in north-northeast China. Annales geophysicae 2 (6), 611–620.

McKenzie, D., Jackson, J., Priestley, K., May 2005. Thermal structure of oceanic and continental lithosphere. Earth and Planetary Science Letters 233 (3-4), 337–349.

Menzies, M. A., Xu, Y. G., 1998. Geodynamics of the North China Craton. In: Flower, M. F. J., Chung, S. L., Lo, C. H., Lee, T. Y. (Eds.), Mantle Dynamics and Plate Interactions in East Asia. Vol. 27 of Geodynamics Series. American Geophysical Union, Washington, D. C., pp. 155–165.

Montagner, J. P., 1986. Regional three-dimensional structures using long-period surface waves. Annales geophysicae. Series B. Terrestrial and planetary physics 4 (3), 283–294.

Nataf, H. C., Ricard, Y., May 1996. 3SMAC: an a priori tomographic model of the upper mantle based on geophysical modeling. Physics of the Earth and Planetary Interiors 95 (1-2), 101–122.

Obrebski, M., Allen, R. M., Zhang, F., Pan, J., Wu, Q., Hung, S. H., Jan 2012. Shear wave tomography of China using joint inversion of body and surface wave constraints. Journal of Geophysical Research 117 (B1), 1–15.

Pilidou, S., Priestley, K., Gudmundsson, O., Debayle, E., Dec 2004. Upper mantle S -wave speed heterogeneity and anisotropy beneath the North Atlantic from regional surface wave tomography: the Iceland and Azores plumes. Geophysical Journal International 159 (3), 1057–1076.

Priestley, K., Debayle, E., McKenzie, D., Pilidou, S., Oct 2006. Upper mantle structure of eastern Asia from multimode surface waveform tomography. Journal of Geophysical Research 111 (B10), 1–20.

Priestley, K., McKenzie, D., Debayle, E., Pilidou, S., Dec. 2008. The African upper mantle and its relationship to tectonics and surface geology. Geophysical Journal International 175 (3), 1108–1126.

Priestley, K., Tilmann, F., Apr 2009. Relationship between the upper mantle high velocity seismic lid and the continental lithosphere. Lithos 109 (1-2), 112–124.

Ritzwoller, M. H., Levshin, A. L., 1998. Eurasian surface wave tomography: Group velocities. Journal of Geophysical Research 103 (B3), 4839–4878.

Romanowicz, B. A., 1982. Constraints on the structure of the Tibet Plateau from pure path phase velocities of Love and Rayleigh waves. Journal of Geophysical Research 87 (B8), 6865–6883.

Royden, L. H., Burchfiel, B. C., van der Hilst, R. D., Aug 2008. The geological evolution of the Tibetan Plateau. Science 321 (5892), 1054–8.

Shearer, P. M., 1991. Constraints on upper mantle discontinuities from observations of long-period reflected and converted phases. Journal of Geophysical Research 96 (B11), 18147.

Sieminski, A., Lévêque, J. J., Debayle, E., October 2004. Can finite-frequency effects be accounted for in ray theory surface wave tomography ? Geophysical Research Letters 31, 1–4.

Sodoudi, F., Yuan, X., Liu, Q., Kind, R., Chen, J., Sep 2006. Lithospheric thickness beneath the Dabie Shan, central eastern China from S receiver functions. Geophysical Journal International 166 (3), 1363–1367.

Takeuchi, H., Saito, M., 1972. Seismic surface waves. In: Bolt, B. A. (Ed.), Seismology: Surface Waves and Earth Oscillations. Vol. 11 of Methods In Computational Physics. Academic Press, San Diego, Calif., pp. 217–295.

Tarantola, A., Valette, B., 1982. Generalized nonlinear inverse problems solved using the least squares criterion. Reviews of Geophysics 20 (2), 219.

Wesnousky, S. G., Jones, L. M., Scholz, C. H., Deng, Q., 1984. Historical seismicity and rates of crustal deformation along the margins of the Ordos block, north China. Bulletin of the . . . 74 (5), 1767–1783.

Windley, B. F., Alexeiev, D., Xiao, W., 2007. Tectonic models for accretion of the Central Asian Orogenic Belt. Journal of the Geological Society London 164 (2004), 31–47.

Woodhouse, J. H., Jun. 1974. Surface Waves in a Laterally Varying Layered Structure. Geophysical Journal International 37 (3), 461–490.

Xu, Y. G., Jun. 2007. Diachronous lithospheric thinning of the North China Craton and formation of the Daxin'anling–Taihangshan gravity lineament. Lithos 96 (1-2), 281–298.

Yin, A., Harrison, T. M., May 2000. Geologic Evolution of the Himalayan-Tibetan Orogen. Annual Review of Earth and Planetary Sciences 28 (1), 211–280.

Zhang, Z., Yang, L., Teng, J., Badal, J., Jan 2011. An overview of the earth crust under China. Earth-Science Reviews 104 (1-3), 143–166.

Zhao, J., Yuan, X., Liu, H., Kumar, P., Pei, S., Kind, R., Zhang, Z., Teng, J., Ding, L., Gao, X., Xu, Q., Wang, W., Jun 2010. The boundary between the Indian and Asian tectonic plates below Tibet. Proceedings of the National Academy of Sciences of the United States of America 107 (25), 11229–33.

Figure 1 : Topography map of China and the adjacent regions with major tectonic units. Red and blue lines define borders of major tectonic units. Black dashed line denotes the North-South Gravity Lineament (Xu, 2007). Abbreviation are: SGFS, Songpan-Ganzi fold system; QFS, Qinling fold system; QDFS, Qing-Dabie fold system; SB, Sichuan basin; OB, Ordos block; KF, Kunlun fault; JRS, Jinsha-River suture; BNS, Bangong-Nujiang suture, YZS, Yarlung-Zangbu suture.

Figure 2 : Map of stations and Ray coverage. Triangles denote the seismic stations used in the study. The path density, coded by colors, is defined by number of paths crossing a grid of $2^\circ \times 2^\circ$. The path density is over 200 in the most of the area.

Figure 3 : Rayleigh wave sensitivities as a function of depth at different periods for the fundamental and the 4 higher modes.

Figure 4 : Path length distribution.

Figure 5 : Flat model resolution tests. (a) Average final model (red) and the two models (green and blue) for the flat model resolution test. (b) Result of the 5% flat model test. (c) Result of the 15% flat model test.

Figure 6 : Horizontal and vertical slices of the checker board resolution test. Alternating high and low velocity perturbations with a size of 500×500 km in horizontal and 100 km in depth and a magnitude of 6% are separated by zero-anomaly background in the input model.

Figure 7 : Horizontal sections of the Sv-velocity perturbations at depths of 100, 125, 150, 175, 200 and 300 km. The percentage of the anomalies for depths of 100-175 km and for depths of 200-300 are denoted by different scales. Where the crust is thicker than about 60 km in the 3SMAC model, the perturbations in the 100 km slice partly reflect the starting model. Azimuthal anisotropy is presented by the short black lines on the maps denoting the fast directions of the shear wave speed. Locations of the 6 profiles shown in Figure 8 are indicated on the map of 100 km depth. Gray lines mark borders of major tectonic units from Figure 1. Green dashed line denotes the North-South Gravity Lineament.

Figure 8 : Cross-sections of Sv velocity perturbation and absolute velocity along 3 EW lines A-C and 3 NS lines D-F. Locations of the profiles are indicated in Fig. 7. Color scales for relative and absolute velocities are indicated at the bottom. Surface topography is plotted on top of each profile with major tectonic units indicated. Black dots denote the relocated earthquakes from the EHB catalog (Engdahl and Hilst, 1998) within 100 km either side of the profile. In DD", dashed lines mark the base of the Indian and Asian mantle lithosphere; arrows indicate vertical lithospheric streams. The delaminated lithosphere below Songliao basin, NCC and YC is enclosed by dashed lines in CC" and FF". The dashed line at 80 km depth below SCFS and YC denotes the visible thin lithosphere. Abbreviations: QFS, Qilian fold system; CAOB, Central Asia Orogenic Belt; SCFS, South China fold system; YC, Yangtze craton; NCC, North China craton.

Figure 9 : Comparison of the upper mantle model with a SS precursor profile (Heit et al., 2010). (A) Location of the SS precursor profile, along with three receiver function profiles shown in Fig. 10. (B) Comparison of average upper mantle velocity along the profile derived by the surface wave inversion (black line) and the perturbation of the S410S time (red line). (C) Upper mantle absolute velocities along the profile. (D) Velocity perturbations along the profile.

Figure 10 : Comparison of the upper mantle model with three RF profiles in Tibet (Zhao et al., 2010). Along each profile, the upper panel shows the comparison of average upper mantle velocity along the profile derived by the surface wave inversion (black line) and the perturbation of the P410s time (red line) and the lower panel shows the upper mantle absolute velocities along the profile. Locations of the Moho and the LAB derived by receiver functions from Zhao et al. (2010) are indicated in the velocity profiles.

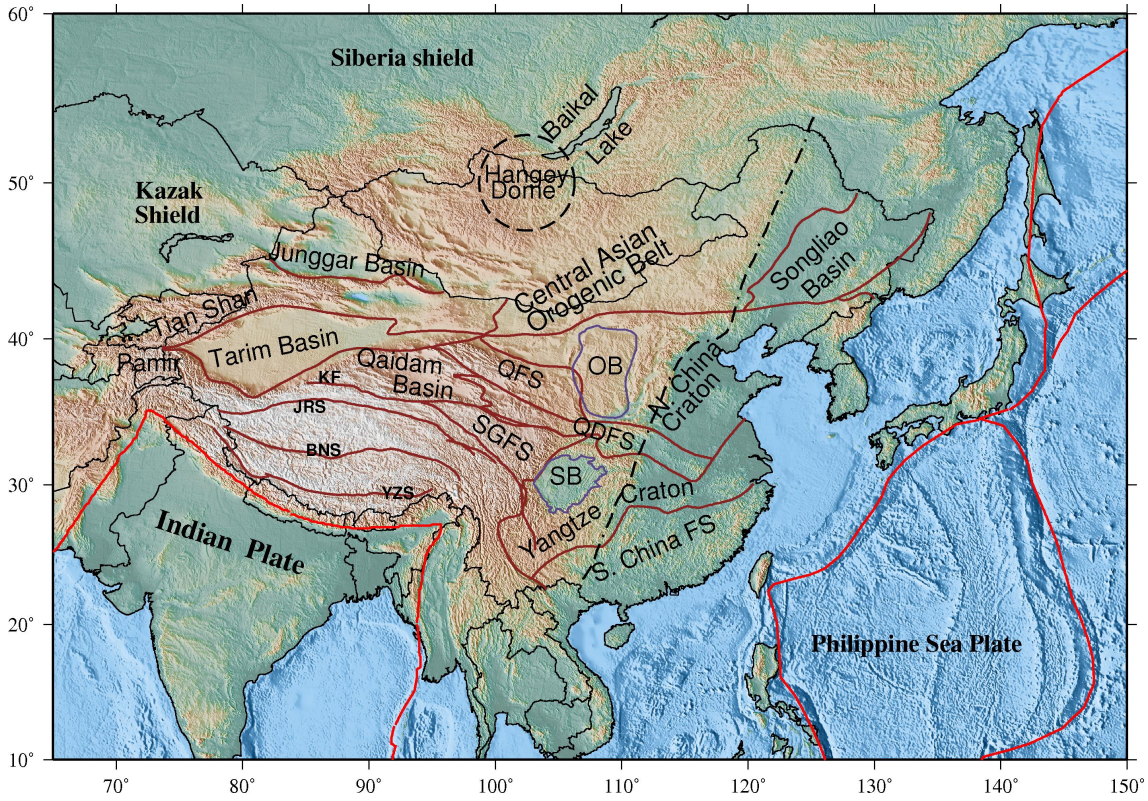
Siberia shield
Baikal
Lake
Hangey
Dome
Kazak
Shield
Junggar Basin
Central Asian
Orogenic Belt
Songliao
Basin
Tian Shan
Tarim Basin
Pamir
Qaidam
Basin
KF
JRS
BNS
YZS
QFS
OB
N. China
Craton
SGFS
QDFS
SB
Craton
Yangtze
S. China FS
Indian Plate
Philippine Sea Plate
60°
50°
40°
30°
20°
10°
70°
80°
90°
100°
110°
120°
130°
140°
150°

Fig. 1

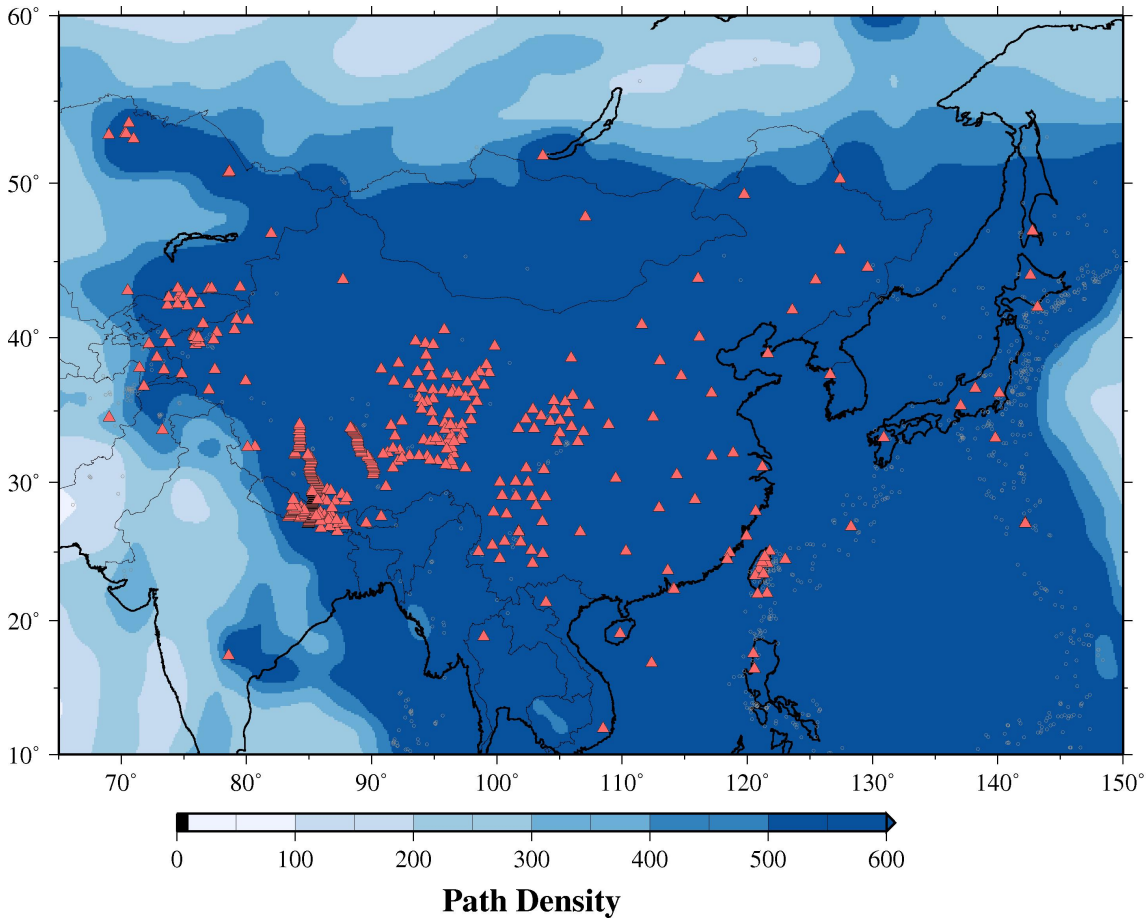
60°
50°
40°
30°
20°
10°
70°
80°
90°
100°
110°
120°
130°
140°
150°
0
100
200
300
400
500
600
Path Density

Fig. 2

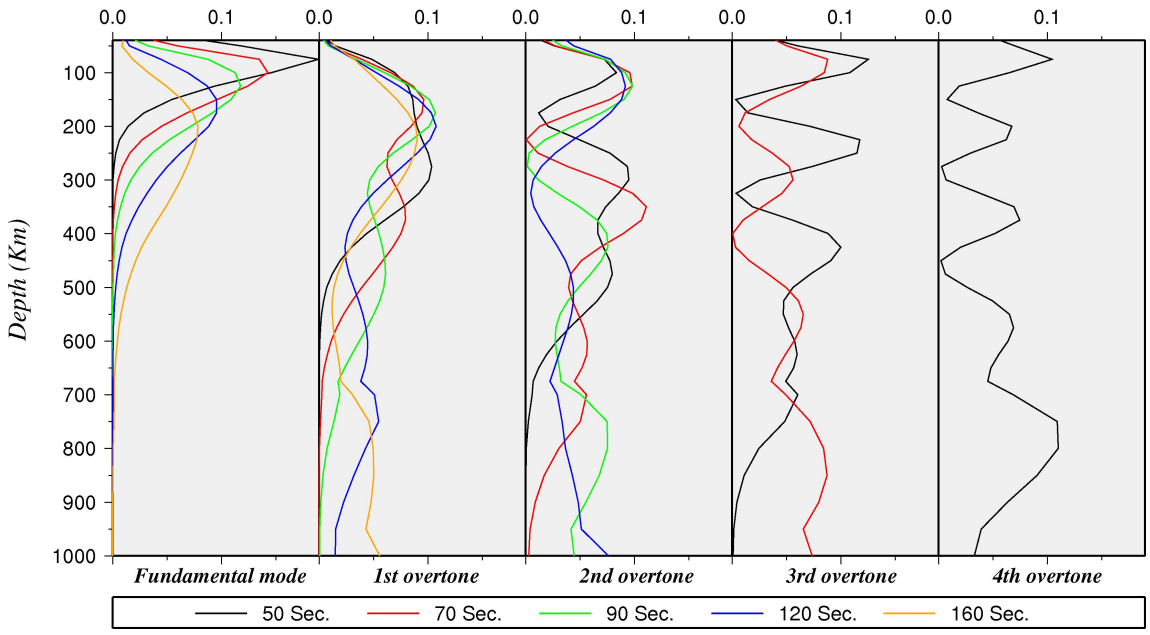
0.0
0.1
0.0
0.1
0.0
0.1
0.0
0.1
0.0
0.1
100
200
300
400
500
600
700
800
900
1000
Depth (Km)
Fundamental mode
1st overtone
2nd overtone
3rd overtone
4th overtone
50 Sec.
70 Sec.
90 Sec.
120 Sec.
160 Sec.

Fig. 3

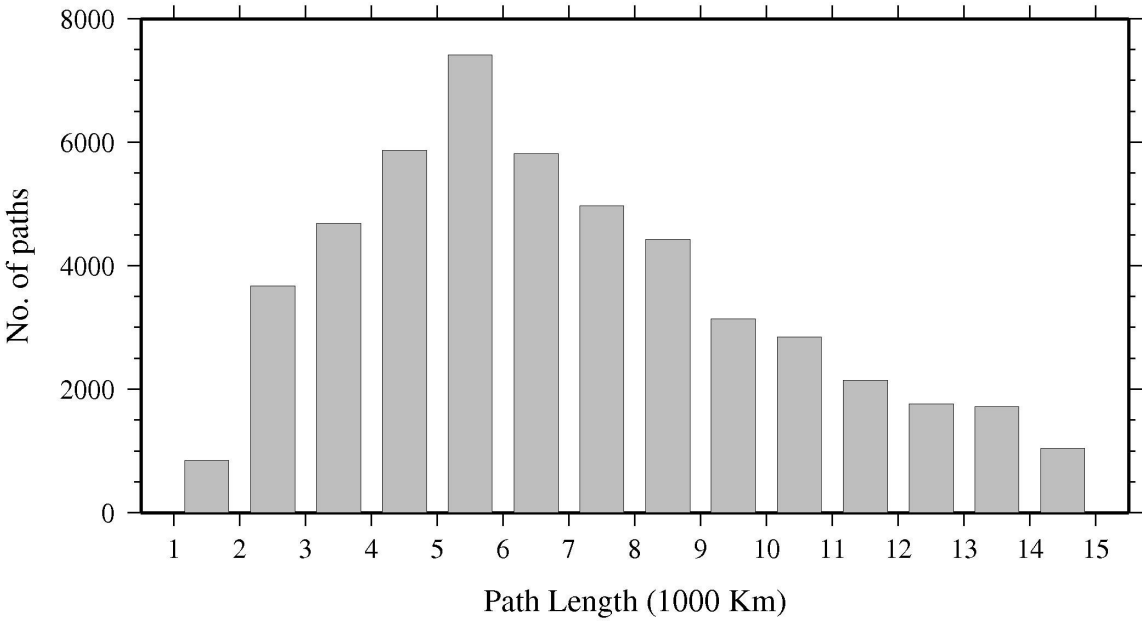
8000
6000
4000
2000
0
No. of paths
1
2
3
4
5
6
7
8
9
10
11
12
13
14
15
Path Length (1000 Km)

Fig. 4

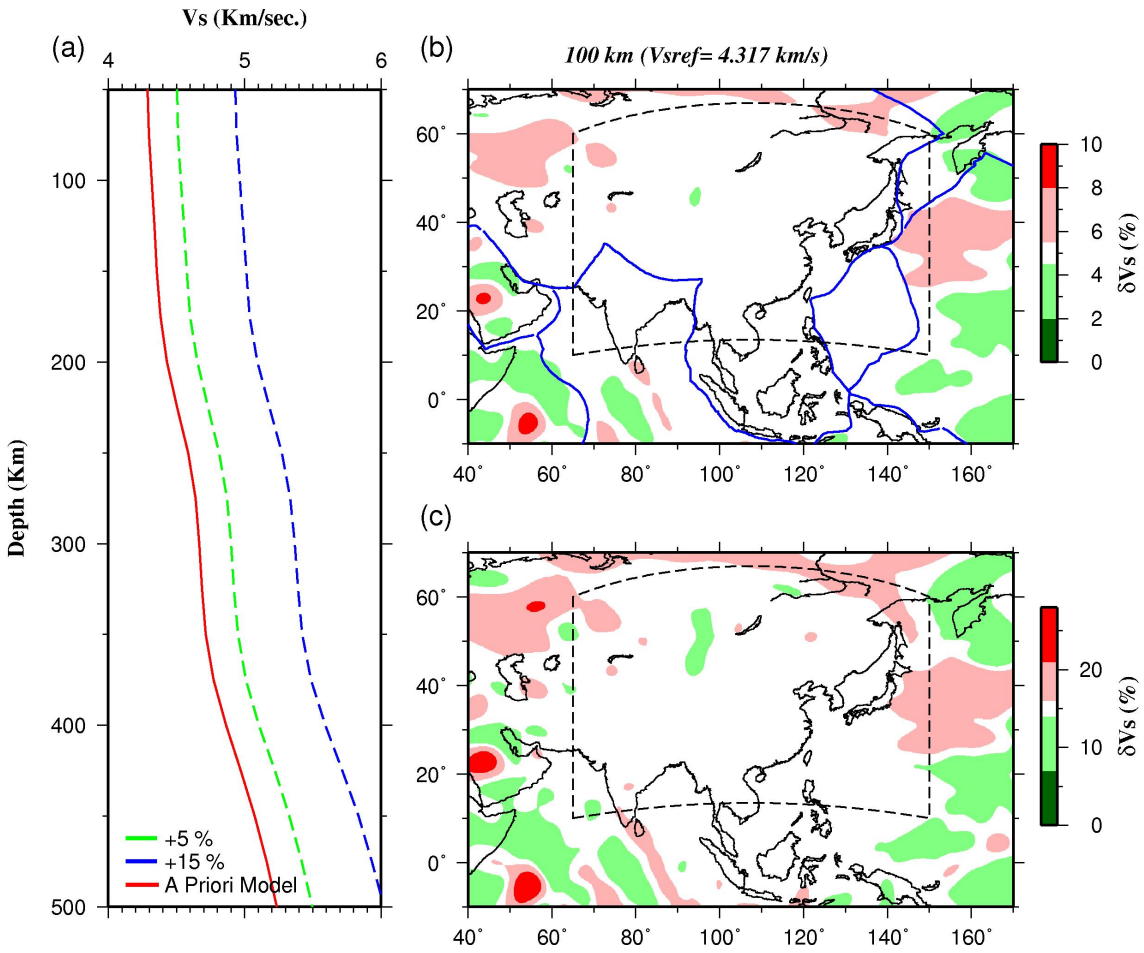
(a)
Vs (Km/sec.)
4
5
6
Depth (Km)
100
200
300
400
500
+5 %
+15 %
A Priori Model
(b)
100 km (Vsref= 4.317 km/s)
60˚
40˚
20˚
0˚
40˚
60˚
80˚
100˚
120˚
140˚
160˚
10
8
6
4
2
0
δVs (%)
(c)
60˚
40˚
20˚
0˚
40˚
60˚
80˚
100˚
120˚
140˚
160˚
20
10
0
δVs (%)

Fig. 5

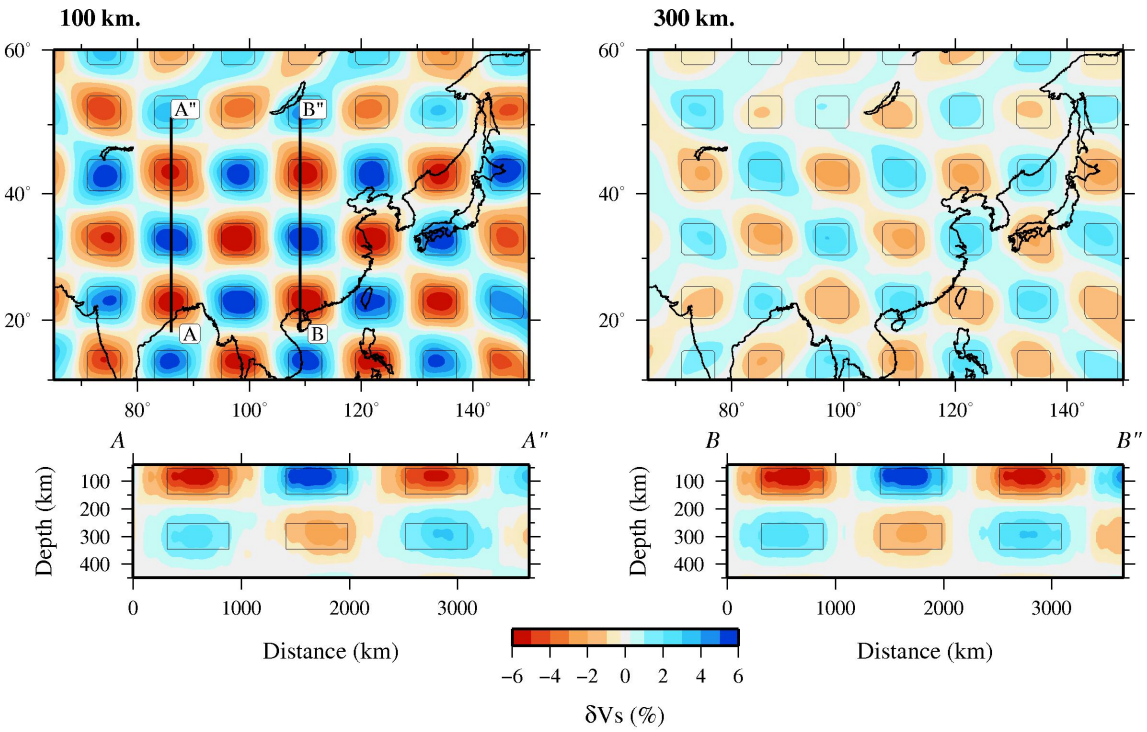
100 km.
300 km.
60°
40°
20°
80°
100°
120°
140°
A"
B"
A
B
A
A"
B
B"
Depth (km)
100
200
300
400
0
1000
2000
3000
Distance (km)
−6 −4 −2 0 2 4 6
δVs (%)

Fig. 6

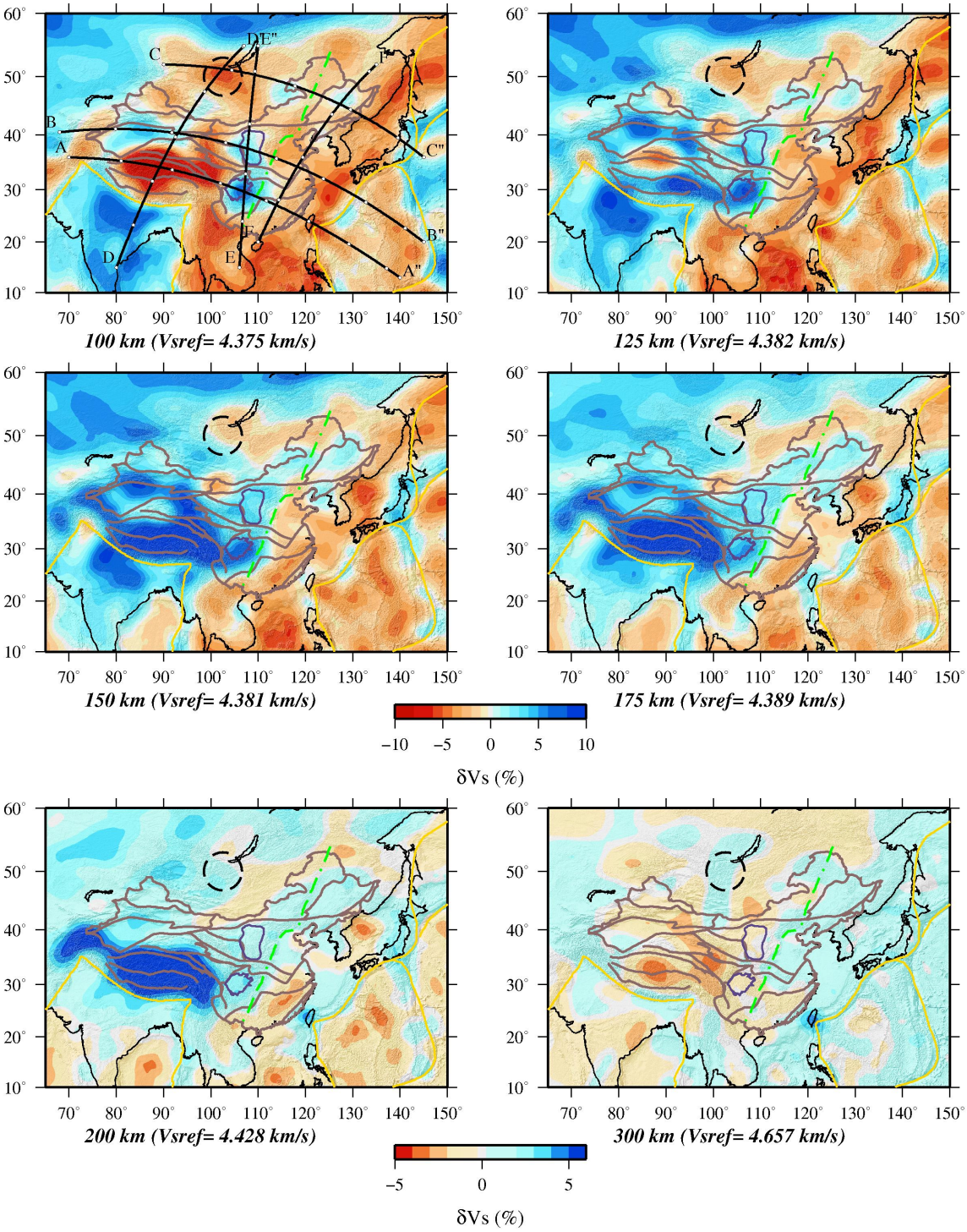
100 km (Vsref= 4.375 km/s)
125 km (Vsref= 4.382 km/s)
150 km (Vsref= 4.381 km/s)
175 km (Vsref= 4.389 km/s)
200 km (Vsref= 4.428 km/s)
300 km (Vsref= 4.657 km/s)
δVs (%)
δVs (%)

Fig. 7

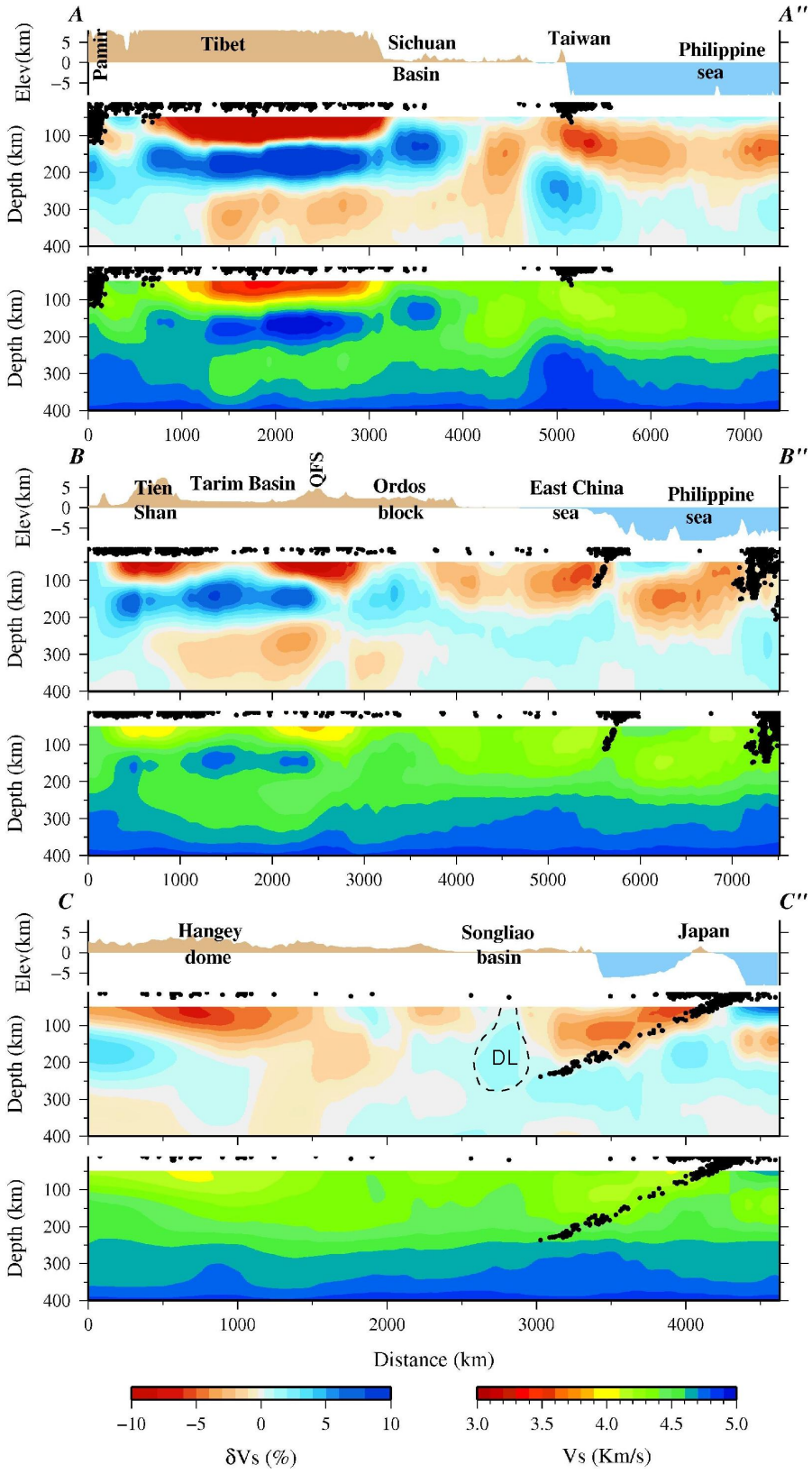
A
A''
Elev(km)
Pamir
Tibet
Sichuan
Basin
Taiwan
Philippine
sea
Depth (km)
B
B''
Tien
Shan
Tarim Basin
QFS
Ordos
block
East China
sea
Philippine
sea
C
C''
Hangey
dome
Songliao
basin
Japan
DL
Distance (km)
δVs (%)
Vs (Km/s)

Fig. 8

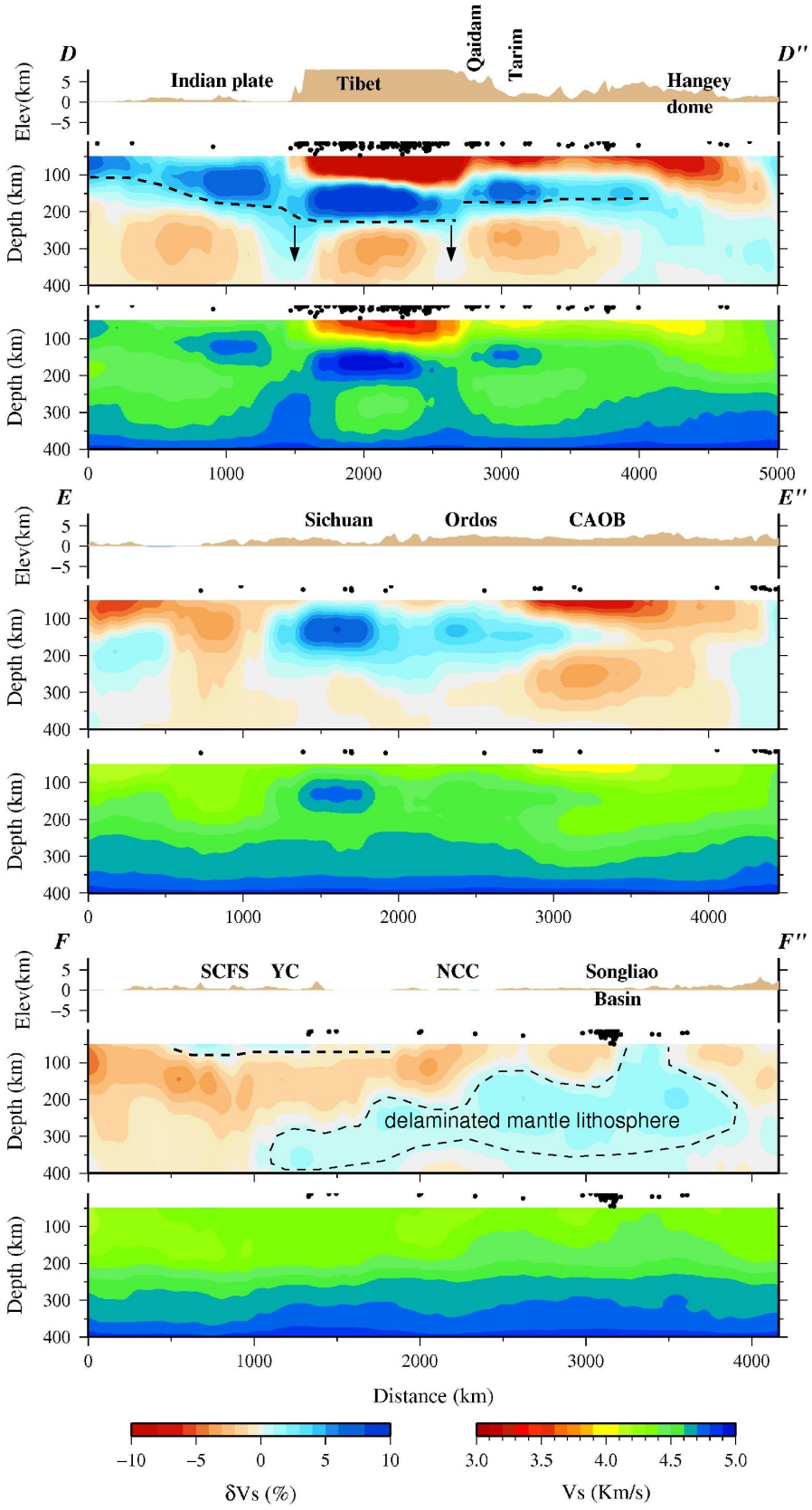

Fig. 8, continued

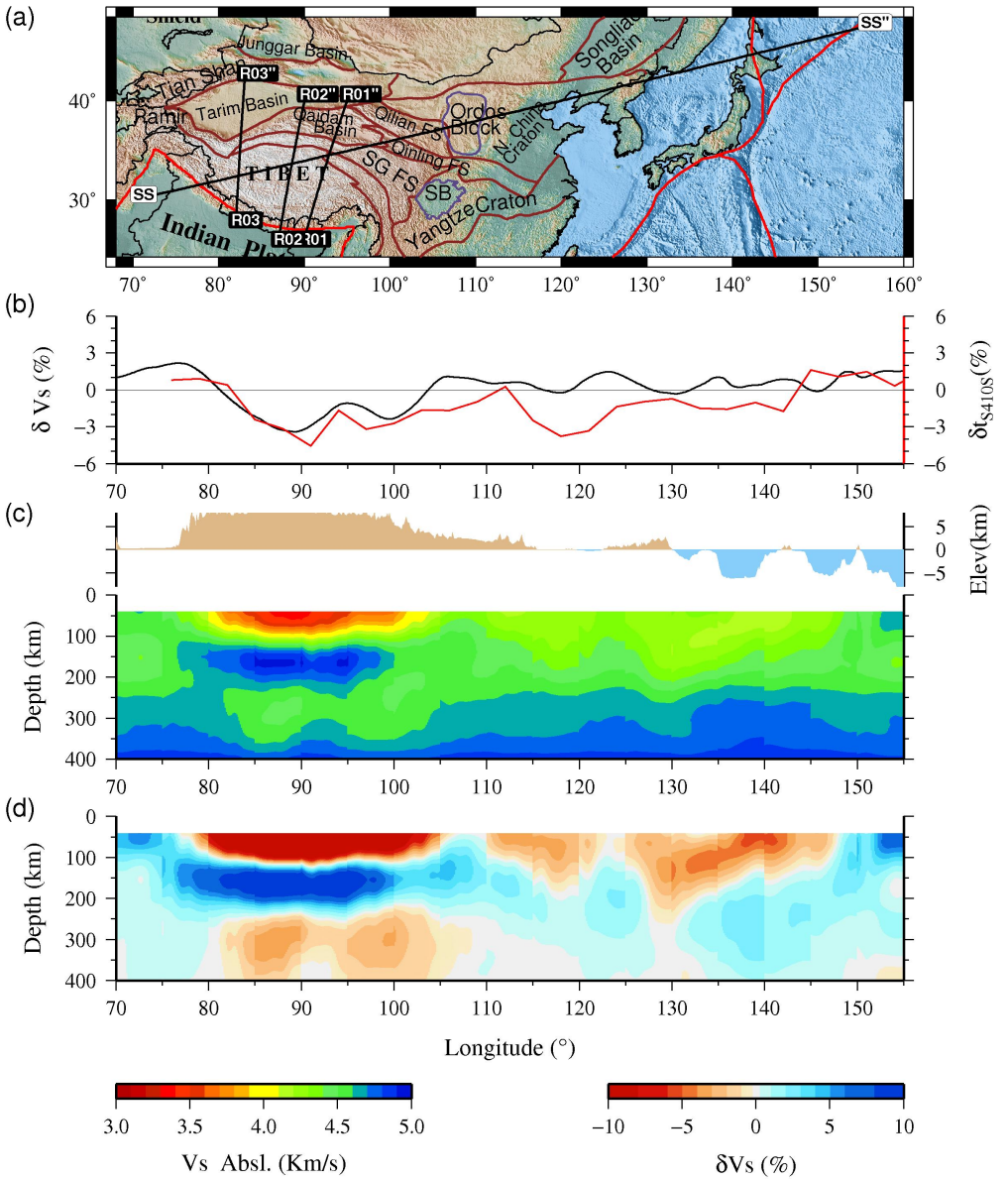
(a)
Junggar Basin
Tian Shan
Songliao Basin
R03"
R02"
R01"
Tarim Basin
Ramlr
Qaidam Basin
Qilian Fs
Ordos Block
N. China Craton
Qinling Fs
SG FS
SB
TIBET
SS
SS"
R03
R02
R01
Yangtze Craton
Indian Plate
40°
30°
70°
80°
90°
100°
110°
120°
130°
140°
150°
160°
(b)
δ Vs (%)
δt_S410S(%)
(c)
Elev(km)
Depth (km)
(d)
Depth (km)
Longitude (°)
Vs Absl. (Km/s)
δVs (%)

Fig. 9

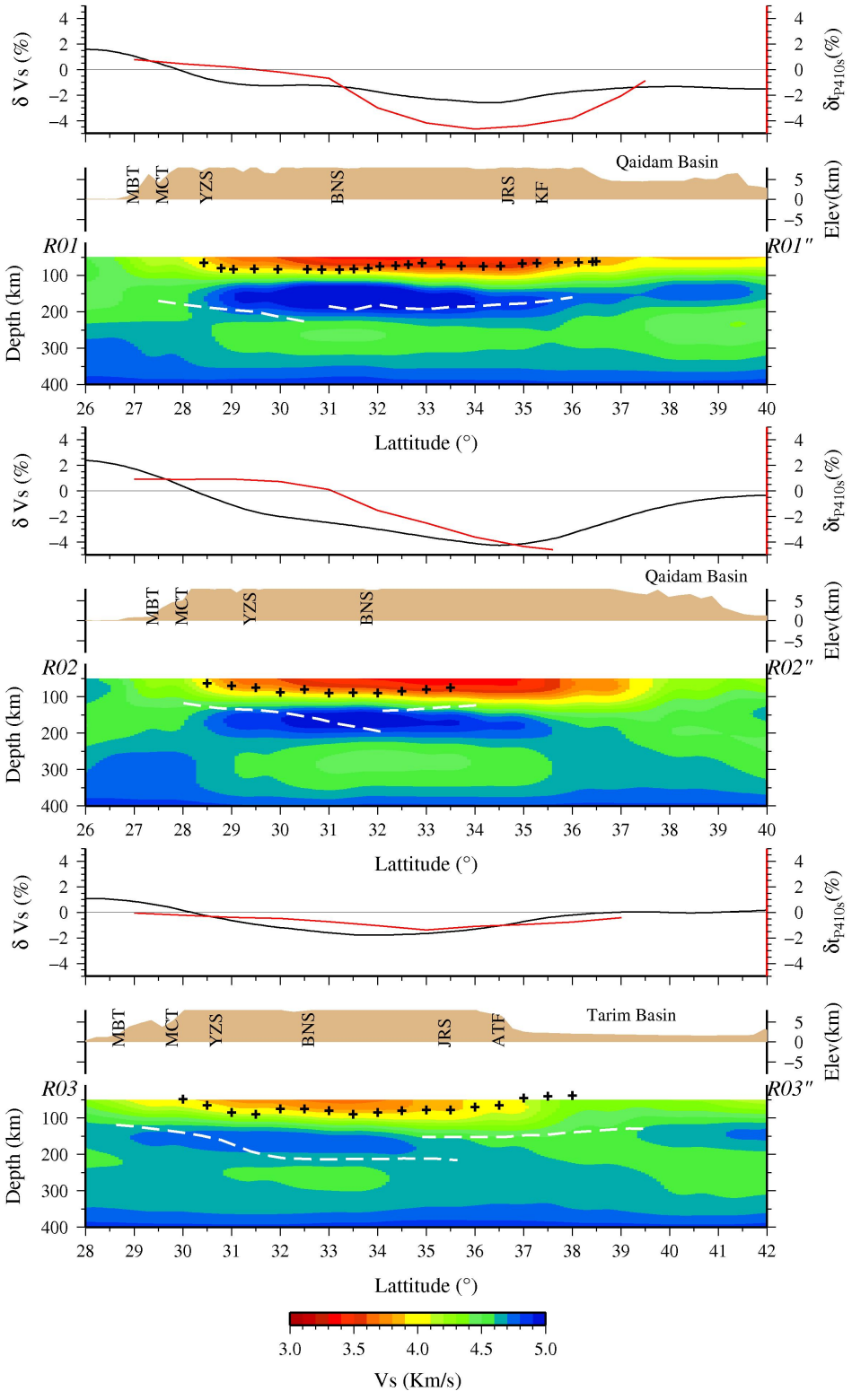
δ Vs (%)
δtP410s(%)
Qaidam Basin
MBT
MCT
YZS
BNS
JRS
KF
Elev(km)
R01
R01″
Depth (km)
Lattitude (°)
R02
R02″
Tarim Basin
ATF
R03
R03″
3.0
3.5
4.0
4.5
5.0
Vs (Km/s)

Fig. 10

Supplementary Figures

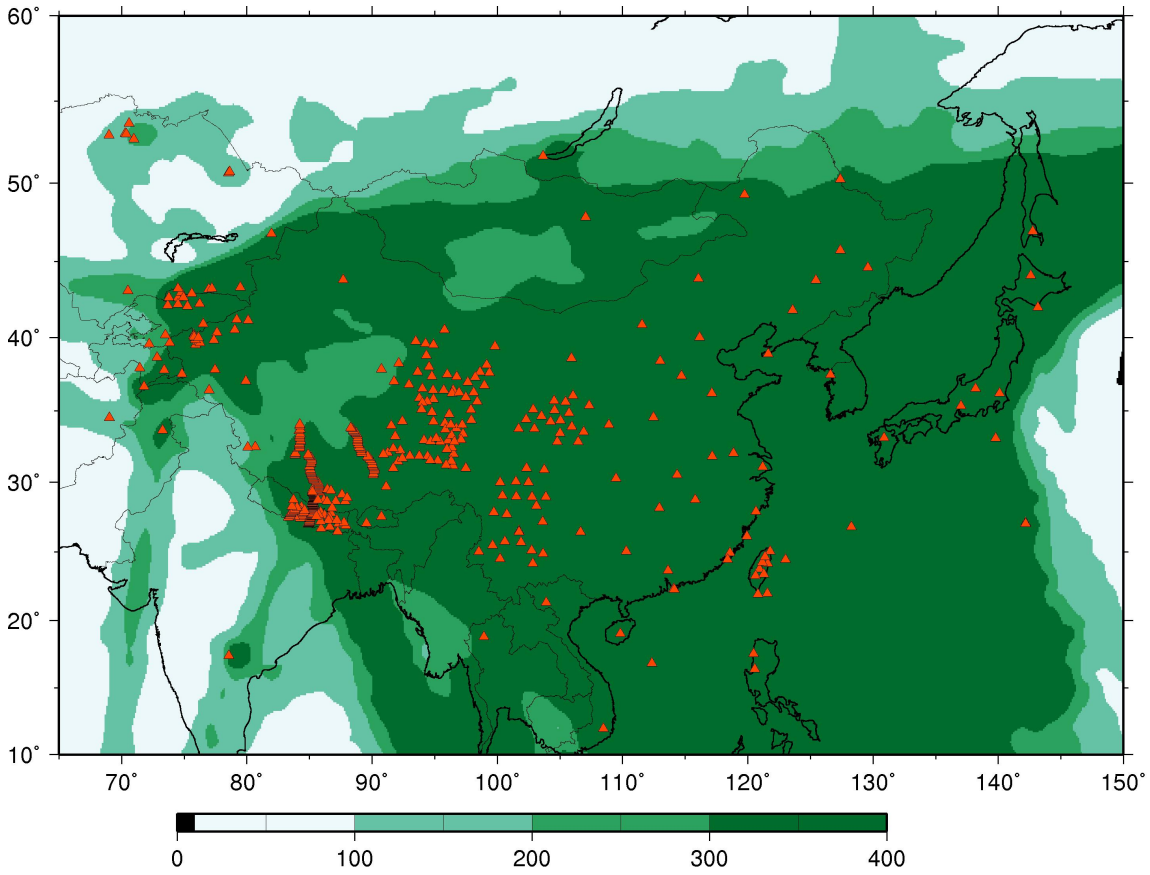

Fig. S1: Similar to the path density map of Fig. 1 in the main text but excluding paths longer than 60°.

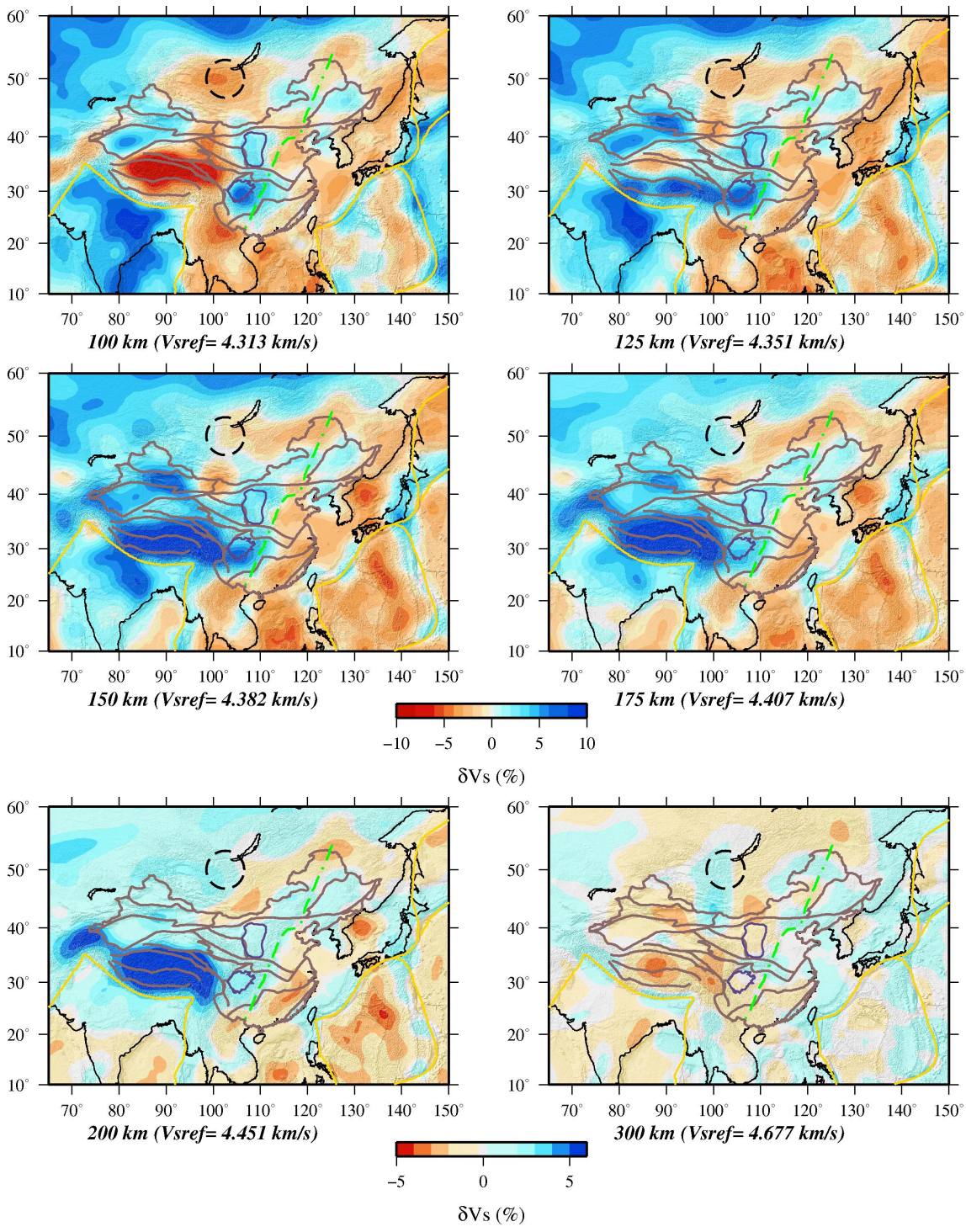

Fig. S2: Horizontal slices of the inversion using paths shorter than 60°.

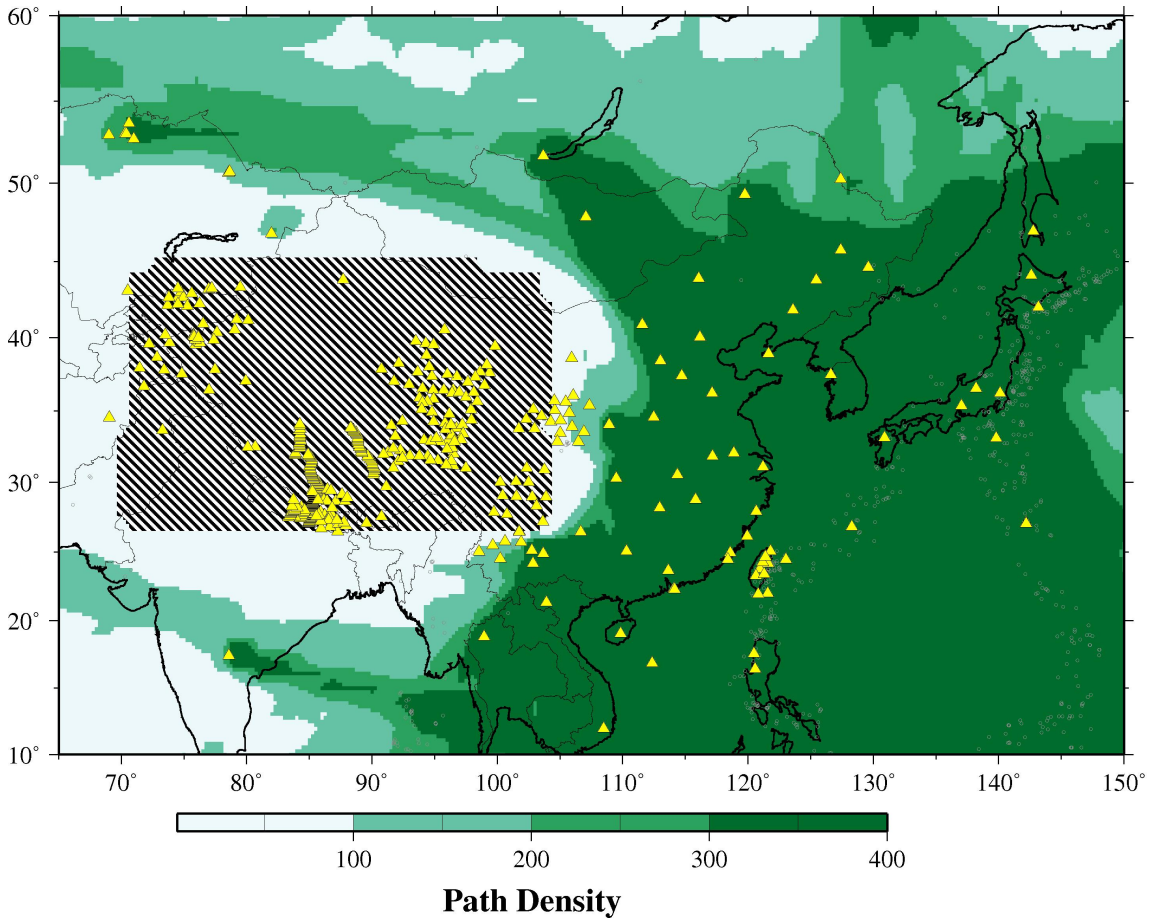

Fig. S3: Path density map excluding paths passing through western part of China where the crust is thicker than 50 km.

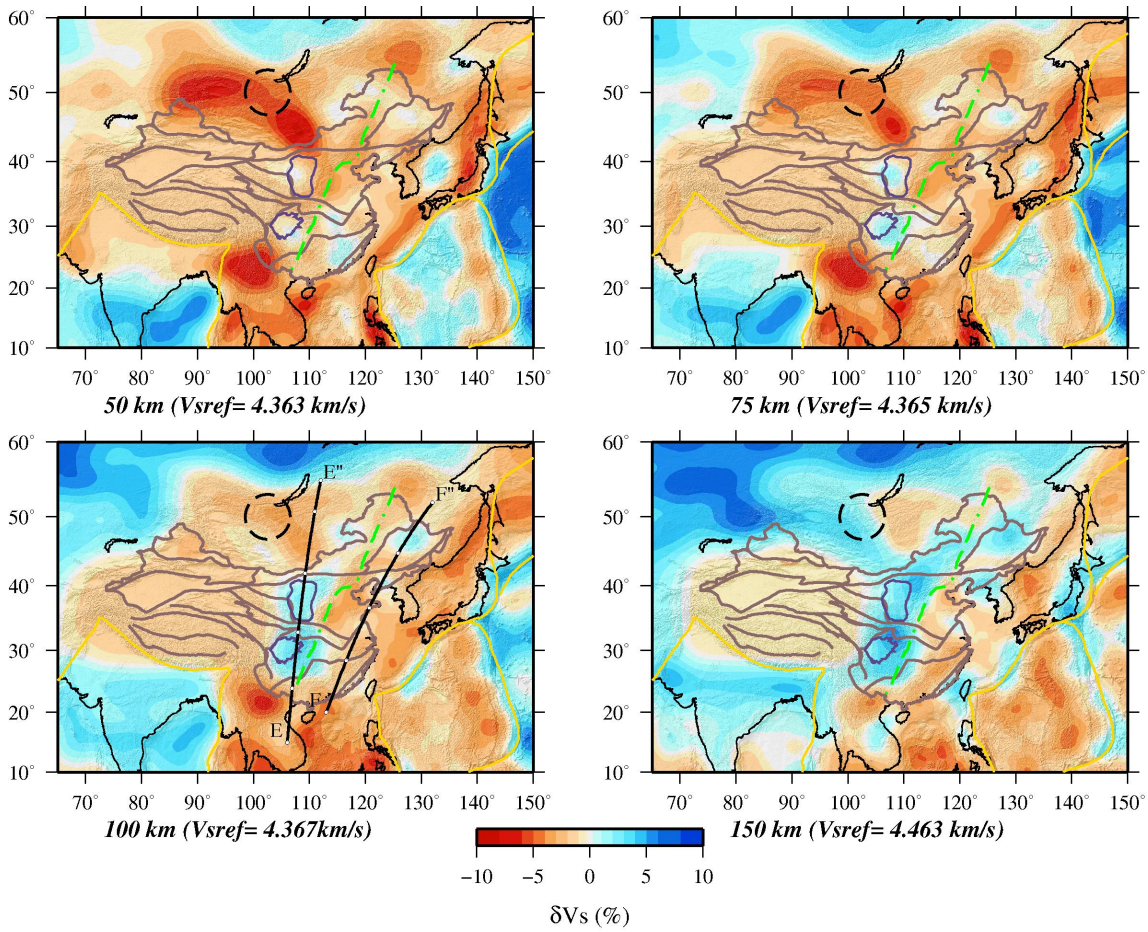

Fig. S4: Horizontal sections of the 3D inversion at different depths using data excluding paths passing through western part of China where the crust is thicker than 50 km.

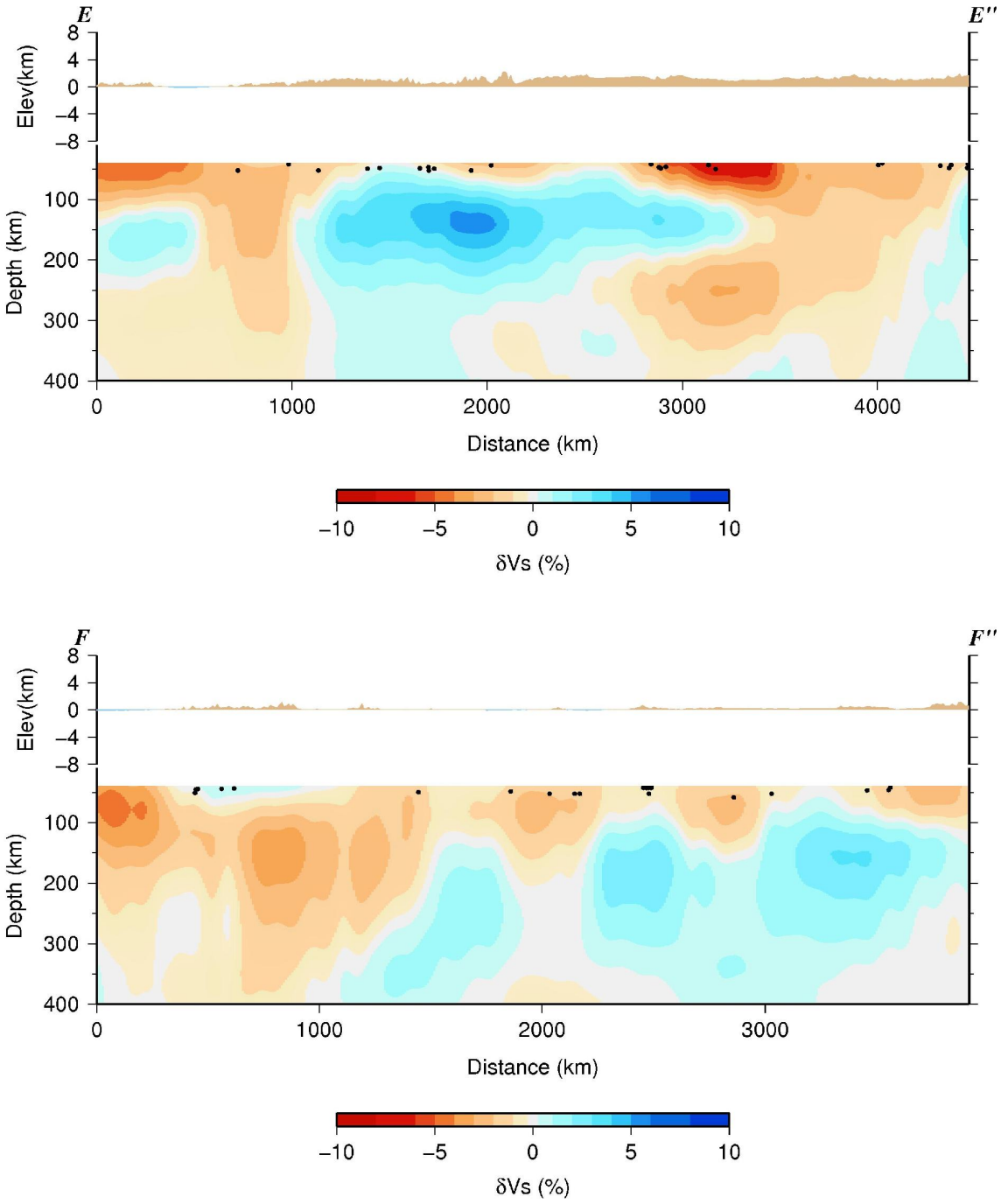

Fig. S5: Vertical sections of the 3D inversion using data excluding paths passing through western part of China where the crust is thicker than 50 km.

Curriculum Vitae

For reasons of data protection, the curriculum vitae is not included in the online version.

Aus Gründen des Datenschutzes erscheint der Lebenslauf nicht in der elektronischen Fassung.

Curriculum Vitae

For reasons of data protection, the curriculum vitae is not included in the online version.

Aus Gründen des Datenschutzes erscheint der Lebenslauf nicht in der elektronischen Fassung.